ISSN 2959-0663 (Print)
ISSN 2959-0671 (Online)
ISSN-L 2959-0663

EURASIAN JOURNAL OF CHEMISTRY

2026. Vol. 31 No. 1(121)

Special Issue

Advanced Polymers and Nanomaterials for Drug Delivery and Other Biomedical Applications

Guest Editor: Professor Vitaliy V. Khutoryanskiy

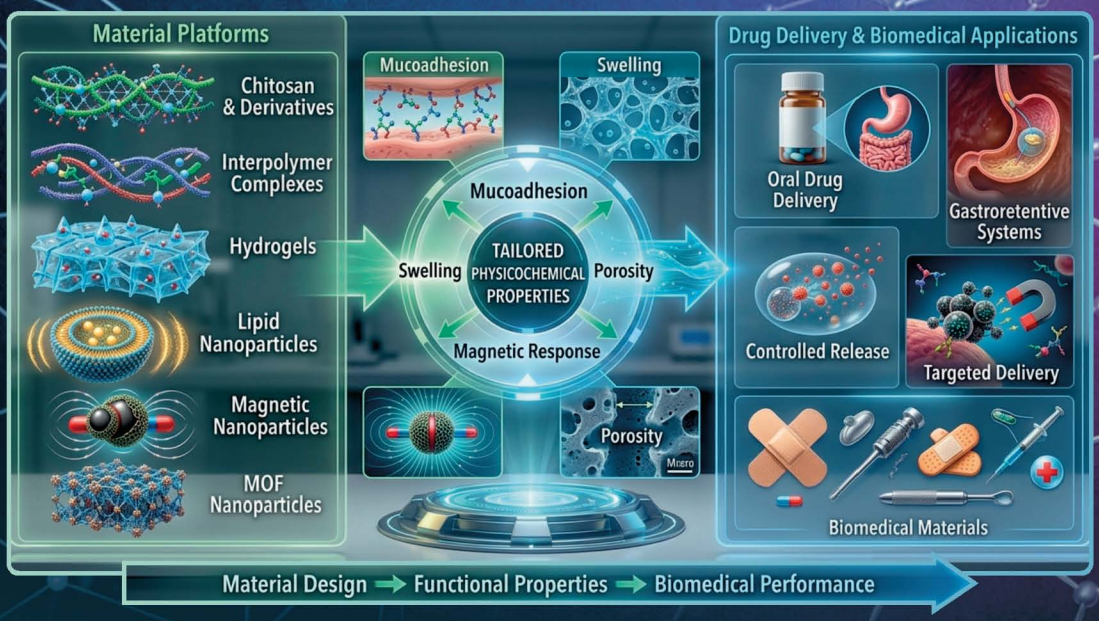

ISSN 2959-0663 (Print)
ISSN 2959-0671 (Online)
ISSN-L 2959-0663

EURASIAN JOURNAL OF CHEMISTRY

2026

Volume 31, No. 1 (121)

Special Issue

Advanced Polymers and Nanomaterials for Drug Delivery and Other Biomedical Applications

Guest Editor: ***Professor Vitaliy V. Khutoryanskiy,***

March 30th, 2026

Founded in 1996

Published 4 times a year

Karaganda
2026

Publisher: **Karaganda National Research University named after Academician Ye.A. Buketov**
Postal address: 28, Universitetskaya Str., Karaganda, 100024, Kazakhstan
E-mail: EJC@karnu-buketov.edu.kz; chemistry.vestnik.ksu.kz@gmail.com
Tel./fax: +7(7212) 34-19-40.
Web-site: https://ejc.buketov.edu.kz

Proofreader I.N. Murtazina

Computer layout V.V. Butyaikin

Eurasian Journal of Chemistry. — 2026. — Vol. 31, No. 1(121). — Special Issue "Advanced Polymers and Nanomaterials for Drug Delivery and Other Biomedical Applications". — 163 p.

ISSN 2959-0663 (Print). ISSN 2959-0671 (Online). ISSN-L 2959-0663

Proprietary: NLC "Karaganda National Research University named after academician Ye.A. Buketov".

Registered by the Ministry of Culture and Information of the Republic of Kazakhstan. Re-registration certificate No. KZ02VPY00134144 dated 14.11.2025.

Signed in print 30.03.2026. Format 60×84 1/8. Offset paper. Volume 20,38 p.sh. Circulation 200 copies. Price upon request. Order № 25.

Printed in the Publishing house of NLC "Karaganda National Research University named after academician Ye.A. Buketov".
28, University Str., Karaganda, 100024, Kazakhstan. Tel.: +7(7212) 35-63-16. E-mail: printed@karnu-buketov.edu.kz

Front cover: OpenAI-generated base image, modified and finalized by the Guest Editor Khutoryanskiy, V.

CONTENTS

PREFACE

ADVANCED POLYMERS AND NANOMATERIALS FOR DRUG DELIVERY AND OTHER BIOMEDICAL APPLICATIONS

How to Cite: Khutoryanskiy, V.V. (2026). Preface to the Special Issue "Advanced Polymers and Nanomaterials for Drug Delivery and Other Biomedical Applications". *Eurasian Journal of Chemistry, 31, 1(121), 5–7.* https://doi.org/10.31489/2959-0663/1-26-0

PREFACE

Editorial

Received: 10 March 2026 | Published online: 19 March 2026

https://doi.org/10.31489/2959-0663/1-26-0

Vitaliy V. Khutoryanskiy

University of Reading, Reading, UK

Preface to the Special Issue "Advanced Polymers and Nanomaterials for Drug Delivery and Other Biomedical Applications"

Guest Editor of the Special Issue "Advanced Polymers and Nanomaterials for Drug Delivery and Other Biomedical Applications" is Professor Vitaliy V. Khutoryanskiy.

Vitaliy V. Khutoryanskiy is Professor of Formulation Science at the University of Reading, United Kingdom. His research interests focus on polymers, biomaterials, and drug delivery systems, particularly mucoadhesive materials and other advanced systems for biomedical applications. E-mail: v.khutoryanskiy@reading.ac.uk; https://orcid.org/0000-0002-7221-2630

Water-soluble polymers and their crosslinked hydrogel counterparts are increasingly used in biomedical technologies owing to their distinctive physicochemical properties. These materials not only improve drug delivery but also provide important functions for addressing medical challenges. They can also serve as platforms for the design of nanomaterials with tailored properties for a wide range of biomedical applications. In this context, the Special Issue "Advanced Polymers and Nanomaterials for Drug Delivery and Other Biomedical Applications" brings together 10 original research papers from experts in Iraq, Kazakhstan, Russia, and Uzbekistan.

In the opening article of this Special Issue, researchers from the Institute of Polymer Chemistry and Physics in Tashkent, Uzbekistan, focus on chitosan, a naturally derived polysaccharide well known for its biocompatibility, biodegradability, low toxicity, mucoadhesive properties, and ability to coordinate metal ions through its amino and hydroxyl groups. These distinctive features make chitosan an especially attractive material for biomedical applications, including drug delivery systems, wound dressings, tissue engineering scaffolds, and nanocomposite design. While chitosan is most commonly obtained by deacetylation of chitin from crustacean shells, this study highlights a more unusual and regionally distinctive source: *Bombyx mori* (silkworm). Using chitosan derived from *Bombyx mori*, the authors investigate the *in situ* synthesis of manganese-containing nanoparticles and demonstrate that the chemisorption method enables effective control over nanoparticle size and morphology. Their findings show how this silkworm-derived biopolymer can act as a stabilizing matrix for metal-containing nanostructures, opening new opportunities for the development of biocompatible nanocomposites and their future applications in biomedical engineering.

Another important study from the Institute of Polymer Chemistry and Physics (Tashkent, Uzbekistan) describes the development of chitosan–caffeine nanocapsules via a self-assembly approach. By using

Bombyx mori chitosan as the shell material, the researchers obtained stable nanostructures with high encapsulation yields, further underscoring the value of this distinctive silkworm-derived polysaccharide for the preparation of advanced nanocarriers and other functional biomedical systems.

The theme of chitosan-based materials is further developed in a study from Buketov Karaganda National Research University (Kazakhstan), which focuses on mucoadhesive chitosan nanoparticles for the delivery of the anti-tuberculosis drug rifampicin. Using a central composite design to optimise the formulation, the authors show that ionotropic gelation can be successfully employed to produce spherical nanoparticles with high drug loading and favourable drug release profiles, highlighting the promise of these systems for mucosal drug delivery applications.

Despite the unique properties of chitosan itself, there is sometimes a need to chemically modify this biopolymer, imparting new properties to the resulting products. In this regard, the next article in this special issue, from the Institute of Polymer Chemistry and Physics (Tashkent, Uzbekistan), reports the synthesis of chitosan sulfate from *Bombyx mori* chitosan. They demonstrate how the degree of sulfation, controlled by reaction temperature, directly influences the polymer's structural amorphization and hydrophilicity. With this polymer, they investigate the anticoagulant activity of the chitosan derivative.

Beyond chitosan, a number of cellulose-derived polysaccharides are also water-soluble. One such example is hydroxypropyl cellulose, which is widely used in pharmaceutical formulations. In their article, researchers from Kazan State Medical University (Russia) exploited the ability of hydroxypropyl cellulose to interact with lightly crosslinked poly(acrylic acid) in mixed systems and designed floating tablets for gastroretentive drug delivery. Sodium bicarbonate was incorporated into these formulations, and the tablets were loaded with acyclovir. The authors reported the *in situ* formation of hydrogen-bonded interpolymer complexes during tablet swelling in the acidic environment of the stomach.

Polymeric hydrogels continue to play an important role in a wide range of biomedical applications, including contact lens materials, wound dressings, drug delivery systems, and tissue engineering scaffolds. Researchers from the Department of Organic Chemistry and Polymers at Buketov Karaganda National Research University (Kazakhstan) present a study on pH- and temperature-sensitive hydrogels based on poly(ethylene glycol)maleate. Their investigation shows how external physicochemical factors influence the behaviour of these terpolymers, which exhibit a remarkably high swelling capacity and a porous network structure.

The second part of this special issue was devoted to nanomaterials for drug delivery and biomedical applications, and several papers explored different classes of such materials. Among them, researchers from the University of Sulaimani (Iraq) reported the development of solid lipid nanoparticles (SLNs) for oral drug delivery. Their study compared itraconazole-loaded SLNs prepared with different solid lipids, including myristic and stearic acids. The findings demonstrated that both lipid chain length and surfactant type, such as Pluronic F127 and Tween 80, play an important role in enhancing the solubility of poorly water-soluble antifungal agents and achieving controlled drug release under varying pH conditions.

A collaborative study by researchers from several Russian institutions, including Surgut State University and the Moscow Aviation Institute, investigates the design of biocompatible goethite (α-FeOOH) nanoparticles. The authors present the first comprehensive analysis of how different iron precursors and alkaline media affect the transformation of ferrihydrite into phase-pure goethite. Through the use of advanced characterisation techniques, including ^{57}Fe Mössbauer spectroscopy and electron microscopy, this work demonstrates the promise of iron-based nanomaterials as stable and safe platforms for biomedical and technological applications.

Further highlighting the importance of precise control over magnetic nanomaterials, researchers from the Moscow Aviation Institute and the Federal Research Center of Problems of Chemical Physics and Medicinal Chemistry (Russia) investigate how the size and magnetization of magnetite (Fe_3O_4) nanoparticles can be tuned. Their study systematically explores the effects of temperature and solvent ratios on nanoparticle stoichiometry and the rheological behaviour of ferrofluids. By revealing a clear relationship between the magnetic induction gradient and nanoparticle capture efficiency in flow-through systems, this work offers valuable guidance for the optimisation of magnetic fluids for magnetotargeting and other advanced biomedical applications.

Metal–organic frameworks (MOFs) are a versatile class of porous nanomaterials constructed from metal centres and organic linkers, and their scientific significance was recently underscored by the 2025 Nobel Prize in Chemistry, awarded for the development of metal–organic frameworks. Bringing the Special Issue to a close, a study by researchers from the Moscow Aviation Institute and the Sklifosovsky Research Institute for Emergency Medicine (Russia) emphasises the crucial influence of processing methods on the func-

tional properties of nanomaterials. Their work on magnetic MOF nanoparticles demonstrates that even routine procedures, such as mechanical grinding and ultrasonication, may trigger substantial structural changes, including variations in magnetite stoichiometry and MOF stability.

In summary, this Special Issue presents an excellent variety of examples demonstrating the applications of polymeric and nanomaterials in drug delivery and biomedicine. The papers collectively showcase the versatility of these systems and underline the importance of rational material design in achieving improved therapeutic performance and broader biomedical functionality. Taken together, they emphasise the continuing impact of advanced materials research on the development of next-generation pharmaceutical and biomedical technologies.

How to Cite: Ergashev, K.Kh., Vokhidova, N.R., & Rashidova, S.Sh. (2026). Synthesis of Stabilized Manganese-Containing Nanoparticles with *Bombyx mori* Chitosan Macromolecules under *In Situ* Conditions. *Eurasian Journal of Chemistry, 31, 1(121), 8–29.* https://doi.org/10.31489/2959-0663/1-26-1

ADVANCED POLYMERS AND NANOMATERIALS FOR DRUG DELIVERY AND OTHER BIOMEDICAL APPLICATIONS

Article

Received: 21 November 2025 | Revised: 23 February 2026 | Accepted: 2 March 2026 | Published online: 10 March 2026

UDC 541.64: 547.458.61:544.773

https://doi.org/10.31489/2959-0663/1-26-1

Kandiyor Kh. Ergashev*, Noira R. Vokhidova, Sayyora Sh. Rashidova

Institute of Polymer Chemistry and Physics, Tashkent, Uzbekistan
*(*Corresponding author's e-mail: kandiyor_ergashev@yahoo.com)*

Synthesis of Stabilized Manganese-Containing Nanoparticles with *Bombyx mori* Chitosan Macromolecules under *In Situ* Conditions

Manganese nanoparticles are highly reactive and tend to aggregate and oxidize, which limits their practical application. Therefore, the aim of this study was to synthesize and stabilize Mn nanoparticles using *Bombyx mori* chitosan as a natural biopolymer matrix under controlled *in situ* conditions and to investigate their structural and physicochemical properties. Samples containing Mn nanoparticles stabilized with chitosan in the presence of reducing agents, with hydrodynamic dimensions of 118 nm (97 %) and 144 nm (96 %), were synthesized under *in situ* conditions. The structural and morphological characteristics were studied using IR spectroscopy, X-ray diffraction (XRD), dynamic light scattering (DLS), and electron microscopy. IR spectroscopic studies revealed local rearrangements within the repeating units of the chitosan polymer chain and interactions between the –NH and –C=O functional groups and manganese-containing nanoparticles. XRD analysis confirmed the reduction of Mn^{2+} ions. Morphological studies of chitosan–manganese films showed the formation of 50 nm tetragonal and 90 nm spherical metal nanoparticles under the selected synthesis conditions. The results confirm the stabilization of Mn nanoparticles with *Bombyx mori* chitosan by the chemisorption method and demonstrate effective control of particle size and morphology. Further research should focus on evaluating long-term stability, functional properties, and potential biomedical applications of the synthesized nanocomposites.

Keywords: manganese nanoparticles, chitosan, *Bombyx mori*, nanocomposites, *in situ* synthesis, chemisorption, biopolymers, nanoparticle stabilization, particle morphology, size control

Introduction

Manganese (Mn) is an essential trace element for the body, providing enzyme activity, antioxidant protection, and hormonal balance. The role of this element in the reproductive system has been the focus of attention in recent years, and its effects can be positive or negative depending on the dose [1–3]. Manganese plays a crucial role in antioxidant protection, particularly by stimulating the activity of superoxide dismutase (Mn-SOD), which reduces oxidative stress in spermatozoa and oocytes [1, 4]. Additionally, Mn enhances energy metabolism, particularly glycolysis, and promotes follicle development in granulosa and oocyte cells [5, 6]. Manganese activates enzymes involved in the synthesis of cholesterol-based hormones (testosterone, progesterone). In this way, it regulates the secretion of FSH (Follicle-Stimulating Hormone) and LH (Luteinizing Hormone), thereby maintaining hormonal balance through the hypothalamic-pituitary-ovarian axis [7, 8]. High doses of manganese reduce sperm count and motility, lower testosterone levels, and can minimize ovarian mass by up to 25–30 % [8, 9]. These effects are dose-dependent and show a U-shaped

dose-response relationship [10]. Manganese enhances the glycolysis pathway in granulosa cells, increasing the expression of the enzymes GLUT4 (*Glucose Transporter Type 4*) and PFKL (*Phosphofructokinase, Liver Type*) [5]. This activates the mTOR (mechanistic *Target of Rapamycin*) and PI3K/Akt (*Phosphoinositide 3-Kinase / Protein Kinase B (Akt)*) signaling cascades, which stimulate follicular development [10, 11].

In addition, it can also affect the ovulatory process through the IGF1 (Insulin-like Growth Factor 1)/mTOR signaling cascade, kisspeptin expression, and gene regulation [12, 13]. Manganese is an essential trace element for the reproductive system, and while it is beneficial at moderate doses, it can be toxic at high doses. Recent studies have focused on uncovering the precise molecular mechanisms of these effects, which could provide a solid basis for clinical studies [14]. The dual effects of manganese on reproductive health and its high dose sensitivity highlight the need for its delivery in a bioavailable, stable, and controlled form. In this regard, the synthesis of manganese in nanoparticle form is a crucial scientific direction for the development of targeted therapeutic applications in the reproductive system, as it enhances its bioavailability, tissue specificity, and pharmacokinetic properties.

The methods used to synthesize manganese nanoparticles determine the size, shape, degree of crystallinity, and function of the particle. There are various methods for synthesizing manganese (Mn) nanoparticles, each with its own advantages and disadvantages. One of the traditional methods, the co-precipitation method, is simple, inexpensive, and allows for the obtaining of large quantities of nanoparticles; however, it is difficult to precisely control the particle size, and the possibility of agglomeration is high [15]. Hydrothermal and solvothermal methods enable the formation of crystal structures under high temperatures and pressures. In the hydrothermal method, water serves as the primary medium, whereas in the solvothermal method, organic solvents are the primary medium. The advantages of this method are high phase purity and easy control of shape and size [16, 17]. One of the modern methods, "green synthesis", converts Mn salts into nanoparticles using plant extracts (phytochemicals such as flavonoids and polyphenols). It is also possible to oxidize Mn^{2+} using microorganisms (some bacteria and fungi) to produce bio-nanoparticles. The green synthesis method is environmentally friendly, convenient, and inexpensive; however, the reaction time is long, and scaling up presents difficulties [18, 19]. Additionally, microwave and ultrasonic (sonochemical) synthesis methods offer energy-efficient and rapid reaction conditions. In the microwave method, the reaction is heated uniformly and quickly. In ultrasonic synthesis, the particles are crushed due to the cavitation effect [20]. Today, manganese ferrite nanoparticles ($MnFe_2O_4$) are used in magnetic materials (MRI), sensors, catalytic, and environmental purification technologies. Co-precipitation, sol-gel, microwave, and "combined" methods are mainly used for their synthesis [21].

However, it should be noted that these methods have primarily synthesized nanoparticles of manganese oxides, such as MnO, MnO_2, α-MnO_2, β-MnO_2, and Mn_3O_4. The synthesis of elemental manganese (Mn^0) nanoparticles remains a significant challenge and is relatively poorly understood in the scientific literature. Several factors can be identified as the primary issues in the synthesis. Since manganese atoms show a high affinity (oxophily) for oxygen, it isn't easy to stably maintain and synthesize its elemental state (Mn^0).

Manganese is rapidly oxidized upon exposure to air, forming oxide phases such as MnO, Mn_3O_4, and MnO_2 [22]. Even when synthesized in an inert environment, the formation of an oxidized layer is likely to occur [23]. Potent reducing agents are required to obtain Mn from manganese salts. However, these substances (e.g., $NaBH_4$, H_2, $LiAlH_4$) are highly reactive, hazardous to handle, and difficult to control. Additionally, even under these chemical reduction conditions, the particles are not completely reduced, and mixed phases (Mn/MnO and Mn_3O_4) are formed [24]. Synthesized manganese nanoparticles are prone to agglomeration and lose their uniformity in size and shape. This negatively affects their catalytic, optical, and magnetic properties [25]. Due to their high density, they are not stable in suspension in water or organic media [26].

Most scientific research has focused on the study of the oxide forms of manganese (MnO, MnO_2, Mn_3O_4), and not enough attention has been paid to elemental Mn particles. According to a literature review, the number of articles on Mn^0 nanoparticles published over the last 10 years is minimal, and even those that have been published have primarily been in the context of catalysis or nanocomposites [22, 27].

Recent studies have demonstrated that stable Mn nanoparticles can be synthesized under inert atmospheres (Ar, N_2) using microwave energy [23, 28]. Another promising approach is to protect manganese particles from oxidation by coating them with organic ligands or polymers. For example, the use of stabilizers based on oleyl amine, polyethylene glycol, or cellulose can ensure the stability of Mn in air [25, 26]. Therefore, this work aims to synthesize stabilized Mn in the presence of *Bombyx mori* chitosan

(CS), which has stabilizing properties, to overcome the problems associated with the oxidation susceptibility and agglomeration of manganese nanoparticles.

Experimental

Chemicals and Materials

For the research work, *Bombyx mori* chitosan (molecular mass 41×10^3 Da; deacetylation degree 86 %), $MnCl_2\cdot4H_2O$ with a purity of ≥ 99.0 % (Shanghai Aladdin Biochemical Technology Co., Ltd.), $NaBH_4$ with a purity of 98 % (Sinopharm Chemical Reagent Co., Ltd.), and mild reducing agent $C_6H_8O_6$ (Macklin Biochemical Co., Ltd.) were used. All reagents were of "analytical grade" grade, with a purity of ≥99.0 %, and were used without additional purification procedures. All solutions were prepared in deionized water.

Infrared Spectroscopy (FTIR) Analysis

IR spectroscopic analysis was performed on a Bruker INVENIO-S-S model (in the range of 400–4000 cm^{-1}). The samples were prepared in the form of tablets in the presence of potassium bromide (KBr) salt. FTIR spectra of chitosan and chitosan-stabilized Mn nanosystems were recorded for characterization of their functional groups [29–31].

X-Ray Diffraction (XRD)

The phase composition and crystallinity of the samples were investigated using a DRON-3M X-ray diffractometer under Co Kα radiation (U = 22 kV, I = 16 mA). The crystallite size was calculated using the Debye-Scherrer equation (K = 0.9; β — FWHM; RD patterns were recorded using Co Kα radiation (λ = 1.7902 Å).). The degree of crystallization was determined by the ratio of the intensities of J (crystalline peak) and J_a (amorphous background) [32].

Atomic Force Microscopy (AFM)

The morphological characteristics of the samples were analyzed using atomic force microscopy (Agilent 5500, USA). Silicon cantilevers ($k \approx 9.5$ N/m; resonant frequency ≈ 145 kHz) were used. The scanning area was 15×15 μm^2 in the X and Y axes, and ≈ approximately one μm in the Z axis. Images were acquired at 22 °C in tapping mode. The average particle size and distribution were estimated by histogram analysis.

Scanning Electron Microscopy (SEM) and Energy Dispersive Spectroscopy (EDS)

The surface morphology of the samples was studied using a JEOL JSM–IT210 scanning electron microscope. The operating voltage ranged from 5 to 15 kV, and the working distance was ≈ approximately 10.8 mm. Images at various scales were obtained using the InTouchScope software. Energy dispersive spectroscopy (EDS) analyses were performed to determine the elemental composition. The content of carbon (C), nitrogen (N), oxygen (O), and manganese (Mn) was noted; silicon (Si) peaks were explained by the effect of the glass substrate (SiO_2).

Synthesis of Mn Particles without Polymer Matrix (Control Experiment S-1, S-2)

In the control experiment (without chitosan), 20 ml of a 0.0012 mol/L solution of $MnCl_2$ was used. The reaction was carried out at 30 °C with intensive stirring at 600 rpm. A 0.025 mol/L solution of $NaBH_4$ was added dropwise to this system.

The main reduction reaction takes place in the following form [33, 34]:

$$MnCl_2 + 2NaBH_4 + 6H_2O \rightarrow Mn(s) + 2NaCl + 2B(OH)_3 + 7H_2\uparrow$$

In sample S-1, only $NaBH_4$ was used as a reducing agent.

In sample S-2, ascorbic acid ($C_6H_8O_6$, 3.5×10^{-5} mol/L) was added together with $NaBH_4$ [33–38]:

$$MnCl_2 + NaBH_4 + C_6H_8O_6 \rightarrow Mn + NaCl + H_2 + B(OCH_2)_3 + \\ + \text{(Mn-borate complex and similar by-products)}$$

$NaBH_4$, as a potent reducing agent, quickly reduces Mn^{2+} ions to the Mn state. In contrast, ascorbic acid, as a relatively mild reducing agent, controls the kinetics of particle growth, limits agglomeration, and ensures the stability of the resulting suspension [39–41].

Synthesis of Mn Nanoparticles under in situ Conditions (S-3, S-4)

In the *in situ* synthesis process, a chitosan solution (0.06 mol/L) was added to the reaction medium prior to the commencement of the reaction. Then, a 0.0012 mol/L $MnCl_2$ solution was stirred at 30 °C and 600 rpm, and a 0.025 mol/L $NaBH_4$ solution was added dropwise. In sample S-3, only $NaBH_4$ was used as a reducing agent. In sample S-4, ascorbic acid (3.5×10^{-5} mol/L) was added along with $NaBH_4$. The polycationic nature of chitosan creates an electrostatic barrier around the particle core, thereby limiting the growth and agglomeration of the core. Thus, chitosan enhances the colloidal stability of the suspension, ensures the hydrophilicity of the resulting nanoparticles, and facilitates their uniform size distribution [42–44].

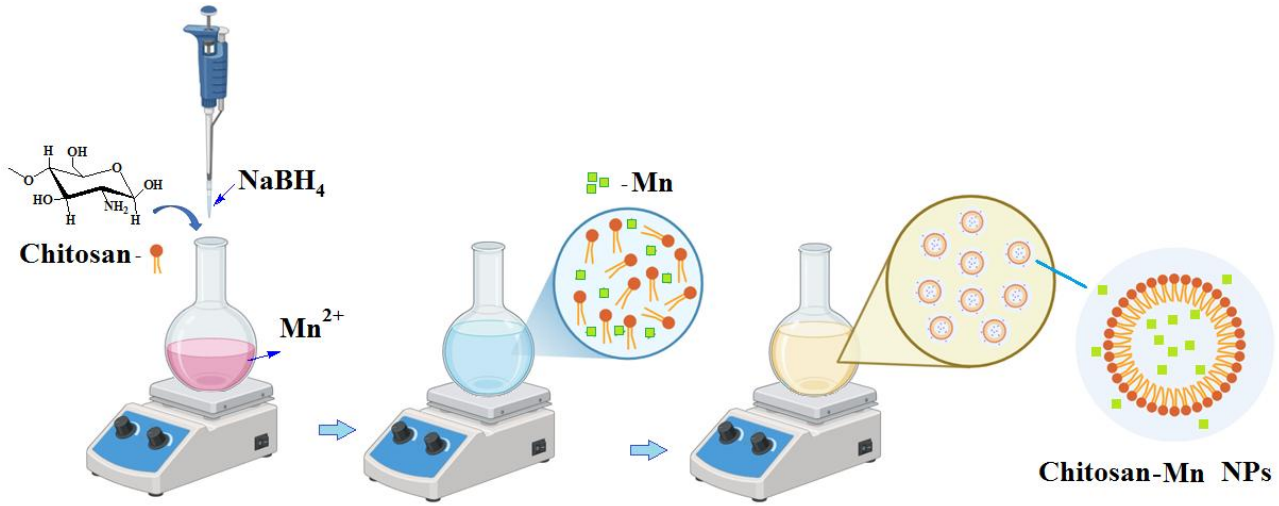

a) Synthesis of CS-Mn nanoparticles in the presence of $NaBH_4$ reducing agent under *in situ* conditions

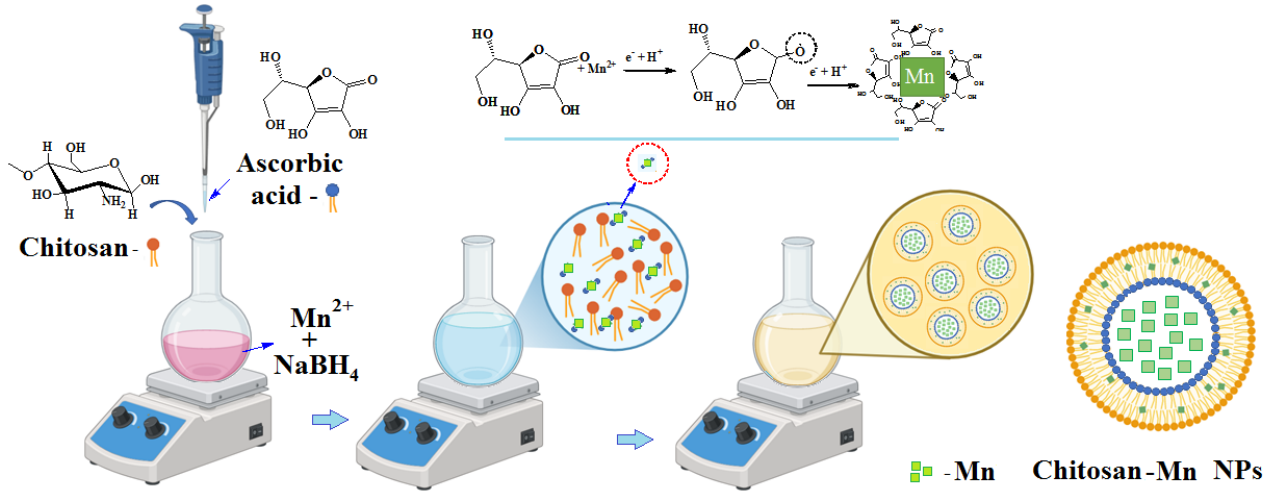

b) Synthesis of CS-Mn nanoparticles in the presence of $NaBH_4/C_6H_8O_6$ reducing agent under *in situ* conditions

Figure 1. Synthesis of CS-Mn nanoparticles under *in situ* conditions
Illustration created in BioRender. Ergashev, Q. (2026) https://BioRender.com/qy5h0tq

The chitosan/Mn suspensions obtained after synthesis were purified from excess ions and small molecules by dialysis. For this purpose, a cellulose acetate membrane was used (nominal cutoff size ≈500 nm). The dialysis process was carried out for 24 hours, with the dialysis water being replaced every 3 to 4 hours. This effectively cleared the colloidal system of excess salts and reaction products [29].

Dynamic Light Scattering (DLS) Analysis

DLS determined the hydrodynamic size and distribution of the particles, and the analysis was performed using a Photocor Compact spectrometer with a He-Ne laser source at a wavelength of 632.8 nm. The samples were prepared in an aqueous medium and stored at a thermostated temperature of 25 °C ± 0.1 °C. The sample concentration was maintained at 0.05 mg/mL, a low level designed to prevent

aggregation. Each sample was measured for 3 minutes in at least three replicates. The particle size range was determined to be between 1 nm and 100 μm. DLS analysis was primarily employed to evaluate the hydrodynamic size distribution of nanoparticles and to assess the influence of chitosan on particle size control.

Statistical Analysis

All experiments were repeated at least three times ($n = 3$), and the results are presented as mean ± standard deviation (SD). The Shapiro–Wilk test was used to test the hypothesis of normal distribution. Differences between groups were tested by one-way ANOVA*; when significant differences were noted, Tukey's post hoc test was used. All calculations and graphs were performed using OriginPro 2023 (OriginLab, USA) and GraphPad Prism 9.0 (GraphPad Software, USA). The significance level in all statistical tests was set at $p < 0.05$.

Results and Discussion

Hydrodynamic Sizes (DLS Analyses)

Dynamic light scattering (DLS) analysis of the chitosan solution (CS) showed a broad number-weighted hydrodynamic size distribution with an average size in the range of approximately 3–4 μm, indicating a polydisperse system with a dominant population in the micrometer range.

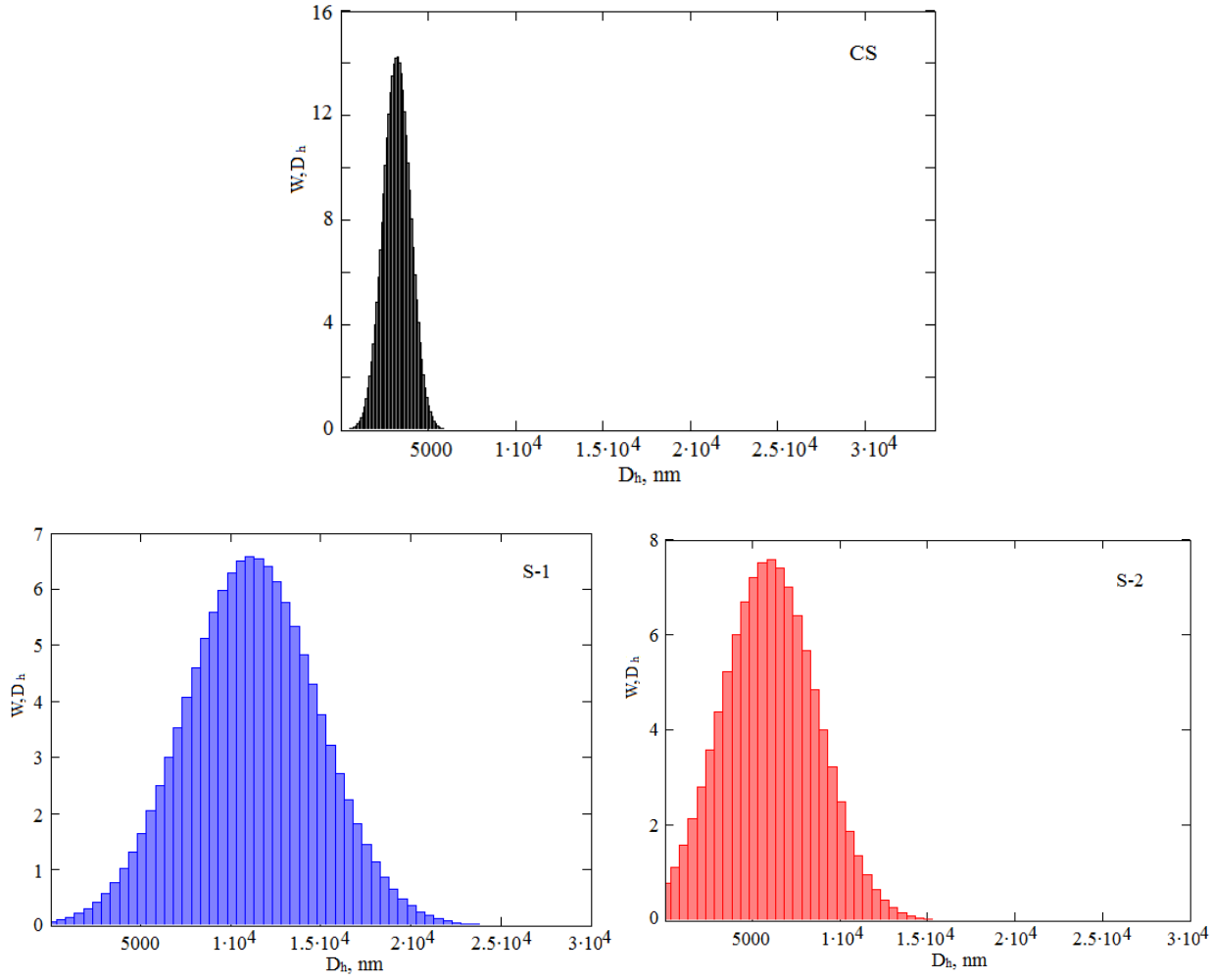

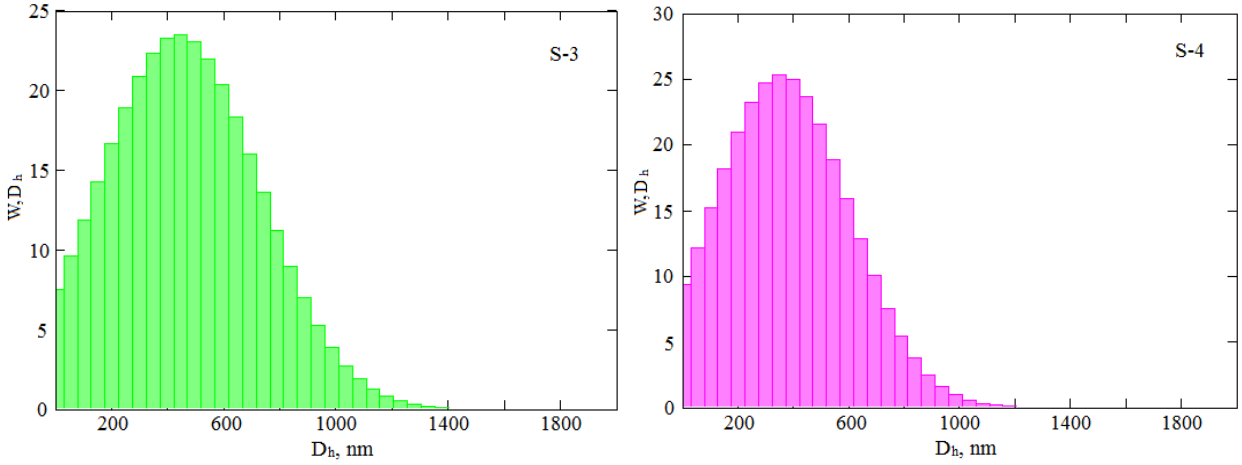

Figure 2. Hydrodynamic radius distributions of manganese-containing particles obtained under control conditions without polymer matrix (S-1, S-2) and by *in situ* synthesis in the presence of chitosan (S-3, S-4)

The results indicate that, in the control experiments performed in the absence of chitosan, DLS analysis revealed apparent hydrodynamic sizes predominantly in the micrometer range. Specifically, the S-1 sample exhibited a single broad population with an average hydrodynamic size of approximately 10–12 μm. In contrast, the S-2 sample showed a dominant population with average hydrodynamic sizes in the range of 6–8 μm (Fig. 2). It should be emphasized that such micrometer-scale DLS signals are most likely associated with pronounced particle aggregation and partial sedimentation occurring in the absence of a stabilizing polymer matrix, rather than with the presence of stable primary nanoparticles. The strong reducing capability of $NaBH_4$ promotes rapid reduction of Mn^{2+} ions, resulting in uncontrolled nucleation and extensive aggregation. In contrast, the use of ascorbic acid as a weaker reducing agent (S-2) leads to slower nucleation, allowing the transient formation of smaller species prior to aggregation, in agreement with previously reported studies [45–47].

The hydrodynamic size distributions of manganese-containing particles obtained via *in situ* synthesis in the presence of chitosan revealed a dominant nanoscale population. For both samples S-3 and S-4, the average hydrodynamic particle sizes were found to be in the range of approximately 300–500 nm (Fig. 2). In comparison with the control experiments, this shift toward smaller and more uniform sizes indicates a moderated nucleation–growth process. Such behavior reflects the stabilizing influence of chitosan on manganese-containing particles formed under *in situ* synthesis conditions, leading to reduced aggregation and a more controlled particle size distribution [38, 40-41, 46].

IR-Spectroscopic Analysis

In the IR spectrum of the original chitosan, characteristic absorption bands corresponding to the macromolecule were observed. In particular, a broad band in the range of 3400–3450 cm^{-1} is characteristic of stretching vibrations of the –OH and $–NH_2$ groups, which has a relatively broad appearance due to the strong N–N bonds in chitosan molecules. The peaks at 2920–2930 cm^{-1} and 2850 cm^{-1} correspond to asymmetric and symmetric C–H stretching vibrations of the $–CH_2$ and –CH groups. The peak in the range of 1650–1660 cm^{-1} (Amid I) mainly refers to stretching vibrations of the C=O bond. The peak in the region of 1560–1580 cm^{-1} is associated with deformation vibrations of the N–H bond (Amid II). The peaks at 1410–1430 cm^{-1} and 1375 cm^{-1} represent the stretching and bending vibrations of the $–CH_2$ and $–CH_3$ groups, respectively. The band observed between 1150–1070 cm^{-1} is assigned to asymmetric C–O–C glycosidic stretching vibrations of chitosan (Fig. 3, *1*) [42–44].

It is well established from the literature that, upon interaction with various metals and their oxides, chitosan exhibits adsorption on its surface through its –OH and $–NH_2$ functional groups. This process is mainly ensured by hydrogen bonds, electrostatic interactions, and polymer-matrix structure [45]. In the IR spectrum of the S-3 composite formed by chitosan with manganese nanoparticles, shifts in the vibration peaks of the amine and amide groups were observed at ~1544 cm^{-1} → ~1636 cm^{-1} and ~1402 cm^{-1} → ~1374 cm^{-1} (Fig. 3, *2*). This indicates the electrostatic interaction of $–NH_2$ and C–N groups with Mn particles on the surface [43, 45]. In some cases, the amide I/II peaks shifted from 1647 cm^{-1} to ~1560 cm^{-1}, indicating donor-acceptor interactions through the –C=O and $–NH_2$ groups.

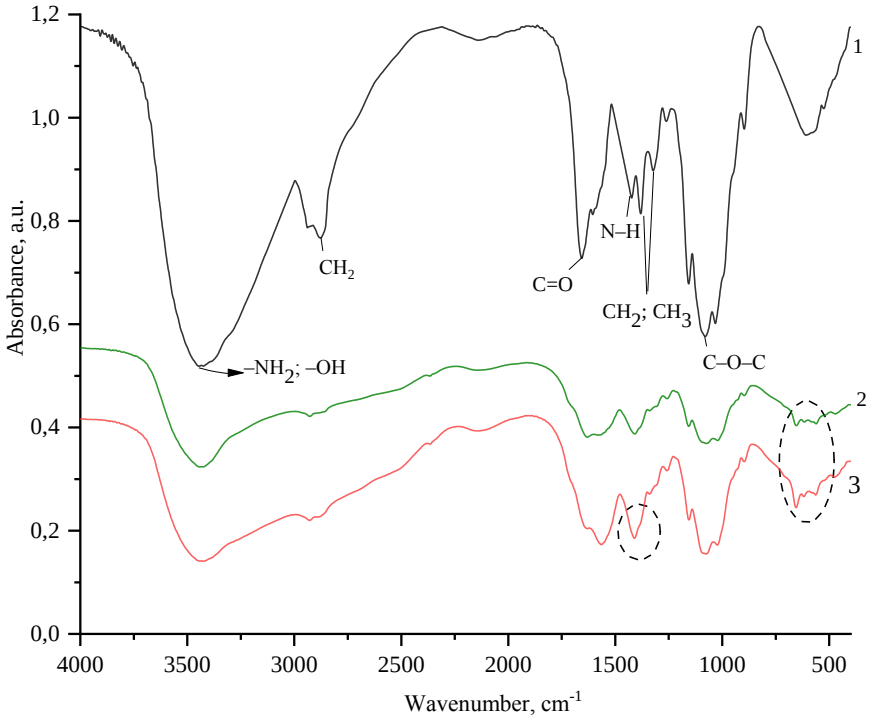

Figure 3. IR spectrum of chitosan (*1*), S-3 (*2*), and S-4 (*3*) samples

The peaks in the range of 1155, 1073, and 1021 cm^{-1}, characteristic of C–O–C glycosidic bonds, are largely preserved. However, the decrease in intensity at 1258 cm^{-1} may indicate the possibility of non-covalent interactions of the Mn–OH or Mn–OH type through hydroxyl groups. These results are consistent with the literature [47]. Additionally, the shift of the CH_2/CH_3 vibration peaks from 1423 cm^{-1} to 1383 cm^{-1} is attributed to local structural changes in the polymer environment. Although manganese NPs are not oxidized, they exhibit metal-polymer surface interactions through weak but consistent peaks around ~560–600 cm^{-1} in the IR spectrum [48, 49]. These peaks are due to the metal interacting with –OH and $–NH_2$ groups through surface activity.

The IR spectrum of the S-4 sample, shows shifts in the –N–H and –C=O vibrational bands associated with $–NH_2$, C=O, and C–N (amide) groups, indicating the presence of intermolecular hydrogen bonding or electrostatic interactions between chitosan and manganese species.The shift of the peaks belonging to the CH_3/CH_2 and C–O groups indicated that these structural units participate in the stabilization of the nanoparticles within the matrix through peripheral adsorption (Fig. 3, *3*) [50–52]. The new peak appearing at 895 cm^{-1} can be interpreted as a local geometric rearrangement in the chitosan skeleton or a metal-hydroxyl (Mn–OH) bond. Peaks in the range of 654–617–562 cm^{-1} indicate the strength of Mn–O or Mn–OH bonds, suggesting a “tunnel-like” arrangement of nanoparticles within chitosan. Although ascorbic acid is involved in the formation, IR results indicate that it does not directly react chemically with chitosan, but instead acts physically, i.e., as a passive stabilizer [50–54].

XRD Analysis

The phase structures of chitosan and its stabilized S-3 and S-4 samples were studied by X-ray diffraction analysis. The crystalline structure of chitosan is in a semi-amorphous state, which shows two prominent diffraction peaks: 2θ = 10.49° (020) (amid I “$–N–CO–CH_3$”) and 19.95° (110) (amid II “$–NH_2$”) (Fig. 4) [55–57].

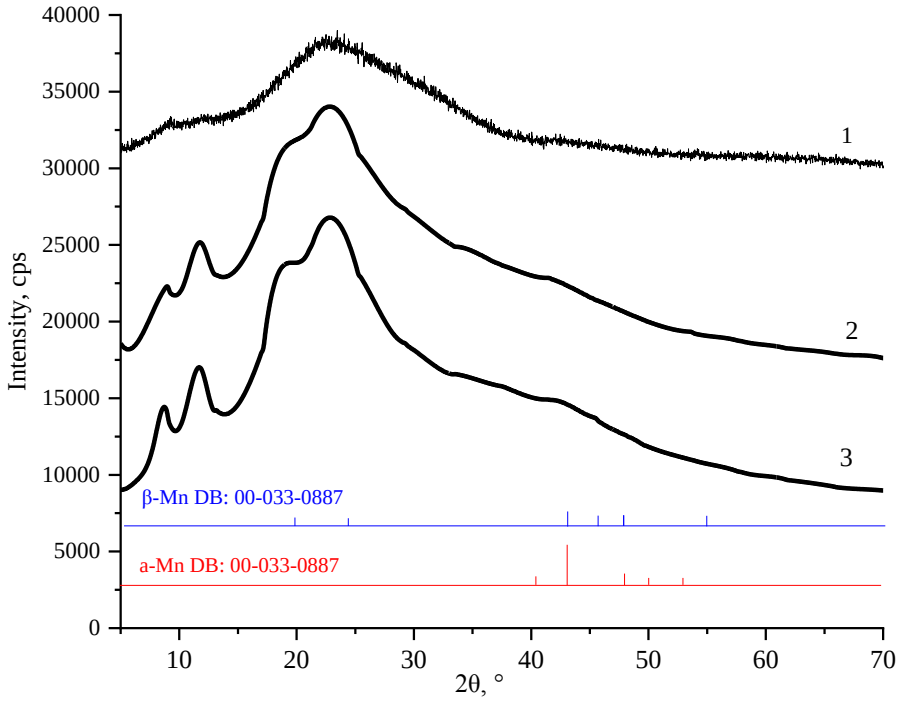

Figure 4. XRD patterns of chitosan (*1*), S-3 (*2*), and S-4 (*3*) samples

Manganese is a 3*d*-metal with various allotropic forms. Its main crystalline phases, α-Mn and β-Mn, are distinguished by their atomic structure, thermodynamic stability, and X-ray diffraction characteristics. Based on XRD analyses of these phases in the literature, the prominent diffraction peaks for α-Mn are located in the following positions in Cu Kα light: 2θ 38.5°, 44.8°, 65.1°. These peaks correspond to the (220), (311), (400) orientations, respectively [58]. The β-Mn phase is stable at high temperatures (T > 973 K) and has a cubic (chiral) structure [59, 60]. The prominent simulated XRD peaks for the β-Mn phase are: 2θ 38.5°; 44.8°; 65.1°; 78°, 82° and these peaks are mainly associated with the (220), (311), and (400) bonds [61, 62].

The diffraction peaks and crystal parameters of the S-3 and S-4 samples, as determined by XRD analysis, are presented in Table 1.

Table 1

Crystal parameters and crystal sizes of chitosan, S-3, and S-4 samples

No.	2θ, °	d, Å	(FWHM) β, °	(Size) L, Å	Crystallinity, %
CS					
1	10.49	8.43	2.54	3.28	38
2	19.95	4.44	1.98	4.3	
Sample S-3					
3	8.53	10.36	1.36	61	53
4	11.73	7.53	2.38	35.0	
5	18.26	4.85	2.51	33.4	
6	21.78	4.07	7.97	10.60	
7	43.63	2.07	6.4	14.1	
Sample S-4					
8	8.49	10.41	1.91	43.5	48
9	11.58	7.64	2.37	35.1	
10	18.48	4.79	2.5	34	
11	21.94	4.04	7.49	11.28	
12	43.40	2.08	5.3	16.9	
13	60.5	1.52	9	11	

In the XRD pattern of sample S-3, 2θ 8.53°, 11.73°, 18.26°, and 21.78° are the peaks that are shifted due to the interaction of chitosan with Mn nanoparticles. These peaks are due to structural rearrangement, interaction of manganese nanoparticles with chitosan chains through electrostatic and hydrogen bonding, and these interactions disrupt the ordered arrangement between chitosan molecules, causing a shift in the position of the diffraction peaks [63]. Such peaks have also been observed in chitosan–metal oxide composites [64]. The 2θ 43.63° peak indicates that the Mn^0 metallic state is stable in the nanoparticles, which is mainly reflected on the (111) crystal surface [65–67]. The composition of sample S-3 produced CS/Mn crystal types consisting of α-Mn cubic (*a* — 5.218, *b* — 5.218, *c* — 5.218 Å), β-Mn cubic (*a* — 4.433, *b* — 4.433, *c* — 4.433 Å) and tetragonal structure (*a* — 10.784, *b* — 11.329, *c* — 4.449 Å) was determined to be.

In the XRD pattern of sample S-4, the peaks at 2θ 8.53° (020) and 11.73° (110) are shifts of the 10.49° peak in pure chitosan. The peaks at 2θ 18.26° and 21.78° are shifts of the 19.95° peak in pure chitosan. The reasons for these shifts have been explained above [63, 64]. Ascorbic acid changes the hydrogen bonds between water molecules and hydroxyl groups in the chains, causing local disorder. It is also possible that after these Mn nanoparticles enter the chitosan matrix, local disorders occur in the order of the molecular chains, which leads to broadening and shifting of the peaks [68]. The peak at 2θ 43.63° (111) belongs to the crystalline phase of metallic manganese (Mn). Ascorbic acid more effectively chemically reduced Mn^{2+} ions to the Mn state, and manganese nanoparticles were formed with a high degree of crystallinity. In addition, a new 2θ 60.5° peak was formed in sample S-4. This peak was based on metal–carboxyl or metal–amine bonds, and it was noted that a new crystal or quasi-crystalline structure was formed in the composite structure, or that metal complexes of chitosan in the sources gave a peak around 2θ ≈ 60°. It was found that the composition of sample S-4 was α-Mn cubic (*a* — 5.218, *b* — 5.218, *c* — 5.218 Å), β-Mn cubic (*a* — 4.433, *b* — 4.433, *c* — 4.433 Å) and the formation of new crystal types of the CS-Mn system with a tetragonal structure (*a* — 11.81, *b* — 7.860, *c* — 4.072 Å). The results obtained in the S-5 sample show that ascorbic acid, as a reducing agent in the reaction, converts Mn^{2+} ions to the Mn state and interacts with chitosan chains, changing their molecular order [69, 70].

It should be noted that the diffraction peak observed at 2θ ≈ 43° cannot be considered unambiguous evidence of the presence of Mn alone, as this region may overlap with reflections of MnO, Mn_3O_4, or mixed manganese-containing phases. Furthermore, IR spectroscopy does not allow a clear distinction to be made between metallic manganese and its oxide compounds. Given the aqueous synthesis conditions and exposure to air, partial oxidation of the surface of the Mn nanoparticles or the formation of mixed Mn/Mn_xO_y nanostructures cannot be ruled out. Similar surface oxidation phenomena have been widely described for manganese-containing nanoparticles synthesized in polymer matrices [63, 64, 68–70]. Therefore, the resulting nanoparticles are more accurately described as manganese-containing nanoparticles, potentially consisting of a metal core with an oxidized surface layer.

AFM Analysis

AFM analyses show that chitosan films often have a rough, granular or cross-linked morphology. This is dependent on the molecular weight and degree of deacetylation of chitosan. For example, it has been reported that a decrease in the molecular weight of chitosan leads to the formation of small blocks on the surface and a decrease in crystallinity [71]. The surface morphology and particle distribution of chitosan films were analyzed by atomic force microscopy (AFM). The results of 3D topography showed that the surface of the chitosan film is not uniform, but is characterized by a globular morphology. The maximum value of the vertical relief (*Z*-axis) is on average around 360 nm, which is associated with the predominantly amorphous structure of the chitosan chains and the formation of surface defects (Fig. 5). Such rough surface morphology has been noted in AFM studies as a characteristic of the natural polysaccharide nature of chitosan [72, 73].

Histogram analysis revealed that the average particle size was 0.308 μm and that they were mainly distributed in the range of 0.154–0.462 μm. These parameters indicate that the chitosan film is homogeneous at the nanoscale and consists of globular structures. The presence of chitosan particles in nanometers can enhance its sorption capacity and have a positive effect on the process of complex formation with metal ions, the formation of nanostructures with various morphologies with metals [71–73]. It can be seen that the particles with a relief pattern height of 100–200 nm on the surface formed a heterogeneous surface.

In order to fully study the morphological structure of the chitosan-Mn-based nanosystem, AFM images were obtained. The AFM image of sample S-3 confirmed the XRD and SEM results and showed that it consists of nanoparticles with a cubic and tetragonal structure. The formed nanoparticles formed

agglomerates densely located and less than 1 μm in size. The particle distribution histogram with respect to the surface is asymmetric, with nanoparticles distributed in the range from 10 nm to 110 nm, with an average size of 50 nm accounting for 14 %. It can be seen that the distribution of Mn nanoparticles along the polymer matrix on the surface of the film is not uniform on the uneven surface (Fig. 6).

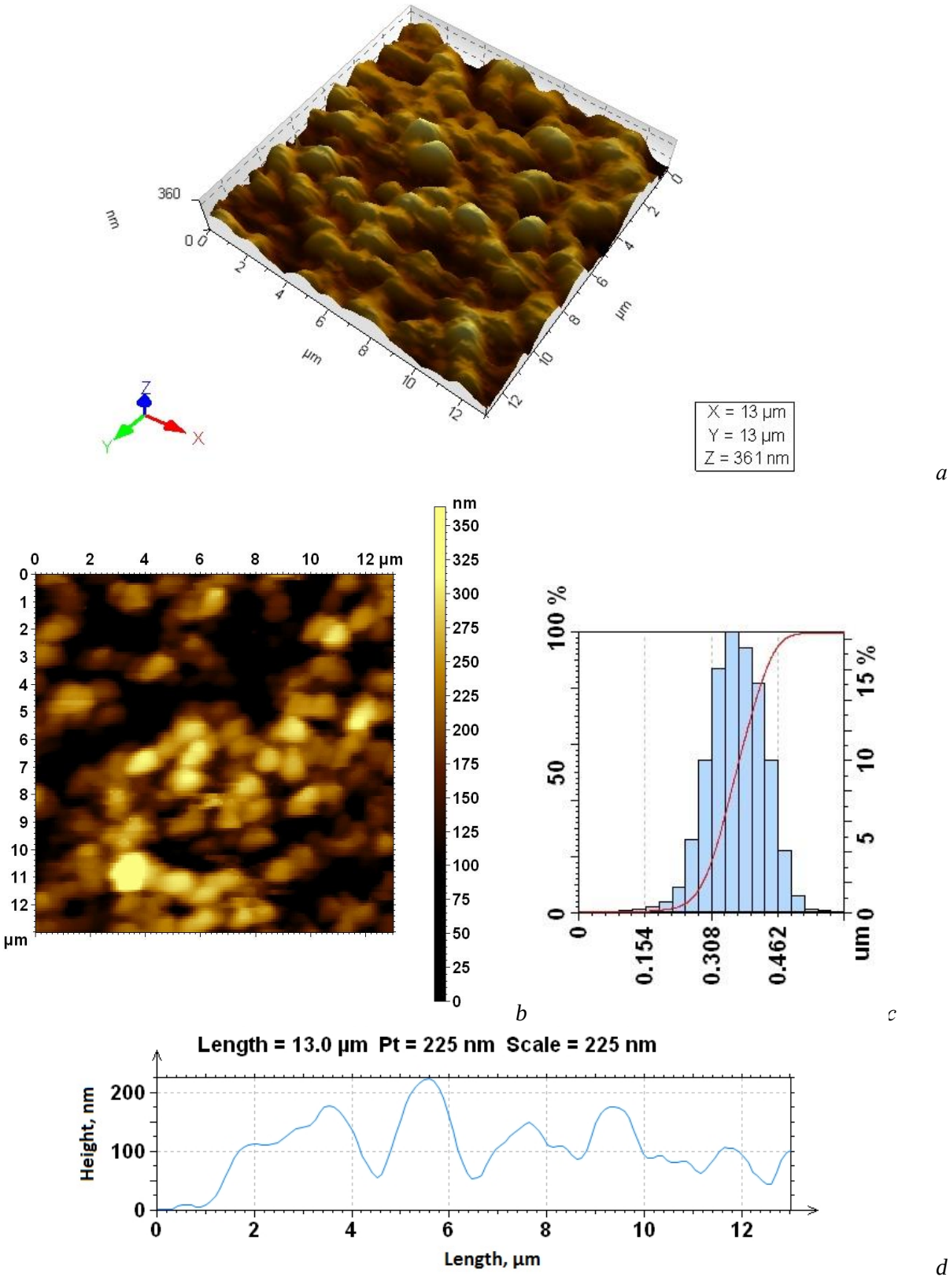

Figure. 5. AFM image (*a*, *b*), distribution histogram (*c*) and surface relief (*d*) of a *Bombyx mori* chitosan film

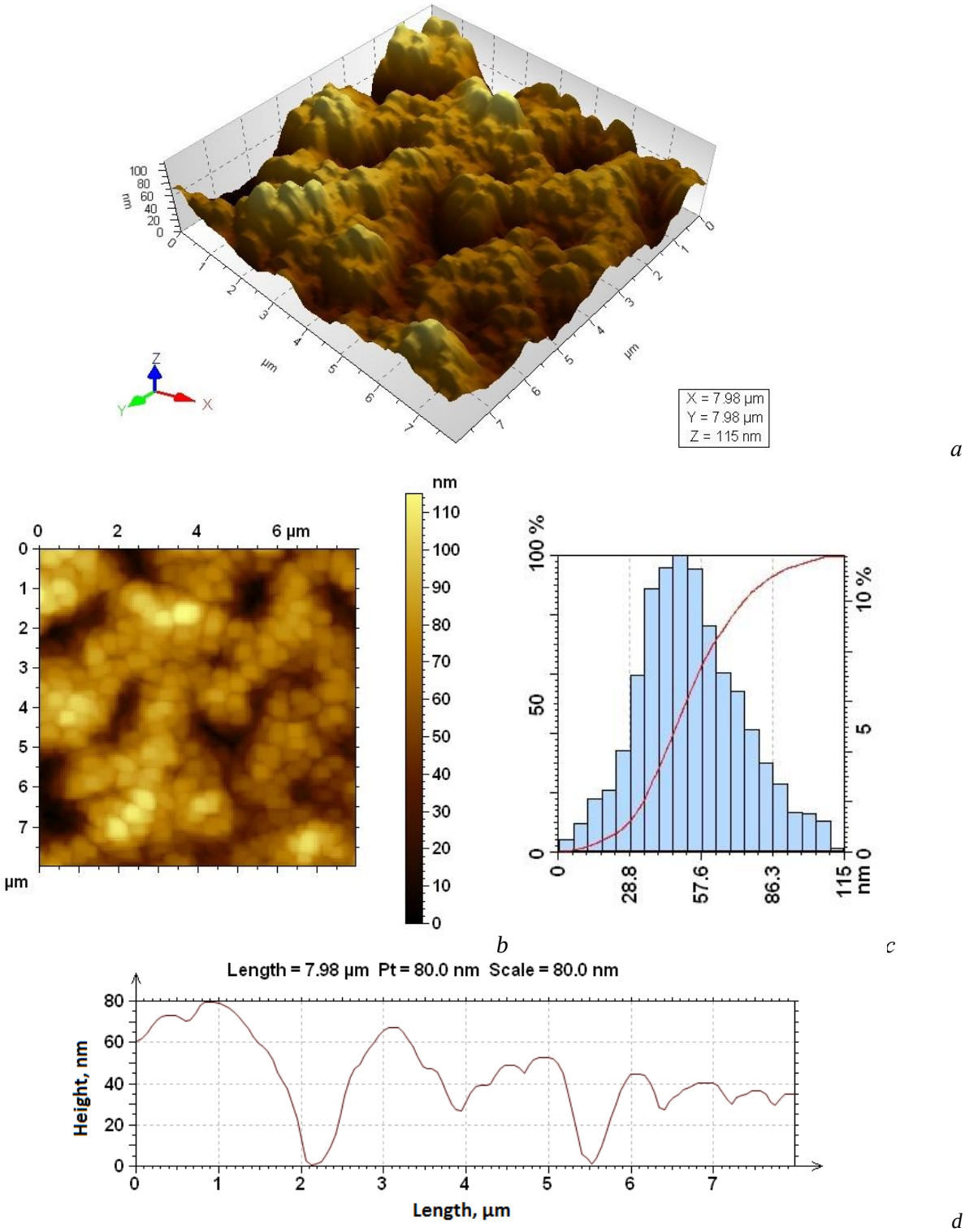

Figure 6. AFM image (*a*, *b*), distribution histogram (*c*) and surface relief (*d*) of the film of sample S-3 (in the presence of $NaBH_4$)

In the AFM image of the S-4 sample, the NPs are more sparsely distributed in the chitosan matrix compared to the S-3 sample, and the number of larger agglomerates is also less. The particle distribution histogram with respect to the surface is also asymmetric in the S-4 sample, with the nanoparticles having sizes in the shorter range from 50 to 100 nm, with an average of 40 % of the nanoparticles being 90 nm. The film surface is smoother than that of the S-4 sample, but the distribution of Mn NPs along the chitosan matrix is unevenly distributed (Fig. 7).

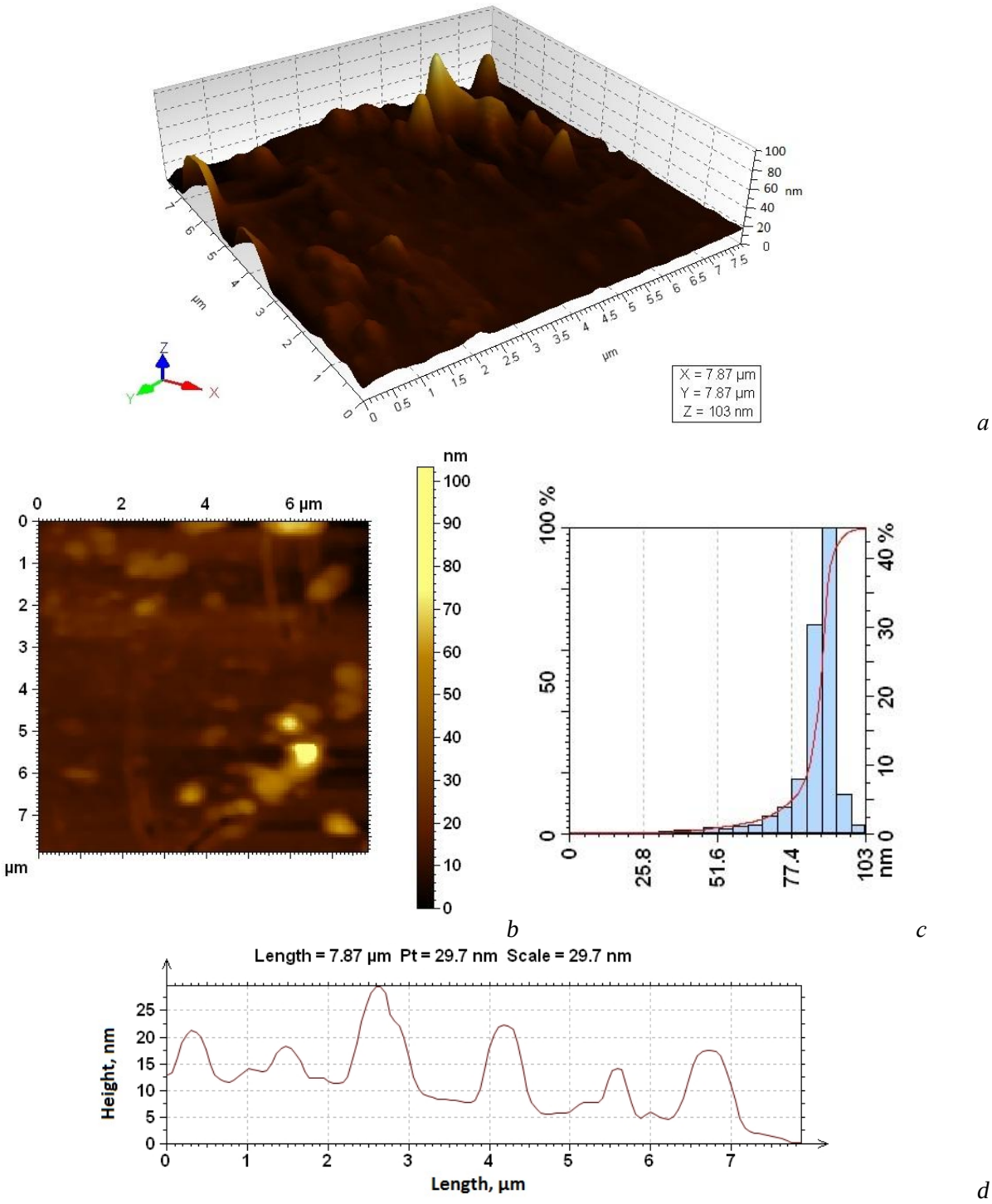

Figure 7. AFM image (*a*, *b*), distribution histogram (*c*), and surface relief (*d*) of the film of sample S-4 (in the presence of $NaBH_4/C_6H_8O_6$)

In general, the results of the AFM study indicate that the nature, amount, and presence of co-reducing agents in the formation of manganese nanoparticles in a chitosan matrix affect the formation of different morphologies. In particular, it was found that the reduction of Mn^{2+} in the presence of $NaBH_4$ resulted in cubic, tetragonal, widely spaced, densely packed nanoparticles, while the reduction in the presence of $NaBH_4/C_6H_8O_6$ resulted in mainly spherical, short-spaced, granular nanoparticles.

SEM Analysis

SEM examination of the chitosan matrix reveals a heterogeneous and non-uniform surface morphology with the presence of porous structures in the resulting films. The observed structures are distributed on the micron scale; however, it should be noted that SEM provides mainly qualitative information on the surface morphology. Therefore, the observed porous structures are discussed in terms of morphological heterogeneity rather than as a quantitative measure of porosity. Such surface characteristics are consistent with the amorphous nature of chitosan and its tendency to form irregular, loosely packed structures upon drying of the films (Fig. 8). Such morphological behavior has been widely described for chitosan-based systems and is known to promote interactions with metal ions and contribute to the stabilization and morphological control of nanoparticles [45, 52].

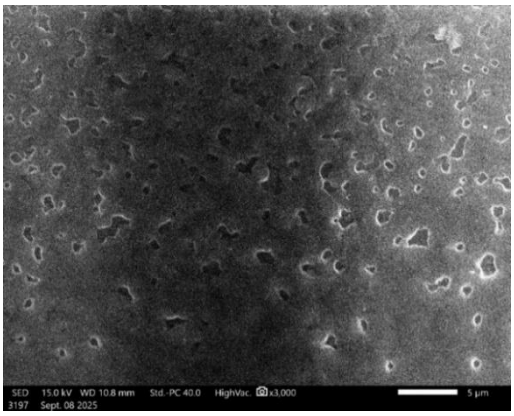

Figure 8. SEM image of the CS sample

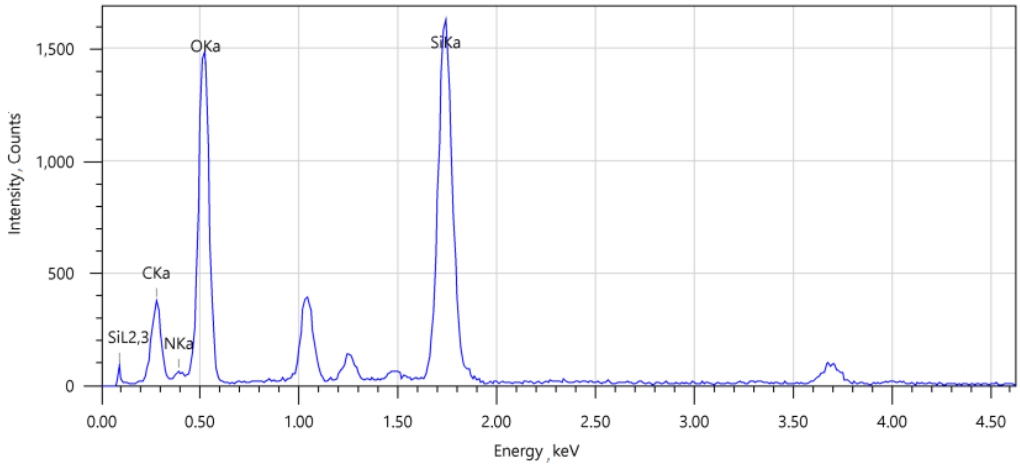

a

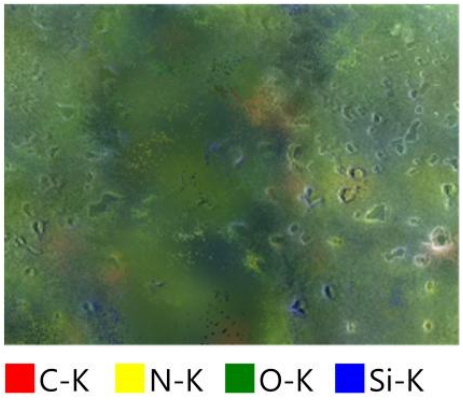

b

Figure 9. Energy dispersive spectroscopic (EDS) analysis of chitosan (*a*) and EDS element distribution map (*b*)

According to the results of energy dispersive analysis, the chitosan sample was found to contain mainly C, N, and O elements. The elemental composition analysis revealed a large proportion of Si (23 wt%) and O (41 wt%), which is explained by the fact that the sample was tested on a SiO_2-based glass substrate. It was also confirmed that chitosan itself contains 27 wt% C and a small amount of N (Fig. 9).

According to the SEM results, it was found that the chitosan-stabilized Mn nanoparticles constituting the S-3 sample were mainly formed in cubic and tetragonal shapes. Since the samples were observed in a film state, the formed particles in it grew and agglomerated in certain areas. In general, the size of the nanoparticles ranged from 100 nm to 800 nm (Fig. 10).

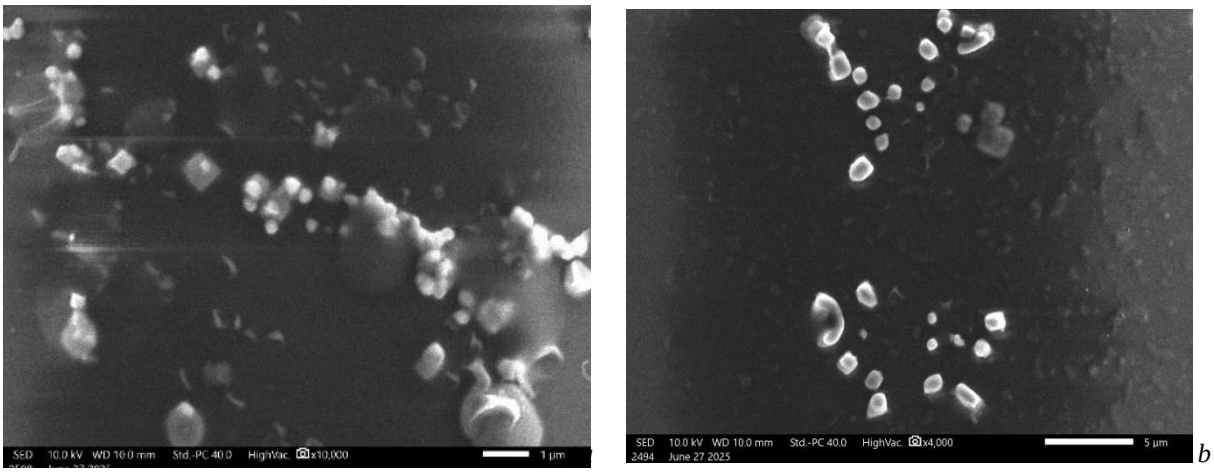

b

Figure 10. SEM micrographs of sample S-3: (*a*) 1 µm scale bar; (*b*) 5 µm scale bar

The formation of nanoparticles with different structures mainly depends on the reducing potential of the reducing agents and the chemical nature of the reaction medium, which control the nucleation and growth mechanisms of particles in a certain direction during the synthesis process. As a result, the formation of nanoparticles with different morphology and crystal structure is observed in the nanosystems formed by the chemical reduction reaction of Mn^{2+} ions in the presence of $NaBH_4$ and $NaBH_4/C_6H_8O_6$ in a chitosan medium. The formation of the morphology of the S-3 sample affects the growth and formation of particles in the process of chitosan as a matrix, but there is no additional antioxidant or complex-forming effect. As a result, a low-energy and crystallized tetragonal crystal structure is formed [74].

The EDS mapping results of the S-3 sample show that the nanoparticles contain carbon (C), nitrogen (N), oxygen (O) and manganese (Mn). This indicates a high level of salinity. The EDS spectrum of the S-3 sample shows a carbon content of 10.17 wt.%, as well as a very small amount of nitrogen and 12.8 wt.% manganese (Fig. 11).

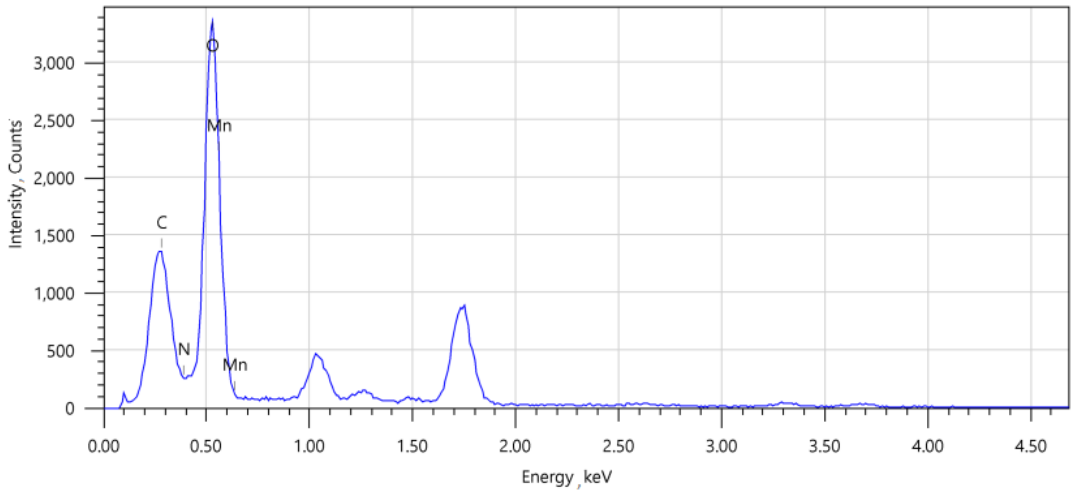

a

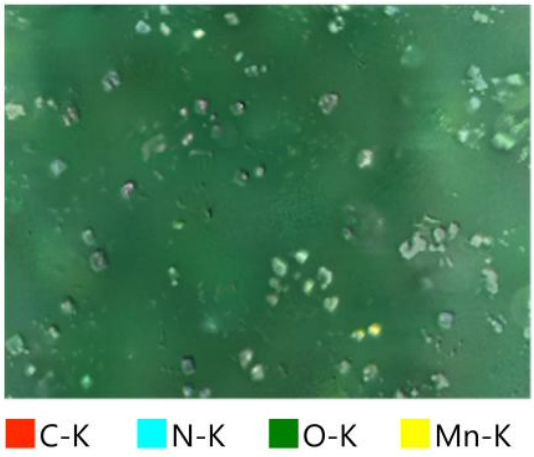

b

Figure 11. Energy dispersive spectroscopic (EDS) analysis (*a*) and element distribution map (*b*) of sample S-3

SEM analysis of the S-4 sample showed that the nanoparticles were mainly spherical in shape, with the size of the nanoparticles ranging from 500 to 750 nm (Fig. 12). In the S-4 sample (Mn^{2+}/$NaBH_4$/$C_6H_8O_6$/–CS), the reaction with manganese ions complexed with chitosan controls the growth and aggregation of the particles. Nanoparticles form predominantly spherical aggregated structures, energetically favorable due to their symmetrical geometry. The presence of ascorbic acid reduces excessive cross-linking during the interaction of manganese compounds with chitosan, thereby promoting the formation of more compact and symmetrical low-energy aggregates. However, the spherical formations observed in SEM images correspond to aggregated particles, not individual primary nanoparticles, and therefore cannot be considered direct evidence of the shapes of individual particles. Accordingly, the effect of ascorbic acid is manifested primarily through its influence on the reduction process and interparticle interactions that determine the aggregation behavior of the system, rather than through the formation of clearly defined shapes of the primary nanoparticles [75, 76].

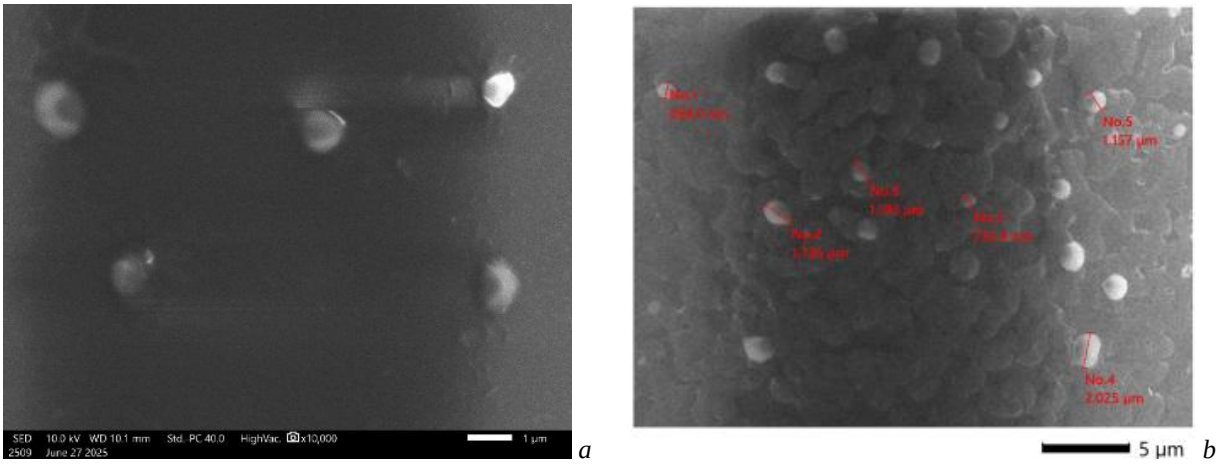

a *b*

Figure 12. SEM micrographs of sample S-4: (*a*) 1 µm scale bar; (*b*) 5 µm scale bar

The EDS mapping results of the S-4 sample indicate that the nanoparticles contain carbon (C), nitrogen (N), oxygen (O), and manganese (Mn). The EDS spectrum of the S-4 sample shows a carbon content of 13.7 wt.%, as well as a very small amount of nitrogen and 11.3 wt.% manganese (Fig. 13).

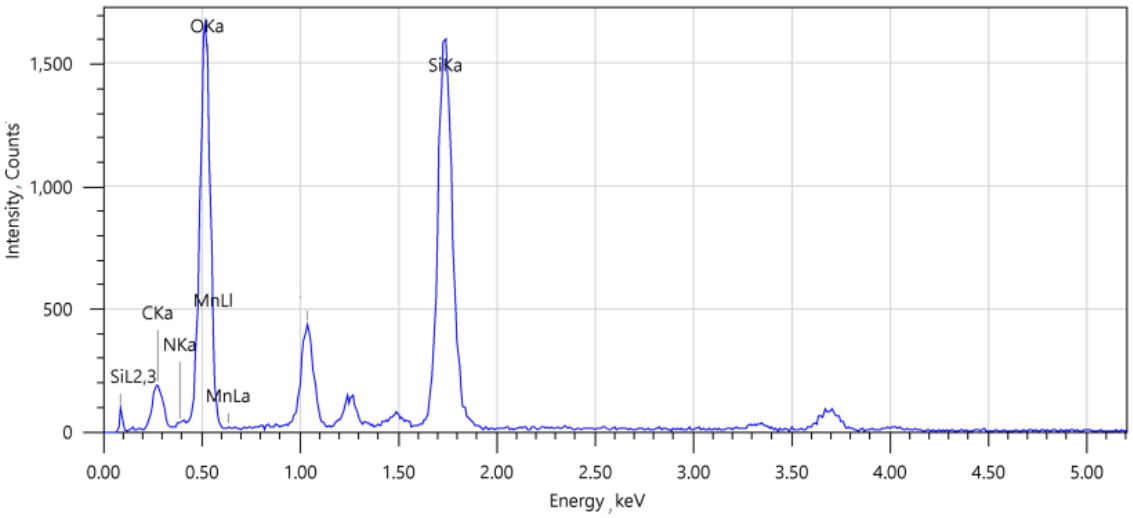

a

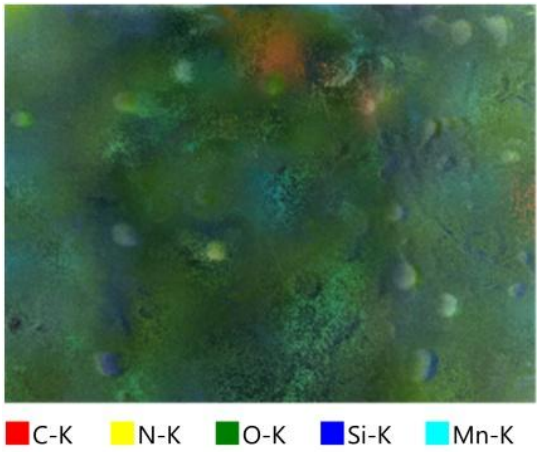

b

Figure 13. Energy dispersive spectroscopic (EDS) analysis (*a*) and element distribution map (*b*) of sample S-4

The nanoparticle of manganese is currently poorly studied in the literature, and most studies have focused on analyzing the nanostructures of its hybrid and composite forms. In particular, nanoparticles based on manganese ferrite ($MnFe_2O_4$) with chitosan have formed spherical [77–79], hillock, rod and sheet structures with $ZnMn_2O_4$ [77], patch-shaped structures with carbon nanofibers of Mn [80], spherical structures with $Mn_{0.8}Zn_{0.2}Fe_2O_4$ with chitosan [81], and spherical structures with chitosan–Mn complexes in liquid [82]. Manganese nanoparticles were present in various composites, including ferrite, metal, hybrid, and complex forms, and were mainly observed in spherical, rod-shaped, or lamellar morphologies, with sizes in the 10–150 nm range. In all cases, chitosan coating was found to be an important factor in improving dispersion, reducing aggregation, and enhancing bioactivity.

Comparative Analysis

The general properties of manganese nanoparticles synthesized in the presence and absence of chitosan were comparatively analyzed (Table 2). In the control samples synthesized in the absence of chitosan (S-1 and S-2), the particles exhibited a pronounced tendency toward aggregation. DLS analysis revealed that their size distribution was predominantly in the micrometer range (6–12 μm), while SEM images showed large particles with irregular morphology. On the contrary, in the samples obtained in the presence of chitosan (S-3, S-4), the hydrodynamic dimensions were determined in the range of 300–500 nm, and the morphology was manifested in cubic and spherical shapes in SEM analysis, and dense and ordered particles in the range of 50–100 nm were observed in AFM studies.

Table 2

Composition and structural characteristics of manganese particles formed with and without chitosan

№	Sample	Mass of Mn, mg	Mass of CS, mg	DLS nm/μm	SEM results	AFM results	EDS Mn (%) → Mn content: 0.5–1.0 wt%	Explanation
1	S-1 (control)	1.32	–	10–12 μm (aggregated)	–	–	–	Rapid nucleation and enlargement
2	S-2 (control)	1.32	–	6–8 μm (aggregated)	–	–	–	Ascorbic acid controlled growth, but large
3	S-3 (*in situ*)	1.32	60	300–500 nm	Cubic, tetragonal, 100–800 nm (aggregates)	50 ± 10 nm	12.8 % → 0.128 g	Colloidal stability is high
4	S-4 (*in situ*)	1.32	60	300–500 nm	Spherical, 500–750 nm	90 ± 20 nm	11.3 % → 0.113 g	Symmetric sphere morphology
5	Mn biological requirement (daily)	2–5 mg [83]	–	50–300 [23, 31]	Mn is spherical or cubic in its pure state, while CS can have spherical, cubic, rod-shaped, tetragonal, and other morphologies; 10–800 [45, 52]	20–250 nm [60, 67]	–	WHO/EFSA standards [83]

Note: DLS and AFM values are presented as average ± standard deviation based on at least three independent measurements. SEM data are given as size ranges due to aggregation effects. EDS values are semi-quantitative with an estimated instrumental error of ±1 wt%.

According to EDS data, the mass fraction of manganese in the chitosan matrix is 11–13 %, which corresponds to 0.113–0.128 g of Mn per gram of sample. These values are quite small in nanoscale when compared with the recommended daily intake for humans (2–5 mg), and are of great importance from the point of view of biological safety. Thus, the results presented in the table clearly demonstrate the effectiveness of chitosan in stabilizing manganese nanoparticles and their morphological and physicochemical advantages.

Conclusions

In conclusion, Manganese-containing nanoparticles were successfully synthesized in the presence of *Bombyx mori* chitosan using $NaBH_4$ and $NaBH_4/C_6H_8O_6$ as reducing systems under controlled *in situ* conditions. Dynamic light scattering analysis demonstrated the formation of stable nanosystems with hydrodynamic sizes of 118–144 nm and narrow dominant distributions (96-97 %), indicating effective stabilization by the polymer matrix. IR spectroscopic analysis confirmed structural rearrangements within the chitosan framework and the involvement of –NH and –C=O functional groups in nanoparticle binding, supporting a chemisorption-based stabilization mechanism. X-ray diffraction results verified the reduction of Mn^{2+} ions and revealed the presence of crystalline phases, while also indicating partial oxidation during nanoparticle formation.

SEM and AFM analyses showed well-dispersed metal nanoparticles embedded in the chitosan matrix, with predominant sizes of approximately 50 nm (tetragonal) and 90 nm (spherical), confirming morphology control under the selected synthesis parameters. Surface topology studies further demonstrated uniform particle distribution without large-scale aggregation. Overall, the combined structural and morphological analyses confirm that chitosan effectively regulates nucleation, growth, and stabilization of manganese nanoparticles. Thus, the resulting manganese-containing nanosystems are of interest for their application in veterinary medicine.

Funding

This study was conducted with the basic funding of the Academy of Sciences of the Republic of Uzbekistan.

*Author Information**

**The authors' names are presented in the following order: First Name, Middle Name and Last Name*

Kandiyor Khorun ogli Ergashev (*corresponding author*) — PhD, Junior Researcher, Institute of Polymer Chemistry and Physics; National Pedagogical University of Uzbekistan, 100128, Tashkent, Uzbekistan; e-mail: kandiyor_ergashev@yahoo.com; https://orcid.org/0000-0001-7494-5988

Noira Rakhimovna Vokhidova — Doctor of Chemical Sciences, Professor, Head of the Laboratory of Interpolyelectrolyte Complexes and Metallopolymers, Institute of Polymer Chemistry and Physics, 100128, Tashkent, Uzbekistan; e-mail: noira_vokhidova@yahoo.de; https://orcid.org/0000-0003-0477-3708

Sayyora Sharafovna Rashidova — Doctor of Chemical Sciences, Professor, Academician, Consultant of the Director, Institute of Polymer Chemistry and Physics, 100128, Tashkent, Uzbekistan; e-mail: polymer@academy.uz; https://orcid.org/0000-0003-1667-4619

Author Contributions

The manuscript was written through contributions of all authors. All authors have given approval to the final version of the manuscript. CRediT: **Ergashev Kandiyor Khorun ogli** investigation, validation, writing-original draft; formal analysis, editing; **Vokhidova Noira Rakhimovna** conceptualization, data curation, formal analysis, validation, writing-review & editing; **Sayyora Sharafovna Rashidova** conceptualization, supervision, editing.

Acknowledgments

Figure 1 and Graphical Abstract were created in *BioRender. Ergashev, Q. (2026) https://BioRender.com/qy5h0tq*

Conflict of Interest

The authors declare no conflict of interest

References

1 Tunc, O., Thompson, J., & Tremellen, K. (2010). Development of the NBT assay as a marker of sperm oxidative stress. *International Journal of Andrology, 33*(1), 13–21. https://doi.org/10.1111/j.1365-2605.2008.00941.x

2 Horning, K. J., Caito, S. W., Tipps, K. G., Bowman, A. B., & Aschner, M. (2015). Manganese is essential for neuronal health. *Annual Review of Nutrition, 35*, 71–108. https://doi.org/10.1146/annurev-nutr-071714-034419

3 Dorman, D.C., Struve, M.F., James, R.A., McManus, B.E., Marshall, M.W., & Wong, B.A. (2001). Influence of dietary manganese on the pharmacokinetics of inhaled manganese sulfate in male CD rats. *Toxicological Sciences, 60*(2), 242–251. https://doi.org/10.1093/toxsci/60.2.242

4 Grujicic, J., & Allen, A.R. (2025). Manganese superoxide dismutase: Structure, function, and implications in human disease. *Antioxidants, 14*(7), 848. https://doi.org/10.3390/antiox14070848

5 Studer, J. M., Schweer, W. P., Gabler, N. K., & Ross, J. W. (2022). Functions of manganese in reproduction. *Animal Reproduction Science, 238*, Article 106924. https://doi.org/10.1016/j.anireprosci.2022.106924

6 Cheema, R. S., Bansal, A. K., Bilaspuri, G. S. (2009). Manganese provides antioxidant protection for sperm cryopreservation that may improve fertilizing ability of buffalo (*Bubalus bubalis*) spermatozoa. *Oxidative Medicine and Cellular Longevity*, *2*(3), 152–159. https://doi.org/10.4161/oxim.2.3.8804

7 De Pascali, F., Tréfier, A., Landomiel, F., Bozon, V., Bruneau, G., Yvinec, R., Poupon, A., Crépieux, P., & Reiter, E. (2018). Follicle-stimulating hormone receptor: Advances and remaining challenges. *International Review of Cell and Molecular Biology, 338*, 1–58. https://doi.org/10.1016/bs.ircmb.2018.02.001

8 Lee, B., Pine, M., Johnson, L., Rettori, V., Hiney, J. K., & Dees, W.L. (2006). Manganese acts centrally to activate reproductive hormone secretion and pubertal development in male rats. *Reproductive Toxicology*, *22*(4), 580–585. https://doi.org/10.1016/j.reprotox.2006.03.011

9 Yang, H., Wang, J., Yang, X., Wu, F., Qi, Z., Xu, B., Liu, W., & Deng, Y. (2019). Occupational manganese exposure, reproductive hormones, and semen quality in male workers: A cross-sectional study. *Toxicology and Industrial Health, 35*(1), 53–62. https://doi.org/10.1177/0748233718810109

10 Kim, E. A., Cheong, H. -K., Joo, K.-D., Shin, J.-H., Lee, J. S., Choi, S.-B., Kim, M.-O., Lee, I. J., & Kang, D. M. (2007). Effect of manganese exposure on the neuroendocrine system in welders. *NeuroToxicology*, *28*(2), 263–269. https://doi.org/10.1016/j.neuro.2006.07.013

11 Roy, T., Boateng, S. T., Uddin, M. B., Banang-Mbeumi, S., Yadav, R. K., Bock, C. R., Folahan, J. T., Siwe-Noundou, X., Walker, A. L., King, J. A., Buerger, C., Huang, S., & Chamcheu, J. C. (2023).The PI3K-Akt-mTOR and associated signaling pathways as molecular drivers of immune-mediated inflammatory skin diseases: Update on therapeutic strategy using natural and synthetic compounds. *Cells, 12*(12), 1671. https://doi.org/10.3390/cells12121671

12 Srivastava, V. K., Hiney, J. K., Dees, W. L. (2013). Early life manganese exposure upregulates tumor-associated genes in the hypothalamus of female rats: relationship to manganese-induced precocious puberty. *Toxicological Sciences, 136*(2), 373–381. https://doi.org/10.1093/toxsci/kft195

13 Tinkov, A. A., Paoliello, M. M. B., Mazilina, A. N., Skalny, A. V., Martins, A. C., Voskresenskaya, O. N., Aaseth, J., Santamaria, A., Notova, S. V., Tsatsakis, A., Lee, E., Bowman, A. B., & Aschner, M. (2021). Molecular targets of manganese-induced neurotoxicity: A five-year update. *International Journal of Molecular Sciences, 22*(9), 4646. https://doi.org/10.3390/ijms22094646

14 Peng, Y., & He, Q. (2024). Reproductive toxicity and related mechanisms of micro(nano)plastics in terrestrial mammals: Review of current evidence. *Ecotoxicology and Environmental Safety, 279*, 116505. https://doi.org/10.1016/j.ecoenv.2024.116505.

15 da Silva, J. D. O., dos Santos, H. C., Bento, G. S., Oliveira, J. F. R., Abud, A. K. S., & Gimenez, I. de F. (2024). Green synthesis of manganese dioxide (MnO_2) nanoparticles produced with acerola (*Malpighia emarginata*) leaf extract. *Materials Chemistry and Physics, 315*, 128963. https://doi.org/10.1016/j.matchemphys.2024.128963

16 Tazim, T. Q., Kawsar, M., Hossain, M. S., Bahadur, N. M., & Ahmed, S. (2025). Hydrothermal synthesis of nano-metal oxides for structural modification: A review. *Next Nanotechnology, 7*, 100167. https://doi.org/10.1016/j.nxnano.2025.100167

17 Huo, Y., Xiu, S., Meng, L.-Y., & Quan, B. (2023). Solvothermal synthesis and applications of micro/nano carbons: A review. *Chemical Engineering Journal, 45*1, 138572. https://doi.org/10.1016/j.cej.2022.138572

18 Kirubakaran, D., Wahid, J. B. A., Karmegam, N., Jeevika, R., Sellapillai, L., Rajkumar, M., & SenthilKumar, K.J. (2025). A comprehensive review on the green synthesis of nanoparticles: Advancements in biomedical and environmental applications. *Biomedical Materials & Devices, 4*, 388–413. https://doi.org/10.1007/s44174-025-00295-4

19 Chaschin, I. S., Perepelkin, E. I., Levin, E. E., Abramchuk, S. S., Anuchina, N. M., Kizas, O. A., Ryzhova, Y. V., & Bakuleva, N. P. (2025). Green synthesis of silver nanoparticles using chitosan in carbonic acid solutions: Effect of pressure and temperature on the structure and antimicrobial properties. *Journal of Inorganic and Organometallic Polymers and Materials, 35*, 2287–2299. https://doi.org/10.1007/s10904-024-03212-2

20 Kustov, L., & Vikanova, K. (2023). Synthesis of metal nanoparticles under microwave irradiation: Get much with less energy. *Metals, 13*(10), 1714. https://doi.org/10.3390/met13101714

21 Karadi, I., Hiremath, V. J., & Timmanagoudar, S. (2025). Nano ferrites: Synthesis, properties and emerging applications — A comprehensive review. *Journal of Advancements in Material Engineering, 10*(2), 1–21. https://doi.org/10.46610/JoAME.2025.v10i02.001

22 Zhang, X., Sathiyaseelan, A., Naveen, K. V., Lu, Y., & Wang, M.-H. (2023). Research progress in green synthesis of manganese and manganese oxide nanoparticles in biomedical and environmental applications — A review. *Chemosphere, 337*, 139312. https://doi.org/10.1016/j.chemosphere.2023.139312

23 Luo, Z. C., Cui, Y. X., Liu, Z. X., Liu, T. L., Yin, F. X., & Zheng, K. H. (2024). Oxidation mechanism of high-manganese heat-resistant steels reinforced by *in situ* second-phase particles. *Corrosion Science, 227*, 111720. https://doi.org/10.1016/j.corsci.2023.111720

24 Li, K., Li, H., Xiao, T., & Zhang, G. (2020). Zero-valent manganese nanoparticles coupled with different strong oxidants for thallium removal from wastewater. *Frontiers of Environmental Science & Engineering, 14*(2). https://doi.org/10.1007/s11783-019-1213-5

25 Akduman, H. Ö., & Özdemir, E. (2025). Zirconia supported bimetallic Co–Mn–B catalyst with superior catalytic activity for hydrolysis of sodium borohydride. *International Journal of Hydrogen Energy, 100*, 67–78. https://doi.org/10.1016/j.ijhydene.2024.12.261

26 Szczyglewska, P., Feliczak-Guzik, A., & Nowak, I. (2023). Nanotechnology–General aspects: A chemical reduction approach to the synthesis of nanoparticles. *Molecules, 28*(13), 4932. https://doi.org/10.3390/molecules28134932

27 Ullah, R., & Dutta, J. (2008). Photocatalytic degradation of organic dyes with manganese-doped ZnO nanoparticles. *Journal of Hazardous Materials, 156*(1–3), 194–200. https://doi.org/10.1016/j.jhazmat.2007.12.033

28 Bao, C., Serrano-Lotina, A., Niu, M., Portela, R., Li, Y., Lim, K. H., Liu, P., Wang, W. -j., Bañares, M. A., & Wang, Q. (2023). Microwave-associated chemistry in environmental catalysis for air pollution remediation: A review. *Chemical Engineering Journal, 466*, 142902. https://doi.org/10.1016/j.cej.2023.142902

29 Zenner, J., Tran, K., Kang, L., Kinzel, N. W., Werlé, C., DeBeer, S., Bordet, A., & Leitner, W. (2024). Synthesis, Characterization, and Catalytic Application of Colloidal and Supported Manganese Nanoparticles. *Chemistry — A European Journal, 30*, e202304228. https://doi.org/10.1002/chem.202304228

30 Trofimova, O. Y., Ershova, I. V., Maleeva, A. V., et al. (2024). Synthesis and Properties of Manganese(II) and Nickel(II) 1-D Coordination Polymers Based on 2,5-di-hydroxy-3,6-di-tert-butyl-para-quinone. *Journal of Inorganic and Organometallic Polymers and Materials, 34*, 2779–2787. https://doi.org/10.1007/s10904-024-03013-7

31 Xu, Z., Zhao, W., Liu, J., Fan, J. (2023). Research on the Surfactant-Assisted Synthesis of MnZn Ferrite Precursor Powders. *Magnetochemistry, 9*(6), 146. https://doi.org/10.3390/magnetochemistry9060146

32 Wang, W., Ding, Z., Zhao, X., Wu, S., Li, F., Yue, M., & Liu, J. P. (2015). Microstructure and magnetic properties of MFe_2O_4 (M = Co, Ni, and Mn) ferrite nanocrystals prepared using colloid mill and hydrothermal method. *Journal of Applied Physics*, *117*(17), 17A328. https://doi.org/10.1063/1.4917463

33 Hu, M., Yan, X., Hu, X., Feng, R., & Zhou, M. (2019). Synthesis of silver decorated silica nanoparticles with rough surfaces as adsorbent and catalyst for methylene blue removal. *Journal of Sol-Gel Science and Technology*, *89*(3), https://doi.org/10.1007/s10971-018-4871-z

34 Rostami, S., Mehdinia, A., & Jabbari, A. (2017). Seed-mediated grown silver nanoparticles as a colorimetric sensor for detection of ascorbic acid. *Spectrochimica Acta Part A: Molecular and Biomolecular Spectroscopy*, *180*, 204–210. https://doi.org/10.1016/j.saa.2017.03.020

35 Varin, R. A., Mattar, D. K., Bidabadi, A. S., & Polański, M. K. (2017). Synthesis of amorphous manganese borohydride in the ($NaBH_4$–$MnCl_2$) system, its hydrogen generation properties and crystalline transformation during solvent extraction. *Journal of Energy Chemistry*, *26*(1), 24–34. http://dx.doi.org/10.1016/j.jechem.2016.08.011

36 Wang, M., Pang, P., Koopal, L. K., Suib, S.; Wang, Y., & Liu, F. (2014). One-step synthesis of δ-MnO_2 nanoparticles using ascorbic acid and their scavenging properties to Pb(II), Zn(II) and methylene blue. *Materials Chemistry and Physics*, *148*(3), 1149–1156. https://doi.org/10.1016/j.matchemphys.2014.09.037

37 Siddique, M. A. R., Khan, M. A., Bokhari, S. A. I., Ismail, M., Ahmad, K., Haseeb, H. A., Kayani, M. M., Khan, S., Zahid, N., & Khan, S.B. (2024). Ascorbic acid-mediated selenium nanoparticles as potential antihyperuricemic, antioxidant, anticoagulant, and thrombolytic agents. *Green Processing and Synthesis*, *13*, 20230158. https://doi.org/10.1515/gps-2023-0158

38 Patra, S. K., Molla, M. R., Singh, A. K., Ghosh, P. K., & Jana, R. N. (2021). Synthesis and purification of metal nanoparticles by membrane filtration. *Journal of Inorganic and Organometallic Polymers and Materials*, *31*(4), 1357–1366. https://doi.org/10.1007/s10904-021-01927-3

39 Alam, M. A., Ahmed, S., Bishwas, R. K., Mostofa, S., & Jahan, S. A. (2025). X-ray crystallographic diffraction study by whole powder pattern fitting (WPPF) method: Refinement of crystalline nanostructure polymorphs TiO_2. *South African Journal of Chemical Engineering*, *51*, 68–77. https://doi.org/10.1016/j.sajce.2024.10.010

40 Ben Amor, I., Hemmami, H., Grara, N., Aidat, O., Ben Amor, A., Zeghoud, S., & Bellucci, S. (2024). Chitosan: A Green Approach to Metallic Nanoparticle/Nanocomposite Synthesis and Applications. *Polymers*, *16*(18), 2662. https://doi.org/10.3390/polym16182662

41 Eltaweil, A. S., El-Tawil, A. M., Abd El-Monaem, E. M., & El-Subruiti, G. M. (2021). Zero Valent Iron Nanoparticle-Loaded Nanobentonite Intercalated Carboxymethyl Chitosan for Efficient Removal of Both Anionic and Cationic Dyes. *ACS Omega*, *6*(9), 6348–6360. https://doi.org/10.1021/acsomega.0c06251

42 Rinaudo, M. (2006). Chitin and chitosan: Properties and applications. *Progress in Polymer Science*, *31*(7), 603–632. https://doi.org/10.1016/j.progpolymsci.2006.06.001

43 Sajna, P., Varma, A., & Vasudevan, G. (2008). Application of Spectroscopic Methods for Structural Analysis of Chitin and Chitosan. *Marine Drugs*, *8*(5), 1567–1587. https://doi.org/10.3390/md8051567

44 Hu, Z., Lu, S., Cheng, Y., Kong, S., Li, S., Li, C., & Yang, L. (2019). Investigation of the effects of molecular parameters on the hemostatic properties of chitosan. *International Journal of Biological Macromolecules*, *136*, 327–336. https://doi.org/10.3390/molecules23123147

45 Wang, Y., Chen, X., Liu, J., Zhang, L., & Zhao, X. (2021). Synthesis of chitosan–metal nanocomposites for biomedical applications. *Materials Science and Engineering: C*, *124*, 112051. https://doi.org/10.1016/j.msec.2021.112051

46 Filippov, S. K., Khusnutdinov, R., Murmiliuk, A., Inam, W., Zakharova, L. Ya., Zhang, H., & Khutoryanskiy, V. V. (2023). Dynamic light scattering and transmission electron microscopy in drug delivery: A roadmap for correct characterization of nanoparticles and interpretation of results. *Materials Horizons*, *10*, 5354–5370. https://doi.org/10.1039/d3mh00717k

47 Kim, S. et al. (2020). Structural insights into chitosan–ZnO nanocomposites using FTIR and XRD. *Journal of Molecular Structure*, *1212*, 128118. https://doi.org/10.1016/j.molstruc.2020.128118

48 Faizan, M., Naz, M. Y., Shah, S. A. S. A., Shakir, I., Khaliq, M., Busharat, M. A., & Pan, D. (2025). Mesoporous magnetic $MnFe_2O_4$@SiO_2-chitosan nanocomposite for efficient adsorptive removal of Zn(II) and Cd(II) ions from aqueous media. *Desalination and Water Treatment*, *324*, 101488. https://doi.org/10.1016/j.dwt.2025.101488

49 Rodrigues de Sá, M., Mendes da Silva, T., Souza, E.S., Soares de Carvalho, A., Filho, M. R. A. A., Silva-Araújo, E. R. (2025). Magnetic and fluorescent manganese silicate nanostructures for advanced applications. *ChemistrySelect*, *10*(24), e02098. https://doi.org/10.1002/slct.202502098

50 Kumar, S., Yadav, B., Sharma, P., Singh, R., & Gupta, A. (2021). Preparation and Characterization of Chitosan-Coated Manganese Ferrospinel Nanoparticles Conjugated with Laccase for Environmental Bioremediation. *Polymers*, *13*(22), 3921. https://doi.org/10.3390/polym13223921

51 Lahouti, S., & Naeimi, H. (2020). Chitosan-encapsulated manganese ferrite particles bearing sulfonic acid group catalyzed efficient synthesis of spiro indenoquinoxalines. *RSC Advances*, *10*(55), 33334–33343. https://doi.org/10.1039/d0ra04925e

52 Nguyen, T. V., Le, H. T., Pham, H. T., & Nguyen, D. T. (2023). Chitosan based nanosorbents for removal of heavy metals: Cd, Co, Cu, and Pb. *Scientific Reports*, *13*, Article 16958. https://doi.org/10.1038/s41598-023-44014-5

53 Patel, R., Mehta, A., & Joshi, M. (2018). Synthesis of $MnFe_2O_4$@chitosan nanocomposites for magnetic hyperthermia and drug delivery applications. *Materials*, *11*(12), 2542. https://doi.org/10.3390/ma11122542

54 Zhang, Q., Liu, J., Wang, X., Li, Y., & Chen, H. (2021). Catalytic application of Pd–Chitosan@$MnFe_2O_4$ nanocomposites: Structure and interaction analysis. *Journal of Molecular Liquids*, *339*, 117222. https://doi.org/10.1016/j.molliq.2021.117222

55 Goy, R. C., de Britto, D., & Assis, O. B. G. (2009). A review of the antimicrobial activity of chitosan. *Polímeros, 19*(3), 241–247. https://doi.org/10.1590/S0104-14282009000300006

56 Niu, Y., Hu, W. (2024). Preparation, characterization and application in environmental protection of low-molecular-weight chitosan: a review. *Sustain Environ Res 34*, 29. https://doi.org/10.1186/s42834-024-00236-8

57 Podgorbunskikh, E., Kuskov, T., Rychkov, D., Lomovskii, O., & Bychkov, A. (2022). Mechanical amorphization of chitosan with different molecular weights. *Polymers, 14*(20), 4438. https://doi.org/10.3390/polym14204438

58 Lawson, A. C., Vandervoort, K. G., Welp, U., & Hinks, D.G. (1994). Magnetic structure of α-manganese. *Journal of Applied Physics, 76*(10), 7049–7051. https://doi.org/10.1063/1.358261

59 Yamauchi, H., Sari, D. P., Watanabe, I., & Yasui, Y. (2020). High-temperature short-range order in Mn_3RhSi. *Communications Materials, 1*, 43. https://doi.org/10.1038/s43246-020-0042-1

60 Pardeep, Bitla, Y., Lalita, Patra, A. K., & Basheed, G. A. (2023). In-field critical behaviour of β-Mn type Co–Zn–Mn skyrmion-host. *Physica B: Condensed Matter, 654*, 414669. https://doi.org/10.1016/j.physb.2023.414669

61 Hornfeck, W., & Kuhn, P. (2014). Octagonal symmetry in low-discrepancy β-manganese. *Acta Crystallographica Section A Foundations and Advances, 70*(5), 441–447. https://doi.org/10.1107/s2053273314009218

62 Karube, K., White, J. S., Ukleev, V., Dewhurst, C. D., Cubitt, R., Kikkawa, A., Tokunaga, Y., Rønnow, H. M., Tokura, Y., & Taguchi, Y. (2020). Metastable skyrmion lattices governed by magnetic disorder and anisotropy in β-Mn-type chiral magnets. *Physical Review B, 102*(6), 064408. https://doi.org/10.1103/PhysRevB.102.064408

63 Bakshi, P. S., Singha, M., & Rathi, P. (2013). Structural modification in chitosan after metal oxide incorporation: An XRD analysis. *Carbohydrate Polymers, 98*, 599–606. https://doi.org/10.1016/j.carbpol.2013.07.083

64 Wang, X., Chen, X., Zhang, Y., Li, Y., & Zhao, J. (2015). Synthesis and characterization of Mn nanoparticles via reduction of $MnCl_2$. *Journal of Alloys and Compounds, 648*, 837–843. https://doi.org/10.1016/j.jallcom.2015.07.164

65 Rasaee, M. J., Esfandiari, M., Soleimani, M., Azimi, S., & Fazeli, M. (2022). Structural and antimicrobial properties of chitosan‐based nanoparticles. *Polymers, 14*(24), 5324. https://doi.org/10.3390/polym14245324

66 Shoemaker, C. B., Shoemaker, D. P., Hopkins, T. E., & Yindepit, S. (1978). Refinement of the structure of β-manganese and of a related phase in the Mn–Ni–Si system. *Acta Crystallographica Section B Structural Crystallography and Crystal Chemistry, 34*(12), 3573–3576. https://doi.org/10.1107/s0567740878011620

67 Pandey, R., & Shukla, S. (2023). Nanocomposites of chitosan with transition metals: synthesis and physicochemical properties. *Materials Chemistry and Physics, 303*, 127596. https://doi.org/10.1016/j.matchemphys.2023.127596

68 Liu, Y., Zhang, X., Li, J., & Wang, S. (2021). Structural properties of chitosan‐based nanocomposites with transition metals. *Polymers, 13*(16), 2714. https://doi.org/10.3390/polym13162714

69 Zhuo, Shujuan; Fang, Jing; Li, Meng; Wang, Jing; Zhu, & Changqing; Du, Jinyan (2019). Manganese(II)-doped carbon dots as effective oxidase mimics for sensitive colorimetric determination of ascorbic acid. *Microchimica Acta, 186* (745). https://doi.org/10.1007/s00604-019-3887-6

70 Deshmukh, Aarti R., & Kim, Beom Soo. (2019). Chitosan–Vitamin C Nanoparticles. *KSBB Journal, 34* (4), 221–232. https://doi.org/10.7841/ksbbj.2019.34.4.221

71 Podgorbunskikh, E., et al. (2022). Mechanical Amorphization of Chitosan with Different Molecular Weights. *Polymers, 14*(20), 4438. https://doi.org/10.3390/polym14204438

72 Nosal, W. H., Thompson, D. W., Yan, L., Sarkar, S., Subramanian, A., & Woollam, J. A. (2005). Infrared optical properties and AFM of spin-cast chitosan films chemically modified with 1,2 epoxy-3-phenoxy-propane. *Colloids and Surfaces B: Biointerfaces, 46*(1), 26–31. https://doi.org/10.1016/j.colsurfb.2005.08.006

73 Ferreira, A. M., et al. (2023). AFM surface characterization of chitosan films for biomedical applications. *Nanomaterials, 13*(4), 720. https://doi.org/10.3390/nano13040720

74 Li, Z., Gao, K., Han, G., Wang, R., Li, H., Zhaoabc X.S., & Guo. P. (2015). Solvothermal synthesis of $MnFe_2O_4$ colloidal nanocrystal assemblies and their magnetic and electrocatalytic properties. *New Journal of Chemistry, 39*, 361–368. https://doi.org/10.1039/C4NJ01466A

75 Wang, L., Hu, C., Nemoto, Y., Tateyama, Y., & Yamauchi, Y. (2010). On the role of ascorbic acid in the synthesis of single-crystal hyperbranched platinum nanostructures. *Crystal Growth & Design, 10*(8), 3454–3460. https://doi.org/10.1021/cg100207q

76 Elshoky, H. A., Salaheldin, T. A., Ali, M. A., & Gaber, M. H. 2018). Ascorbic acid prevents cellular uptake and improves biocompatibility of chitosan nanoparticles. *International Journal of Biological Macromolecules, 115*, 358–366. (https://doi.org/10.1016/j.ijbiomac.2018.04.055

77 Plikeva, S., Ivanov, D., Petrova, T., & Kolev, D. (2021). Preparation and characterization of chitosan-coated manganese-ferrite nanoparticles. *Polymers, 13*(9), 1453. https://doi.org/10.3390/polymers13091453

78 Ebadi, M., Asikin-Mijan, N., Jamil, M.S. Md., Iqbal, A., Yousif, E., Zain, A.R. Md, Aziz, T. H. T., & Rahimi Yusop, M. (2023). Palladium nanoparticles on chitosan coated superparamagnetic manganese ferrite. *Polymers, 15*(1), 232. https://doi.org/10.3390/polym15010232

79 Rashid, K., Ahmed, S., & Khan, M. (2020). Chitosan-encapsulated manganese ferrite bearing sulfonic acid catalyzed spiro indenoquinoxaline synthesis. *RSC Advances, 10*, 4925. https://doi.org/10.1039/D0RA04925E

80 Kumar, R., Chen, S.-M., & Lee, C.-H. (2016). Carbon nanotubes decorated with manganese nanoparticles for electrochemical determination of vitamin C. *Journal of Alloys and Compounds, 648*, 837–843. https://doi.org/10.1016/j.jallcom.2015.12.110

81 Patel, D., Singh, U., & Ghosh, S. (2023). Nanohybrid based on $Mn_{0.8}Zn_{0.2}Fe_2O_4$ functionalized with chitosan and sodium alginate for curcumin loading. *AAPS PharmSciTech*. https://doi.org/10.1208/s12249-023-02683-9

82 Davidson, E., Pereira, J., Giannelli, G. G., Murphy, Z., Anagnostopoulos, V., & Santra, S. (2023). Multi-functional chitosan nanovesicles loaded with bioactive manganese for potential wound healing applications. *Molecules, 28*(16), 6098. https://doi.org/10.3390/molecules28166098

83 Turck, D., Bohn, T., Castenmiller, J., de Henauw, S., Hirsch-Ernst, K., Knutsen, H. K., Maciuk, A., Mangelsdorf, I., McArdle, H. J., Pentieva, K., Siani, A., Thies, F., Tsabouri, S., Vinceti, M., Bornhorst, J., Cubadda, F., Dopter, A., FitzGerald, R., … Naska, A. (2023). Scientific opinion on the tolerable upper intake level for manganese. *EFSA Journal, 21*(12). https://doi.org/10.2903/j.efsa.2023.8413

How to Cite: Ergasheva, Kh.A., & Vokhidova, N.R. (2026). *Bombyx mori* Chitosan–Caffeine Nanocapsules: Formation, Structural Features, and Physicochemical Properties. *Eurasian Journal of Chemistry, 31, 1(121), 30–44.* https://doi.org/10.31489/2959-0663/1-26-2

Article

Received: 6 November 2025 | Revised: 26 February 2026 | Accepted: 2 March 2026 | Published online: 11 March 2026

UDC 541.64:547.458.6: 544.77.032.1 https://doi.org/10.31489/2959-0663/1-26-2

Khusnibonu A. Ergasheva*, Noira R. Vokhidova

Institute of Polymer Chemistry and Physics Academy of Sciences of Uzbekistan, Tashkent, Uzbekistan
*(*Corresponding author's e-mail: khusnibonu_ea@mail.ru)*

Bombyx mori Chitosan–Caffeine Nanocapsules: Formation, Structural Features, and Physicochemical Properties

This study aimed to engineer *Bombyx mori* chitosan–caffeine nanocapsules via a self-assembly approach and to comprehensively characterize their structural architecture, physicochemical properties, and release kinetics under precisely controlled pH conditions. Chitosan–caffeine nanocapsules were synthesized in aqueous medium at low temperature under controlled acidic conditions (pH 3.2 and 4.5), achieving yields of 91–94 %. Their physicochemical properties were analyzed using UV and FTIR spectroscopy, X-ray diffraction, scanning electron microscopy, and transmission electron microscopy. The results showed that hydrogen bonding and electrostatic interactions between the protonated amino groups of chitosan and the carbonyl groups of caffeine promoted the formation of spherical and oval nanostructures with diameters in the range of 100–400 nm. Spectroscopic analysis confirmed the intermolecular interactions responsible for encapsulation, while X-ray diffraction indicated a decrease in caffeine crystallinity after incorporation into the polymer matrix. SEM and TEM micrographs demonstrated efficient encapsulation of caffeine within the chitosan matrix and confirmed the formation of stable core–shell nanostructures. Release profile analysis showed that approximately 20 % of the total caffeine content was released from the chitosan nanocapsules over the monitored period, confirming their controlled release behavior. These chitosan-caffeine nanocapsules hold potential for future use in the development of drugs with prolonged release properties.

Keywords: chitosan, *Bombyx mori*, caffeine, nanoparticles, self-assembly, drug delivery systems, core–shell structures, controlled release

Introduction

Caffeine (CF, $C_8H_{10}N_4O_2$) is a biologically active compound widely used in pharmaceutical, nutraceutical, and cosmetic formulations due to its stimulant, antioxidant, and anti-inflammatory properties [1, 2]. However, its practical application is often limited by volatility, formulation-dependent solubility, local irritancy at elevated concentrations, and rapid diffusion in biological media. These factors are particularly critical in applications where stabilization and controlled release are required, such as topical, oral, and mucosal delivery systems [1–4].

Encapsulation into nanoscale carriers has been shown to improve caffeine stability, mask bitterness, and modulate release behavior [1–4]. Alongside polymeric nanoparticles and liposomal systems, supramolecular approaches based on cyclodextrins and calixarenes have also been reported to enhance caffeine performance through host–guest interactions [5, 6]. Nevertheless, multicomponent supramolecular systems often involve overlapping interaction mechanisms, which complicates the interpretation of structure–property relationships and limits systematic optimization [7, 8].

Chitosan (CS), a cationic polysaccharide obtained by deacetylation of chitin, is an attractive carrier owing to its biocompatibility, biodegradability, mucoadhesive properties, and suitability for controlled drug delivery [9–13]. Despite these advantages, chitosan-based systems face important challenges, including pH-dependent solubility, aggregation under physiological ionic strength, and limited retention of small, water-soluble molecules such as caffeine [14–17]. Various preparation techniques have been proposed, including ionic gelation, emulsification–crosslinking, and self-assembly, each yielding distinct structural and release characteristics [16, 18–23].

In the self-assembly approach, chitosan macromolecules interact with drug molecules under defined pH and ionic conditions, leading to the formation of nanocapsules in which the polymer constitutes the surrounding shell. Compared with other encapsulation techniques, self-assembly offers several advantages for chitosan–caffeine systems. The process is simple and environmentally friendly, as it does not require chemical crosslinkers or elevated temperatures, thereby preserving the chemical integrity and bioactivity of caf-

feine. The resulting nanocapsules are stabilized by natural intermolecular interactions, which promote structural stability and effective drug retention. In addition, the intrinsic affinity between chitosan and caffeine facilitates efficient drug loading, while modulation of formulation parameters enables control over capsule size and structural organization. Owing to these features, self-assembly is a suitable approach for the fabrication of chitosan–caffeine nanocapsules [20–22].

Chitosan–caffeine nanocapsules represent a promising platform for pharmaceutical delivery, and their modular nature allows the potential incorporation of additional bioactive components, such as vitamins, minerals, or polyphenols, to develop multifunctional systems [19–21]. Despite numerous studies on caffeine encapsulation using liposomes, nanoliposomes, and simple polymeric carriers, and reports showing that chitosan coating improves liposomal stability and mucoadhesion [23–28], several key limitations remain. Many studies rely on a single encapsulation strategy, such as chitosan-coated nanoliposomes or basic ionic-gelation particles, without systematically examining the influence of self-assembly parameters—particularly pH and chitosan-to-caffeine ratio—on caffeine stabilization. Furthermore, controlled-release claims are often not supported by detailed in vitro release analysis, and the physicochemical mechanisms governing the interaction of weakly basic molecules like caffeine with chitosan matrices are still insufficiently clarified. In addition, co-encapsulation of caffeine with other bioactive compounds in chitosan nanocapsules has been only rarely investigated with validated stability and release performance [29–37].

Based on the above, the aim of this study is to obtain nanocapsules based on chitosan *Bombyx mori* and caffeine by the "self-assembly" technique, as well as to study their morphology, physicochemical, and prolonged properties.

Experimental

Bombyx mori chitosan (CS) with a molecular mass (MM) of 84,000 and a deacetylation degree (DD) of 86 % was used, synthesized in laboratory conditions. Caffeine (CF) was purchased from China (CAS: 58-08-2). Additionally, 0.1 % analytical standard HCl and tetrahydrofuran (C_4H_8O) were used as the solvents. All the above, the reagents were AR grade.

Preparation of Chitosan-Caffeine Nanocapsules. To obtain chitosan-caffeine nanocapsules, a 1.0 % (w/v) solution of *Bombyx mori* chitosan in 0.1 N HCl and a 0.25 % (w/v) solution of CF in C_4H_8O were prepared. A homogeneous solution of chitosan was obtained at 25 ± 1 °C and continuous stirring at 500 rpm for ≈ 6 h. A 1 % (w/v) solution of caffeine in tetrahydrofuran (THF, C_4H_8O) was prepared for 50 min with vigorous stirring at 400 rpm. Nanocapsules were obtained at 35 ± 1 °C, 600 rpm for 1.5 h, and the mass ratios of the components were CS : CF = 1:0.3 and CS : CF = 1:0.03, respectively. The pH of the reaction mixture was adjusted to pH 3.2 ± 0.1 and pH 4.5 ± 0.1 using 0.1 N NaOH. Nanocapsule formation was induced by slowly adding 0.1 M Na_2SO_4 solution at a rate of 1 mL min^{-1}, which served as an ionic cross-linking and precipitating agent.

The suspension was then kept for 16 hours at 20 °C to achieve structural stabilization of the nanocapsules. The final product was separated by centrifugation for 10 min at 2000 rpm. The resulting powder was then repeatedly washed with bidistilled water to pH 7 and freeze-dried at –50 °C and 0.03 mbar (Christ Alpha 1-4 LDplus) for 24 hours to constant weight. All experiments were performed in triplicate to ensure reproducibility. Selected synthesis parameters, such as polymer concentration, mass ratio, pH, temperature, and stirring time, were optimized through preliminary screening to achieve encapsulation efficiency and obtain monodisperse nanoparticles. The results are presented in Table 1.

Table 1

Effect of pH and mass ratios of the initial reaction components on the production of CS-CF nanocapsules. τ = 1.5 h; v = 600 rpm

No	Designation in the text	Samples, mass ratio	pH	Reaction yield, %
1	Sample 1	CS-CF=1:0.3	3.2	91
2	Sample 2	CS-CF=1:0.3	4.5	94
3	Sample 3	CS-CF=1:0.03	4.5	92

Dynamic Light Scattering (DLS) Method. The size and distribution of particles in solutions were determined by dynamic light scattering (DLS) using a Photocor Compact-Z analyzer (Photocor Ltd., Moscow, Russia) equipped with a helium-neon laser operating at λ = 632.8 nm and 90° angle. The test solutions were

maintained at a thermostatted temperature of 25 ± 0.1 °C. The sample concentration was maintained at 0.05 mg/mL to minimize aggregation effects. Each measurement was performed for 3 minutes and repeated at least three times.

UV-Spectroscopic Studies. Measurements were performed on a SPECORD 210 spectrophotometer (Analytik Jena AG, Germany) in the wavelength range of 190–1000 nm with a 1 nm step and a scan rate of 2 nm/s. The accuracy of UV photometry was studied using potassium dichromate in accordance with the requirements of the European Pharmacopoeia, with an error of ±0.01. UV–Vis spectra were recorded in a quartz cuvette with an optical path length of 1 cm. Solutions of the studied samples were prepared in 2 % acetic acid, where the concentration was 0.002 mol/L. The pH of the reaction system was determined using a "pH-150".

Fourier Transform Infrared (FTIR) spectroscopy in the range of 400–4000 cm^{-1} using a Bruker INVENIO-S spectrophotometer (Bruker Optik GmbH, Ettlingen, Germany) was used to study the structure of the samples. Samples were prepared as tablets containing potassium bromide (150–250 mg KBr), and the solid sample (1.5–2 mg) was finely ground using a porcelain mortar. The sample mixture was placed in a mold and maintained under vacuum conditions, then pressed under a pressure of 7×10^8 Pa for 2 minutes.

X-Ray Diffraction (XRD) analysis of the samples was performed on a DRON-3M ("Burevestnik", St. Petersburg, Russia) X-ray diffractometer using monochromatic Co Kα radiation at 16 mA and 22 kV. Powdered samples were used for the study. The degree of crystallization (DC) of the samples was calculated by evaluating the intensity of the maximum diffraction curve based on the following formula:

$$DC = \frac{(I - I_a)i - K}{(I_c - I_a)i},$$

where, I_c and I_a are the intensities characteristic of the crystalline and amorphous regions, respectively [38].

Scanning Electron Microscope (SEM, JSM-IT 210, JEOL, Japan) was used to study the film morphology. During measurements, the accelerating voltage (EHT—Extra High Tension) was applied in the range of 5 kV to 15 kV, and the working distance was 10.8 mm. Images at various scales were obtained using InTouch Scope software. Energy dispersive spectroscopy (EDS) was used to determine the elemental composition of the synthesized samples, obtaining both spectra and elemental mapping images.

Transmission Electron Microscope (TEM, Talos F-200i from Thermo Fisher Scientific, USA)—a high-resolution TEM was used to determine nanoparticle sizes and film morphology. The voltage range was 20–200 kV. TEM images were obtained using samples deposited on standard carbon-coated copper grids.

In vitro Release Profile of Caffeine from Chitosan Nanocapsules (UV–Vis Spectroscopic Determination). The release profile of caffeine from chitosan nanocapsules was investigated using UV–spectrophotometry under *in vitro* conditions. CS-CF nanocapsules were prepared and suspended in an aqueous medium, and their release behavior was monitored over a specified period [39–45]. Release measurements were performed using a UV-Vis spectrophotometer with quartz cuvettes (optical path length of 1 cm). Absorption spectra were recorded in the wavelength range of 230–310 nm at selected time intervals (0, 900, 1800, 3600, 5400, 7200, and 9000 s). The analytical wavelength was set at the maximum of λ = 242 ± 2 nm, which corresponds to the characteristic absorption band of caffeine. At each time point, the average absorbance value was recorded on the display. To correct for background absorption, control spectra of a chitosan solution in 0.1 N HCl in the absence of caffeine were recorded under the same conditions. Corrected values were obtained by subtracting the control spectra from the spectra of the CS-CF sample, ensuring that the measured intensity reflects only caffeine release.

The corrected absorbance values at each time point were normalized to the value at the final time point (9000 s), which was defined as 100 % release. The cumulative release percentage (%R) was calculated using the following equation:

$$\%R(t) = \frac{A_t - A_{blank}}{A_{final} - A_{blank}} \times 100,$$

A_t is the absorbance at time t, A_{blank} is the absorbance of the blank solution, and A_{final} is the absorbance at the final time point (9000 s).

The release data were further analyzed using standard kinetic models. The Higuchi model was applied to evaluate diffusion-controlled release ($M_t/M_\infty = kH_t$), and the Korsmeyer–Peppas model ($M_t/M_\infty = k \cdot t^n$) was used to determine the release exponent n. An exponent value close to 0.5 indicates Fickian diffusion, while

higher values suggest anomalous (non-Fickian) transport. Regression fitting was performed to estimate kinetic parameters and interpret the release mechanism [39–45].

According to the *Higuchi model*, the release is proportional to the square root of time (t), which serves as the diffusion controller. The results deviate from the model at the initial points due to the "burst", but in the range of 1800–5400 s, they fit the Higuchi line relatively well. Also, according to the Korsmeyer–Peppas model, $M_t/M_\infty \approx k \cdot t^n$. If $n \approx 0.5 \rightarrow$ Fick diffusion; if $n > 0.5 \rightarrow$ anomalous (erosion + diffusion) mechanism. Accordingly, n is approximately in the range of 0.45–0.55, which indicates diffusion-controlled release [39-40].

For statistical analysis of the experimental results, particle size and encapsulation efficiency measurements were performed in triplicate, and the results are expressed as mean ± standard deviation (SD). The statistical significance of differences between groups was assessed using a one-way analysis of variance (ANOVA) followed by a Tukey post-hoc test to determine pairwise differences between the different formulations. A significance level of $p < 0.05$ was considered statistically significant. This approach ensures the reliability and reproducibility of the obtained results, as is widely reported in nanomaterials and pharmaceutical research [46, 47].

Results and Discussion

Hydrodynamic Sizes of Chitosan–caffeine Samples

A suspension of the obtained CS-CF samples was prepared, and the hydrodynamic particle sizes were studied using DLS (Fig. 1).

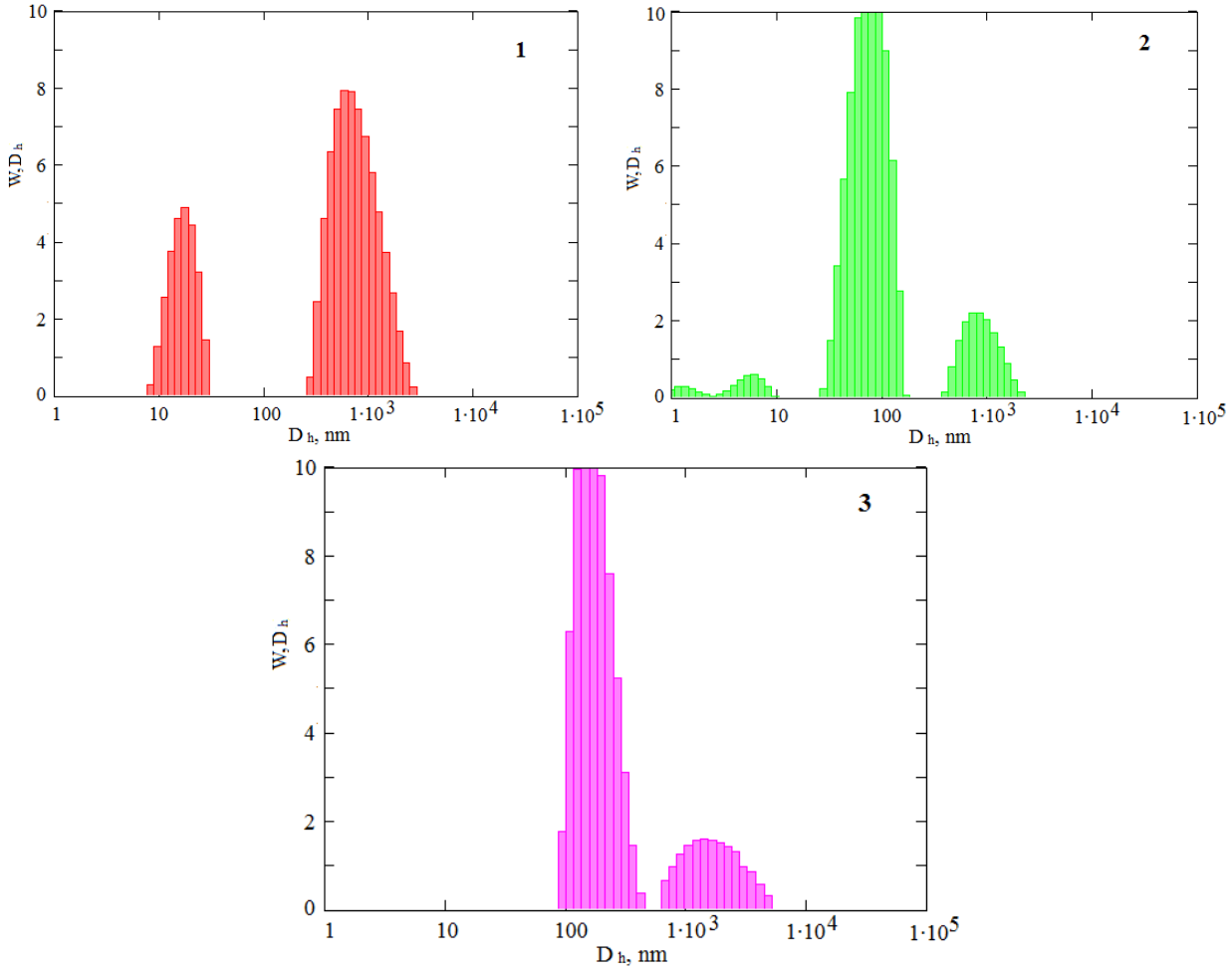

Figure 1. Hydrodynamic diameters and particle size distribution for samples of sample 1 (*1*), sample 2 (*2*), and sample 3 (*3*)

For samples 1 and 2, the predominant size range corresponded to average hydrodynamic diameters of 400–600 nm, while the histogram for sample 3 demonstrated comparatively larger particles with average sizes in the range of 500–700 nm. Overall, the results in Figure 1 demonstrate that the CS-CF samples exhibit a high degree of size polydispersity, ranging from approximately 20 nm to 1.5 μm. The polydispersity index (PDI) values ((Standard Deviation/Mean)²) are 0.580 for sample 1, 0.604 for sample 2, and 0.477 for sample 3 [48]. It appears that the formation of nanoparticles under the selected conditions for producing chitosan–caffeine nanocapsules is regulated by self-assembly mechanisms. That is, nanostructures are formed through electrostatic interactions between the protonated amino groups of chitosan and the polar regions of caffeine, supplemented by hydrogen bonds between the –NH groups of chitosan, as well as the C=O and heterocyclic –N atoms of caffeine. These non-covalent interactions promote the cooperative association of components, suppress the crystallization of caffeine, and stabilize the nanoscale structures.

UV-Spectroscopy

In spite of chitosan lacking a chromophore with high absorbance, its UV spectrum shows an absorption peak corresponding to π→π transitions in the range with a maximum at λ = 198–204 nm. In addition, a broad absorption band at λ = 280–310 nm is due to electronic transitions associated with amine and amide groups, as well as electronic transitions of conjugated structures (*n*→π*) [49]. In caffeine, the absorption band observed around 205 nm can be attributed to π→π* transitions associated with the conjugated ring system and carbonyl groups, while the band near 272 nm corresponds to n→π* transitions of the carbonyl moieties [50]. The expansion at 280–294 nm has been shown to be a result of their interaction with other molecules (Fig. 2) [51].

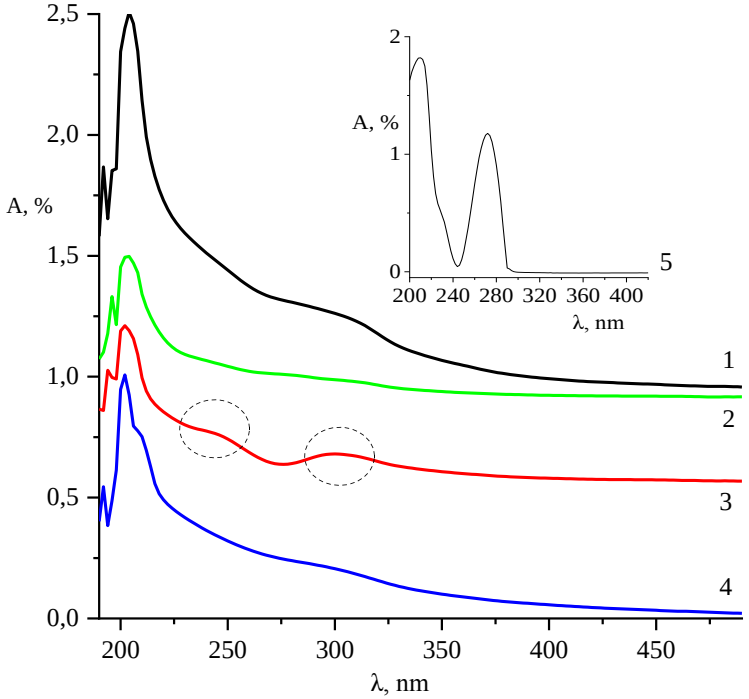

Figure 2. UV-spectra samples of chitosan (*1*); sample 1 (*2*); sample 2 (*3*); sample 3 (*4*), and caffeine samples (*5*)

The UV spectra of the chitosan–caffeine samples show the interaction of chitosan macromolecules with caffeine. The caffeine peak at λ = 266–273 nm is slightly shifted toward lower wavelengths, indicating the encapsulation of caffeine through the formation of hydrogen bonds ($–NH_3^+$ … O=C) between the protonated form of the amino groups of chitosan ($–NH_3^+$) and the carbonyl groups of caffeine (C=O) [52]. Such a bond partially "strains" the π-electron system of caffeine, and the energy required for electron transfer increases, which leads to a shift of λ_{max} toward shorter wavelengths. It is evident that an additional absorption band at 304 nm appears in the spectrum of sample 2, which is explained by the presence of conjugated structures in the chitosan molecule [53-54]. Thus, the UV analysis confirms the encapsulation of caffeine in the chitosan matrix.

FTIR Spectroscopy

The IR spectrum of chitosan exhibits a broad absorption band at 3400–3200 cm^{-1}, which is associated with the stretching vibrations of hydroxyl (OH) and amino (NH) groups. The absorption band at 2920–2850 cm^{-1} corresponds to the stretching vibrations of CH in the aliphatic groups (CH, CH_2, CH_3) of chitosan. Vibrations in the absorption band at 1650–1600 cm^{-1} are very important and are related to the complex structure; in particular, the absorption band at 1600 cm^{-1} is characteristic of the stretching vibrations of the primary amine (NH_2). Stretching vibrations corresponding to C–N bonds were also observed at 1420 cm^{-1}, and deformation vibrations of –CH groups at 1380 cm^{-1}. The absorption band at 1150–1000 cm^{-1} is the "saccharide" absorption band, which corresponds to the stretching vibrations of glycosidic bonds. The absorption bands at 1070 cm^{-1} and 1030 cm^{-1} are characteristic of the C=O bond, and the absorption band at 1150 cm^{-1} is characteristic of the C–O–C bridge (Fig. 3, 1) [21, 49].

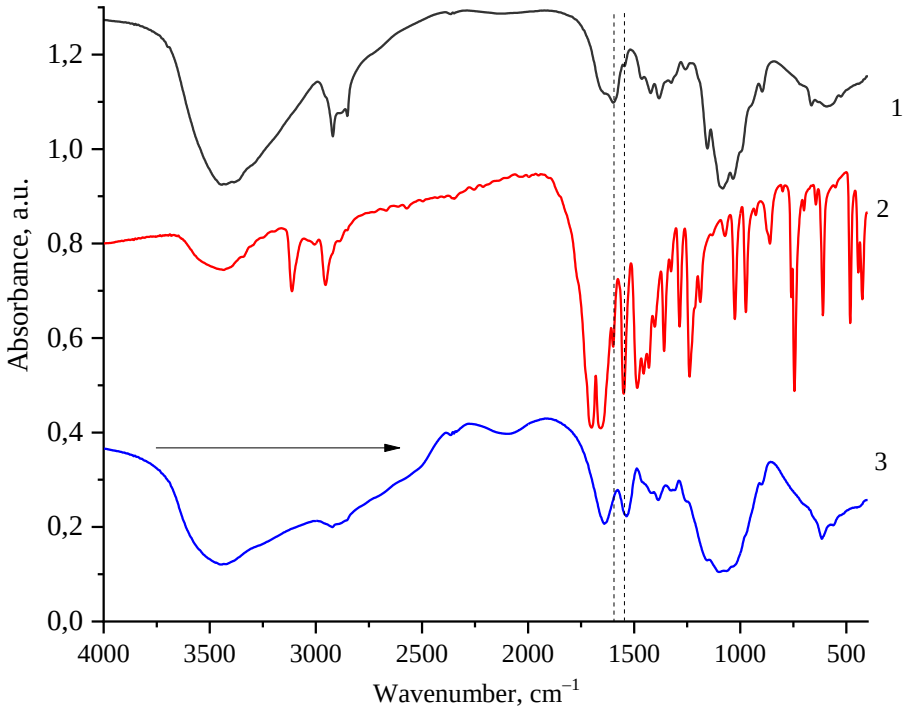

Figure 3. IR spectra of samples: chitosan (*1*), caffeine (*2*), and sample 2 (*3*)

The IR spectrum of caffeine displays CH stretching vibrations at 2950–2850 cm^{-1}, which are characteristic of the methyl groups attached to the nitrogen atoms in caffeine. These absorption bands are typically recorded in the spectrum of caffeine and are used to confirm the presence of methyl groups. The absorption bands at 1700 cm^{-1} and ~1650 cm^{-1} characterize C=O stretching vibrations of the carbonyl groups. Caffeine has two carbonyl groups, the exact position of which can vary slightly depending on the crystal form or environment. These carbonyl bands are considered the "fingerprint" of caffeine and are important for its identification. In addition, the absorption band in the 1550 cm^{-1} region is attributed to vibrations of the –C=N groups of the imidazole ring. The absorption bands at 1480 cm^{-1} and ~1450 cm^{-1} are characterized by C=C stretching vibrations of the aromatic ring and –CH bending vibrations of the methyl groups [55]. These peaks indicate the presence of a heterocyclic ring system in caffeine. The stretching vibrations at 1235 cm^{-1} are associated with –C=N bonds connecting the methyl groups to the nitrogen atoms in the ring. The region below 1200 cm^{-1} contains complex vibrations associated with –CN and C=O stretching, as well as ring deformations [56] (Fig. 3, 2).

The IR spectrum of sample 2 of CS-CF nanocapsules shows a broadening of the vibrational range of 3400–3200 cm^{-1}, characteristic of the –OH and –NH groups. The change in the width and intensity of this band indicates the interaction of chitosan with caffeine through their hydroxyl and amino groups. Also, a shift of the intense absorption band of the stretching vibrations of the amide I and amide II bonds of chitosan at 1640–1540 cm^{-1} is possibly associated with the interaction of caffeine with chitosan through hydrogen

bonds. Furthermore, due to a decrease in the intensity of the characteristic peaks of caffeine in CS-CF, it is assumed that under the chosen synthesis conditions, caffeine is encapsulated by chitosan [56–58] (Fig. 3, 3).

X-Ray Diffraction Patterns

X-ray diffraction study of the structure of caffeine reveals a high degree of crystallinity, which is reflected in its diffraction pattern by intense peaks at 2θ 11.79°; 12.43°; 20.88°; 23.66°; 24.01°; 26.14°; 26.38°; 26.79°; 27.02°; 28.35°; 29.49°; 30.26°; 36.36°; 38.06°; 39.01° and 39.58°, as well as other weak crystalline peaks (Fig. 4) [58, 59]. The size of caffeine single crystals at the indicated 2θ angles varied from 2 to 50 nm, averaging 25 nm. X-ray diffraction analysis of chitosan reveals that the polysaccharide has a semicrystalline structure. A weak diffraction peak at 2θ ≈ 10.4° indicates partial ordering of the chitosan chains, while a more pronounced peak at 2θ ≈ 19.95° is characteristic of the hydrated crystalline form of chitosan (MM 84 kDa; DD 86 %) (Fig. 4; line 3). These features are due to intra- and intermolecular hydrogen bonds in the polymer structure. The intensity and width of these peaks depend on factors such as the chitosan source, the degree of deacetylation, and processing conditions [60].

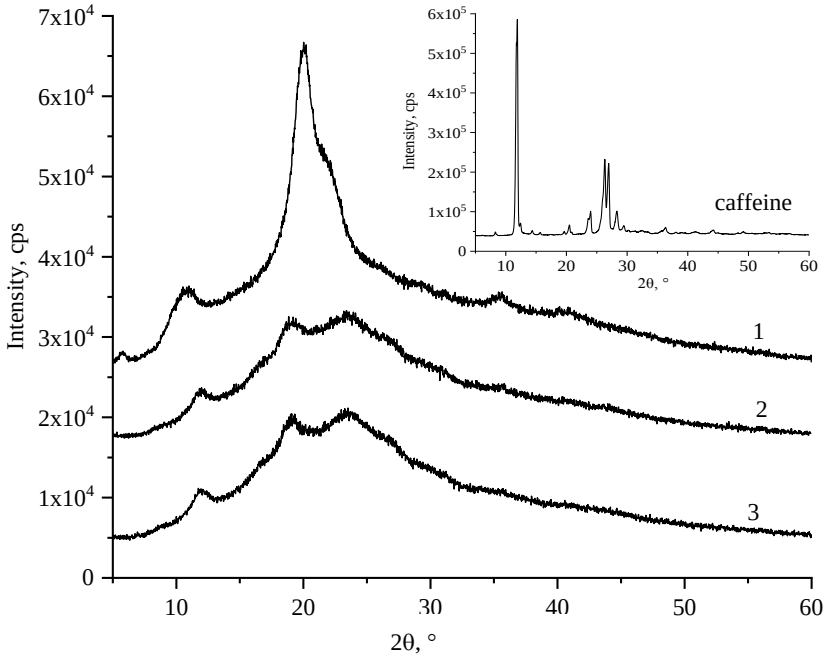

Figure 4. X-ray diffraction patterns of the sample 1 (*1*), sample 2 (*2*), and chitosan (*3*)

The X-ray diffraction patterns of the CS-CF nanocapsule samples differ significantly from those of the original CS and CF (Fig. 4; lines 1 and 2). It emerged that in the CS-CF samples, a shift in the characteristic crystalline peaks of CF at 2θ 11.8°, 18.7°, 23.1°, 35.8°, and 43.7° was observed, and the intensity of the characteristic peak associated with the semicrystalline structure of chitosan decreased, although it became broader. This behavior indicates a partial disruption of the semicrystalline structure of chitosan caused by its interaction with caffeine. The incorporation of caffeine molecules into the CS macromolecule disrupts the inter- and intramolecular hydrogen bonds between the chitosan chains, which leads to a decrease in crystallinity rather than to a complete destruction of the structure. At the same time, X-ray diffraction data indicate that the interaction is predominantly localized at the phase boundary, where the surface region of the caffeine core interacts with the surrounding chitosan shell, while some caffeine may retain residual crystalline order within the capsule. Shifts in the crystal peaks at 2θ further indicate interaction between caffeine and chitosan at the molecular level. The parameters of the crystalline unit cell of chitosan and nanocapsules were also calculated and are presented in Table 2.

Table 2

Crystal cell parameters of CS and CS-CF nanocapsules

No.	2θ, °	*d*, Å	(FWHM) β, °	(Size) L, nm
Chitosan				
1	10.49	8.43	2.54	3.28
2	19.95	4.44	1.98	4.3
CS-CF Sample 1				
3	11.89	7.44	1.41	5.93
4	18.73	4.735	2.02	4.17
5	23.17	4.01	2.9	3
6	35.82	2.505	0.75	11.7
7	43.75	2.067	1.3	6. 8
CS-CF Sample 2				
8	11.92	7.42	1.62	5.13
9	18.96	4.677	1.43	5.9
10	23.17	4.01	2.9	2.9
11	35.23	2.545	3.3	2.6
12	44.5	2.03	3.6	2.5

The sample 2 nanocapsules showed that it has a monoclinic type crystal structure: *a* — 7.211 Å, *b* — 2.806 Å, *c* — 9.305 Å; α — 90º, β — 90º, γ — 90º. Thus, the monoclinic structure provides insights into the stability of the nanocapsules, which is important for their application in drug delivery.

Scanning Electron Microscope (SEM) Results

A SEM image of chitosan demonstrates that it has a generally porous, loose structure with numerous irregularities and channels. A scale estimate shows that the large particles have a diameter of approximately 1–5 μm. Within these structures, the presence of smaller structures, possibly in the range of 100–300 nm, can be predicted (Fig. 5). The particles are round or oval in shape, indicating possible self-assembly. Some areas appear as denser aggregates, which may indicate partial agglomeration of the particles. On the whole, the structure appears well-distributed, without large clumps, indicating a stable distribution of the components [61, 62].

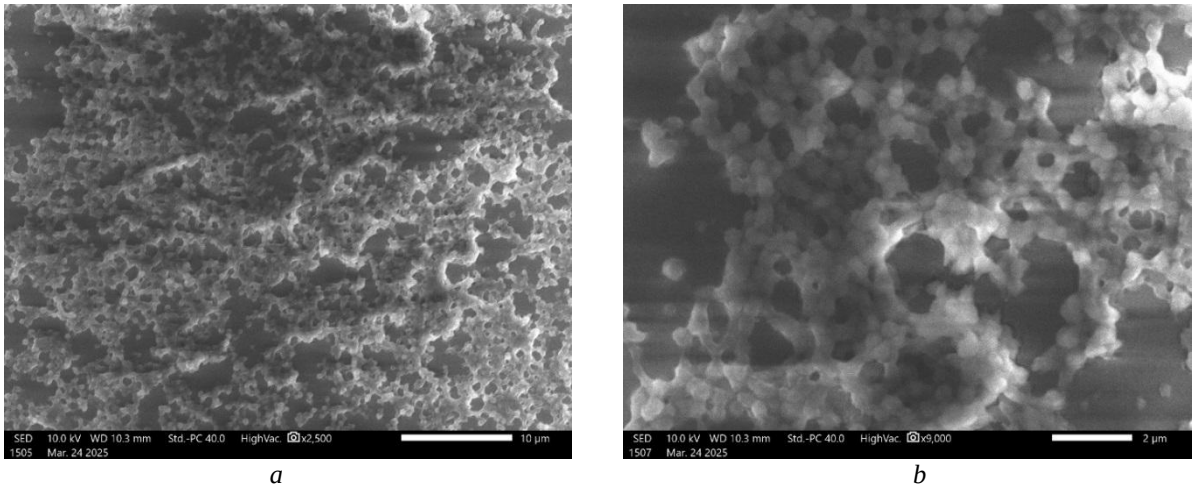

a *b*

Figure 5. SEM micrographs of the surface morphology of chitosan: *a* — ×10 μm; *b* — ×2 μm

SEM micrographs reveal elongated, needle-like structures (Fig. 6), which are characteristic of crystalline caffeine morphology reported in previous studies [63].

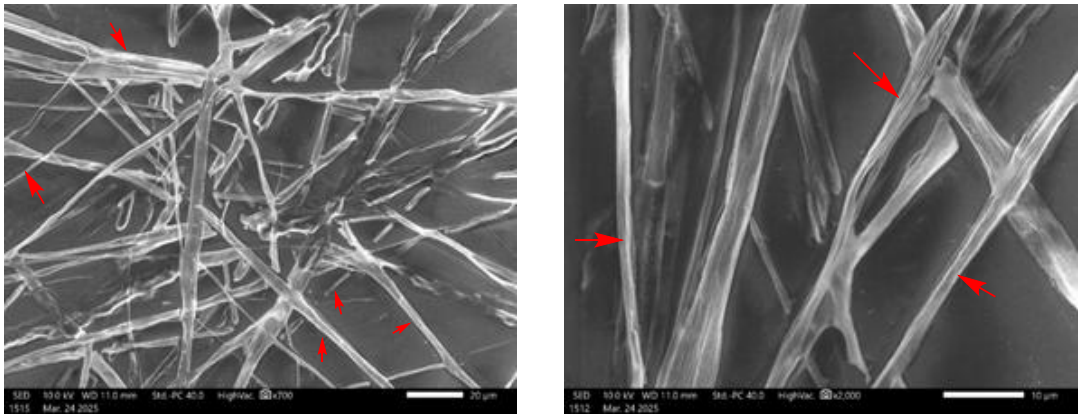

a *b*

Figure 6. SEM micrographs of the surface morphology of caffeine: *a* — ×20 μm; *b* — ×10 μm

Figures 7–9 show the SEM micrographs obtained according to Table 1. The results indicate that the morphology of the nanocapsules depends significantly on the pH of the synthesis and the ratio of chitosan to caffeine. From Figure 7, it is evident that the morphology of sample 1 CS-CF formed particles of different sizes, approximately from 224 nm to 448 nm, within which spherical nanoparticles can be distinguished, indicating a controlled self-assembly and encapsulation process. The spherical morphology is typical of chitosan-based nanocarriers formed through ionic gelation or polyelectrolyte complexation, and similar features have been noted for caffeine-loaded chitosan nanocapsules [2, 21].

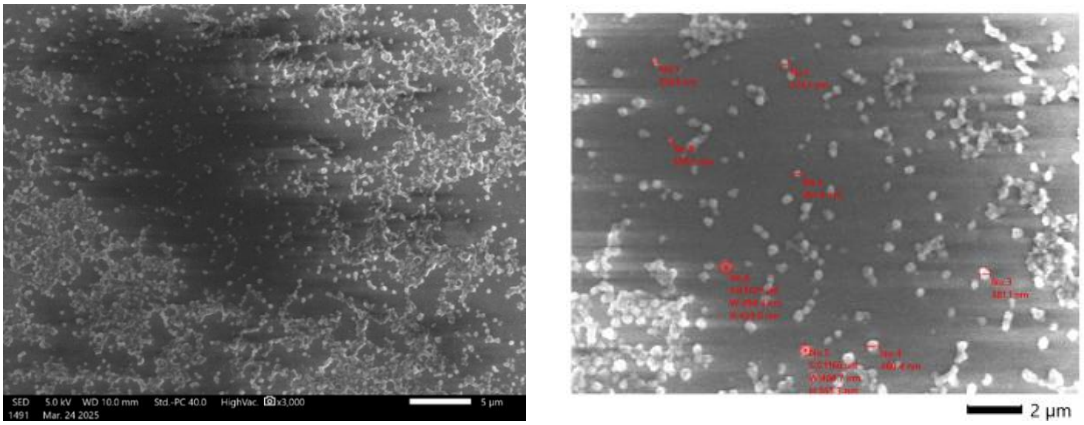

a *b*

Figure 7. SEM micrographs of the surface morphology of sample 1: *a* — ×5 μm; *b* — ×2 μm

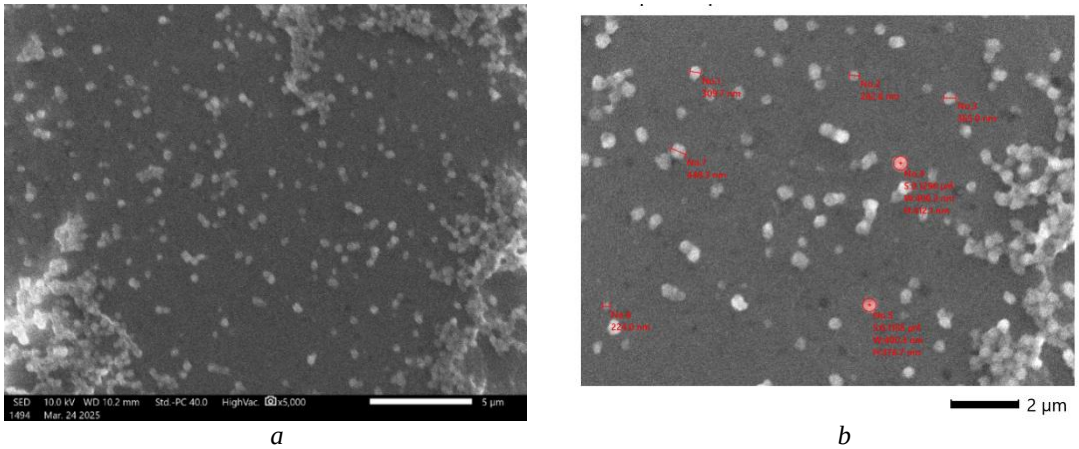

a *b*

Figure 8. SEM micrographs of the surface morphology of sample 2: *a* —×5 μm; *b* — ×2 μm

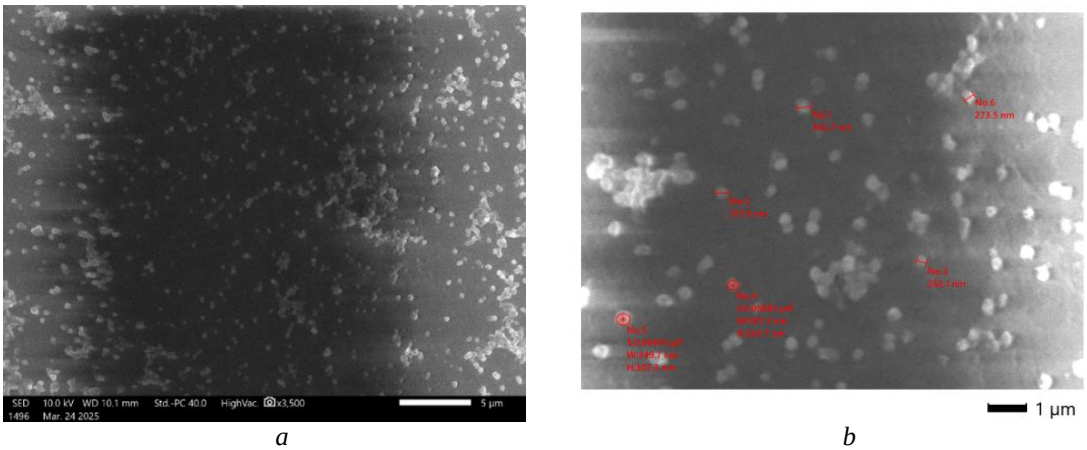

a *b*

Figure 9. SEM micrographs of the surface morphology of sample 3: *a* — ×5 μm; *b* — ×1 μm

It should be emphasized that pH adjustment changes the degree of protonation of chitosan and thus controls the balance between intermolecular attraction and repulsion. After particle formation, the residual positive surface charge of chitosan creates electrostatic repulsion between particles, limiting uncontrolled aggregation and ensuring the formation of stable, self-assembling spherical nanocapsules.

As evidenced by Figure 8, the surface morphology of sample 2 nanocapsules is similar to that of sample 1. Particle size varies: for example, one is approximately 365 nm long, while another is approximately 224 nm, and some are even larger, reaching 448 nm. Surface area (S) and height (H) measurements were taken, indicating the three-dimensional characteristics of the particles.

Results from surface morphology studies of sample 3 show that the largest particles are approximately 120 nm and 116 nm in size (Fig. 9). Smaller particles, approximately 71 nm and 28.4 nm in size, are also present. It is noteworthy that the particles have different sizes and shapes, which may indicate their complex morphology. The difference in size may indicate the presence of aggregates or individual nanoparticles.

Thus, it was demonstrated that the resulting nanocapsules have a distinctive surface morphology compared to the original components. It was found that encapsulating caffeine with chitosan macromolecules results in particles that differ from chitosan and caffeine in both size and shape.

Transmission Electron Microscope (TEM) Results

TEM images of nanocapsules—sample 1 and sample 2 show the presence of capsule-shaped particles with overall dimensions of approximately 215 nm (Fig. 10). In both cases, these particles are surrounded by a shell with a characteristic thickness in the range of approximately 150–200 nm, indicating the formation of well-developed capsule structures. The similarity of the characteristic dimensions confirms the reproducibility of nanocapsule size under different synthesis conditions, while variations in shell thickness reflect differences in the degree of chitosan precipitation and structural compaction.

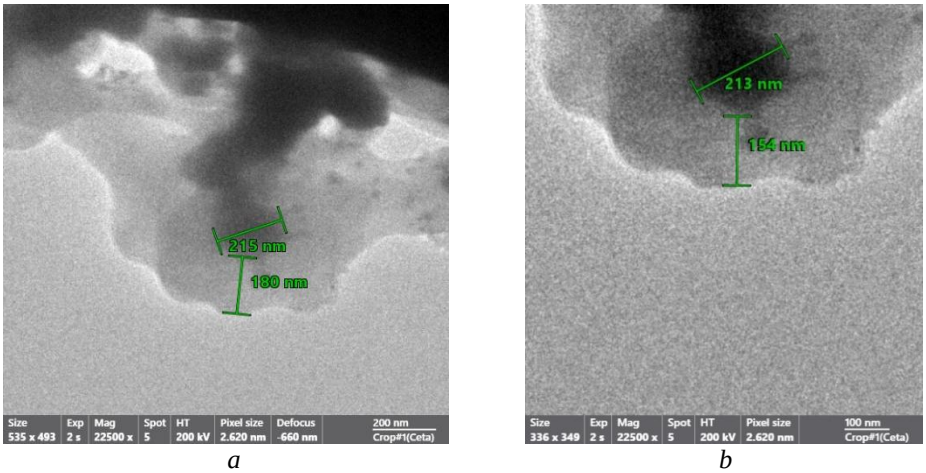

a *b*

Figure 10. TEM images of sample 1 (*a*) and sample 2 (*b*)

The microphotograph of sample 3 shows nanostructures. In the center and left are two particles, 120 nm and 116 nm in size, respectively. Smaller particles extending from them are 71 nm, 51.3 nm, and 28.4 nm. Overall, the images show nanostructures with the expected particle sizes (Fig. 11*a*). Figure 11*b* shows a particle with a length of 81 nm, likely corresponding to a small region or thickness of part of the structure. 107 nm is another measured dimension, possibly the length or width of a particular part. 264 nm and 265 nm are two very similar dimensions that may indicate the width or extent of different parts of the object. The overall scale of the image is 200 nm, indicating that all measurements refer to tiny structures, likely on the micro- or nanoscale (Fig. 11*b*).

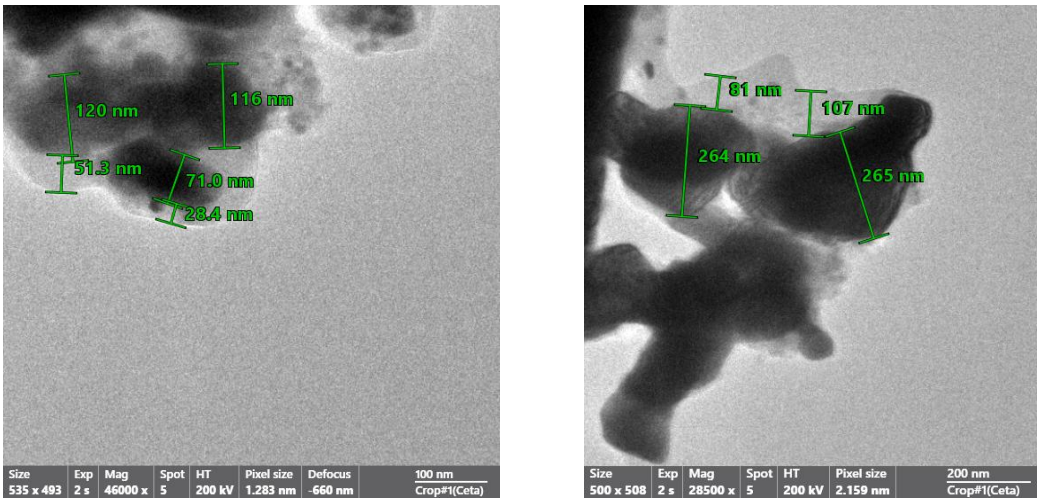

a *b*

Figure 11. TEM images of chitosan-caffeine sample 3

The results of SEM and TEM studies confirm the formation of predominantly spherical and oval chitosan-caffeine nanocapsules. SEM micrographs revealed well-dispersed nanoparticles with a smooth surface and minimal agglomeration, indicating a uniform morphology. TEM images further demonstrate that caffeine was effectively encapsulated within the chitosan matrix, forming core-shell nanostructures with a clear contrast between the polymer shell and the encapsulated core. These results confirm the efficient encapsulation and stable morphology of the synthesized nanocapsules [2, 21].

Controlled Release of Caffeine

Controlled release of caffeine is essential for increasing the bioavailability of drugs and reducing side effects. The results obtained show that at 900 s, $\lambda \approx 242$ nm, A = 1.455 (maximum); thereafter, the peak intensity decreased and stabilized in the range of A = 1.12–1.21 from 3600 to 9000 s. The spectral shift: λ_{peak} gradually shifted from 242 nm → 236 nm. This hypsochromic shift indicates that the microenvironment surrounding caffeine (pH, interaction with the polymer) is changing (Fig. 12).

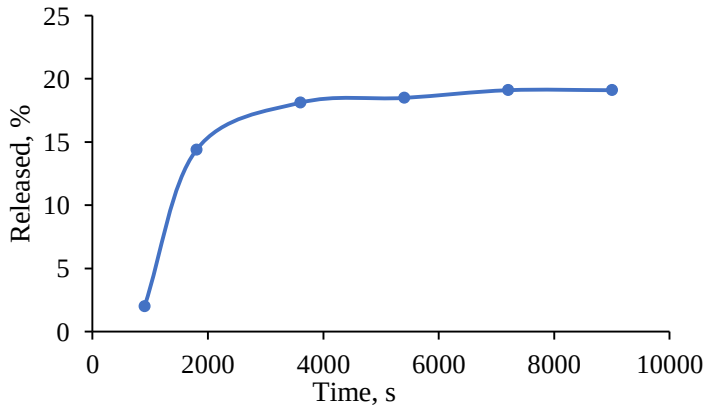

Figure 12. Dependence of the percentage of caffeine release from chitosan nanocapsules on time

Figure 12 manifests that the relatively high intensity in the initial stages of prolongation compared to the final stage indicates that the majority of the caffeine is quickly released from the capsule at 900 s of the process. In other words, a "burst" release is observed. This is explained by the rapid diffusion of caffeine molecules near the surface. Subsequently, the caffeine within the matrix is gradually released, providing a prolonged release phase. Comparison of the obtained results reveals a shift in the λ peaks and an initial high intensity of chitosan capsules in the matrix-solvent medium. This is due to the fact that she protonated amino groups of chitosan interact with caffeine molecules through ionic and hydrogen bonds. Over time, these bonds weaken, and the caffeine is released. Therefore, an initial rapid release (burst) occurs, followed by a slow release phase controlled by diffusion. A biphasic release profile is advantageous in pharmaceuticals, since the first phase provides a rapid therapeutic effect, while the second phase maintains a stable concentration over an extended period (Fig. 12) [64–67]. In conclusion, the release of caffeine from chitosan-caffeine nanocapsules is a two-stage process: Rapid release (~900 s) and diffusion-controlled extended release (1800–9000 s) are observed. The shift in the λ peak confirms the change in the caffeine microenvironment within the chitosan matrix. The kinetic analysis is consistent with the Higuchi and Korsmeyer–Peppas models, indicating that the release occurs predominantly through Fickian diffusion. This profile confirms the potential of chitosan-caffeine nanocapsules as a drug delivery system with rapid and extended release.

Conclusions

The study demonstrated that the formation of chitosan–caffeine nanocapsules is strongly influenced by both the pH of the reaction medium and the mass ratio of the components. Under the selected conditions (pH 3.2 and 4.5), the reaction yields reached 91–94 %, confirming the efficiency of the applied synthesis approach. DLS analysis revealed hydrodynamic particle sizes predominantly in the 400–700 nm range with polydispersity indices of 0.477–0.604, indicating the formation of heterogeneous but stable nanoscale dispersions. UV–Vis spectroscopy showed a hypsochromic shift of the characteristic caffeine absorption band, confirming intermolecular interactions within the polymer matrix. FTIR spectra demonstrated broadening and shifts in the –OH/–NH and amide regions, supporting the formation of hydrogen bonding between chitosan and caffeine. XRD patterns indicated a decrease in the crystallinity of caffeine after encapsulation, reflecting disruption of its ordered structure within the composite system. SEM micrographs revealed predominantly spherical and oval particles with average sizes of approximately 220–450 nm for samples synthesized at higher caffeine ratios and 30–120 nm for the lower-ratio system. TEM analysis further confirmed discrete nanocapsules with characteristic dimensions around 200–400 nm, supporting the formation of structurally organized polymer–drug assemblies distinct from the initial components. The release profile showed that the cumulative percentage of caffeine released from chitosan nanocapsules reached approximately 20 % over the monitored time period. These results collectively confirm the successful formation of chitosan–caffeine nanocapsules and substantiate their potential for controlled drug delivery applications.

Funding

This study was conducted with the basic funding of the Academy of Sciences of the Republic of Uzbekistan.

*Author Information**

**The authors' names are presented in the following order: First Name, Middle Name and Last Name*

Khusnibonu Abdukayum kizi Ergasheva (*corresponding author*) — Junior Researcher, Institute of Polymer Chemistry and Physics, 100128; e-mail: khusnibonu_ea@mail.ru; https://orcid.org/0009-0006-9418-2491

Noira Rahimovna Vokhidova — Doctor of Chemical Sciences, Professor, Head of the Laboratory of Interpolyelectrolyte Complexes and Metallopolymers, Institute of Polymer Chemistry and Physics, 100128, Tashkent, Uzbekistan; e-mail: noira_vokhidova@yahoo.de; https://orcid.org/0000-0003-0477-3708

Author Contributions

The manuscript was written through the contributions of all authors. All authors have given approval to the final version of the manuscript. CRediT: **Khusnibonu Abdukayum kizi Ergasheva** investigation, validation, writing-original draft; formal analysis, editing; **Noira Rahimovna Vokhidova** conceptualization, data curation, formal analysis, validation & editing.

Acknowledgment

The authors acknowledge the staff of the Laboratory of Chemical and physico-chemical research methods at the Institute of Chemistry and Physics of Polymers, in particular candidate of physical and mathematical sciences N.S. Ashurov and junior researcher S. Shakhobiddinov, for their valuable assistance in the interpretation of UV spectroscopy and DLS measurement results.

Conflicts of Interest

The authors declare no conflict of interest

References

1 Abdoli, F., Davoudi, M., Momeni, F., et al. (2024). Estimate the prevalence of daily caffeine consumption, caffeine use disorder, caffeine withdrawal, and perceived harm in Iran: a cross-sectional study. *Scientific Reports*, 14, 7644. https://doi.org/10.1038/s41598-024-58496-8

2 Seyedabadi, M. M., Rostami, H., Jafari, S. M., & Fathi, M. (2021). Development and characterization of chitosan-coated nanoliposomes for encapsulation of caffeine. *Food Bioscience*, 40, 100857. https://doi.org/10.1016/j.fbio.2020.100857

3 Peng, H., Brown, M., Bowdler, P., & Honeychurch, K. C. (2020). Extraction-free, direct determination of caffeine in microliter volumes of beverages by thermal desorption–gas chromatography–mass spectrometry. *International Journal of Analytical Chemistry*, 2020, 5405184. https://doi.org/10.1155/2020/5405184

4 Chow, C. H., Kan, Y. C., & Ho, K. S. (2019). A simple and rapid gas chromatographic method for routine caffeine determination in beverages using a nitrogen–phosphorus detector. *Journal of Analytical Chemistry*, 74, 764–770. https://doi.org/10.1134/S1061934819080045

5 Radeva, L., Kalampalika, E., Yordanov, Y., Petrov, P. D., Tzankova, V., & Yoncheva, K. (2025). Formulation of caffeine–hydroxypropyl-β-cyclodextrin complex in hydrogel for skin treatment. *Gels*, 11, 326. https://doi.org/10.3390/gels11050326

6 Kashapov, R. R., Kashapova, N. E., Ziganshina, A. Y., Syakaev, V. V., Khutoryanskiy, V. V., & Zakharova, L. Y. (2021). Interaction of mucin with viologen and acetate derivatives of calix[4]resorcinols. *Colloids and Surfaces B: Biointerfaces*, 208, 112089. https://doi.org/10.1016/j.colsurfb.2021.112089

7 Chen, X.-M., Chen, Y., Hou, X.-F., Wu, X., Gu, B.-H., & Liu, Y. (2018). Sulfonato-β-cyclodextrin mediated supramolecular nanoparticle for controlled release of berberine. *ACS Applied Materials & Interfaces*, 10, 25555–25563. https://doi.org/10.1021/acsami.8b08651

8 Schneider, H.-J. (2009). Binding mechanisms in supramolecular complexes. *Angewandte Chemie International Edition*, *48*(22), 3924–3977. https://doi.org/10.1002/anie.200802947

9 Ibrahim, A. G., Elgammal, W. E., & Hassan, S. M. (2024). Development of a chitosan derivative bearing the thiadiazole moiety and evaluation of its antifungal and larvicidal efficacy. *Polymer Bulletin*, 81(2), 1291–1302. https://doi.org/10.1007/s00289-023-04765-x

10 Naskar, S., Sharma, S., & Kuotsu, K. (2019). Chitosan-based nanoparticles: An overview of biomedical applications and their preparation. *Journal of Drug Delivery Science and Technology*, 49, 66–81. https://doi.org/10.1016/j.jddst.2018.10.022

11 Duan, C., Meng, X., Meng, J., et al. (2019). Chitosan as a preservative for fruits and vegetables: a review on chemistry and antimicrobial properties. *Journal of Bioresources and Bioproducts*, 4, 11–21. https://doi.org/10.21967/jbb.v4i1.189

12 Fouda, M. M., Wittke, R., Knittel, D., & Schollmeyer, E. (2009). Use of chitosan/polyamine biopolymers based on cotton as a model system to prepare antimicrobial wound dressing. *International Journal of Diabetes Mellitus*, 1, 61–64. https://doi.org/10.1016/j.ijdm.2009.05.005

13 Shaban, N. Z., Aboelsaad, A. M., Shoueir, K. R., et al. (2020). Chitosan-based dithiophenolato nanoparticles: preparation, mechanistic information of DNA binding, antibacterial, and cytotoxic activities. *Journal of Molecular Liquids*, 318, 114252. https://doi.org/10.1016/j.molliq.2020.114252

14 Kou, W., Yang, Y., Fan, H., et al. (2024). Regeneration of dental pulp via collagen hydrogel composited with resveratrol-loaded chitosan nanoparticle in a rabbit model of dental pulp injury. *Polymer Bulletin*, 81, 14235–14248. https://doi.org/10.1007/s00289-024-05318-6

15 Zakharova, N. V., Simonova, M. A., Zelinskii, S. N., et al. (2019). Synthesis, molecular characteristics, and stimulus-sensitivity of graft copolymer of chitosan and poly(N,N-diethylacrylamide). *Journal of Molecular Liquids*, 292, 111355. https://doi.org/10.1016/j.molliq.2019.111355

16 Hu, T., Ma, Y., Huang, J., et al. (2020). Self-organized thermo-responsive poly(lactic-co-glycolic acid)-graft-pullulan nanoparticles for synergistic thermo-chemotherapy of tumor. *Carbohydrate Polymers*, 237, 116104. https://doi.org/10.1016/j.carbpol.2020.116104

17 Roy, H., Nayak, B. S., & Nandy, S. (2020). Chitosan-anchored nanoparticles in current drug development utilizing computer-aided pharmacokinetic modeling: Case studies for target-specific cancer treatment and future perspectives. *Current Pharmaceutical Design*, 26, 1666–1675. https://doi.org/10.2174/1381612826666200203121241

18 Khan, M. M., Madni, A., Torchilin, W., et al. (2019). Lipid–chitosan hybrid nanoparticles for controlled delivery of cisplatin. *Drug Delivery*, 26, 765–772. https://doi.org/10.1080/10717544.2019.1642420

19 Francescato, G., Leitão, M. I. P. S., Orsini, G., & Petronilho, A. (2024). Synthesis and medicinal applications of N-heterocyclic carbene complexes based on caffeine and others. *ChemMedChem*, 19, e202400118. https://doi.org/10.1002/cmdc.202400118

20 Lessa, E. F., Nunes, M. L., & Fajardo, A. R. (2018). Chitosan/waste coffee-grounds composite: An efficient and eco-friendly adsorbent for removal of pharmaceutical contaminants from water. *Carbohydrate Polymers*, 189, 257–266. https://doi.org/10.1016/j.carbpol.2018.02.018

21 Mehrabi-Khozani, Z., Jafari, S. M., Sarabandi, K., Rezaei, A., & Maghsoudlou, Y. (2024). Stabilization of caffeine-loaded nanoliposomes via chitosan coating and spray drying for food product applications. *Carbohydrate Polymer Technologies and Applications*, 8, 100617. https://doi.org/10.1016/j.carpta.2024.100617

22 Xu, Y., Kim, C. S., Saylor, D. M., & Koo, D. (2017). Polymer degradation and drug delivery in PLGA-based drug–polymer applications: A review of experiments and theories. *Journal of Biomedical Materials Research Part B: Applied Biomaterials, 105*(6), 1692–1716. https://doi.org/10.1002/jbm.b.33648

23 Zhang, H., Oh, M., Allen, C., & Kumacheva, E. (2020). Monodisperse chitosan nanoparticles for mucosal drug delivery. *Biomacromolecules, 21*(6), 2244–2252. https://doi.org/10.1021/bm0496211

24 Alvarez-Lorenzo, C., & Concheiro, A. (2014). Smart drug delivery systems: From fundamentals to the clinic. *Chemical Communications*, 50, 7743–7765. https://doi.org/10.1039/C4CC01429D

25 Song, X., Singh, M., Lee, K. E., Vinayagam, R., & Kang, S. G. (2024). Caffeine: A Multifunctional Efficacious Molecule with Diverse Health Implications and Emerging Delivery Systems. *International Journal of Molecular Sciences*, 25(22), 12003. https://doi.org/10.3390/ijms252212003

26 Paul, B., Xie, L., Yahia, Z. O., & Chen, W. (2025). Recent Review on the Stability of Bioactive Substances Through Encapsulation and Their Application in Dairy Products. *Food Reviews International*, 42(2), 605–631. https://doi.org/10.1080/87559129.2025.2492338

27 Layek, B., & Das, S. (2021). Chitosan-based nanomaterials in drug delivery applications. *Biopolymer-Based Nanomaterials in Drug Delivery and Biomedical Applications*, 185–219. https://doi.org/10.1016/b978-0-12-820874-8.00001-4

28 Mohammed, M. A., Syeda, J. T. M., Wasan, K. M., & Wasan, E. K. (2017). An overview of chitosan nanoparticles and their application in non-parenteral drug delivery. *Pharmaceutics, 9*(4), 53. https://doi.org/10.3390/pharmaceutics9040053

29 Grierosu, C., Calin, G., Damir, D., Marcu, C., Cernei, R., Zegan, G., Anistoroaei, D., Moscu, M., Carausu, E. M., Duceac, L. D., Dabija, M. G., Mitrea, G., Gutu, C., Bogdan Goroftei, E. R., & Eva, L. (2023). Development and Functionalization of a Novel Chitosan-Based Nanosystem for Enhanced Drug Delivery. *Journal of Functional Biomaterials*, 14(11), 538. https://doi.org/10.3390/jfb14110538

30 Martins, A. F., Facchi, S. P., Follmann, H. D., et al. (2014). Antimicrobial activity of chitosan derivatives containing N-quaternized moieties in its backbone: A review. *International Journal of Molecular Sciences, 15*(11), 20800–20832. https://doi.org/10.3390/ijms151120800

31 Jiménez-Gómez, C. P., & Cecilia, J. A. (2020). Chitosan: A natural biopolymer with a wide and varied range of applications. *Molecules, 25*(17), 3981. https://doi.org/10.3390/molecules25173981

32 Agnihotri, S. A., Mallikarjuna, N. N., & Aminabhavi, T. M. (2004). Recent advances in chitosan-based micro- and nanoparticles for drug delivery. *Journal of Controlled Release, 100*(1), 5–28. https://doi.org/10.1016/j.jconrel.2004.08.010

33 Illum, L. (1998). Chitosan and its use as a pharmaceutical excipient. *Pharmaceutical Research, 15*(9), 1326–1331. https://doi.org/10.1023/A:1011929016601

34 Elsabee, M. Z., & Abdou, E. S. (2013). Chitosan-based edible films and coatings: A review. *Materials Science and Engineering C, 33*(4), 1819–1841. https://doi.org/10.1016/j.msec.2013.01.010

35 Sogias, I. A., Williams, A. C., & Khutoryanskiy, V. V. (2008). Why is chitosan mucoadhesive? *Biomacromolecules, 9*(7), 1837–1842. https://doi.org/10.1021/bm800276d

36 Bernkop-Schnürch, A., & Dünnhaupt, S. (2012). Chitosan-based drug delivery systems. *European Journal of Pharmaceutics and Biopharmaceutics, 81*(3), 463–469. https://doi.org/10.1016/j.ejpb.2012.04.007

37 Kean, T., & Thanou, M. (2010). Biodegradation, biodistribution, and toxicity of chitosan. *Advanced Drug Delivery Reviews, 62*(1), 3–11. https://doi.org/10.1016/j.addr.2009.09.004

38 Wunderlich, B. (2002). The measurement of the crystallinity of polymers by DSC. *Polymer*, 43, 3873–3878. https://doi.org/10.1016/S0032-3861(02)00235-5

39 Van Bavel, N., Issler, T., Pang, L., Anikovskiy, M., & Prenner, E. J. (2023). A Simple Method for Synthesis of Chitosan Nanoparticles with Ionic Gelation and Homogenization. *Molecules*, 28(11), 4328. https://doi.org/10.3390/molecules28114328

40 Zaman, M., Butt, M. H., Siddique, W., Iqbal, M. O., Nisar, N., Mumtaz, A., Nazeer, H. Y., Alshammari, A., & Riaz, M. S. (2022). Fabrication of PEGylated Chitosan Nanoparticles Containing Tenofovir Alafenamide: Synthesis and Characterization. *Molecules*, 27(23), 8401. https://doi.org/10.3390/molecules27238401

41 Jafernik, K., Kaczmarek, M., Buta, M., et al. (2023). Chitosan-based nanoparticles as effective drug delivery systems: A review. *Molecules, 28*(4), 1963. https://doi.org/10.3390/molecules28041963

42 Borges, M. M. C., Teixeira, H. F., & Sousa, J. J. (2025). Controlled release of perillyl alcohol via pH-responsive polymeric carriers: Fitting to Korsmeyer–Peppas model. *ACS Omega*, 10, 1–11. https://doi.org/10.1021/acsomega.5c04817

43 El-Naggar, N. E. A., Shiha, A. M., Mahrous, H., et al. (2022). Green synthesis of chitosan nanoparticles, optimization, and characterization against biofilms. *Scientific Reports*, 12, 19869. https://doi.org/10.1038/s41598-022-24303-5

44 Gutiérrez-Ruiz, S. C., Cortés, H., González-Torres, M., et al. (2024). Optimize the parameters for synthesis by ionic gelation, purification, and freeze-drying of chitosan-TPP nanoparticles for biomedical applications. *Journal of Biological Engineering*, 18, 12. https://doi.org/10.1186/s13036-024-00403-w

45 Yuan, Q., Shah, J., Hein, S., & Misra, R. D. K. (2010). Controlled and extended drug release behavior of chitosan-based nanoparticle carrier. *Acta Biomaterialia, 6*(3), 1140–1148. https://doi.org/10.1016/j.actbio.2009.08.027

46 Conte, R., De Luca, I., Valentino, A., Cerruti, P., Pedram, P., Cabrera-Barjas, G., Moeini, A., & Calarco, A. (2023). Hyaluronic Acid Hydrogel Containing Resveratrol-Loaded Chitosan Nanoparticles as an Adjuvant in Atopic Dermatitis Treatment. *Journal of Functional Biomaterials, 14*(2), 82. https://doi.org/10.3390/jfb14020082

47 Martín-Escaño, A., Barbuzano, C., Rodríguez-Díaz, J. M., & Pérez-Herrero, E. (2026). Statistical optimization of chitosan-based synthesis strategies to generate albumin nanoparticles. *Drug Delivery and Translational Research*. https://doi.org/10.1007/s13346-026-02046-4

48 Filippov, S. K., Khusnutdinov, R., Murmiliuk, A., Inam, W., Zakharova, L. Ya., Zhang, H., & Khutoryanskiy, V. V. (2023). Dynamic light scattering and transmission electron microscopy in drug delivery: A roadmap for correct characterization of nanoparticles and interpretation of results. *Materials Horizons*, 10, 5354–5370. https://doi.org/10.1039/d3mh00717k

49 Kumirska, J., Czerwicka, M., Kaczynski, Z., et al. (2010). Application of spectroscopic methods for structural analysis of chitin and chitosan. *Marine Drugs, 8*(5), 1567–1636. https://doi.org/10.3390/md8051567

50 Gayathri, G., D'Souza, J. Q., & Sundaram, N. G. (2023). UV induced photocatalytic degradation of caffeine using TiO_2–H-beta zeolite composite. *Minerals, 13*(4), 465. https://doi.org/10.3390/min13040465

51 Bhawani, S. A., Fong, S. S., & Ibrahim, M. N. M. (2015). Spectrophotometric analysis of caffeine. *International Journal of Analytical Chemistry*, 2015, 170239. https://doi.org/10.1155/2015/170239

52 Herdiana, Y., Wathoni, N., Shamsuddin, S., & Muchtaridi, M. (2022). Drug release study of the chitosan-based nanoparticles. *Heliyon, 8*(1), e08674. https://doi.org/10.1016/j.heliyon.2021.e08674

53 Meynaud, S., Huet, G., Brulé, D., Gardrat, C., Poinssot, B., & Coma, V. (2023). Impact of UV irradiation on the chitosan bioactivity for biopesticide applications. *Molecules, 28*(13), 4954. https://doi.org/10.3390/molecules28134954

54 Edwards, A. A., & Alexander, B. D. (2010). Organic applications of UV–visible absorption spectroscopy. In *Encyclopedia of Spectroscopy and Spectrometry* (2nd ed., pp. 2030–2039). https://doi.org/10.1016/B978-0-12-374413-5.00013-0

55 Rajam, K., et al. (2013). Effect of caffeine–Zn^{2+} system in preventing corrosion of carbon steel in well water. *Journal of Chemistry*, 2013, 521951. https://doi.org/10.1155/2013/521951

56 Hamed, A., Ghareeb, D., Mohamed, T. M., Hamed, M., Nofal, M. S., & Gaber, M. (2023). Caffeine–folic acid-loaded chitosan nanoparticles combined with methotrexate as a novel HepG2 immunotherapy targeting adenosine A_2A receptor downstream cascade. *BMC Complementary Medicine and Therapies*, 23, 384. https://doi.org/10.1186/s12906-023-04212-4

57 Stefanowska, K., Woźniak, M., Majka, J., Sip, A., Mrówczyńska, L., Kozak, W., Dobrucka, R., & Ratajczak, I. (2023). Chitosan Films with Caffeine and Propolis as Promising and Ecofriendly Packaging Materials. *Applied Sciences, 13*(22), 12351. https://doi.org/10.3390/app132212351

58 Woźniak, M., Gromadzka, K., & Kwaśniewska-Sip, P. (2022). Chitosan–caffeine formulation as an ecological preservative in wood protection. *Wood Science and Technology*, 56, 1851–1867. https://doi.org/10.1007/s00226-022-01426-6

59 Kamburova, K., Boshkova, N., Radeva, T., Shipochka, M., & Boshkov, N. (2024). Chitosan–alginate nanocontainers with caffeine as green corrosion inhibitors for the protection of galvanized steel. *Crystals, 14*(7), 660. https://doi.org/10.3390/cryst14070660

60 Lehmann, R., & Stowasser, K. (2007). The crystal structure of anhydrous beta-caffeine as determined from X-ray powder-diffraction data. *Chemistry — A European Journal, 13*(10), 2908–2911. https://doi.org/10.1002/chem.200600973

61 Affes, S., Aranaz, I., Acosta Contreras, F. N., & Heras, Á. (2022). Physicochemical and biological properties of chitosan derivatives with varying molecular weight produced by chemical depolymerization. *Biomass Conversion and Biorefinery, 14*(3), 1–11. https://doi.org/10.1007/s13399-022-02662-3

62 Song, W., Zhang, Q., Guan, Y., Li, W., Xie, S., Tong, J., Li, M., & Ren, L. (2022). Synthesis and characterization of porous chitosan/saccharomycetes adsorption microspheres. *Polymers, 14*(11), 2292. https://doi.org/10.3390/polym14112292

63 Khanmohammadi, M., Elmizadeh, H., & Ghasemi, K. (2015). Investigation of the size and morphology of chitosan nanoparticles used in a drug delivery system employing chemometric techniques. *Iranian Journal of Pharmaceutical Research, 14*(3), e125312. https://doi.org/10.22037/ijpr.2015.1761

64 Sarfraz, A., Simo, A., Fenger, R., Christen, W., Rademann, K., Panne, U., & Emmerling, F. (2012). Morphological diversity of caffeine on surfaces: Needles and hexagons. *Crystal Growth & Design, 12*, 583–588. https://doi.org/10.1021/cg101358q

65 Milkova, V., & Goycoolea, F. M. (2020). Encapsulation of caffeine in polysaccharide oil-core nanocapsules. *Colloid and Polymer Science*, 298(8), 1035–1041. https://doi.org/10.1007/s00396-020-04653-0

66 Dash, M., Chiellini, F., Ottenbrite, R. M., & Chiellini, E. (2011). Chitosan — A versatile semi-synthetic polymer in biomedical applications. *Progress in Polymer Science, 36*(8), 981–1014. https://doi.org/10.1016/j.progpolymsci.2011.02.001

67 Naskar, S., Kuotsu, K., & Sharma, S. (2018). Chitosan-based nanoparticles as drug delivery systems: a review on two decades of research. *Journal of Drug Targeting*, 27(4), 379–393. https://doi.org/10.1080/1061186x.2018.1512112

How to Cite: Tazhbayev, Y.M., Galiyeva, A.R., Syrymova, U.Y., Zhaparova, L.Zh., & Zhumagaliyeva, T.S. (2026). Rifampicin Loaded Chitosan-Based Nanoparticles: Optimization, Characterization, and Mucoadhesion. *Eurasian Journal of Chemistry, 31, 1(121), 45–60.* https://doi.org/10.31489/2959-0663/1-26-4

Article

Received: 28 November 2025 | Revised: 27 February 2026 | Accepted: 3 March 2026 | Published online: 13 March 2026

UDC 541.64

https://doi.org/10.31489/2959-0663/1-26-4

Yerkeblan M. Tazhbayev, Aldana R. Galiyeva *, Ulpan Y. Syrymova, Lyazzat Zh. Zhaparova, Tolkyn S. Zhumagaliyeva

Karaganda National Research University named after Academician Ye.A. Buketov, Karaganda, Kazakhstan
*(*Corresponding author's e-mail: aldana_karaganda@mail.ru)*

Rifampicin Loaded Chitosan-Based Nanoparticles: Optimization, Characterization, and Mucoadhesion

One of the important problems in modern pharmaceutical technology is the development of effective and safe drug delivery systems. In this regard, the development of nanostructures that deliver drugs in a targeted manner and increase their bioavailability is of particular importance. Biodegradable polymers form the basis of such systems. Among natural polysaccharides, chitosan deserves special attention. Colloidal particles made from chitosan, especially nanoparticle-based systems, increase the solubility of drugs and enable their effective delivery through the mucosal layer. This study aimed to prepare chitosan nanoparticles loaded with an anti-tuberculosis drug (rifampicin) using the ionotropic gelation method. A central composite design (CCD) was used to study the effects of chitosan concentration, rifampicin concentration, medium pH, and ethanol volume on particle size, polydispersity, and nanoparticle yield. The optimized nanoparticles were spherical in shape with an average particle size of 386±9 nm and a polydispersity index of 0.259±0.025. The rifampicin loading and nanoparticle yield of the optimized nanoparticles were 20 % and 71 %, respectively. The produced nanoparticles were analyzed using thermogravimetric analysis (TGA) and differential scanning calorimetry (DSC), and the results showed no interaction between the drug and the polymer. Drug release from the polymer matrix was studied at different pH values stimulating the gastrointestinal tract. The mucoadhesive activity of rifampicin-loaded chitosan nanoparticles was investigated through the interaction with mucin in acetate buffer solution (pH 5.5) and phosphate buffer solution (pH 6.8). The results showed higher mucoadhesive activity in an acetate buffer solution.

Keywords: drug delivery, rifampicin, bioavailability, nanoparticles, chitosan, tuberculosis, anti-tuberculosis drugs, ionic gelation, mucoadhesion, mucin

Introduction

Tuberculosis represents a significant threat to global health, ranking as the second leading cause of death from infectious diseases after human immunodeficiency virus (HIV). Approximately 10 million people worldwide are diagnosed with tuberculosis annually, and this figure has been increasing since 2020 [1]. Among several anti-tuberculosis drugs, rifampicin (RIF) is considered one of the most effective and plays an important role in short-term therapy. Rifampicin is a model anti-tuberculosis drug with good chemical and physical properties. However, it also has limitations, such as low bioavailability, drug resistance, low permeability through cell membranes, insufficient access to the infected areas, and degradation before reaching its destination [2]. Therefore, it is advisable to develop an alternative delivery system for rifampicin and a method for its implementation. The situation is complicated by the fact that each year more than 15 % of patients are found to have multiple drug resistance or resistance to rifampicin [3] due to non-compliance with the dosage regimen by the patient. The use of natural polymer carriers is a promising solution to these problems. Delivering drugs using nanoscale carriers can increase their bioavailability and significantly prolong the effect of the drug. This is especially important when resistance to anti-tuberculosis drugs develops.

Previously, several polymers were used to manufacture nanoparticles for delivery through the lungs, including polylactide, polylactide-co-glycolide, albumin, chitosan, and alginates [3–6]. The natural polymer chitosan, containing β-(1 → 4)-linked D-glucosamine and N-acetyl-D-glucosamine, is widely used due to its biological solubility, biocompatibility, ability to bind to the mucous membrane (depending on the positive charge in an aqueous environment), low toxicity, and antimicrobial activity [7–10]. In addition, chitosan has high adhesion, enabling it to bind effectively with alveolar macrophages and helps achieve the goal.

Colloidal particles made from chitosan, especially in the form of nanoparticles, increase the solubility of drugs and enable their effective delivery through the mucous layer [11–13]. The large surface area of col-

loidal particles and their special physicochemical properties allow them to be used as carriers for drugs, adsorbents, and biomaterials [14, 15]. However, the process of producing chitosan colloidal particles depends on a number of factors and requires certain conditions. The correct selection of parameters for this process directly affects the properties (size, shape and stability) of the resulting particles. Modern mathematical and statistical methods are used to determine the optimal conditions. One of them is the central composite design (CCD) method. This method allows describing multifactorial systems, determining the relationship between variables, and developing a mathematical model. Its advantage is that it allows obtaining extensive data from a limited number of experiments, which saves time and resources.

In this work, the process was optimized using the central composite design method to produce rifampicin-loaded chitosan colloidal particles (CS-RIF) by a modified ionotropic gelation method. Although rifampicin-loaded chitosan nanoparticles have previously been obtained using ionotropic gelation and optimized using statistical design methods, limitations related to the low solubility of rifampicin and poor control over nanoparticle size and loading efficiency remain insufficiently addressed. In this study, ethanol is introduced as an additional formulation factor in a modified ionotropic gelation process and systematically optimized using a central composite design. The inclusion of ethanol improves the solubility of rifampicin and promotes the formation of nanoparticles with reduced size and a narrower size distribution. Chitosan concentration, rifampicin concentration, pH of the medium, and ethanol volume were selected as factors influencing the particle size and polydispersity index (PDI) of the CS-RIF nanoparticles. The aim of this study is to develop rifampicin-loaded chitosan nanoparticles and to investigate their physicochemical characteristics, drug release kinetics, and mucoadhesive properties.

Experimental

Materials

The following reagents were used in the experiment: low molecular-weight chitosan, rifampicin, sodium tripolyphosphate (TPP), Sodium Acetate Anhydrous (>99 %) and porcine gastric mucin Type II from Sigma-Aldrich (Germany), ethanol 90 % (Dosfarm, Kazakhstan) and acetic acid (Scat Company, Kazakhstan).

Purification of Chitosan

To purify chitosan, we used the method reported by Yang et al [16]. For this purpose, 0.3 g of chitosan was weighed and stirred until completely dissolved in 30 mL of 0.1 M hydrochloric acid (HCl) solution. The solution was continuously stirred in an orbital shaker-incubator at 40 °C overnight. Then the solution was filtered and centrifuged at 10,000 g for 1 hour, and the supernatant was collected. 0.5 M NaOH solution was added dropwise to the supernatant until the pH was reached 10 and a white precipitate appeared. The mixture was centrifuged at 5,000 g for 30 minutes. The supernatant was removed, and the chitosan precipitate remained at the bottom of the tubes. Distilled water was added to the tubes, and the mixture was centrifuged at 5,000 g for 10 minutes. The chitosan precipitate was placed in a Petri dish and dried by lyophilization for 4-5 hours.

Preparation of CS-RIF Nanoparticles

Nanoparticles based on chitosan and rifampicin were synthesized using the ionotropic gelation method with some modifications [17, 18]. Purified chitosan (0.4 g) was dissolved in 0.05 % acetic acid (40 mL) and continuously stirred in an orbital shaker-incubator at 40 °C overnight. The resulting chitosan solution was adjusted to the required pH (4, 5 or 6). The chitosan solution was mixed with deionized water to produce a CS solution with a concentration of 2.5, 5 or 7.5 mg/mL. Rifampicin was dissolved in a 0.15 % DMSO solution to obtain a concentration of 0.25, 0.5 or 0.75 mg/ mL. The resulting drug solution was added to the CS solution and stirred for 10 minutes. To the CS-RIF solution, 4, 6 or 8 mL of 90 % ethanol was added dropwise at a rate of 1 mL/min. Finally, 0.5 % sodium tripolyphosphate (TPP) was added dropwise at a CS:TPP ratio of 3:1, and the resulting mixture was stirred at room temperature for 6 hours. Next, the nanoparticles were separated using a centrifuge (Eppendorf 5420, Hamburg, Germany) at 15,000 rpm for 30 minutes. The nanoparticles were purified with distilled water three times by centrifugation. A schematic representation of the method for producing nanoparticles is shown in Figure 1.

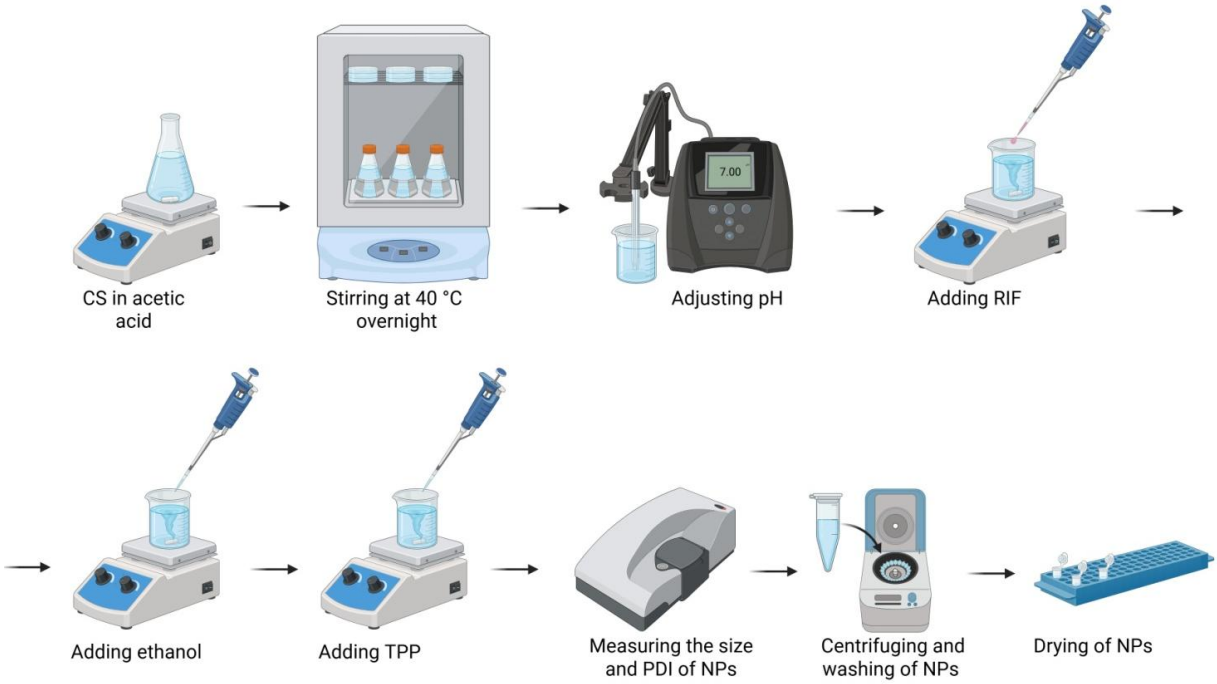

Illustration created in BioRender. Galiyeva, A. (2026) https://BioRender.com/ieb2gof

Figure 1. Schematic illustration of production CS-RIF nanoparticles by ionic gelation method

Central Composite Design for Nanoparticle Optimization

Optimization of CS-RIF nanoparticle production was performed using a central composite design with various factors, including chitosan concentration, rifampicin concentration, medium pH, and ethanol content. Design Expert® software (version 13, Stat-Ease, Minneapolis, Minnesota, USA) was used to create a CCD matrix of four factors with three levels each (Table 1).

Table 1

Experimental factors for CS-RIF nanoparticle synthesis and corresponding levels

Independent Variable	Variable Level		
	Low –1	Center 0	High 1
Concentration of CS, mg/mL	2.5	5	7.5
Concentration of RIF, mg/mL	0.25	0.5	0.75
pH	4	5	6
Ethanol volume, mL	4	6	8

Determination of Particle Size, Polydispersity and ζ-potential of CS-RIF nanoparticles

The nanoparticle size distribution and polydispersity index were measured using Zetasizer Nano S90 (Malvern Instruments Ltd., Malvern, UK) by Dynamic Light Scattering (DLS). For the size analysis of CS-RIF nanoparticles, 5–8 drops of nanoparticles suspension were added to 1.5–2 mL of distilled water. The measurements of the samples were conducted at 25 °C while using a 90° scattering angle for detection.

Evaluation of Drug Loading Efficiency and Nanoparticles' Yield

For spectrophotometric measurements of nanoparticle solutions loaded with a drug substance, RIF solutions were prepared at various concentrations as reference values. Measurements were performed using a UV spectrophotometer (Shimadzu UV-1800 dual-beam scanning spectrophotometer, Japan). The absorbance of the samples was measured at a wavelength of 470 nm (λ) against a 0.15 % DMSO solution.

To determine the yield, the nanoparticles were left to dry for several days and their mass was measured. The loading efficiency of drug and nanoparticles yield were calculated using the following formulas:

$$\text{Loading efficiency}\left(LE, \%\right) = \frac{\text{Total mass of } RIF - \text{mass of free } RIF}{\text{Mass of } NPs} \times 100\ \%$$

$$\text{Nanoparticles yield}\left(\%\right) = \frac{\text{Mass of } NPs}{\text{Total mass of } RIF + \text{mass of } CS + \text{mass of } TPP} \times 100\ \%$$

In Vitro Drug Release from CS-RIF nanoparticles

The kinetics of rifampicin release from the polymer matrix were determined by the dialysis dilute HCl or in phosphate-saline buffer at 37 °C in three different environments (0.2 M HCl with pH 1.2, 0.1 M phosphate buffer with pH 6.8 and 7.4). For this purpose, 24 mg drug-loaded nanoparticles were dispersed in 3 mL phosphate buffer and treated with ultrasound for 10 minutes. The resulting dispersion was transferred to a dialysis membrane (MwCO: 8,000–14,000 D). The membrane was fixed on both sides with clamps, placed in a container with 14 mL dilute HCl or phosphate-saline buffer and placed in a thermostat at 37 °C. The amount of drug released from the polymer nanoparticles was determined by UV spectroscopy (wavelength λ = 470 nm), and the degree of release was calculated using the following formula:

$$\text{Drug release } \left(\%\right) = \frac{\text{Mass of released } RIF}{\text{Mass of total } RIF \text{ in nanoparticles}} \times 100\ \%$$

Thermogravimetry and Differential Scanning Calorimetry Analysis of CS-RIF nanoparticles

Thermogravimetric and differential scanning calorimetric studies were performed using a LabSYS evo TGA/DTA/DSC analyzer (Setaram, Caluire, France). Measurements were performed in the temperature range from 30 °C to 915 °C. The samples were placed in aluminium oxide crucibles and heated at a controlled rate of 10 °C/min. The analysis was carried out in a nitrogen atmosphere at a constant gas flow rate of 30 mL/min.

Infrared Spectroscopic Analysis of CS-RIF nanoparticles

The characteristics of the produced nanoparticles and rifampicin samples were studied using IR spectroscopy with an FSM 1202 spectrometer (Infraspek Ltd., Russia). The potassium bromide pellet method was used to record Fourier transform infrared (FTIR) spectra. The spectra were recorded in the wavenumber range from 4000 to 400 cm^{-1}.

Study of the Mucoadhesive Properties of CS-RIF Nanoparticles

To study the mucoadhesive properties, the turbidimetric method with a Hach 21000AN laboratory turbidimeter (Hach Company, USA) was used [19–21]. To assess the effect of the medium on the mucoadhesive properties, two different buffer solutions were used: an acetate buffer solution (pH 5.5) and a phosphate buffer solution (pH 6.8). In each buffer medium, 0.0015 g of mucin was dissolved and the initial optical density was measured at 255 nm. Then 0.0195 g of rifampicin-loaded chitosan nanoparticles were added to the same solution. The solution was incubated at 37 °C and the optical density was measured for 4 hours to study the dynamics of the mucoadhesive effect. The interaction of mucin with CS-RIF nanoparticles was calculated using the following equation:

$$\text{Mucin binding efficiency}\left(\%\right) = \frac{\text{Absorbance}_{\text{sample}} - \text{Absorbance}_{\text{initial}}}{\text{Absorbance}_{\text{sample}}} \times 100\ \%.$$

Statistical Analysis

All experiments were carried out at least three times. The results are reported as means with standard deviations. To analyze independent groups, a one-way analysis of variance was applied using Minitab19 software. The effect of the suggested experiments on the responses was analyzed using Design Expert software to generate the main effects of various factors regardless of each other, and then an analysis of variance (ANOVA) was performed to determine statistically significant factors. The optimal experimental conditions were identified by selecting the function.

Results and Discussion

There are various methods for producing chitosan-based nanoparticles, including ionotropic gelation, nanoparticle deposition, and emulsification-based methods [22–26]. Among them, ionotropic gelation is one

of the most commonly used methods due to the use of mild reagents, a simple preparation process, and ease of controlling the size of the nanoparticles. In this method, ionic mixing occurs between the protonated amino groups of chitosan and the negatively charged groups of polyanion (sodium tripolyphosphate), thus forming nanoparticles [27]. Using a previously developed technique [17, 18], chitosan nanoparticles loaded with rifampicin were produced at the initial stage. The particle size of CS-RIF NPs and their polydispersity are not good enough (diameter more than 823±11 nm, PDI 0.742±0.049), which limits their potential use as drug delivery systems in the body. Thus, it is necessary to optimize the method specifically for producing chitosan-rifampicin nanoparticles, taking into account the properties and solubility of the active substance. The novelty of this work is the addition of ethanol during the production of CS-RIF nanoparticles. Ethanol plays several roles in the creation of nanoparticles by ionotropic gelation method. Ethanol increases the solubility of rifampicin, thereby improving the drug loading efficiency in the polymer matrix. It also reduces interfacial tension in particle-particle interactions, thus preventing nanoparticle aggregation [28–30]. Therefore, ethanol acts not only as a co-solvent, but also as a key factor in regulating nanoparticle size and drug loading efficiency.

The aim of this study is to optimize the parameters for producing rifampicin-loaded chitosan-based nanoparticles. To achieve this goal, key factors such as chitosan concentration, rifampicin concentration, medium pH and ethanol volume were analyzed. In addition, the physicochemical properties, drug release from the polymer matrix at different pH values, and mucoadhesive properties of the produced CS-RIF nanoparticles were studied.

The central composite design method was used to optimize the above parameters. This optimization method allows the interactions of a large number of variables to be determined by conducting a limited number of experiments. Previously, the CCD method has demonstrated good results in optimizing the synthesis of nanoparticles for the delivery of antituberculosis drugs [3, 31]. To optimize the parameters of CS-RIF nanoparticles, 17 experiments were conducted. Table 2 shows the structure of the orthogonal matrix and the results of measuring the size and polydispersity of the particles, as well as the rifampicin loading efficiency and nanoparticle yield.

Table 2

Formulations of CS-RIF nanoparticles using central composite design and their evaluation parameters

Nanoparticles	[CS], mg/mL	[RIF], mg/mL	pH	Ethanol volume, mL	Size, nm	PDI	LE, %	NPs yield, %
NP 1	5	0.5	5	4	426±8	0.264±0.024	33±9	88±8
NP 2	7.5	0.75	4	4	563±4	0.751±0.122	38±8	20±4
NP 3	2.5	0.75	6	8	461±10	0.226±0.004	49±2	12±7
NP 4	5	0.75	5	6	427±9	0.247±0.014	36±8	94±9
NP 5	2.5	0.75	4	8	575±9	0.236±0.022	41±3	6±4
NP 6	5	0.5	5	6	491±13	0.233±0.030	20±8	28±3
NP 7	5	0.5	4	6	507±5	0.275±0.039	29±2	5±5
NP 8	7.5	0.25	4	8	528±7	0.527±0.049	36±2	4±2
NP 9	2.5	0.5	5	6	376±6	0.242±0.021	31±8	90±6
NP 10	7.5	0.25	6	8	315±9	0.307±0.137	37±4	54±6
NP 11	5	0.5	5	8	493±13	0.257±0.016	15±4	68±1
NP 12	2.5	0.25	6	4	347±2	0.264±0.004	40±8	17±4
NP 13	7.5	0.5	5	6	238±5	0.233±0.028	28±3	54±3
NP 14	2.5	0.25	4	4	425±8	0.364±0.061	38±8	11±3
NP 15	5	0.25	5	6	440±8	0.258±0.011	27±2	75±1
NP 16	7.5	0.75	6	4	371±15	0.434±0.262	45±2	93±8
NP 17	5	0.5	6	6	664±6	0.317±0.048	35±6	91±5

Results are shown as mean ± standard deviation (n = 3)

According to the results obtained (Table 2), depending on the synthesis conditions, CS-RIF nanoparticles with diameters ranging from 238±5 to 664±6 nm can be produced, with polydispersity also varying significantly from 0.226±0.004 to 0.751±0.122. The smallest particle size was in sample NP13 (238±5 nm) with a chitosan concentration of 7.5 mg/mL, rifampicin concentration of 0.5 mg/mL, pH of 5, and ethanol volume of 6 mL. The drug loading and nanoparticle yield values are also significant parameters, ranging from 15±4 % to 49±2 % and from 4±2 % to 93±8 %, respectively.

To determine the applicability and significance of the mathematical model for evaluating particle size, polydispersity, and NP yield, the analysis of variance (ANOVA) was used (Table 3).

Table 3

ANOVA results for particle size, polydispersity, and low-frequency yield

Response	Source	Sum of Squares	Degree of Freedom	Mean Square	F-value	p-value
Size	Model	27906.25	3	9302.08	0.8261	0.5027
	A — Concentration of CS	2859.48	1	2859.48	0.2539	0.6228
	B — Concentration of RIF	11710.08	1	11710.08	1.04	0.3272
	C — pH	19377.60	1	19377.60	1.72	0.2123
	D — Ethanol volume	5669.16	1	5669.16	0.5034	0.4905
	Residual	1.464E+05	13	11260.77		
	Cor Total	1.743E+05	16			
PDI	Model	0.1487	3	0.0496	4.20	0.0278
	A — Concentration of CS	0.0846	1	0.0846	7.16	0.0190
	B — Concentration of RIF	0.0030	1	0.0030	0.2413	0.6321
	C — pH	0.0366	1	0.0366	3.10	0.1019
	D — Ethanol volume	0.0275	1	0.0275	2.32	0.1513
	Residual	0.1536	13	0.0118		
	Cor Total	0.3023	16			
NPs yield	Model	6476.16	3	2158.72	1.93	0.1740
	A — Concentration of CS	792.10	1	792.10	0.7096	0.4148
	B — Concentration of RIF	432.96	1	432.96	0.3690	0.5549
	C — pH	4946.18	1	4946.18	4.43	0.0553
	D — Ethanol volume	737.88	1	737.88	0.6610	0.4308
	Residual	14511.93	13	1116.30		
	Cor Total	20988.08	16			

The ANOVA results showed that the size of the nanoparticles did not significantly depend on the investigated factors, indicating a possible influence of nonlinear effects or interactions. At the same time, the PDI index significantly depended on the chitosan concentration ($p = 0.0190$), confirming its key role in the formation of homogeneous particles. The model was statistically non-significant for nanoparticle yield, but pH showed a near-significant to significant effect ($p = 0.0553$), indicating its potential importance for further optimization. For PDI, the predicted R^2 value meaning which was equal to 0.0325, is not in reasonable agreement with the adjusted R^2 value (0.3747) and a similar discrepancy is observed for nanoparticles yield, where the predicted R^2 of 0.1108 is not as close to the adjusted R^2 of 0.4643. Nevertheless, the Adequate Precision for both responses (for PDI 7.8 and for nanoparticles yield 5.9) indicates an adequate signal and this model can be used to navigate the design space.

The model developed based on CCD for evaluating particle size, polydispersity and NP yield is presented below. In these formulas: A is the chitosan concentration, B is the rifampicin concentration, C is the pH, and D is ethanol.

$$\text{Size} = +449.94 - 16.91A + 34.22B - 44.02C + 23.81D$$

$$\text{PDI} = +0.3197 + 0.0920A + 0.0174B - 0.0605C - 0.0524D$$

$$\textbf{NPs yield} = +48.05 + 8.90A + 6.58B + 22.24C - 8.59D$$

The resulting regression equations showed that the size of nanoparticles depends most on pH, while polydispersity increases with increasing chitosan concentration and decreases with pH optimization and ethanol addition. The yield of nanoparticles is determined mainly by the pH value and, to a lesser extent, by the chitosan concentration. Thus, regulating the acidity of the medium is a key factor both for controlling particle size and uniformity as well as increasing their yield.

The influence of various factors on nanoparticle size, polydispersity, and NP yield is illustrated using a three-dimensional (3D) diagram (Figures 2–4).

Three-dimensional response diagrams show the influence of independent factors on the average size of nanoparticles (Figure 2). On the surface reflecting the combined effect of chitosan and rifampicin concentra-

tions, it can be seen that changes in these parameters have virtually no significant effect on particle size. These graphs are consistent with the results of the analysis of variance (ANOVA), where these factors did not show statistical significance. In contrast, the diagram in Figure 2*b*, reflecting the influence of pH and ethanol volume, shows more pronounced dynamics. With an increase in pH, there is a tendency for particle size to decrease, which is explained by a reduction in the degree of protonation of chitosan amino groups and, as a result, a decrease in electrostatic repulsion between polymer chains and a reduction in their degree of hydration [32]. Analysis of the response surface shows a slight increase in the size of chitosan nanoparticles at higher ethanol volumes (from 426 to 473 nm), although the ANOVA results ($p = 0.4905$) indicate low statistical significance. This suggests that ethanol is not a major independent factor. But it may indirectly influence nanoparticle formation by altering the polarity of the medium and modulating the effect of pH or chitosan concentration.

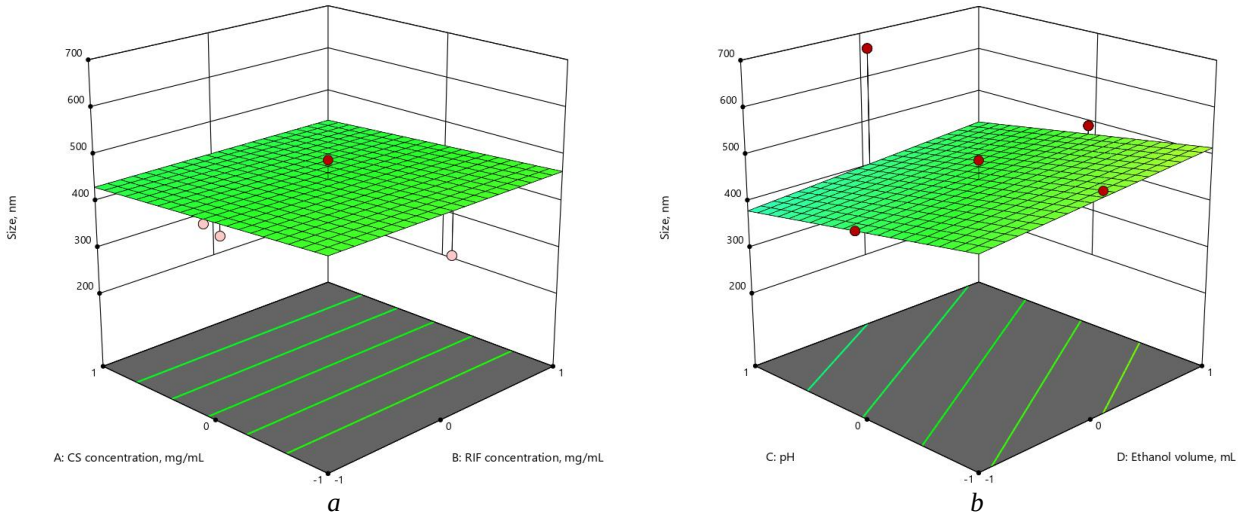

a *b*

Figure 2. Three-dimensional (3D) response surface diagrams of the impact of independent factors on average particle size: (*a*) CS concentration – RIF concentration; (*b*) pH – Ethanol volume

Figure 3 shows 3D diagrams of the influence of independent variables on the polydispersity of the obtained particles. Graph 3a shows that chitosan concentration has a significant influence on PDI, as mentioned in the ANOVA analysis. As the chitosan concentration increases, the polydispersity increases from 0.228 to 0.406.

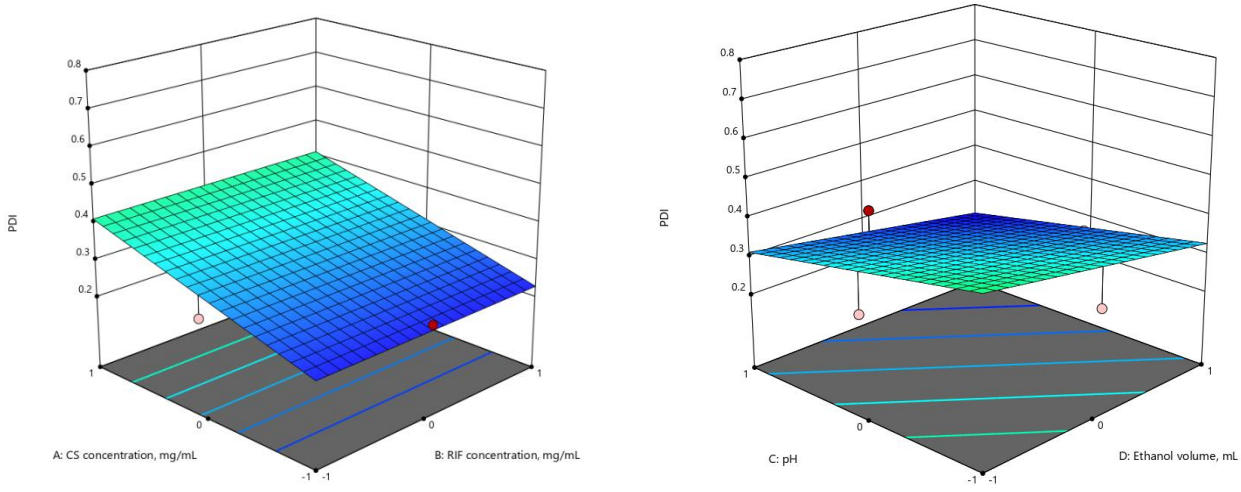

a *b*

Figure 3. Three-dimensional (3D) response surface diagrams of the impact of independent factors on PDI: (*a*) CS concentration – RIF concentration; (*b*) pH – Ethanol volume

The response surface diagrams in Figure 4 show that the yield of nanoparticles increases at high pH, while an increase in ethanol volume leads to a decrease in yield. This dependence is explained by a decrease in the solubility of chitosan and partial destabilization of the ionic cross-linking process in the presence of ethanol. Although the model is not statistically significant (p = 0.174), the observed trend indicates that maintaining a moderate pH value and minimum ethanol content promotes more efficient nanoparticle formation.

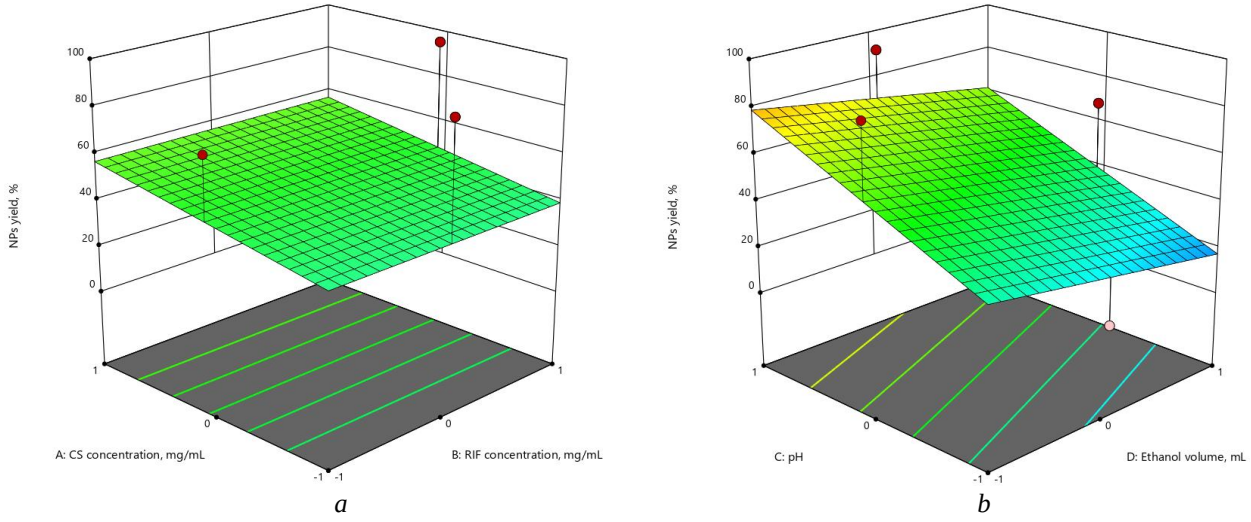

Figure 4. Three-dimensional (3D) response surface diagrams of the impact of independent factors on nanoparticles yield: (*a*) CS concentration – RIF concentration; (*b*) pH – Ethanol volume

After ANOVA analysis, parameters for computer optimization were selected using the Design Expert program. Table 4 shows the criteria used for optimization to obtain CS-RIF nanoparticles with minimum size and maximum yield.

Table 4

Limitations on independent variables and outcomes for optimization production CS-RIF nanoparticles

Name	Goal	Lower Limit	Upper Limit
A: CS concentration	is in range	–1	1
B: RIF concentration	is equal to 0	–1	1
C: pH	is equal to 1	–1	1
D: Ethanol volume	is in range	–1	1
Size	minimize	238.2	663.8
PDI	minimize	0.226	0.751
NPs yield	maximize	4	94.9

The program suggested the following parameters as optimal conditions: chitosan concentration 3.7 mg/mL, rifampicin concentration 0.46 mg/mL, ethanol volume 4 mL, pH value 6.0. Thus, using the recommended program parameters, rifampicin-loaded nanoparticles were synthesized. The characteristics of the produced chitosan nanoparticles were close to the values suggested by the program (Table 5). Consequently, the CCD method is effective for optimizing the synthesis process of CS-RIF nanoparticles (Figure 5).

Table 5

Predicted and experimental results for CS-RIF nanoparticles

	Size, nm	PDI	Yield, %
Predicted	390±10	0.264±0.108	74±3
Experimental	386±9	0.259±0.025	71±2
Error (%)	1	1.9	3.8
All values represent the mean ± S.D. (n = 3)			

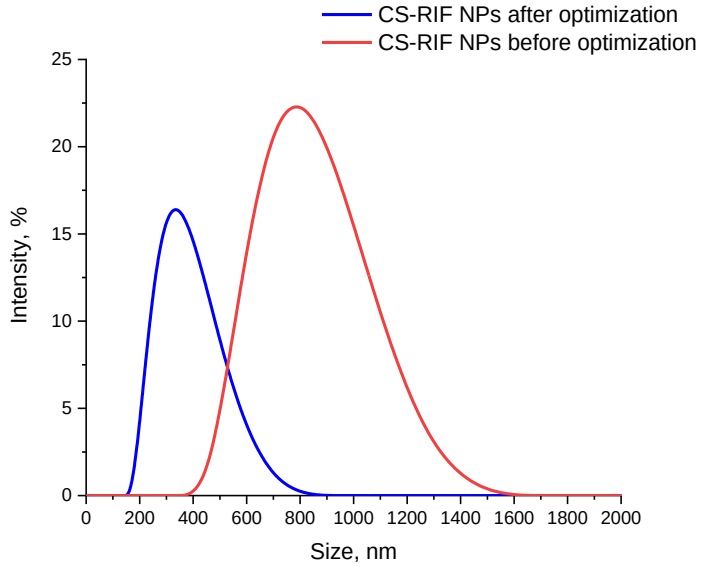

Figure 5. Size distributions of CS-RIF nanoparticles measured by DLS before and after optimization

In order to determine the morphology of nanoparticles obtained under optimal conditions without drugs (CS NPs) and rifampicin-loaded nanoparticles (CS-RIF NPs), scanning electron microscopy (SEM) images were acquired (Figure 6). The images show that the particles are predominantly spherical in shape and relatively homogeneous.

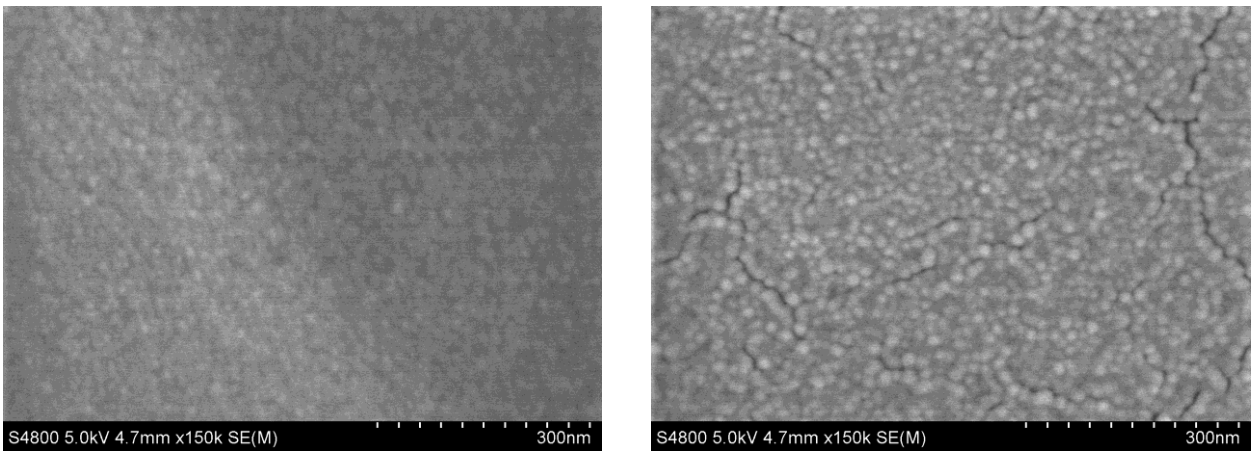

CS NPs CS-RIF NPs

Figure 6. SEM images of CS nanoparticles and CS-RIF nanoparticles at a 300 nm scale

The TGA and DSC results for pure chitosan, rifampicin, and nanoparticles are shown in Figure 7. The first stage of chitosan weight loss (Figure 7*a*) was observed in the temperature range of 40–100 °C, which corresponds to moisture loss (about 10 %). Under a nitrogen flow, chitosan undergoes thermal decomposition in the temperature range from 150 to 600 °C, which indicates chitosan deacetylation, the evaporation, and removal of volatile products [33, 34]. The DSC thermogram of chitosan showed an endothermic peak at 226 °C, which reflects the initial decomposition, and an exothermic peak at 311 °C, which reflects the main thermal decomposition of chitosan. The decomposition of rifampicin occurs in three stages: the main stage begins at 195 °C to 260 °C with a mass loss of 16 %, the second stage proceeded smoothly in the range of 260–450 °C with a mass loss of 44 %, and the third stage (450–900 °C) resulted in a mass loss of 63 % (Figure 7*b*). The endothermic peak at 190 °C is accompanied by no mass loss, thus indicating the melting point of rifampicin. The exothermic peak at 255 °C is characteristic of the recrystallization process [3, 35]. CS-RIF nanoparticles demonstrate increased stability and similar mass loss pattern and thermal peaks (Figure 7*c*). At the same time, the thermal transitions characteristic of rifampicin is noticeably smoothed out, which may

indicate the transition of the substance to an amorphous state or its binding to the polymer matrix due to hydrogen bonding interactions [36].

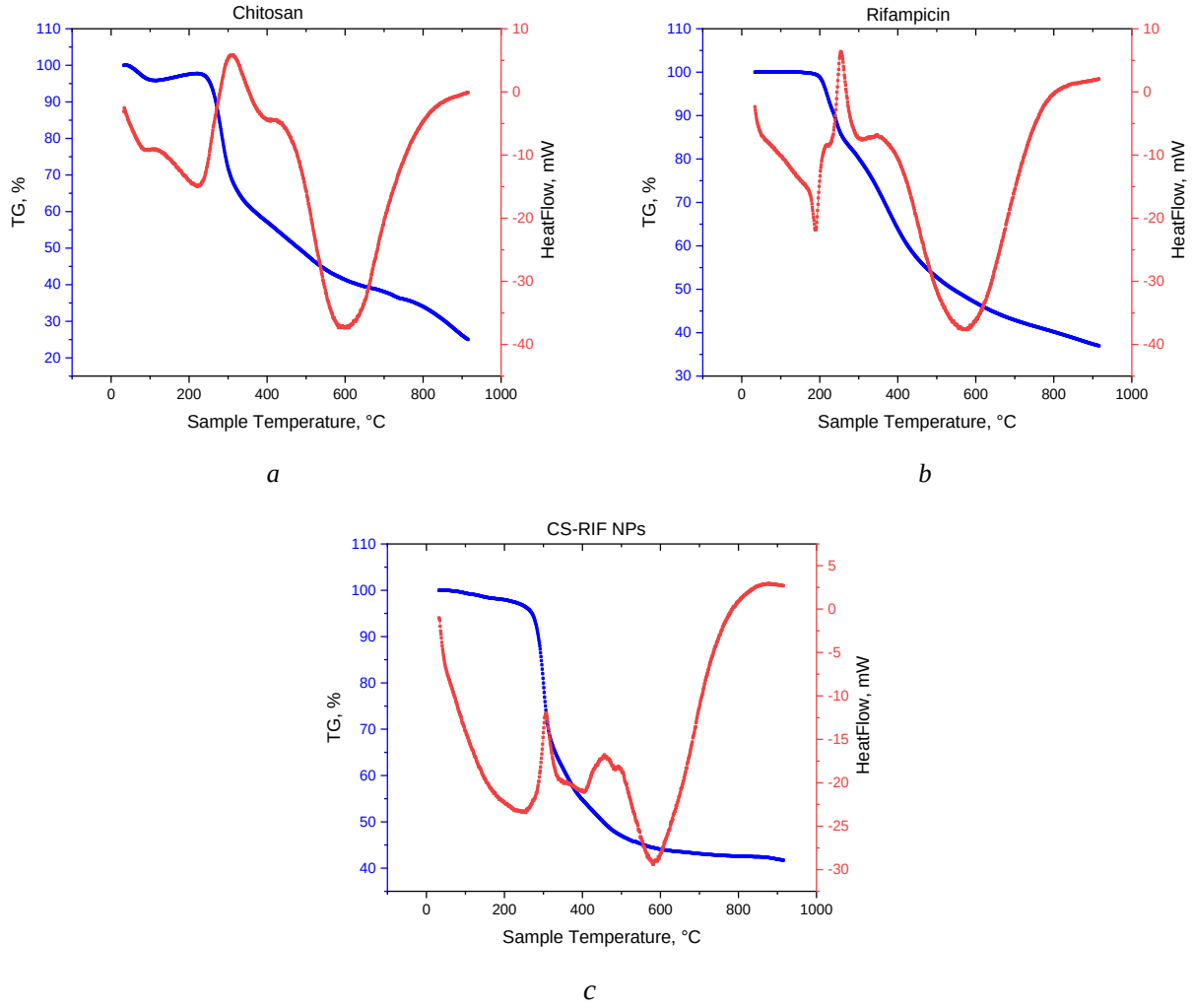

Figure 7. Thermal properties of the system components and the synthesized nanoparticles:
a — Chitosan; *b* — Rifampicin; *c* — CS-RIF nanoparticles

The FTIR technique was also used to determine the chemical composition and functional groups. FTIR spectra of rifampicin, chitosan nanoparticles without drug, and rifampicin loaded chitosan nanoparticles are shown in Figure 8. The chitosan samples show wide and intense absorption bands in the range of 3200–3600 cm^{-1}, which is explained by the overlapping stretching vibrations of –OH and $–NH_2$ characteristic of chitosan [37]. The bands at 2920 cm^{-1} correspond to C–H vibrations, at 1612 cm^{-1} to the C=O stretching of amide I, at 1543 cm^{-1} to the N–H bending and C–N stretching of amide II, at 1061 cm^{-1} to the C–N stretching of the amine, and at 1025 cm^{-1} to the skeletal C–O stretching vibrations [33, 37]. Rifampicin shows characteristic absorption bands at 3483 cm^{-1} associated with NH stretching, 1647 cm^{-1} corresponding to the C=O bond, 1458 cm^{-1} for the C=C bond, and 1381 cm^{-1} associated with CH_2 and C=C [31]. The low-frequency spectrum of CS-RIF nanoparticles shows characteristic peaks for chitosan and the rifampicin structure, indicating the absence of chemical interaction between the carrier and the drug.

Further research determined the *in vitro* rifampicin release kinetics from the chitosan-based nanoparticles matrix. To this end, the drug-loaded nanoparticles were studied using dialysis for 24 hours under conditions simulating the biological environment at different pH values (37 °C, pH 1.2; 6.8; 7.4). The rifampicin release profile is shown in Figure 9.

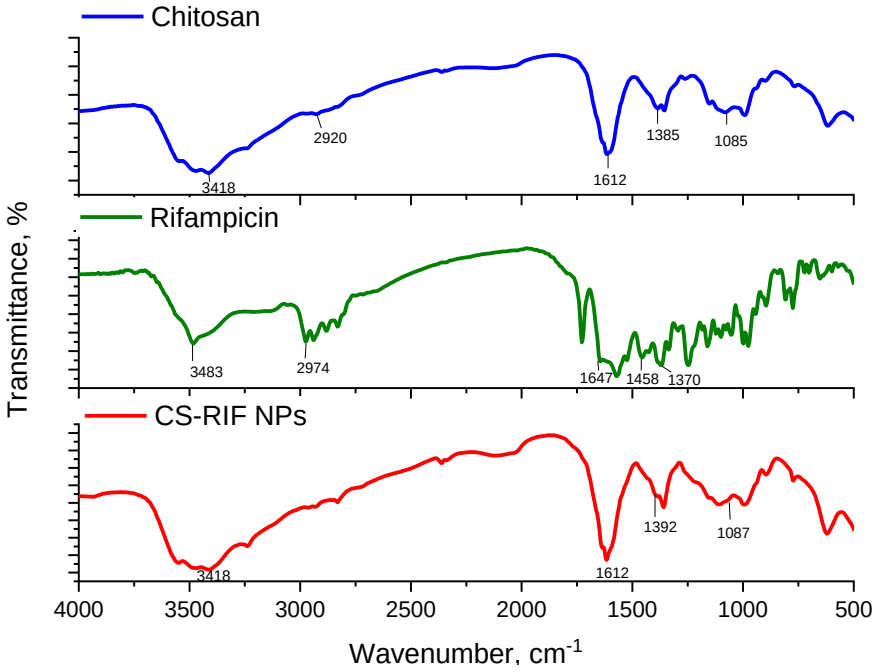

Figure 8. FTIR spectra for the rifampicin and the synthesized nanoparticles

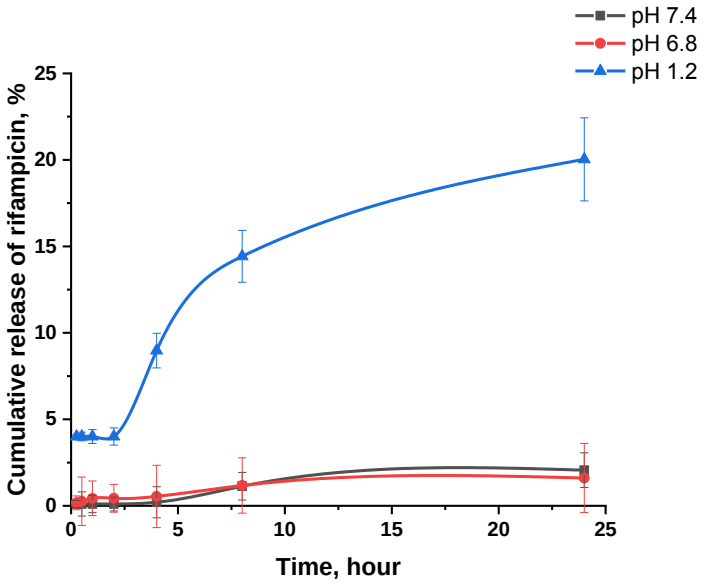

Figure 9. Cumulative release of rifampicin from CS-RIF nanoparticles under different pH conditions
(Values are shown as mean ± standard deviation (n = 3))

As can be seen from the graph, the kinetics of drug release significantly depend on the acidity of the medium. The most intense release is observed at pH 1.2, where the cumulative amount of released rifampicin reaches 20 % within 24 hours. In an acidic environment, partial protonation of the amino groups of chitosan occurs, which leads to an increase in solubility and swelling of the polymer matrix, facilitating the diffusion of the drug [38]. At pH 7.4 and 6.8, the release of rifampicin is significantly lower than 2 % in 24 hours. This can be explained by the limited solubility of chitosan in neutral and slightly alkaline conditions, in which the polymer network remains dense and less permeable to the diffusion of drug molecules [39]. Therefore, the obtained data confirm that the system based on chitosan nanoparticles has a pronounced pH dependence and is capable of providing controlled release of rifampicin.

Table 6 presents the results of a comparative analysis of mathematical models used to describe the kinetics of rifampicin release from chitosan nanoparticles at different pH values of 1.2, 6.8, and 7.4. Four models were evaluated: zero-order ($Q_t = Q_0 + k_0t$), first-order ($dC/dt = -kC$), Higuchi ($M_t/M_\infty = k\sqrt{t}$) and Korsmeyer–Peppas ($M_t/M_\infty = kt^n$) [40–42].

Table 6

Coefficients of determination (R^2) for rifampicin release models from CS-RIF nanoparticles

pH	Zero-order	First-order	Higuchi	**Korsmeyer–Peppas**
1.2	0.8827	0.8961	0.9452	0.8368
6.8	0.8815	0.8824	0.9541	0.9571
7.4	0.9408	0.9416	0.9183	0.6523

The highest correlation coefficient showed that rifampicin release follows Higuchi kinetics at pH 1.2. The release of rifampicin from chitosan nanoparticles at pH 7.4 showed a high correlation with the zero-order and first-order kinetic models, both with $R^2 > 0.94$. Rifampicin release at pH 6.8 is best described by the Higuchi model and the Korsmeyer-Peppas model ($R^2 > 0.95$). In the Korsmeyer-Peppas model for pH 1.2 and 6.8, the n coefficient values are below 0.5, indicating Fickian diffusion, while at pH 7.4, $n > 1$ and the release is based on a complex transport mechanism (super-random transport II) [41]. Thus, the data obtained confirm that the chitosan nanoparticle-based system has a pronounced pH dependence and is capable of providing controlled release of rifampicin.

The study of drug mucoadhesion is necessary to assess its effective retention on the mucous membrane for a long time. This is critical for the development of drug delivery systems to the lungs [43]. Incorporating RIF into chitosan nanoparticles can prolong the contact time of the drug with infected tissues. This is because chitosan is a mucoadhesive polymer that can interact with mucin present on the surface of mucous membranes through non-covalent interactions [44, 45]. Chitosan-based nanoparticles also demonstrate enhanced interaction with pulmonary mucus and alveolar macrophages [46–48]. In this regard, studies of the mucoadhesive properties of CS-RIF nanoparticles in acetate buffer solution (pH 5.5) and phosphate buffer solution (pH 6.8) were conducted, which made it possible to evaluate their behavior at two different pH levels. The pH value of 5.5 was selected to mimic the acidic environment of phagolysosomes in alveolar macrophages, while pH 6.8 represents near-physiological extracellular and mucosal conditions of the respiratory tract [49, 50]. The mucoadhesive properties of the nanoparticles were determined using the turbidimetric method over 4 hours. The results are shown in Figure 10.

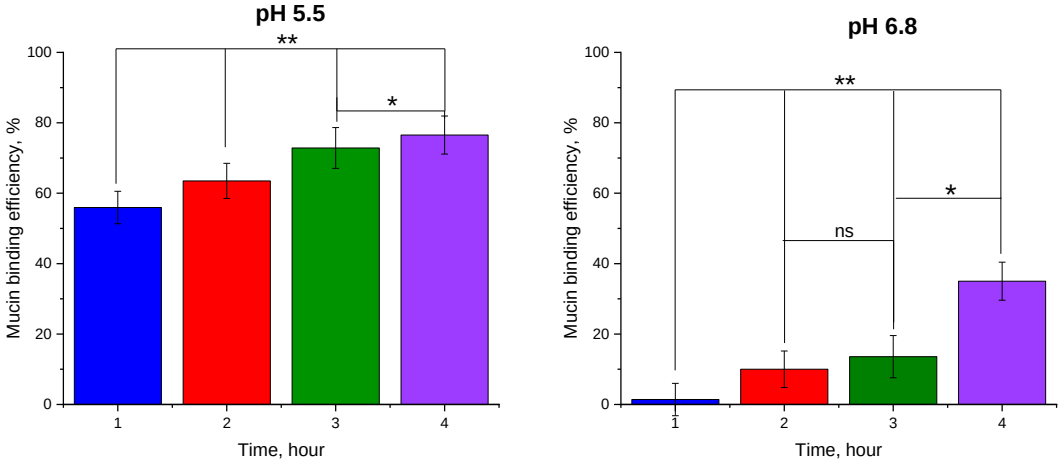

Figure 10. Mucin binding efficiency of CS-RIF nanoparticles with porcine mucin dispersions studied under different pH. "*" and "**" indicate $p < 0.01$ and < 0.005 respectively. ns — denotes no significant difference (Values are shown as mean ± standard deviation ($n = 3$))

As can be seen from the diagrams presented, the mucoadhesion of nanoparticles is better at pH 5.5. This is due to the good solubility of nanoparticles in the acetate buffer solution. Thus, in an acidic environment

(pH 5.5), it was 56 % after 1 hour and 77 % after 4 hours. When using a phosphate buffer solution with a pH of 6.8, the mucoadhesion of nanoparticles was 10 % after 2 hours and increased three times after 4 hours. These results highlighted the ability of chitosan nanoparticles to interact with the mucosa and maintain their adhesive potential across a wide range of physiological conditions, making the system promising for the delivery of rifampicin to the respiratory tract.

Conclusions

In this study, rifampicin-loaded chitosan nanoparticles were successfully prepared, optimized, and characterized. The optimized formula demonstrated nanoscale particle size, high loading efficiency, and controlled drug release profile, confirming the suitability of the developed system for prolonged-release rifampicin delivery. Mucosal adhesion studies at physiological pH values (5.5 and 6.8) showed that the nanoparticles have good adhesive properties and can be used for local delivery and prolonged retention on the mucosal surface. Overall, the results indicate the potential of chitosan-based nanoparticles as a delivery system for rifampicin. The developed system overcomes the significant drawbacks of traditional oral administration, which include low bioavailability and variability in drug concentration, and provides greater resistance to instability and release properties, as well as increased mucoadhesion. These results open up new opportunities for the development of improved inhalation drugs that can be used to reach the desired destination in the lungs and alveolar macrophages, leading to more effective and patient-friendly solutions for the treatment of tuberculosis.

Funding

This research was funded by the Science Committee of the Ministry of Science and Higher Education of the Republic of Kazakhstan under Grant No. AP23484897, titled “Creation of nanocarriers of antituberculosis drugs based on polysaccharide derivatives and their complexes”.

*Author Information**

**The authors' names are presented in the following order: First Name, Middle Name and Last Name*

Yerkeblan Muratovich Tazhbayev — Professor, Doctor of Chemical Sciences, Karaganda National Research University named after Academician E.A. Buketov, Universitetskaya street, 28, 100024, Karaganda, Kazakhstan; e-mail: tazhbaev@mail.ru; https://orcid.org/0000-0003-4828-2521

Aldana Rymzhanovna Galiyeva (*corresponding author*) — Leading researcher of the “Institute of chemical problems”, Karaganda National Research University named after Academician E.A. Buketov, Universitetskaya street, 28, 100024, Karaganda, Kazakhstan; e-mail: aldana_karaganda@mail.ru; https://orcid.org/0000-0002-8551-6297

Ulpan Yerlanqyzy Syrymova — Engineer, Karaganda National Research University named after Academician E.A. Buketov, Universitetskaya street, 28, 100024, Karaganda, Kazakhstan; e-mail: usyrymova@inbox.ru; https://orcid.org/0009-0007-8311-0414

Lyazzat Zhanybekovna Zhaparova — PhD, Associate Professor, Karaganda National Research University named after Academician E.A. Buketov, Universitetskaya street, 28, 100024, Karaganda, Kazakhstan; e-mail: lyazzh@mail.ru; https://orcid.org/0000-0003-1894-0255

Tolkyn Sergazyevna Zhumagaliyeva — Candidate of Chemical Sciences, Associate Professor, Karaganda National Research University named after Academician E.A. Buketov, Universitetskaya street, 28, 100028, Karaganda, Kazakhstan; e-mail: zhumagalieva79@mail.ru; https://orcid.org/0000-0003-1765-752X

Author Contributions

The manuscript was written through contributions of all authors. All authors have given approval to the final version of the manuscript. CRediT: **Yerkeblan Muratovich Tazhbayev** conceptualization, data curation, methodology, validation, visualization; **Aldana Rymzhanovna Galiyeva** data curation, visualization, formal analysis, writing-original draft; **Ulpan Yerlanqyzy Syrymova** investigation, formal analysis; **Tolkyn Sergazyevna Zhumagaliyeva** data curation, formal analysis; **Lyazzat Zhanybekovna Zhaparova** investigation, data curation, formal analysis.

Acknowledgments

Figure 1 and Graphical Abstract were created in *BioRender*. *Galiyeva, A. (2026) https://BioRender.com/ieb2gof*

Conflicts of Interest

The authors declare no conflict of interest.

References

1 World Health Organization (2025). Global tuberculosis report 2025. Geneva: World Health Organization. Retrieved from https://www.who.int/publications/i/item/9789240116924

2 Carnero Canales, C. S., Marquez Cazorla, J. I., Marquez Cazorla, R. M., Roque-Borda, C. A., Polinário, G., Figueroa Banda, R. A., Sábio, R. M., Chorilli, M., Santos, H. A., & Pavan, F. R. (2024). Breaking barriers: The potential of nanosystems in antituberculosis therapy. *Bioactive Materials*, 39, 106–134. https://doi.org/10.1016/j.bioactmat.2024.05.013

3 Yessentayeva, N. A., Galiyeva, A. R., Daribay, A. T., Sadyrbekov, D. T., Moustafine, R. I., & Tazhbayev, Y. M. (2024). Optimization of Polylactide-Co-Glycolide-Rifampicin Nanoparticle Synthesis, In Vitro Study of Mucoadhesion and Drug Release. *Polymers, 16*(17), 2466. https://doi.org/10.3390/polym16172466

4 Galiyeva, A. R., Tazhbayev, Ye. M., Zhumagaliyeva, T. S., & Daribay, A. T. (2022). Encapsulation of Isoniazid in Polylactide-Co-Glycolide Nanoparticles by Nanoprecipitation. *Bulletin of the University of Karaganda — Chemistry, 107*(3), 208–217. https://doi.org/10.31489/2022Ch3/3-22-17

5 Galiyeva, A. R., Tazhbayev, Ye. M., Zhumagaliyeva, T. S., Sadyrbekov, D. T., Kaikenov, D. A., Karimova, B. N., & Shokenova, S. S. (2022). Polylactide-co-glycolide nanoparticles immobilized with isoniazid: optimization using the experimental Taguchi method. *Bulletin of the Karaganda University. Chemistry Series, 105*(1), 69–77. https://doi.org/10.31489/2022ch1/69-77

6 Galiyeva, A. R., Tazhbayev, Y. M., Yessentayeva, N. A., Daribay, A. T., Marsel, D. T., Sadyrbekov, D. T., Zhaparova, L. Zh., & Arystanova, Z. T. (2023). PEGylation of Albumin Nanoparticles Immobilized with the Anti-Tuberculosis Drug "Isoniazid." *Eurasian Journal of Chemistry, 28*(2(110)). https://doi.org/10.31489/2959-0663/2-23-7

7 Sogias, I. A., Williams, A. C., & Khutoryanskiy, V. V. (2008). Why is Chitosan Mucoadhesive? *Biomacromolecules, 9*(7), 1837–1842. https://doi.org/10.1021/bm800276d

8 Žigrayová, D., Mikušová, V., & Mikuš, P. (2024). Advances in Chitosan Derivatives: Preparation, Properties and Applications in Pharmacy and Medicine. *Gels, 10*(11), 701. https://doi.org/10.3390/gels10110701

9 Morin-Crini, N., Lichtfouse, E., Torri, G., & Crini, G. (2019). Fundamentals and Applications of Chitosan. *Sustainable Agriculture Reviews 35*, 49–123. https://doi.org/10.1007/978-3-030-16538-3_2

10 Saputra, H. A., & Andreas. (2025). Chitosan and its biomedical applications: A review. *Next Materials*, 9, 101270. https://doi.org/10.1016/j.nxmate.2025.101270

11 Herdiana, Y., Febrina, E., Nurhasanah, S., Gozali, D., Elamin, K. M., & Wathoni, N. (2024). Drug Loading in Chitosan-Based Nanoparticles. *Pharmaceutics, 16*(8), 1043. https://doi.org/10.3390/pharmaceutics16081043

12 Jafernik, K., Ładniak, A., Blicharska, E., Czarnek, K., Ekiert, H., Wiącek, A. E., & Szopa, A. (2023). Chitosan-Based Nanoparticles as Effective Drug Delivery Systems—A review. *Molecules, 28*(4), 1963. https://doi.org/10.3390/molecules28041963

13 Grewal, A. K., & Salar, R. K. (2024). Chitosan nanoparticle delivery systems: An effective approach to enhancing efficacy and safety of anticancer drugs. *Nano TransMed*, 3, 100040. https://doi.org/10.1016/j.ntm.2024.100040

14 Dago-Serry, Y., Maroulas, K. N., Tolkou, A. K., Kokkinos, N. C., & Kyzas, G. Z. (2024). How the chitosan structure can affect the adsorption of pharmaceuticals from wastewaters: An overview. *Carbohydrate Polymer Technologies and Applications*, 7, 100466. https://doi.org/10.1016/j.carpta.2024.100466

15 Gonciarz, W., Balcerczak, E., Brzeziński, M., Jeleń, A., Pietrzyk-Brzezińska, A. J., Narayanan, V. H. B., & Chmiela, M. (2025). Chitosan-based formulations for therapeutic applications. A recent overview. *Journal of Biomedical Science, 32*(1). https://doi.org/10.1186/s12929-025-01161-7

16 Yang, C., Gao, S., Dagnæs-Hansen, F., Jakobsen, M., & Kjems, J. (2017). Impact of PEG Chain Length on the Physical Properties and Bioactivity of PEGylated Chitosan/siRNA Nanoparticles in Vitro and in Vivo. *ACS Applied Materials & Interfaces, 9*(14), 12203–12216. https://doi.org/10.1021/acsami.6b16556

17 Picchi, V., Gobbi, S., Fattizzo, M., Zefelippo, M., & Faoro, F. (2021). Chitosan Nanoparticles Loaded with N-Acetyl Cysteine to Mitigate Ozone and Other Possible Oxidative Stresses in Durum Wheat. *Plants, 10*(4), 691. https://doi.org/10.3390/plants10040691

18 Rampino, A., Borgogna, M., Blasi, P., Bellich, B., & Cesàro, A. (2013). Chitosan nanoparticles: Preparation, size evolution and stability. *International Journal of Pharmaceutics, 455*(1–2), 219–228. https://doi.org/10.1016/j.ijpharm.2013.07.034

19 Samprasit, W., Opanasopit, P., & Chamsai, B. (2021). Alpha-mangostin and resveratrol, dual-drugs-loaded mucoadhesive thiolated chitosan-based nanoparticles for synergistic activity against colon cancer cells. *Journal of Biomedical Materials Research Part B: Applied Biomaterials, 110*(6), 1221–1233. Portico. https://doi.org/10.1002/jbm.b.34992

20 Vieira, A. C. C., Chaves, L. L., Pinheiro, M., Lima, S. C., Neto, P. J. R., Ferreira, D., Sarmento, B., & Reis, S. (2021). Lipid nanoparticles coated with chitosan using a one-step association method to target rifampicin to alveolar macrophages. *Carbohydrate Polymers*, 252, 116978. https://doi.org/10.1016/j.carbpol.2020.116978

21 Vieira, A. C. C., Chaves, L. L., Pinheiro, S., Pinto, S., Pinheiro, M., Lima, S. C., Ferreira, D., Sarmento, B., & Reis, S. (2018). Mucoadhesive chitosan-coated solid lipid nanoparticles for better management of tuberculosis. *International Journal of Pharmaceutics*, *536*(1), 478–485. https://doi.org/10.1016/j.ijpharm.2017.11.071

22 Yanat, M., & Schroën, K. (2021). Preparation methods and applications of chitosan nanoparticles; with an outlook toward reinforcement of biodegradable packaging. *Reactive and Functional Polymers*, 161, 104849. https://doi.org/10.1016/j.reactfunctpolym.2021.104849

23 Jha, R., & Mayanovic, R. A. (2023). A Review of the Preparation, Characterization, and Applications of Chitosan Nanoparticles in Nanomedicine. *Nanomaterials*, *13*(8), 1302. https://doi.org/10.3390/nano13081302

24 Divya, K., & Jisha, M. S. (2017). Chitosan nanoparticles preparation and applications. *Environmental Chemistry Letters*, *16*(1), 101–112. https://doi.org/10.1007/s10311-017-0670-y

25 Rawal, T., Parmar, R., Tyagi, R. K., & Butani, S. (2017). Rifampicin loaded chitosan nanoparticle dry powder presents an improved therapeutic approach for alveolar tuberculosis. *Colloids and Surfaces B: Biointerfaces*, 154, 321–330. https://doi.org/10.1016/j.colsurfb.2017.03.044

26 Patel, B. K., Parikh, R. H., & Aboti, P. S. (2013). Development of Oral Sustained Release Rifampicin Loaded Chitosan Nanoparticles by Design of Experiment. *Journal of Drug Delivery*, 2013, 1–10. https://doi.org/10.1155/2013/370938

27 Fan, W., Yan, W., Xu, Z., & Ni, H. (2012). Formation mechanism of monodisperse, low molecular weight chitosan nanoparticles by ionic gelation technique. *Colloids and Surfaces B: Biointerfaces*, 90, 21–27. https://doi.org/10.1016/j.colsurfb.2011.09.042

28 Schnell, C. N., Galván, M. V., Solier, Y. N., Inalbon, M. C., Zanuttini, M. A., & Mocchiutti, P. (2021). High strength biobased films prepared from xylan/chitosan polyelectrolyte complexes in the presence of ethanol. *Carbohydrate Polymers*, 273, 118602. https://doi.org/10.1016/j.carbpol.2021.118602

29 Shilova, S. V., Tret'yakova, A. Ya., & Barabanov, V. P. (2018). Association of Chitosan in Aqueous-Alcohol Solutions. Polymer Science, Series A, 60(2), 184–189. https://doi.org/10.1134/s0965545x1802013x

30 Peyrovedin, H., Sajadian, S. A., Bahmanzade, S., Zomorodian, K., & Khorram, M. (2025). Studying the rifampin solubility in supercritical CO_2 with/without co-solvent: Experimental data, modeling and machine learning approach. *The Journal of Supercritical Fluids*, 218, 106510. https://doi.org/10.1016/j.supflu.2024.106510

31 Galiyeva, A., Daribay, A., Zhumagaliyeva, T., Zhaparova, L., Sadyrbekov, D., & Tazhbayev, Y. (2023). Human Serum Albumin Nanoparticles: Synthesis, Optimization and Immobilization with Antituberculosis Drugs. *Polymers*, *15*(13), 2774. https://doi.org/10.3390/polym15132774

32 Jogaiah, S., Mujtaba, A. G., Mujtaba, M., Archana, De Britto, S., Geetha, N., Belorkar, S. A., & Shetty, H. S. (2025). Chitosan-metal and metal oxide nanocomposites for active and intelligent food packaging; a comprehensive review of emerging trends and associated challenges. *Carbohydrate Polymers*, 357, 123459. https://doi.org/10.1016/j.carbpol.2025.123459

33 Alehosseini, E., Shahiri Tabarestani, H., Kharazmi, M. S., & Jafari, S. M. (2022). Physicochemical, Thermal, and Morphological Properties of Chitosan Nanoparticles Produced by Ionic Gelation. *Foods*, *11*(23), 3841. https://doi.org/10.3390/foods11233841

34 Onugwu, A. L., Attama, A. A., Nnamani, P. O., Onugwu, S. O., Onuigbo, E. B., & Khutoryanskiy, V. V. (2022). Development and optimization of solid lipid nanoparticles coated with chitosan and poly(2-ethyl-2-oxazoline) for ocular drug delivery of ciprofloxacin. *Journal of Drug Delivery Science and Technology*, 74, 103527. https://doi.org/10.1016/j.jddst.2022.103527

35 Alves, R., Reis, T. V. da S., Silva, L. C. C. da, Storpírtis, S., Mercuri, L. P., & Matos, J. do R. (2010). Thermal behavior and decomposition kinetics of rifampicin polymorphs under isothermal and non-isothermal conditions. *Brazilian Journal of Pharmaceutical Sciences*, *46*(2), 343–351. https://doi.org/10.1590/s1984-82502010000200022

36 Motiei, M., Pleno de Gouveia, L., Šopík, T., Vícha, R., Škoda, D., Císař, J., Khalili, R., Domincová Bergerová, E., Münster, L., Fei, H., Sedlařík, V., & Sáha, P. (2021). Nanoparticle-Based Rifampicin Delivery System Development. *Molecules*, *26*(7), 2067. https://doi.org/10.3390/molecules26072067

37 Kgoete, M. S., Mokgohloa, C. P., & Macevele, L. E. (2025). Synthesis of Chitosan Nanocomposite Materials Grafted with MWCNTs for the Removal of Tetracycline Pharmaceutical from Water Samples. *Colloids and Interfaces*, *9*(5), 69. https://doi.org/10.3390/colloids9050069

38 Herdiana, Y., Wathoni, N., Shamsuddin, S., & Muchtaridi, M. (2022). Drug release study of the chitosan-based nanoparticles. *Heliyon*, *8*(1), e08674. https://doi.org/10.1016/j.heliyon.2021.e08674

39 Ghosh, R., Mondal, S., Mukherjee, D., Adhikari, A., Ahmed, S. A., Alsantali, R. I., Khder, A. S., Altass, H. M., Moussa, Z., Das, R., Bhattacharyya, M., & Pal, S. K. (2022). Oral drug delivery using a polymeric nanocarrier: chitosan nanoparticles in the delivery of rifampicin. *Materials Advances*, *3*(11), 4622–4628. https://doi.org/10.1039/d2ma00295g

40 England, C. G., Miller, M. C., Kuttan, A., Trent, J. O., & Frieboes, H. B. (2015). Release kinetics of paclitaxel and cisplatin from two and three layered gold nanoparticles. *European Journal of Pharmaceutics and Biopharmaceutics*, 92, 120–129. https://doi.org/10.1016/j.ejpb.2015.02.017

41 Pavaloiu, R.-D., Sha'at, F., Hlevca, C., Sha'at, M., Savoiu, G., & Osman, S. (2021). Evaluation of drug release kinetics from polymeric nanoparticles loaded with poorly water-soluble APIs. *Ovidius University Annals of Chemistry*, *32*(2), 132–136. https://doi.org/10.2478/auoc-2021-0020

42 Jahangiri, S., Amirkhani, L., Akbarzadeh, A., & Hajimohammadi, R. (2023). Study of the Release Kinetic and the Diffusion Coefficient of Doxorubicin-Chrysin Coated with Fe_3O_4 and Polycaprolactone-Polyethylene glycol Copolymers. *Iranian Journal of Chemistry and Chemical Engineering*, *42*(5), 1436–1446.

43 Khutoryanskiy, V. V. (2018). Beyond PEGylation: Alternative surface-modification of nanoparticles with mucus-inert biomaterials. *Advanced Drug Delivery Reviews*, 124, 140–149. https://doi.org/10.1016/j.addr.2017.07.015

44 Kaldybekov, D. B., Shatabayeva, E. O., Polatkhan, A. A., Tuleyeva, R. N., Irmukhametova, G. S., & Khutoryanskiy, V. V. (2024). Development and Investigation of Mucoadhesive Polymers Based on Chitosan for Intravesical Therapy. *Eurasian Journal of Chemistry*, *29*(4(116)), 13–21. https://doi.org/10.31489/2959-0663/4-24-2

45 Phuong Ta, L., Bujna, E., Kun, S., Charalampopoulos, D., & Khutoryanskiy, V. V. (2021). Electrosprayed mucoadhesive alginate-chitosan microcapsules for gastrointestinal delivery of probiotics. *International Journal of Pharmaceutics*, 597, 120342. https://doi.org/10.1016/j.ijpharm.2021.120342

46 Tousian, B., & Khosravi, A. R. (2023). Chitosan-based pulmonary particulate systems for anticancer and antiviral drug carriers: A promising delivery for COVID-19 vaccines. *Results in Chemistry*, 6, 101146. https://doi.org/10.1016/j.rechem.2023.101146

47 Zacaron, T. M., Silva, M. L. S. e, Costa, M. P., Silva, D. M. e, Silva, A. C., Apolônio, A. C. M., Fabri, R. L., Pittella, F., Rocha, H. V. A., & Tavares, G. D. (2023). Advancements in Chitosan-Based Nanoparticles for Pulmonary Drug Delivery. *Polymers*, *15*(18), 3849. https://doi.org/10.3390/polym15183849

48 Rasul, R. M., Tamilarasi Muniandy, M., Zakaria, Z., Shah, K., Chee, C. F., Dabbagh, A., Rahman, N. A., & Wong, T. W. (2020). A review on chitosan and its development as pulmonary particulate anti-infective and anti-cancer drug carriers. *Carbohydrate Polymers*, 250, 116800. https://doi.org/10.1016/j.carbpol.2020.116800

49 Vandal, O. H., Nathan, C. F., & Ehrt, S. (2009). Acid Resistance in Mycobacterium tuberculosis. *Journal of Bacteriology*, *191*(15), 4714–4721. https://doi.org/10.1128/jb.00305-09

50 Nyberg, K., Johansson, U., Rundquist, I., & Camner, P. (1989). Estimation of pH in Individual Alveolar Macrophage Phagolysosomes. *Experimental Lung Research*, *15*(4), 499–510. https://doi.org/10.3109/01902148909069614

How to Cite: Rakhmanova, V.N., Yugay, S.M., Milusheva, R.Yu., Shakhabutdinov, S.Sh., Ashurov, N.Sh., Gulomjonov, Kh.A., Atakhanov, A.A., & Rashidova, S.Sh. (2026). Structural Characteristics, Stability, and Anticoagulant Activity of *Bombyx mori* Chitosan Sulfate. *Eurasian Journal of Chemistry, 31, 1(121), 61–72.* https://doi.org/10.31489/2959-0663/1-26-5

Article

Received: 1 December 2025 | Revised: 2 March 2026 |
Accepted: 10 March 2026 | Published online: 17 March 2026

UDC 544.323.2; 544.723

https://doi.org/10.31489/2959-0663/1-26-5

Vazira N. Rakhmanova*, Svetlana M. Yugay, Rakiya Yu. Milusheva, Sirojiddin Sh. Shakhabutdinov, Nurbek Sh. Ashurov, Khumoyunmirzo A. Gulomjonov, Abdumutolib A. Atakhanov, Sayyora Sh. Rashidova

Institute of Polymer Chemistry and Physics, Tashkent, Uzbekistan
*(*Corresponding author's e-mail: rakhmanova.vazira@gmail.com)*

Structural Characteristics, Stability, and Anticoagulant Activity of *Bombyx mori* Chitosan Sulfate

Chitosan sulfate (CS) is a promising polyelectrolyte for biomedical applications due to its anticoagulant properties. However, the relationship between the synthesis conditions of CS derived from *Bombyx mori* silkworm chitosan, its structural characteristics, and its biological activity remains insufficiently studied. CS samples with varying degrees of substitution (DS) were synthesized via sulfation with chlorosulfonic acid at different temperatures (50, 60, and 80 °C). The structure was characterized using FTIR spectroscopy and X-ray diffraction analysis. The physicochemical properties were evaluated through water vapor sorption, rheology, and solution stability tests conducted over 30 days. The anticoagulant activity of CS was assessed *in vivo* using a rabbit model of hypercholesterolemia. Successful sulfation resulted in DS values ranging from 0.96 to 1.21, leading to significant amorphization of the polymer structure. All CS samples exhibited high hydrophilicity with sigmoid-shaped sorption isotherms and demonstrated typical polyelectrolyte rheological behavior. Aqueous solutions of CS remained stable throughout the observation period. Importantly, the CS sample with the highest DS (1.21) showed the most pronounced anticoagulant effect, reducing platelet aggregation by 20 % compared with the heparin control group. The sulfation temperature is a key parameter determining the DS and, consequently, the properties of *Bombyx mori* chitosan sulfate. The derivative with DS = 1.21 demonstrates anticoagulant activity comparable to heparin, highlighting its potential as a bioactive material. Further research should focus on elucidating the precise molecular mechanisms of its anticoagulant action and evaluating its long-term biocompatibility and efficacy *in vivo*.

Keywords: chitosan sulfate, *Bombyx mori*, degree of substitution, IR spectroscopy, X-ray structural analysis, water sorption, rheology, anticoagulant activity

Introduction

Chitosan and its modified derivatives are of significant interest in the field of biomaterials due to their biocompatibility, low toxicity, and ability to biodegrade [1–5]. Special attention is paid to sulfated chitosan derivatives, which combine polyanionic properties with high hydrophilicity, expanding their potential applications [6–16]. These derivatives exhibit a range of biological activities, including antimicrobial, anticoagulant, and immunomodulatory properties, making them promising candidates for the development of new drugs [17–27].

A promising source for obtaining chitosan is the chitin of *Bombyx mori* silkworm pupae [28–32]. Sulfation of chitosan allows for the production of a polyampholyte that contains both basic (amino) and highly acidic (sulfate) groups in its structure. This gives the derivative unique properties: water solubility over a wide pH range, high charge density, and the ability to interact electrostatically, which determines its biological activity and low toxicity [33–40].

Despite active research in this area, the relationship between the synthesis conditions (such as the sulfation temperature), the degree of substitution, the supramolecular structure, the physical and chemical properties, and the biological activity of *Bombyx mori* chitosan sulfate has not been sufficiently studied. In particular, the effect of the degree of substitution on structural and rheological characteristics, sorption behavior with respect to water, and solution stability requires detailed analysis. In addition, it is necessary to assess the anticoagulant potential of such derivatives under conditions as close to physiological as possible.

This work aimed to establish a relationship between the synthesis conditions, structure, properties, and biological activity of *Bombyx mori* chitosan sulfate.

The work was aimed at synthesizing a series of chitosan sulfate samples with varying degrees of substitution by changing the reaction temperature, studying their chemical and supramolecular structure using IR-Fourier spectroscopy and X-ray diffraction analysis, and investigating the dependence of their sorption characteristics on water vapor and the rheological properties of their solutions. In addition, it was planned to evaluate the stability of aqueous solutions of the obtained derivatives and study their anticoagulant activity in an animal experiment with a model of hypercholesterolemia.

Experimental

Chemicals and Materials

Objects and Methods of Research

Chitosan obtained from chitin isolated from the pupae of the silkworm *Bombyx mori* was used as the main object for sulfation according to the methods [13, 40]. Its characteristics include degree of deacetylation, solubility, and molecular weight. Chlorosulfonic acid (CAS 7790-94-5), dimethyl sulfoxide (CAS 67-68-5), sodium acetate (CAS 127-09-3), sodium chloride (CAS 7647-14-5), sodium hydroxide (CAS 1310-73-2).

Synthesis of Chitosan Sulfate (CS)

Sulfation was carried out with chlorosulfonic acid in dimethyl sulfoxide medium by a modified technique [13] at temperatures of 50, 60, and 80 °C. The obtained samples are designated as CS (I), CS (II), and CS (III), respectively.

Determination of the Degree of Substitution (DS)

The degree of substitution by sulfonic groups was determined by titration on an EC 215 conductivity meter (Hanna Instruments, Germany) according to the method [35, 41]. The calculated values of the CX were: 1.12 (CX I), 1.21 (CX II), 0.96 (CX III). The non-monotonic dependence of the *DS* on temperature (maximum at 60 °C) can be explained by the competition between the sulfation processes and the possible degradation of the polymer chain at elevated temperatures (80 °C).

IR Spectroscopic Studies (FTIR)

Spectra were recorded on the Invenio-S Fourier spectrometer (Bruker, Germany) in the range of 400–4000 cm^{-1} with a resolution of 4 cm^{-1}. The samples were prepared as tablets with KBr [42]. The spectrum of native *Bombyx mori* chitosan was used for comparison [43, 44].

X-Ray Diffraction Analysis (XRD)

Diffraction measurements were performed on a Miniflex 600 diffractometer (Rigaku, Japan) with CuKα-radiation (λ = 1.5418 Å, 40 kV, 15 mA) in the Bragg-Brentano mode in the range of angles 2θ = 2–40° [45].

Investigation of Water Vapor Sorption

Sorption-desorption isotherms of water vapor were obtained on a high-vacuum unit with a McBain quartz balance (similar to the gravimetric method) at temperatures of 20, 25, and 30 °C (±0.1 °C) and residual pressure 10^{-3}–10^{-4} Pa [46]. The samples (~100 mg) were pre-dried to a constant mass at 50 °C. The equilibrium moisture content was determined by stepwise changes in relative humidity (p/p_0 from 0.05 to 0.95) [47]. The criterion for achieving equilibrium at each stage was the constant mass of the sample over a period of 2 hours [48]. The classical BET (Brunauer–Emmett–Teller) analysis, which is used to process data in the range of p/p_0 = 0.05–0.35 and is represented by formulas (1–4), has limitations in its applicability to hydrophilic polymer systems where swelling and bulk dissolution of the sorbate are possible [49]. Therefore, the obtained parameters (monolayer capacity, specific surface area, etc.) should be considered as effective, comparative characteristics.

Rheological Studies

The measurements were carried out on an MCR 92 rheometer (Anton Paar, Austria) in a shear mode in a system of coaxial cylinders for NaCl 0.1 N solutions and in an oscillation mode with parallel plates. The temperature range is 20–45 °C [50].

Conductometric Titration and Calculation of the Degree of Substitution

The quantitative characteristics of sulfogroup substitution were determined by titration on an EC 215 conductometer (Hanna Instruments, Germany) [51]. The change in electrical conductivity (*G*) was controlled

as a function of the volume (V) of the added titrant NaOH 0.5 N to the solutions of CS in HCl 0.1 N. The content of sulfur (ω_S) and nitrogen (ω_N) was calculated using the formulas [41, 35]:

$$\omega_S = \frac{km_S\Delta V_S}{m_{CS}}, \quad \omega_N = \frac{km_N\Delta V_N}{m_{CS}}, \tag{1}$$

where k is the normality of the titrant; m_S and m_N are molecular weights of sulfur and nitrogen; ΔV_S and ΔV_N are titrant volumes used for titration of sulfo- and amino groups, respectively; m_{CS} is the weight of the CS suspension.

The degree of substitution of sulfogroups (γ_S) was calculated using the formula:

$$\gamma_S = \frac{168.4 * \omega_S}{3200 - 81\omega_S}. \tag{2}$$

Determination of the Molecular Weight and Stability of Solutions

The characteristic viscosity (η) and molecular weight (M_η) were determined viscometrically using a Ubbelode viscometer in a water + 2 % NaCl system at 25 °C using the Mark-Kuhn-Hauvink equation [52–55]:

$$\eta = 4.97 \times 10^{-5} M_\eta^{0.77} \text{ dl/g}. \tag{3}$$

The stability of the solutions was assessed by changes in relative viscosity:

$$\eta_{отн} = \frac{\tau_i}{\tau_0}, \tag{4}$$

where τ_i is the expiration time of the solution, $\tau_0 \approx 92.8$ s is the expiration time of water for 30 days of storage at room temperature.

Investigation of Anticoagulant Activity In Vivo

Experiments were performed on male Chinchilla rabbits (n = 10 per group) with a model of atherosclerosis induced by an atherogenic diet [56]. CS samples were administered intragastrically at a body weight 5 mg/kg dose daily for 30 days. The control drug was heparin. At the end of the course, platelet aggregation, thrombin time, and the level of soluble fibrin-monomer complexes (RFMC) were determined on a Human analyzer (Germany). All procedures are performed in accordance with ethical standards [57].

Statistical Analysis

All experimental data were collected in triplicates and the data were expressed as average ± standard deviation. Data were compared using a one-way ANOVA with post-Bonferroni test using GraphPad Prism 5.04 (GraphPad Software Inc.)

Results and Discussion

IR Spectroscopic Analysis

The IR spectrum of the native *Bombyx mori* chitosan [40, 48] shows a wide absorption band in the 3000–3600 range with a maximum of about 3444, characteristic of valence vibrations and groups involved in hydrogen bonds. The bands at 2920 and 2980 correspond to the valence vibrations of the bonds. The characteristic bands of amide-I and amide-II are located at 1655 and 1591, respectively.

New intense absorption bands are observed on the IR spectra of all sulfated samples (Fig. 1). The appearance of bands in the region of 898, 1106, and 1156 corresponds to valence fluctuations of bonds and sulfate groups, which is direct evidence of successful sulfation. The key change is the shift of the amide-II band from 1591 (native chitosan) to the region of 1530–1533 for all samples of CS. This shift indicates substitution mainly by the amino group at the C-2 atom of the glucosamine unit, which is consistent with the literature data.

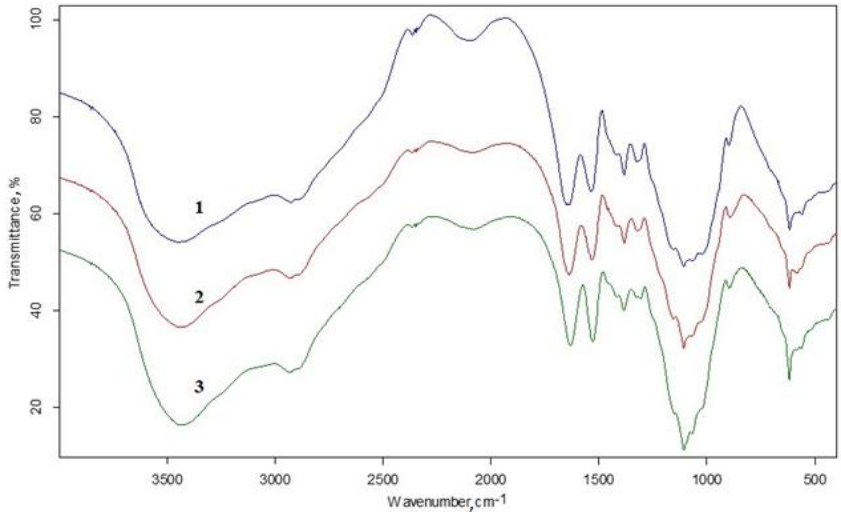

1 — CS (I-50 °C); *2* — CS (II-60 °C); *3* — CS (III-80 °C)

Figure 1. The IR Fourier spectra of the samples

The intensity of the new band in the 1530 region correlates with the degree of substitution. The highest intensity is observed for the CS (II) sample (DS = 1.21), which confirms the maximum content of sulfogroups. For the CS (III) sample (DS = 0.96), the intensity of this band is lower, which is consistent with the results of conductometric titration.

X-Ray Diffraction Analysis (XRD)

Diffractograms of the CS samples (Fig. 2) show significant changes in the supramolecular structure compared with native chitosan. Native chitosan is characterized by intense reflexes at 2θ ≈ 10° and 20° (corresponding to interplane distances and $d \approx 8.8$Å and 4.4Å), indicating its high crystallinity [41].

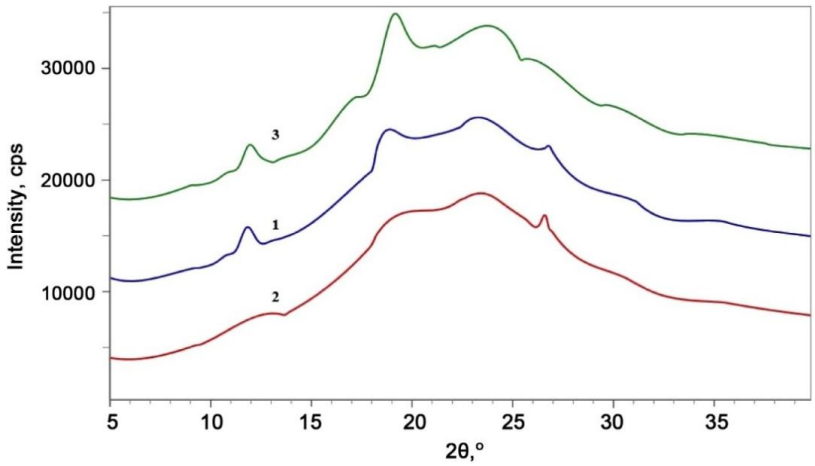

1 — CS (I-50 °C); *2* — CS (II-60 °C); *3* — CS (III-80 °C)

Figure 2. Diffractograms of samples

As a result of sulfation, significant amorphization of the structure occurs. Weak and blurred reflexes are observed for the sample of CS (I) (DS = 1.12). The most intense maximum at 2θ = 21.40° (d = 4.15Å) can be attributed to the reflex (130) of the hydrated form of chitosan. This indicates the preservation of residual crystallinity due to the ordered packing of polymer chains on a nanometer scale (inter-chain distances). The CS (II) sample (DS = 1.21) is characterized by the most diffuse diffraction pattern with a wide amorphous halo (maximum about 2θ = 20.5°, $d \approx 4.3$Å). This indicates the maximum destructurization of crystalline regions caused by a high degree of substitution, which disrupts the regularity of macromolecule packaging. The diffractogram of the CS (III) sample (DS = 0.96) shows a greater number and higher intensity of reflexes at 2θ = 11.96° (d = 7.39Å), 16.75° (d = 5.29Å), 19.04° (d = 4.66Å), etc. The increase in the degree of

crystallinity at a lower DS is explained by the fact that the replaced chains retain a greater similarity to the original structure of chitosan and are capable of more orderly packing.

The data obtained allow us to conclude that the sulfation process leads to significant amorphization of chitosan, and the degree of structurization of the crystalline phase directly correlates with the degree of substitution by sulfate groups.

Investigation of Sorption Characteristics

The isotherms of water vapor sorption by samples of CS obtained at temperatures 20, 25, and 30 °C are shown in Figures 3–5. All isotherms have the classic sigmoid shape typical of hydrophilic polymer materials. This shape indicates a complex multi-stage process, including initial monolayer adsorption on active centers, subsequent multilayer coating, and, at high relative humidity ($p/p_0 > 0.7–0.8$), capillary condensation in mesopores and the process of volumetric swelling of the polymer matrix.

The influence of the degree of substitution (DS). Samples with different DS demonstrate similar qualitative behavior, but differ in absolute sorption capacity. It is interesting to note that the samples with the most different DS — CS (II) (1.21) and CS (III) (0.96) — show similar sorption values, especially in the region of high humidity ($p/p_0 > 0.7$). This can be explained by the balance of two competing factors: 1) a higher concentration of hydrophilic sulfogroups in CS(II) increases water resistance; 2) the more amorphous structure of the same sample (according to XRD, Section 3.2) facilitates penetration and swelling, while the more ordered structure of CS(III) may limit this process. The CS (I) sample with an average CS = 1.12 occupies an intermediate position.

Effect of Temperature

In the entire studied range (20–30 °C), an increase in temperature leads to a decrease in the equilibrium water content at a fixed relative humidity for all samples. This dependence is characteristic of a process dominated by exothermic interactions, such as the hydration of ionic sulfonic groups and the formation of hydrogen bonds [58]. The observed minimum sorption capacity at 25 °C for a number of samples (Table 1) may be related to changes in the flexibility of polymer chains and the availability of sorption sites in this temperature range, but data obtained at only three temperatures are insufficient for a definitive conclusion about thermodynamic parameters (sorption enthalpy).

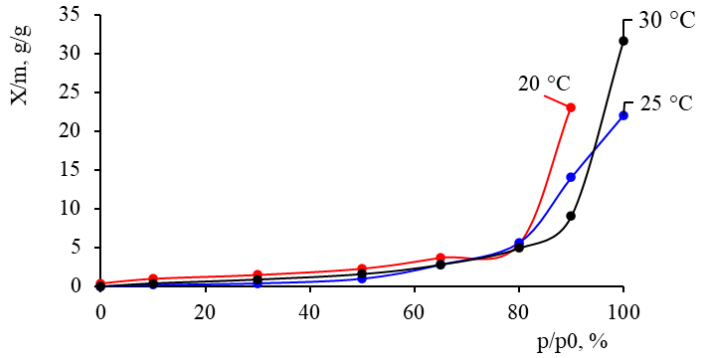

Figure 3. Sorption isotherms of water vapor by the CS (I) sample at 20, 25, and 30 °C

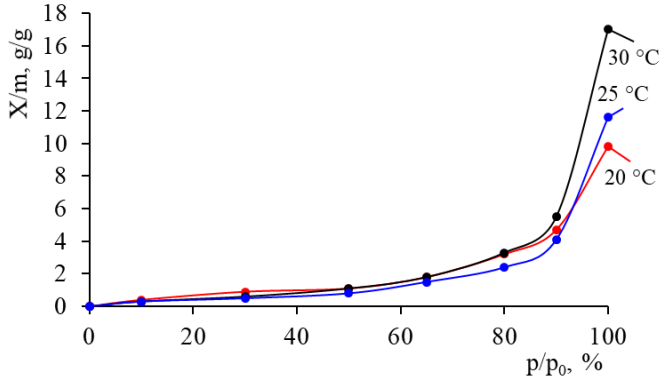

Figure 4. Sorption isotherms of water vapor by the CS (II) sample at 20, 25, and 30 °C

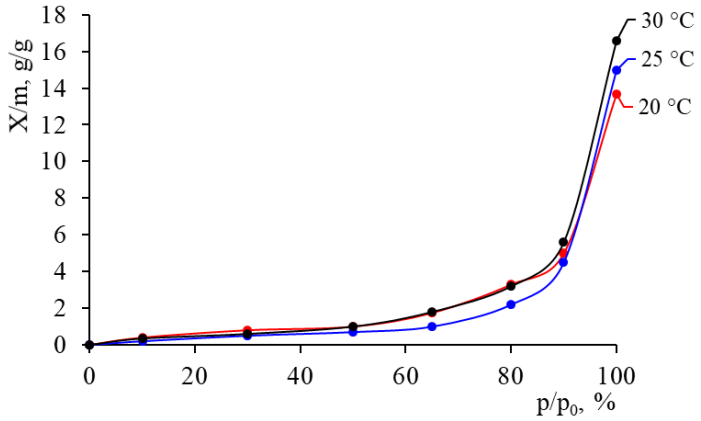

Figure 5. Sorption isotherms of water vapor by the CS (III) sample at 20, 25, and 30 °C

Notes on Data Analysis

In the original version, the BET equation was used to process isotherms in the range of relative pressures 0.05–0.35, and effective parameters (monolayer capacity, specific surface area, etc.) were calculated based on this equation. These parameters are presented in Table 1.

Table 1

Effective parameters of water vapor sorption for CS samples calculated using the BET model in the range p/p_0 = 0.05–0.35

Sample	Temperature, °C	X_m, g/g	SSA, m^2/g	W_o, cm^3/g	r_k, Å
CS (I)	20	0.0056	19.81	0.23	232.2
	25	0.0036	12.67	0.22	347.4
	30	0.0058	20.54	0.32	307.7
CS (II)	20	0.0051	17.84	0.10	109.9
	25	0.0041	14.28	0.17	238.1
	30	0.0035	12.32	0.12	188.4
CS (III)	20	0.0048	16.76	0.14	163.5
	25	0.0028	9.79	0.15	306.4
	30	0.0042	14.80	0.17	224.3

It should be emphasized that the classical BET theory is designed for adsorption on impermeable surfaces and does not take into account the possibility of sorbate penetration into the polymer volume (swelling), which is typical for hydrophilic systems [59, 60]. Therefore, the obtained numerical values should be interpreted with caution, considering them not as absolute characteristics of the porous structure, but as comparative parameters reflecting changes in the availability of sorption centers and affinity for water for different samples of CS. To correctly determine the specific surface area and porosity parameters of dry samples, nitrogen sorption is required, and small-angle X-ray scattering (SAXS) is required to study the structure in the swollen state.

Thus, the conducted studies confirm the high hydrophilicity of all synthesized chitosan sulfate samples due to the presence of ionic sulfonic groups. The sorption capacity is complexly dependent on the degree of substitution, which determines the chemical nature of the polymer, and the supramolecular structure, which affects the kinetics of swelling.

Rheological Properties of CS Solutions

A study of the rheological properties of CS solutions (0.1 N NaCl) showed their pronounced non-Newtonian behavior. The dependence of the effective viscosity (η) on the shear rate gradient (γ) for all samples (Fig. 6) demonstrates the shear (pseudoplasticity: viscosity decreases with increasing strain rate) characteristic of dilute electrolyte solutions. This is due to the destruction of the temporary grid of hydrogen and electrostatic bonds and the deformational ordering of macromolecules in the flow.

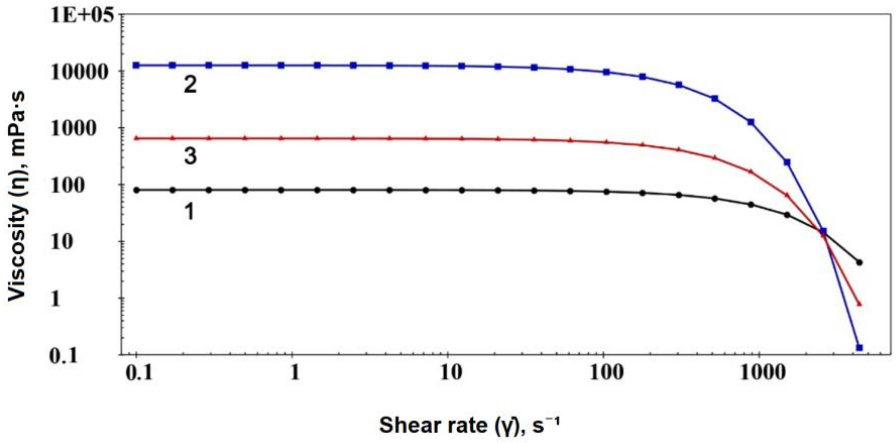

1 — CS (I, DS = 1.12); *2* — CS (II, DS = 1.21); *3* — CS (III, DS = 0.96)

Figure 6. Dependence of the effective viscosity (η) on the shear rate gradient (γ) for chitosan sulfate solutions in 0.1 N NaCl at 25 °C

The effect of the degree of substitution is clearly visible: as the degree of substitution increases, the viscosity of the solution increases in the low shear gradient region. The highest viscosity values were shown by the CS (II) sample with a maximum DS of 1.21, while the CS (III) sample with a minimum DS of 0.96 had the lowest viscosity. The increase in viscosity with increasing SC is due to an increase in the charge density on the macromolecule, which leads to increased electrostatic repulsion between the chains, resulting in a more extended conformation in solution and, consequently, more intense intermolecular interactions.

Solubility and Stability of Solutions

The substitution of amino and hydroxyl groups with sulfate groups resulted in the production of water-soluble derivatives. As can be seen from Figure 7, the solubility (S) of the samples in water at 25 °C increases sharply when the degree of substitution ($\gamma_s \approx 0.85$) reaches the threshold value and exceeds 95 % for samples with $\gamma_s > 0.85$. This confirms the successful synthesis of hydrophilic derivatives and is consistent with the well-known principle that the introduction of highly hydrated ionogenic groups dramatically improves the water solubility of polysaccharides.

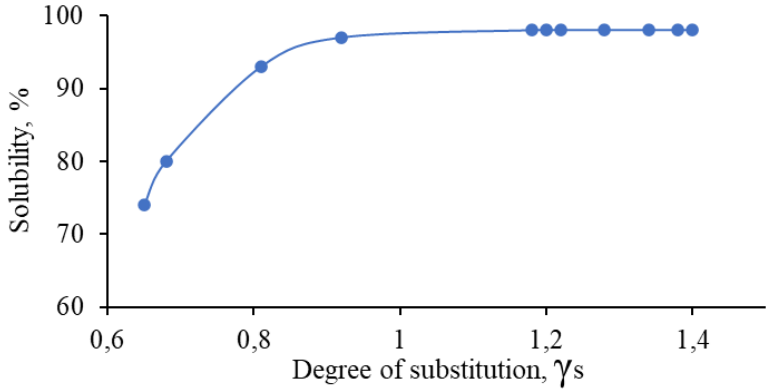

Figure 7. Dependence of the solubility (S) on the degree of substitution of sulfonic groups (γ_s) of chitosan sulfate samples in water at 25 °C

The stability of diluted aqueous solutions (Debye criterion $C[\eta] \leq 0.5$) of CS with different γ_s (from 0.81 to 1.40) was monitored for 30 days by measuring the relative viscosity (η_{rel}). As shown in Figure 8, the initial values η_{rel} correlate with the degree of substitution. During the entire observation period, the values for η_{rel} in all nine samples remained almost constant.

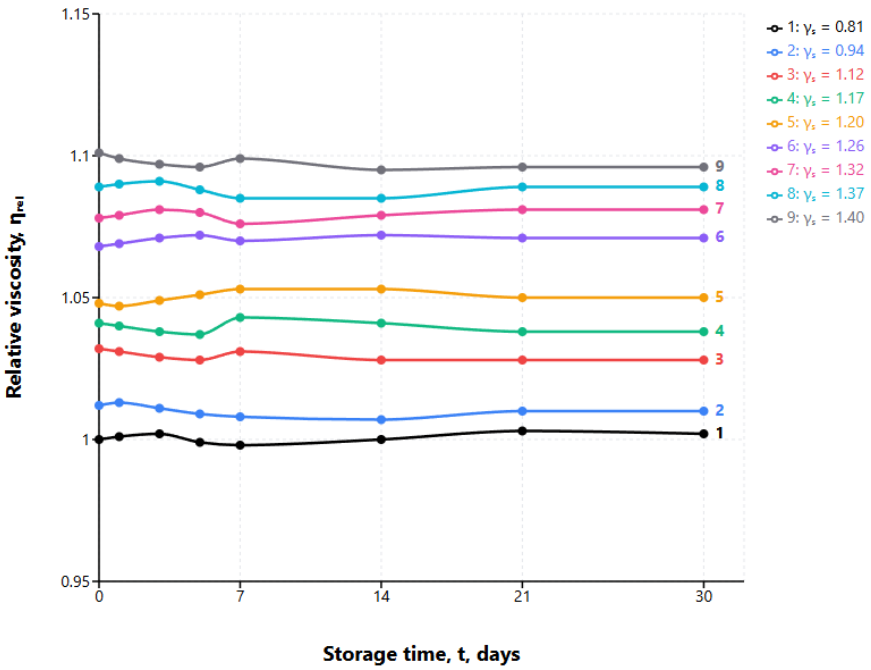

γ_s: *1* — 0.81; *2* — 0.94; *3* — 1.12; *4* — 1.17; *5* — 1.20; *6* — 1.26; *7* — 1.32; *8* — 1.37; *9* — 1.40

Figure 8. Dependence of the relative viscosity (η_{rel}) on the storage time (t) for aqueous solutions of chitosan sulfate samples with different γ_s

The absence of a decrease in viscosity indicates that there is no noticeable destruction or aggregation of the CS macromolecules in aqueous solutions at room temperature, which confirms their high colloidal stability.

Anticoagulant Activity in Animal Experiments

The anticoagulant potential of the CS samples was evaluated in an animal experiment (*in vivo*) using a hypercholesterolemia model in rabbits. The results of the effect of 30-day oral administration of CS on key hemostasis indicators are presented in Table 3.

Table 3

Effect of chitosan sulfate samples on hemostasis parameters in rabbits with experimental atherosclerosis (M±SD, *n* = 10)

Indicator	Heparin	CS-I (DS = 1.12)	CS-II (DS = 1.21)	CS-III (DS = 0.96)
Platelet aggregation, %	30.0 ± 0.58	31.33 ± 2.74	24.0 ± 1.15	36.33 ± 1.96
Thrombin time, with s	14.02 ± 0.00	14.08 ± 0.00	13.83 ± 0.17	14.11 ± 0.00
Soluble fibrin-monomer complex, mg %	3.04 ± 0.09	3.65 ± 0.93	3.02 ± 0.06	3.62 ± 0.14
Note: $p < 0.05$ compared to the group that received heparin				

The most pronounced effect was demonstrated by the CS (II) sample with a maximum DS of 1.21. Its administration led to a statistically significant 20 % reduction in platelet aggregation compared to the group that received heparin ($p < 0.05$). The samples of CS (I) and CS (III) also exhibited anticoagulant activity, which did not differ significantly from heparin in terms of the parameters studied. Thus, the anticoagulant effect of *Bombyx mori* chitosan sulfate depends on the degree of substitution, reaching a maximum at DS = 1.21.

Conclusions

As a result of the study, a relationship was established between the synthesis conditions, the degree of substitution (DS), the structural features, the physical and chemical properties, and the biological activity of

chitosan sulfate (CS) obtained from the chitin of the *Bombyx mori* silkworm. It has been shown that the sulfation temperature (50, 60, 80 °C) is a key parameter that determines the DS (0.96–1.21), which in turn has a significant impact on the properties of the polymer.

The successful introduction of sulfate groups and the amorphization of the polymer structure as a result of the sulfation reaction were confirmed using IR-Fourier spectroscopy and X-ray diffraction analysis. The study of water vapor sorption revealed the high hydrophilicity of all CS samples and the typical sigmoid shape of the isotherms, which is characteristic of hydrophilic polymers. Rheological measurements confirmed the poly-electrolyte behavior of aqueous solutions of CS. Good stability of the studied solutions during 30 days was established. The most significant result of the work is the proof of the pronounced anticoagulant activity of the synthesized chitosan sulfate with a high degree of substitution (DS = 1.21). In an experiment using an animal model of hypercholesterolemia, it was shown that this sample is comparable to heparin in terms of its effect on reducing platelet aggregation.

*Author Information**

**The authors' names are presented in the following order: First Name, Middle Name and Last Name*

Vazira Norqulovna Rakhmanova (*corresponding author*) — PhD, Junior researcher, Institute of Polymer Chemistry and Physics, Kadiry st., 7b, 100128, Tashkent, Uzbekistan; e-mail: rakhmanova.vazira@gmail.com; https://orcid.org/0000-0003-2024-5294

Svetlana Mihaylovna Yugay — Candidate of Chemical Sciences, Junior researcher, Institute of Polymer Chemistry and Physics, Kadiry st., 7b, 100128, Tashkent, Uzbekistan; e-mail: s-yugai@list.ru; https://orcid.org/0000-0001-6829-4111

Rakiya Yunusovna Milusheva — Candidate of Chemical Sciences, Senior researcher, Institute of Polymer Chemistry and Physics, Kadiry st., 7b, 100128, Tashkent, Uzbekistan; e-mail: rumilusheva@gmail.com; https://orcid.org/000-0003-2573-1013

Sirojiddin Shamsutdinovich Shakhabutdinov — Junior researcher, Institute of Polymer Chemistry and Physics, Kadiry st., 7b, 100128, Tashkent, Uzbekistan; e-mail: sirojiddin_55555@mail.ru; https://orcid.org/0000-0003-3804-9750

Nurbek Shodievich Ashurov — Candidate of Physical and Mathematical Sciences, Senior researcher, Institute of Polymer Chemistry and Physics, Kadiry st., 7b, 100128, Tashkent, Uzbekistan; e-mail: ansss72@mail.ru; https://orcid.org/0000-0001-5246-434X

Khumoyunmirzo Adakhamjon o'g'li Gulomjonov — PhD student, Junior researcher, Institute of Polymer Chemistry and Physics, Kadiry st., 7b, 100128, Tashkent, Uzbekistan; e-mail: khumoyungulomjonov@gmail.com; https://orcid.org/0009-0005-0330-0097

Abdumutolib Abdupatto o'g'li Atakhanov — Doctor of Technical Sciences, Professor, Director of Institute of Polymer Chemistry and Physics, Kadiry st., 7b, 100128, Tashkent, Uzbekistan; e-mail: a-atakhanov@yandex.com; https://orcid.org/0000-0002-4975-3658

Sayyora Sharafovna Rashidova — Doctor of Science, Professor, Academician, Consultant of the Director of the Institute of Polymer Chemistry and Physics, Kadiry st., 7b, 100128, Tashkent, Uzbekistan; e-mail: polymer@academy.uz; https://orcid.org/0000-0003-1667-4619

Author Contributions

The manuscript was written through the contributions of all authors. All authors have given approval to the final version of the manuscript. CRediT: **Vazira Norqulovna Rakhmanova** investigation, validation, visualization, writing-original draft, **Svetlana Mihaylovna Yugay** investigation, methodology, formal analysis; **Rakiya Yunusovna Milusheva** conceptualization, data curation, investigation, writing-review & editing, **Sirojiddin Shamsutdinovich Shakhabutdinov** investigation, methodology, formal analysis, **Nurbek Shodievich Ashurov** conceptualization, data curation, investigation, methodology, visualization, writing-original draft, writing-review & editing; **Khumoyunmirzo Adakhamjon o'g'li Gulomjonov** investigation, methodology, formal analysis, **Abdumutolib Abdupatto o'g'li Atakhanov** conceptualization, data curation, formal analysis, validation, writing-review & editing; **Sayyora Sharafovna Rashidova** conceptualization, supervision, editing.

Conflict of Interest

The authors declare no conflict of interest.

Acknowledgment

The authors express their gratitude to Prof. F.Kh. Inoyatova (Tashkent Medical Academy) for conducting medical and biological research.

References

1 Wang, W., Meng, Q., Li, Q., Liu, J., Zhou, M., Jin, Z., & Zhao, K. (2020). Chitosan Derivatives and Their Application in Biomedicine. *International Journal of Molecular Sciences*, *21*(2), 487. https://doi.org/10.3390/ijms21020487

2 Žigrayová, D., Mikušová, V., & Mikuš, P. (2024). Advances in chitosan derivatives: Preparation, properties, and applications in pharmacy and medicine. *Gels*, *10*(11), 701. https://doi.org/10.3390/gels10110701

3 Hemmami, H., Ben Amor, A., Zeghoud, S., Ahmed, S., & Alnazza Alhamad, A. (2023). Chitosan, its derivatives, sources, preparation methods, and applications: A review. *Journal of the Turkish Chemical Society Section A: Chemistry*, *11*(1), 341–354. https://doi.org/10.18596/jotcsa.1336313

4 Sashiwa, H., Kawasaki, N., Nakayama, A., et al. (2003). Chemical modification of chitosan. Part 15: Synthesis of novel chitosan derivatives by substitution of hydrophilic amine using N-carboxyethylchitosan ethyl ester as an intermediate. *Carbohydrate Research*, *338*(6), 557–561. https://doi.org/10.1016/S0008-6215(02)00492-5

5 Chen, Q., Qi, Y., Jiang, Y., Quan, W., Luo, H., Wu, K., Li, S., & Ouyang, Q. (2022). Progress in Research of Chitosan Chemical Modification Technologies and Their Applications. *Marine Drugs*, 20(8), 536. https://doi.org/10.3390/md20080536

6 Wang, Z., Zheng, L., Li, C., Wu, S., & Xiao, Y. (2017). Preparation and antimicrobial activity of sulfopropyl chitosan in an ionic liquid aqueous solution. *Journal of Applied Polymer Science*, *134*(15), 44989. https://doi.org/10.1002/app.44989

7 Petrova, Y. S., Neudachina, L. K., Mekhaev, A. V., & Pestov, A. V. (2014). Simple synthesis and chelation capacity of N-(2-sulfoethyl)chitosan, a taurine derivative. *Carbohydrate Polymers*, 112, 462–468. https://doi.org/10.1016/j.carbpol.2014.06.028

8 Pestov, A. V., Petrova, Y. S., Bukharova, A. V., Neudachina, L. K., et al. (2013). Synthesis in a gel and sorption properties of N-2-sulfoethyl chitosan. *Russian Journal of Applied Chemistry*, *86*(2), 269–272. https://doi.org/10.1134/S1070427213020225

9 Petrova, V. A., Chernyakov, D. D., Moskalenko, Y. E., Gasilova, E. R., Strelina, I. A., et al. (2017). O,N-(2-sulfoethyl)chitosan: Synthesis and properties of solutions and films. *Carbohydrate Polymers*, 157, 866–874. https://doi.org/10.1016/j.carbpol.2016.10.058

10 Petrova, Y. S., Pestov, A. V., Usoltseva, M. K., & Neudachina, L. K. (2015). Selective adsorption of silver(I) ions over copper(II) ions on a sulfoethyl derivative of chitosan. *Journal of Hazardous Materials*, 299, 696–701. https://doi.org/10.1016/j.jhazmat.2015.08.001

11 Pestov, A. V., Koryakova, O. V., Leonidov, I. I., & Yatluk, Y. G. (2010). Gel-synthesis, structure, and properties of sulfur-containing chitosan derivatives. *Russian Journal of Applied Chemistry*, *83*(5), 787–794. https://doi.org/10.1134/S1070427210050058

12 Petrova, Y. S., Pestov, A. V., & Neudachina, L. K. (2016). Removal of metal ions in fixed bed from multicomponent solutions using N-(2-sulfoethyl)chitosan-based sorbents. *Separation Science and Technology*, *51*(9), 1437–1445. https://doi.org/10.1080/01496395.2016.1157085

13 Ginting, N. H. (2004). Synthesis of chitosan sulfate through sulfonation reaction of chitosan with chlorosulfonic acid in solvent N,N-dimethylformamide. *Journal of Chemical Natural Resources*, *4*(1), 1–8. https://doi.org/10.32734/jcnar.v4i1.9353

14 Sun, Z., Shi, C., Wang, X., Fang, Q., & Huang, J. (2017). Synthesis, characterization, and antimicrobial activities of sulfonated chitosan. *Carbohydrate Polymers*, 155, 321–328. https://doi.org/10.1016/j.carbpol.2016.08.069

15 Xie, W., Xu, P., & Liu, Q. (2001). Antioxidant activity of water-soluble chitosan derivatives. *Bioorganic & Medicinal Chemistry Letters*, *11*(13), 1699–1701. https://doi.org/10.1016/S0960-894X(01)00285-2

16 Holme, K. R., & Perlin, A. S. (1997). Chitosan N-sulfate: A water-soluble polyelectrolyte. *Carbohydrate Research*, *302*(1–2), 7–12. https://www.google.com/search? q=https://doi.org/10.1016/S0008-6215(97)00117-1

17 Qin, C., Li, H., Xiao, Q., Liu, Y., & Zhu, J. (2006). Water-solubility of chitosan and its antimicrobial activity. *Carbohydrate Polymers*, *63*(3), 367–374. https://doi.org/10.1016/j.carbpol.2005.09.023

18 Seidi, F., Heshmati, P., Galehdari, S., Tajehmiri, A., & Salimi, H. (2016). Synthesis of water-soluble quaternary chitosan derivative via protection-deprotection strategy and investigation of its antibacterial effect. *Polymer Science, Series B*, *58*(3), 341–346. https://doi.org/10.1134/S1560090416030143

19 Chouljenko, A., Chotiko, A., Reyes, V., Alfaro, L., Liu, C., et al. (2016). Application of water-soluble chitosan to shrimp for quality retention. *LWT — Food Science and Technology*, 74, 571–579. https://doi.org/10.1016/j.lwt.2016.08.024

20 Wu, S. (2016). Preparation of water-soluble chitosan and its suppressive effect on the denaturation of scallop adductor muscle myofibrillar protein during frozen storage. *Journal of Aquatic Food Product Technology*, *25*(8), 1368–1374. https://doi.org/10.1080/10498850.2015.1077299

21 Hou, J. W., Qian, L., Kou, J. M., Zhang, C. W., Jia, X. J., et al. (2015). Effect of water-soluble chitosan on the osteoblast function in MC3T3-E1 cells. *International Journal of Biological Macromolecules*, 72, 1041–1043. https://doi.org/10.1016/j.ijbiomac.2014.10.012

22 Sahariah, P., & Masson, M. (2017). Antimicrobial chitosan and chitosan derivatives: A review of the structure–activity relationship. *Biomacromolecules, 18*(11), 3846–3868. https://doi.org/10.1021/acs.biomac.7b01058

23 Martins, A. F., Facchi, S. P., Follmann, H. D., Pereira, A. G., Rubira, A. F., et al. (2014). Antimicrobial activity of chitosan derivatives containing N-quaternized moieties in its backbone: A review. *International Journal of Molecular Sciences*, 15(11), 20800–20832. https://doi.org/10.3390/ijms151120800

24 Seedevi, P., Moovendhan, M., Vairamani, S., & Shanmugam, A. (2017). Evaluation of antioxidant activities and chemical analysis of sulfated chitosan from Sepia prashadi. *International Journal of Biological Macromolecules*, 103, 519–529. https://doi.org/10.1016/j.ijbiomac.2017.03.012

25 Vino, A. B., Ramasamy, P., Shanmugam, V., & Shanmugam, A. (2012). Extraction, characterization, and *in vitro* antioxidative potential of chitosan and sulfated chitosan from cuttlebone of Sepia aculeata Orbigny, 1848. *Asian Pacific Journal of Tropical Biomedicine*, *2*(1), S334–S341. https://doi.org/10.1016/S2221-1691(12)60184-1

26 Vongchan, P., Sajomsang, W., Kasinrerk, W., Subyen, D., & Kongtaweleri, P. (2002). Anticoagulant activities of the chitosan polysulfate synthesized from marine crab shell by semi-heterogeneous conditions. *Carbohydrate Research, 337*(13), 1239–1242. https://doi.org/10.1016/S0008-6215(02)00098-8

27 Dinoro, J., Maher, M., Talebian, S., Jafarkhani, M., Mehrali, M., Orive, G., Foroughi, J., et al. (2019). Sulfated polysaccharide-based scaffolds for orthopaedic tissue engineering. *Biomaterials*, 214, 119214. https://doi.org/10.1016/j.biomaterials.2019.05.025

28 Zhang, M., Haga, A., Sekiguchi, H., & Hirano, S. (2000). Structure of insect chitin isolated from beetle larva cuticle and silkworm (*Bombyx mori*) pupa exuvia. *International Journal of Biological Macromolecules, 27*(1), 99–105. https://doi.org/10.1016/S0141-8130(99)00123-3

29 Milusheva, R., & Rashidova, S. Sh. (2019). Bombyx mori chitosan nanoparticles: Synthesis and properties. *Open Journal of Organic Polymer Materials, 9*(4), 63–73. https://doi.org/10.4236/ojopm.2019.94004

30 Vokhidova, N. R., Mamasoliyev, U. M., Yugay, S. M., et al. (2023). Synthesis and study of the structure of N-succinyl chitosan *Bombyx mori* and their biological applications. *Polymer Bulletin*, 80, 12907–12921. https://doi.org/10.1007/s00289-023-04680-1

31 Milusheva, R. Y., & Rashidova, S. Sh. (2017). Bioactive properties of nanochitosan *Bombyx mori*. *Polymer Science, Series C, 59*(1), 29–34. https://doi.org/10.1134/S1811238217010088

32 Milusheva, R. Y., & Rashidova, S. Sh. (2022). Obtaining chitosan nanoparticles from *Bombyx mori*. *Russian Chemical Bulletin, 71*(2), 232–239. https://doi.org/10.1007/s11172-022-3402-9

33 Jayakumar, R., Nwe, N., Tokura, S., & Tamura, H. (2007). Sulfated chitin and chitosan as novel biomaterials. *International Journal of Biological Macromolecules, 40*(3), 175–181. https://doi.org/10.1016/j.ijbiomac.2006.06.021

34 Dimassi, S., Tabary, N., Chai, F., Blanchemain, N., & Martel, B. (2018). Sulfonated and sulfated chitosan derivatives for biomedical applications: A review. *Carbohydrate Polymers*, 202, 382–396. https://doi.org/10.1016/j.carbpol.2018.09.011

35 Rakhmanova, V. N., Nud'ga, L. A., Milusheva, R. Y., et al. (2009). Determination of the degree of sulfation of *Bombyx mori* chitosan by conductometric titration. *Russian Journal of Applied Chemistry, 82*(12), 2192–2196. https://doi.org/10.1134/S1070427209120192

36 Pokharkar, V., Dhar, S., Bhumkar, D., et al. (2009). Acute and subacute toxicity studies of chitosan-reduced gold nanoparticles: A novel carrier for therapeutic agents. *Journal of Biomedical Nanotechnology, 5*(2), 233–239. https://doi.org/10.1166/jbn.2009.1027

37 Hirano, S., Kinugawa, J., & Nishioka, A. (1986). Sulfated derivatives of chitosan and their characterization with respect to biological activity. In R. Muzzarelli, C. Jeuniaux, & G.W. Gooday (Eds.). *Chitin in Nature and Technology* (pp. 461–468). Plenum Press. https://doi.org/10.1007/978-1-4613-2167-5_54

38 Furman, R. H., & Robinson, C.W. Jr. (1961). Hypocholesterolemic agents. *Medical Clinics of North America, 45*(4), 935–959. https://doi.org/10.1016/S0025-7125(16)33854-8

39 Figueroa, F. A., Abdala-Díaz, R. T., Pérez, C., Casas-Arrojo, V., Nesic, A., Tapia, C., Durán, C., Valdes, O., Parra, C., Bravo-Arrepol, G., Soto, L., Becerra, J., & Cabrera-Barjas, G. (2022). Sulfated Polysaccharide Extracted from the Green Algae Codium bernabei: Physicochemical Characterization and Antioxidant, Anticoagulant and Antitumor Activity. *Marine Drugs, 20*(7), 458. https://doi.org/10.3390/md20070458

40 Ergashev, K.H., Vokhidova, N.R., Rashidova S.Sh. (2022) Synthesis and application of Chitosan hydroxyapatite: Review. *Progress on Chemistry and Application of Chitin and its Derivatives*, 27, 5–34. https://doi.org/10.15259/PCACD.27.001.

41 Garcia, J., & Schultz, L. D. (2016). Determination of sulfate by conductometric titration: An undergraduate laboratory experiment. *Journal of Chemical Education, 93*(5), 910–914. https://doi.org/10.1021/acs.jchemed.5b00941

42 Smith, B. (2018). *Infrared Spectral Interpretation*. CRC Press. https://doi.org/10.1201/9780203750841

43 Yugay, S. M., Shakhabutdinov, S. S., Atakhanov, A. A., & Rashidova, S. Sh. (2019). IR-Fourier spectroscopic research of *Bombyx mori* chitosan and its derivatives. *Chemical Journal of Kazakhstan*, 254–265. https://chemjournal.kz/index.php/journal/article/view/224

44 Duarte, M. L., Ferreira, M. C., Marvão, M. R., & Rocha, J. (2002). An optimised method to determine the degree of acetylation of chitin and chitosan by FTIR spectroscopy. *International Journal of Biological Macromolecules, 31*(1–3), 1–8. https://doi.org/10.1016/s0141-8130(02)00039-9

45 Clark, G. L., & Smith, A. F. (1936). X-ray diffraction studies of chitin, chitosan and derivatives. *Journal of Physical Chemistry*, *40*(7), 863–879. https://doi.org/10.1021/j150376a001

46 Tager, A. A. (1972). *Physical chemistry of polymers*. Mir Publishers. Moscow.

47 Gregg S.J. & Sing K.S.W. (1982). *Adsorption, Surface Area, and Porosity* (2nd ed.). Academic Press, New York.

48 Poyet, S., Trentin, K., & Amblard, E. (2016). The use of sorption balance for the characterization of the water retention curve of cement-based materials. *Journal of Advanced Concrete Technology*, *14*(7), 354–367. https://doi.org/10.3151/jact.14.354

49 Mali, S., Sakanaka, L. S., Yamashita, F., & Grossmann, M. V. E. (2005). Water sorption and mechanical properties of cassava starch films and their relation to plasticizing effect. *Carbohydrate Polymers, 60*(3), 283–289. https://doi.org/10.1016/j.carbpol.2005.01.003

50 Mezger, T. (2020). *The rheology handbook: For users of rotational and oscillatory rheometers*. European Coatings. https://doi.org/10.1515/arh-2002-0029

51 Hanna Instruments. (n.d.). *User manual for EC 215 conductivity meter*. https://www.hannainst.com

52 Korshak, V. V., & Vinogradova, S. V. (1968). Dependence of thermal stability of polymers on their chemical structure. *Russian Chemical Reviews*, *37*(11), 885. https://doi.org/10.1070/RC1968v037n11ABEH001712

53 Masuelli, M. A. (2014). Mark-Houwink parameters for aqueous-soluble polymers and biopolymers at various temperatures. *Journal of Polymer and Biopolymer Physics Chemistry*, *2*(2), 37–43. https://pubs.sciepub.com/jpbpc/2/2/2/

54 (2022). *American Polymer Standards Corporation*. Mark-Houwink parameters for polymer.

55 Brandrup, J., Immergut, E. H. & Grulke, E. A. (2003). *Polymer Handbook* (4th ed.). New York: Wiley.

56 Vogel, H. G. (Ed.). (2008). *Drug Discovery and Evaluation*. https://doi.org/10.1007/978-3-540-70995-4

57 Directive 2010/63/EU of the European Parliament and of the Council of 22 September 2010 on the protection of animals used for scientific purposes. (2010). *Official Journal of the European Union*, L 276/33. https://eur-lex.europa.eu/eli/dir/2010/63/oj/eng

58 Znamenskaya, Y., Sotres, J., Engblom, J., Arnebrant, T., & Kocherbitov, V. (2012). Effect of hydration on structural and thermodynamic properties of pig gastric and bovine submaxillary gland mucins. *The Journal of Physical Chemistry B, 116*(16), 5047–5055. https://doi.org/10.1021/jp212495t

59 Digaitis, R., Falkman, P., Oltner, V., Briggner, L. E., & Kocherbitov, V. (2022). Hydration and dehydration induced changes in porosity of starch microspheres. *Carbohydrate Polymers*, 291, 119542. https://doi.org/10.1016/j.carbpol.2022.119542

60 Argatov, I., & Kocherbitov, V. (2021). An empirical model for sorption by glassy polymers: An assessment of thermodynamic parameters. *Polymer Testing*, 99, 107220. https://doi.org/10.1016/j.polymertesting.2021.107220

How to Cite: Zabolotnaya, U.N., Timergalieva, V.R., Nasibullin, Sh.F., & Moustafine, R.I. (2026). Design of Floating Tablets Based on Hydroxypropyl Cellulose and Weakly Cross-Linked Poly(acrylic acid) for Gastroretentive Drug Delivery. *Eurasian Journal of Chemistry, 31, 1(121), 73–86.* https://doi.org/10.31489/2959-0663/1-26-7

Article

Received: 1 December 2025 | Revised: 24 February 2026 | Accepted: 27 February 2026 | Published online: 10 March 2026

UDC 541.64; 615.45

https://doi.org/10.31489/2959-0663/1-26-7

Ulyana N. Zabolotnaya, Venera R. Timergalieva, Shamil F. Nasibullin, Rouslan I. Moustafine*

Institute of Pharmacy, Kazan State Medical University, Kazan, Russia
*(*Corresponding author's e-mail: ruslan.mustafin@kazangmu.ru)*

Design of Floating Tablets Based on Hydroxypropyl Cellulose and Weakly Cross-Linked Poly(acrylic acid) for Gastroretentive Drug Delivery

Floating or buoyant dosage forms are kind of gastroretentive delivery system specifically designed to achieve localized drug release in the upper gastrointestinal tract (GI). The aim of this study is to select a composition for creating a floating matrix system based on hydroxypropyl cellulose (HPC) and Carbopol® 71G (C71G) with an evaluating of the effect of sodium bicarbonate (Na-bicarbonate) on the complexation process, and to design a gastroretentive system for acyclovir delivering. The tablets are based on physical mixtures (PhMs) HPC/C71G 1:2; 1:1. All matrices containing sodium bicarbonate showed a flotation time of less than 3 minutes, with the exception of a 2:1 PhM with 10 mg of sodium bicarbonate. PhM HPC/C71G (1:1) was observed greater matrix erosion compared to a 1:2 ratio due to the lower C71G content. During the swelling process of the matrices, interaction of polymers occurs, which is confirmed by a spectral shift in the ATR-FTIR spectra and T_g by mDSC. The addition of sodium bicarbonate did not increase the release rate due to the effervescent effect. A slightly higher release rate was observed for matrices with a 1:1 polymer ratio, due to erosion of the soluble HPC polymer.

Keywords: floating tablet, gastroretentive system, sustained release, interpolymer complexes, cellulose derivatives, hydroxypropyl cellulose, Carbopol®

Introduction

Over the past decades, scientists have focused their attention on improving the key characteristics of drugs, such as controlled release, increased bioavailability, and reduced side effects [1, 2]. The development of new gastroretentive drug delivery systems is one of the relevant trends in this direction. It is an oral delivery system capable of remaining in the stomach for a specified period, providing modified release of the active pharmaceutical ingredient (API) [3–5]. Floating tablets are one of the simplest and most widely used methods for creating a gastroretentive delivery system. They possess all the advantages of tablet dosage forms: convenience of use, storage, and transportation, as well as cost-effective production [4, 6, 7].

The effectiveness of oral therapy is limited by the low bioavailability of many drugs due to their specific properties [8, 9]. Considering that the main absorption occurs in the stomach and proximal small intestine, prolonging the residence time of the drug in this area is a critical factor for increasing the effectiveness of therapy for APIs with a narrow "absorption window" (acyclovir, riboflavin, levodopa, etc.). Some of them act only in the stomach due to pH-dependent absorption (furosemide, cinnarizine, ofloxacin, etc.) or are insoluble at alkaline pH values (atenolol, diazepam, etc.); for APIs that are unstable in the intestinal media (captopril, verapamil, etc.), as well as those with a local effect in the stomach (amoxicillin, metronidazole, etc.), incorporation into a gastroretentive delivery system is also preferred [10–12].

The operating principle of this system is based on reducing the density of the dosage form, causing it to float and remain in the upper part of the stomach, like a buoy, for several hours. This effect is achieved through gas-forming components (e.g., carbonates) included in the tablet's composition, which release carbon dioxide upon contact with stomach acid. There is a study in which menthol was used as a pore-forming agent [13]. The resulting gas bubbles "lift" the tablet, while the swelling polymers form a porous gel barrier around it, maintaining buoyancy and controlling drug release. Thus, the floating mechanism physically prevents the tablet from entering the intestine prematurely, which is key to prolonging the action of drugs absorbed in the upper gastrointestinal tract [14–19].

Currently, there are many studies on the development of floating tablets based on cellulose derivatives, including 3D printing [1, 20–27]. However, the use of chemically complementary polymers to form

interpolymer complexes (IPC) is currently a developing area [28]. The result of the interaction is the formation of IPCs, the unique properties of which are different from the properties of the original polymers and can be corrected in the required direction [29–31]. There are two options for using these systems: synthesis of IPC, with its subsequent use as a matrix-forming component, or complexation between a PhM of complementary polymers, under the influence of an acidic media simulating the environment of the stomach [32].

The ability of polymers to interact increases in an acidic media (at low pH values), because the carboxyl groups of Carbopol® are in a protonated, non-ionized form. A stable IPC is formed only at a pH below a critical pH value (pH_{crit}), which is unique for each specific pair of polymers [33–40]. Thus, the acidic media of stomach acid serves as the key physiological condition for IPC formation between HPC and C71G, and also acts as an activator for flotation. This highlights the high relevance of research in the field of gastroretentive delivery systems.

The aim of this study is to select a composition for creating a floating matrix system based on HPC and C71G with an evaluating of the effect of Na-bicarbonate on the complexation process, and to design a gastroretentive system for acyclovir delivering.

Experimental

Materials

HPC (SHANDONG HEAD CO., LTD, China) and C71G (Lubrizol Advanced Materials, USA) were used as pharmaceutical polymers, from which PhMs were prepared in various molar ratios. Acyclovir (Zhejiang Zhebei Pharmaceutical Co., Ltd., China) was used as the API. Na-bicarbonate (LLC Spectr-Chem, Russia) served as the flotation agent. Indicator is methyl red (Eco Pharm, Russia). Distilled water was used for all experiments. All reagents used were of laboratory-grade purity.

Selection of the Composition

HPC and C71G were physically mixed using a mortar and pestle in various molar rations 1:2; 1:1; 2:1, respectively. Tablets with 50 mg of PhMs, 100 mg of acyclovir and appropriate amount of Na-bicarbonate 10, 15, 20 or 25 mg were made from the physical mixtures in a 9-mm die using a programmable hydraulic press PressPRO Programmable Hydraulic Pellet Press (PIKE Technologies, USA) at compression force of 5 tons with a holding time of 5 s by direct compression. The tablets were exposed to 80 ml of 0.1 M HCl using glass beakers in a water bath IKA® IC control (IKA-Werke GmbH&Co. KG., Germany) at 37 ± 0.5 °C for 24 h. The time it took for the tablet to float (Lag time) and the total time the system remained on the surface of the media (Floating time) were measured.

Determination of the Degree of Swelling

Swelling properties were investigated by incubating matrices of PhMs with and without Na-bicarbonate with different levels of Na-bicarbonate (0, 10, 15, and 20 mg per tablet) in a temperature-controlled water bath IKA® IC control (IKA-Werke GmbH&Co. KG., Germany) maintained at 37 ± 0.5 °C. The swelling study was conducted without API. The matrices, prepared as 0.15 g tablets with a 9 mm diameter, were produced by direct compression of PhMs and PhMs with Na-bicarbonate using a programmable hydraulic pellet press PressPRO Programmable Hydraulic Pellet Press (PIKE Technologies, USA) under a pressure of 5 tons with a 5-second holding time. Each matrix was placed in a tared basket, which was immersed into glass beakers with 40 ml of 0.1 M HCl media, simulating stomach acid. The samples were placed in a quiescent media without stirring. The basket was removed from the media every 30 min during 6 h and after 24 h followed by removal of residual media with a dry wipe, the matrix was carefully dried using a filter paper and weighed on an analytical balance Shinko Denshi (VIBRA, Japan). The swelling degree (H%) was determined according to established formulas cited in the literature [41, 42].

The degree of swelling (H%) was calculated by the formula:

$$H\% = \frac{m_2 - m_1}{m_1} \times 100\ \%,$$

in which m_1 is the mass of the dry sample; m_2 is mass of swollen sample.

To assess the influence of the media and impact of Na-bicarbonate on possible structural transformations of PhMs to polycomplex matrices during swelling, matrix samples were collected after 2 h, 4 h, 6 h and 24 h of exposure in an acidic media.

Determination of the Micro-Environmental pH in the Matrix During Swelling

The preparation of the matrices for this study was carried out according to the described method for determining the degree of swelling with the addition of a methyl red indicator (0.15 % w/w) [43]. Studying the penetration of the media into the matrix were performed in acidic media pH 1.2 as described above. The pH change was recorded after 2 h, 4 h, 6 h, and 24 h of exposure in an acidic media. After a certain time, a cross-section of the matrix was made and the color change of the indicator was observed throughout the entire volume of the matrix.

Sample Preparation

Samples, taken during swelling studies, were frozen in laboratory freezer and then freeze-dried in FreeZone dryer (Labconco, USA) for 12 h at –50 °C and 0.08 mbar. After lyophilization tablets were dried in a VD 23 vacuum drying oven (BINDER GmbH, Germany) at 40 ± 0.5 °C to constant weight. The samples were ground to a powder using a ball mill ShaklR (PIKE Technologies, USA). The structural properties of the matrices during swelling were studied using the Fourier Transform Infra-Red (ATR-FTIR) spectroscopy (Thermo Scientific, Waltham, MA, USA) and modulated Differential Scanning Calorimetry (mDSC) methods for evaluation the influence of the media and impact of Na-bicarbonate on possible structural transformations of PhMs to polycomplex matrices while in an acidic media, simulating the stomach acid.

Fourier-Transformed Infrared (ATR-FTIR) Spectroscopy

The structural differences were studied using ATR-FTIR Spectroscopy. ATR-FTIR spectra were recorded by a Nicolet iS5 FTIR spectrometer (Thermo Fisher Scientific, USA) with the iD5 smart single bounce ZnSe ATR crystal in the range from 1500 to 1900 cm^{-1}. The absorption bands were interpreted in accordance with literature data [35, 38, 44].

Thermal Analysis

mDSC analysis was performed on a Discovery DSC™ instrument (TA Instruments, New Castle, DE, USA) with an RCS90 refrigerated cooling attachment. The instrument was calibrated for temperature using indium and n-octadecane standards, for enthalpy using indium, and for heat capacity using a sapphire standard. Tzero® aluminum pans (TA Instruments, USA) were used in all calorimetric studies. The empty pan was used as a reference and the mass of the reference pan and of the sample pans were taken into account. A dry nitrogen purge at a flow rate of 50 mL/min was maintained through the DSC cell. Samples in the mass range from 5 mg to 6 mg were placed in Tzero® aluminum pans (TA Instruments, USA), which were then transferred into the calorimeter's thermal cell using an autosampler. The scan was performed over a temperature range from 0 to 200 °C at a heating rate of 2 °C/min in modulated mode (period 60 s, amplitude 0.6360 °C). The method employed two consecutive heating and cooling segments. First, the sample was cooled at a rate of 20 °C/min to 0 °C and held for 5 minutes. It was then heated at 2 °C/min to 160 °C in modulated mode (period 60 s, amplitude 0.6360 °C). Following this, the sample was cooled back to 0 °C and maintained at this temperature for 5 minutes. Finally, it was heated again at a rate of 2 °C/min to 200 °C in modulated mode with the same parameters: period 60 s, amplitude 0.6360 °C. Data were collected and processed using TRIOS™ software version 5.1.1.46572 (TA Instruments, USA). Glass transition temperatures (T_g) were derived from the reversing heat flow signal. All analyses were conducted in triplicate.

Tablet Preparation

Six different PM of HPC/C71G, Na-bicarbonate and acyclovir were prepared using a mortar and pestle at HPC:C71G molar ratios of 1:2; 1:1 and with different levels of Na-bicarbonate (10, 15, and 20 mg per tablet). 1 tablet contained 50 mg of PhM, 100 mg of acyclovir and 10, 15 or 20 mg of Na-bicarbonate. The total tablet weight varied from 160 to 170 mg depending on the Na-carbonate content. Floating tablets were obtained by pressing into tablets in a 9-mm die using a programmable hydraulic press PressPRO Programmable Hydraulic Pellet Press (PIKE Technologies, USA) at compression force of 5 tons with a holding time of 5 s by direct compression.

Study of Drug Release

Release was carried out using a DT 626 Dissolution tester (ERWEKA GmbH, Germany) at 37±0.5 °C using type II “paddle method” and a paddle rotation speed of 50 rpm. 0.1 M HCl was used as the dissolution media in a volume of 900 ml, simulating stomach acid. The preparation of tablets for the experiment is described above. The experiment was conducted for 6 h. Samples (5 ml) were collected for analysis every

15 minutes during the first half hour of the experiment, and then every 30 minutes with volume replacement of pure media. Experimental results were calculated by measuring the optical density of the samples using a UV/Vis-spectrophotometer Lambda 25 (PerkinElmer, USA) at a wavelength of 255 nm [33].

Statistical Analysis

Microsoft Excel Mondo 2016 (Version 2108 Build 14332.20651) was used for the statistical analysis of all data, which were obtained from experiments performed in triplicate. Mean values ± standard deviations were calculated using one-way analysis of variance (ANOVA) and t-Test (Two-Sample Assuming Equal Variances), where probability was $p < 0.05$ as a significant criterion.

Results and Discussion

Justification of the Optimal Composition

To identify the optimal composition of floating tablets and subsequently study the complexation properties between HPC and C71G, to investigate the impact of Na-bicarbonate on complexation process, three types of PhMs were selected. PhMs HPC:C71G 1:2 and 2:1 contained an excess of each polymers and a 1:1 molar ratio, respectively. Each tablet consists of 50 mg of the corresponding PhM, 100 mg of acyclovir and different amounts of Na-bicarbonate (0 mg, 10 mg, 15 mg, 20 mg, 25 mg). After immersing the tablets of different compositions in a media, simulating stomach acid, the time to float (lag time) and the duration of flotation on the media surface (floating time) were measured. Upon contact with the acidic media, Na-bicarbonate generates carbon dioxide. The resulting CO_2 bubbles, trapped within the swollen gel layer surrounding the matrix, facilitate rapid flotation and an extended floating duration by reducing the density below 1 g/cm^3 [13–19, 32]. Tablets without Na-bicarbonate did not exhibit buoyancy. All matrices, containing Na-bicarbonate, except one (PhM 2:1 with 10 mg of Na-bicarbonate), demonstrated an optimal lag time (less than 3 minutes). The floating results for the different matrices are reported in Table 1.

After 24 hours of testing, all samples based on the PhM 2:1 (with an excess of HPC) disintegrated regardless of their Na-bicarbonate content. This is likely due to the solubility of HPC in the media and its inability to withstand the disruptive effect. Other samples with the highest Na-bicarbonate content (25 mg) were also destroyed. In large quantities, Na-bicarbonate exerts a disintegrating effect on matrices in an acidic media [11, 32]. Tablet samples of PhM 1:2 and PhM 1:1 containing 10 mg, 15 mg and 20 mg of Na-bicarbonate, exhibited all necessary floating parameters (lag time — less than 3 min, floating time — over 24 h) [11, 45, 46]. These samples were selected as optimal for further investigation.

Table 1

Effect of Na-bicarbonate level on floating parameters of matrices made of HPC/C71G at different molar ratios

HPC:C71G molar ratio	Na-bicarbonate, mg	Lag time	Floating time
1:2	0	–	No floatation observed
1:2	10	17 s	24 h
1:2	15	12 s	24 h
1:2	20	9 s	24 h
1:2	25	10 s	Disintegrated within 24 hours
1:1	0	–	No floatation observed
1:1	10	29 s	24 h
1:1	15	17 s	24 h
1:1	20	10 s	24 h
1:1	25	10 s	Disintegrated within 24 hours
2:1	0	–	No floatation observed
2:1	10	> 3 min	Disintegrated within 24 hours
2:1	15	37 s	Disintegrated within 24 hours
2:1	20	37 s	Disintegrated within 24 hours
2:1	25	37 s	Disintegrated within 24 hours

Determination of the Degree of Swelling of Matrices

Evaluating the behavior of matrices based on PhMs without API is necessary for prediction of the possibility of application of tablets as carriers for drug delivery systems (DDS). In addition, it was necessary to assess the complexation between the two polymers, as well as the influence of Na-bicarbonate on this process in acidic media, simulating fasted stomach, for the development of gastroretentive DDS. It was noted that matrices based on PhMs of both ratios retained their shape, increased in size and surface layer of matrices transformed into a hydrogel structure (Figure 1). The PhM with an excess of C71G (PhM 1:2) exhibited a higher swelling degree than the PhM 1:1. Furthermore, by the end of the experiment, the swelling degree of the PhM 1:1 began to decrease, which may indicate the erosion of HPC from the matrix (Figures 2-3) by reducing the mass. The influence of Na-bicarbonate on the swelling degree is more pronounced for PhM 1:1. As the Na-bicarbonate content increases, a decrease in the swelling degree is observed, which may also potentiate its disruptive effect on the matrix by facilitating the erosion of the HPC.

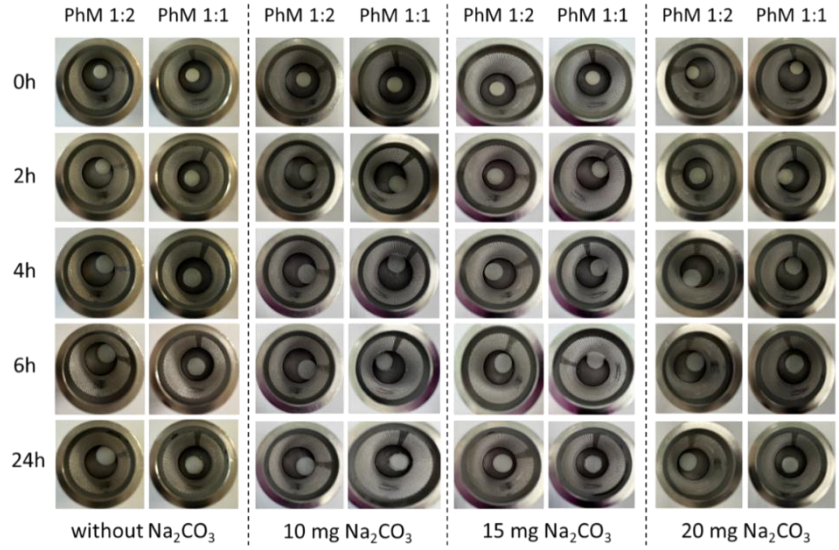

Figure 1. External appearance of PhM matrices during the swelling test

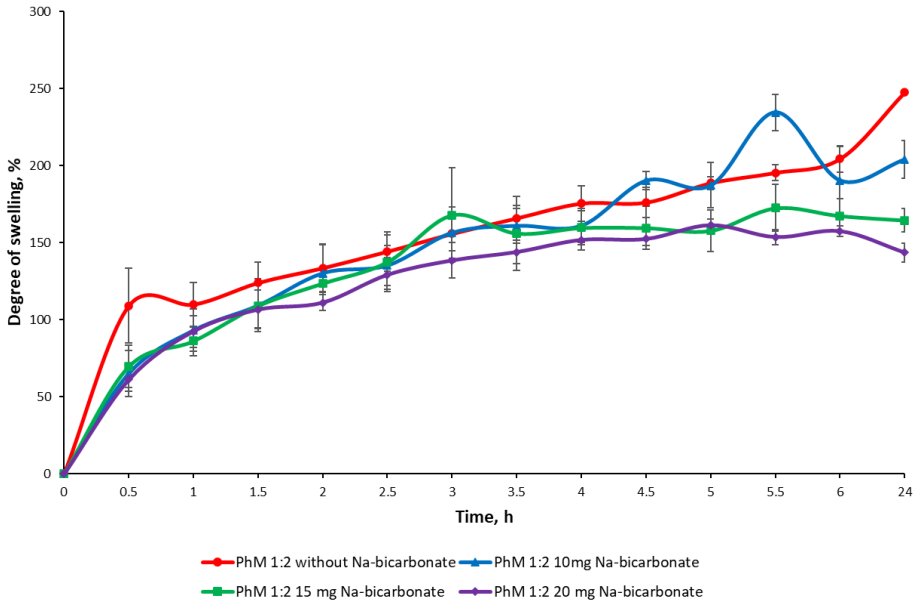

Figure 2. Swelling profiles of PhM 1:2 matrices with and without Na-bicarbonate in mimicking fasted stomach media (0.1 M HCl) (n = 3, mean ± SD)

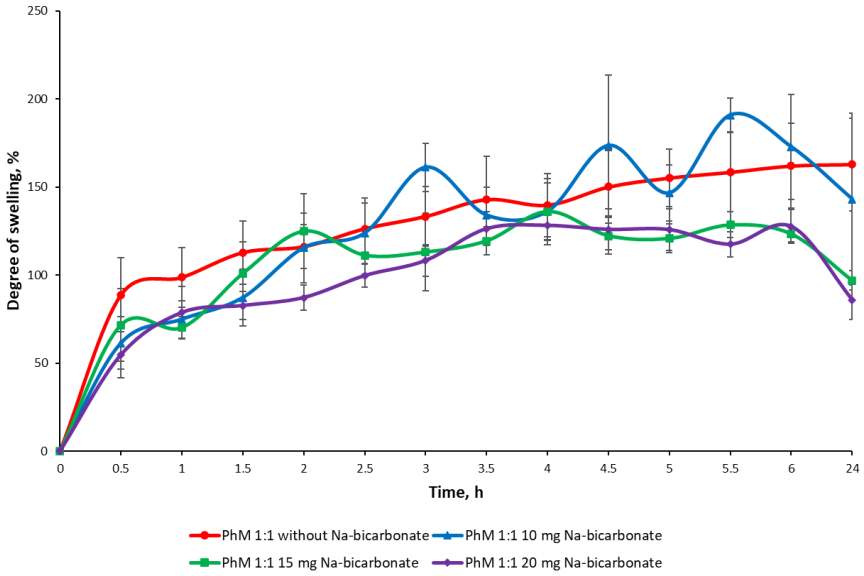

Figure 3. Swelling profiles of PhM 1:1 matrices with and without Na-bicarbonate in mimicking fasted stomach media (0.1 M HCl) (n = 3, mean ± SD)

Carbopol® as a weakly crossed-linked PAA, has a weak solubility in an acidic environment. Carbopol® polymers are bearing very good sorption property and they are capable of swelling to form a gel layer [47]. The thickening effect arises from the formation of hydrogen bonds between the carboxyl group and one or more hydroxyl donors [48, 49]. They provide gelation, viscosity, and mechanical strength necessary for structural integrity, resulting in denser, more robust matrices. HPC also is necessary for raft formation and stability. However, due to its reduced amount following erosion from the matrix, this led to the gel layer surrounding the tablet core becoming less viscous. Furthermore, the presence of the Na-bicarbonate increased the tablet's porosity, which disrupted the continuous gel structure of the soluble polymer, allowing a greater amount of water to penetrate into the swelling matrix [20, 50]. We have previously studied the swelling behavior of matrices based on these polymers, which is consistent with our assumptions [33].

Determination of the pH in the Matrix

To further investigate the micro-environmental pH, the pH indicator methyl red (0.15 % w/w) was added to the matrix to visually monitor the pH within the matrices during the penetration of media. This indicator is red at acidic pH and yellow at pH values >5.8 [43]. The appearance of the matrices during the experiment is shown in the Figure 4.

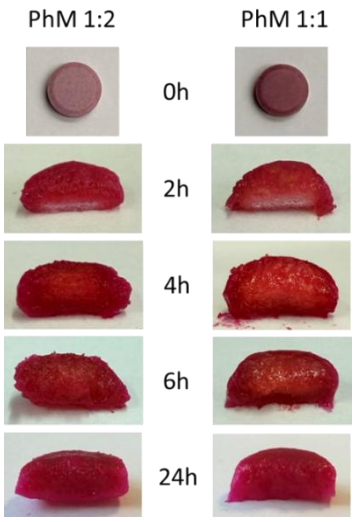

Figure 4. External appearance of PhM matrices during the media penetration

When the matrices were immersed in an acidic medium with a pH 1.2, a bright red staining of the matrix surface was observed. The Na-bicarbonate solution has an alkaline pH value [51, 52]. Since the matrix contains Na-bicarbonate, when interacting with the media, it will change the pH inside the matrix. By changing the color of the indicator, it is possible to monitor the change in the pH value during the penetration of the media into the matrix and identify the equilibrium of the reaction. The experiments showed that the outer hydrogel layer of the matrix remained red (low pH), whereas the core color of the slowly turned to yellow (high pH), from the edge towards the center. Thus, the pH within the core of the matrix turned yellow under the action of Na-bicarbonate during the penetration. 2 hours of exposure in the media showed its incomplete penetration into the entire volume of the matrix. With deeper penetration, a more pronounced change in the color of the indicator was observed (4 h, 6 h). After 24 hours of the experiment, the matrix turned red, which indicates that the reaction has completely passed and reached equilibrium in the system.

Evaluation of IPC. ATR-FTIR Spectroscopy

To assess possible structural changes in the PhM matrices, occurring under the influence of an media with a low pH value and also to evaluate the influence of Na-bicarbonate on the complexation between polymers, samples were collected after exposure to an acidic media, simulating stomach acid. The samples were specially prepared for further analysis using the method described above (Sample preparation).

ATR-FTIR spectroscopy can be used to analyze hydrogen-bonded complexation between C71G and HPC by monitoring the shift of the characteristic absorbance band. Hydrogen bonding primarily occurs between the hydroxyl (–OH) or ester (–O–) groups of HPC and the carboxylic (–COOH) groups of C71G. In pure C71G powder, the carbonyl peak is usually located at 1700~1710 cm^{-1}. The hydrogen bonding between hydroxyl or ether groups and the carboxylic groups disrupts the existing hydrogen bonding network among the –COOH groups of C71G. Consequently, compared to pure C71G powder, the C=O stretching vibration in the FT-IR spectra exhibits shift. This spectral shift is an indicator of the extent of hydrogen bonding between HPC and C71G, it was investigated by us earlier [33]. A greater degree of hydrogen bond formation between C71G and HPC results in a higher shift of the C=O band relative to pure C71G [35, 38, 44]. This shift is also typical for IPCs with similar structures [53].

The ATR-FTIR spectra of the samples are presented in Figures 5-6. In the ATR-FTIR spectra of the individual polymers, the C71G exhibits an absorption band in the region of 1703–1707 cm^{-1}. This characteristic band confirms the stretching vibrations of the carboxyl groups in their structure. No absorption bands in this region were observed for the HPC. The ATR-FTIR spectra, obtained after different periods of matrix residence (2 h, 4 h, 6 h, 24 h) in the acidic media, confirmed that with increased residence time, the shift of the characteristic band increases. Since the PhM 1:1 is stoichiometric, more pronounced shifts are observed compared to the PhM 1:2 for both compositions with and without Na-bicarbonate. This is indicative of complex formation associated with a greater number of hydrogen bonds.

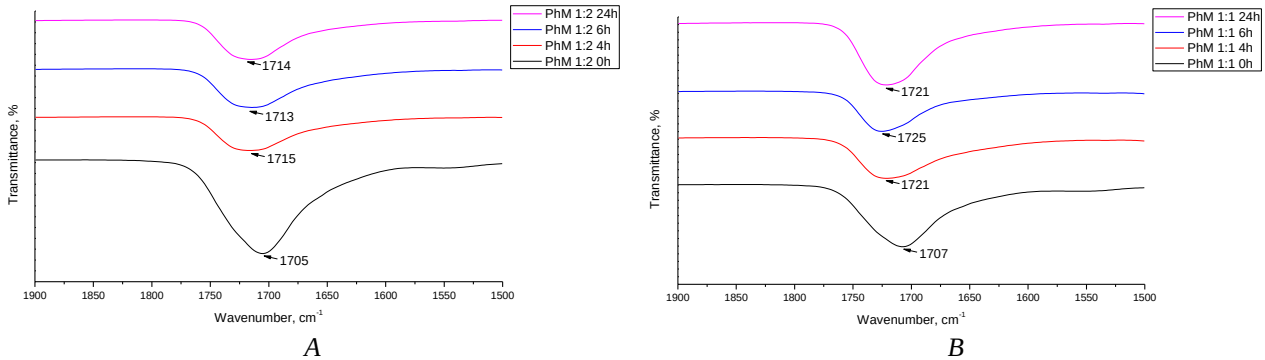

A *B*

A — PhM 1:2; *B* — PhM 1:1 (ordinate — transmission, %; abscissa — wavenumber, cm^{-1})

Figure 5. IR-spectra of PhMs without Na-bicarbonate

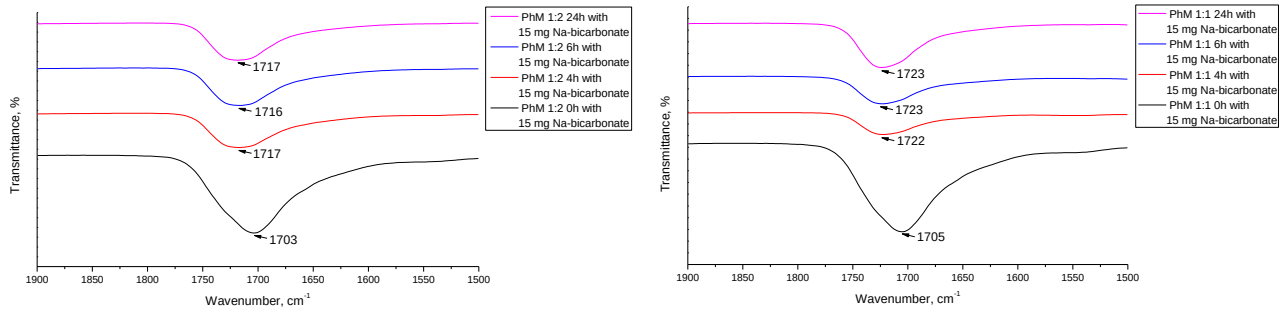

A *B*

A — PhM 1:2; *B* — PhM 1:1 (ordinate — transmission, %; abscissa — wavenumber, cm^{-1})

Figure 6. IR-spectra of PhMs with Na-bicarbonate

Thermal Analysis

The procedure for preparing the samples is detailed in the Sample preparation.

Figures 7-8 show the mDSC thermograms of the analyzed samples: PhMs without Na-bicarbonate, PhMs with Na-bicarbonate before swelling and after being in an acidic media for 4 h and 6 h. PhMs until swelling (0 h) have glass transition temperature (T_g) in the region 128.4–128.7 °C. This is typical for a pure C71G [33, 54]. A 4-hour exposure of the PhMs leads to a reduction in its T_g, which is likely due to the formation of hydrogen bonds. Extended exposure to the acidic media resulted in a more substantial lowering of the T_g. For PhMs without Na-bicarbonate, this is most pronounced for the 1:1 composition, which is probably due to the stoichiometric interaction T_g = 95.1 °C. In the case of mDSC-thermograms with Na-bicarbonate, the formation of IPC during swelling occurs in the case of both 1:1 and 1:2 formulations. At the same time, regardless of the time (4 or 6 h), a more intense shift in T_g was observed (T_g = 92.5–97.7 °C). According to literature data, the T_g of HPC is recorded in the range of 40 to 45 °C [55]. Based on literature findings, the T_g of polycomplex lies in the range between the T_g's of the initial components. The resulting T_g's for IPCs are recorded precisely in this range (T_g = 92.5–97.7 °C) [53]. This is a result of the formation of a cooperative system of intermolecular hydrogen bonds, which is consistent with our previous studies [33]. Observation of a non-classical (broadened) T_g in the swollen PhMs suggests the possible formation of a limited number of hydrogen bonds during complexation. The obtained mDSC results correlate with the ATR-FTIR results. As can be observed, the shifts of characteristic bands for the PhM 1:1 are more pronounced (1721–1725 cm^{-1}) than for the PhM 1:2 (1713–1715 cm^{-1}) without carbonate, as well as with Na-bicarbonate: PhM 1:1 (1722–1723 cm^{-1}), PhM 1:2 (1716–1717 cm^{-1}), which also indicates a IPC formation process between the polymers.

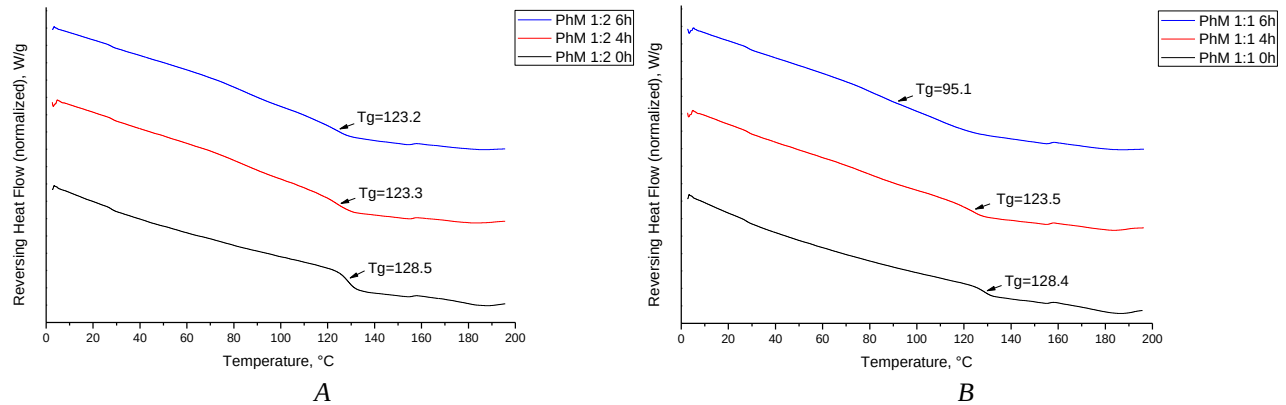

A *B*

A — PhM 1:2; *B* — PhM 1:1 (ordinate — reversing heat flow, W/g; abscissa — temperature, °C)

Figure 7. mDSC thermograms of PhMs without Na-bicarbonate

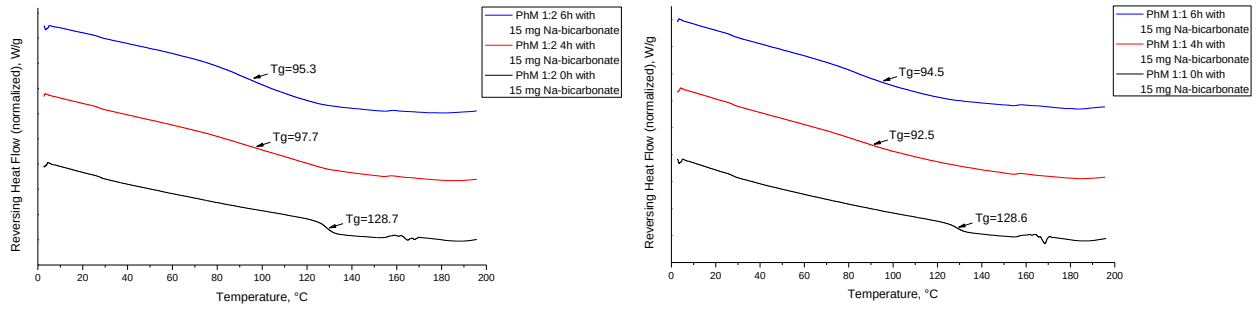

A *B*

A — PhM 1:2; *B* — PhM 1:1 (ordinate — reversing heat flow, W/g; abscissa — temperature, °C)

Figure 8. mDSC thermograms of PhMs with Na-bicarbonate

The observed changes in the DSC-thermograms of both PhMs before swelling, in the range of 150–170 °C, are associated with the decomposition of Na-bicarbonate in the mixture [56, 57]. As a result of swelling in an acidic media, the formation of two T_g characteristic of the individual polymers is not observed, which confirms the interaction between the polymers in the PhM. A single resultant T_g indicates the formation of a IPC.

Study of Drug Release

Acyclovir release in 0.1 M HCl was studied from floating tablets. The composition of the floating tablets is reported in Table 2. This is done in order to illustrate the effect of Na-bicarbonate as well as combination of HPC and C71G in matrices on the drug release of acyclovir.

Table 2

Composition of floating tablet matrices

HPC:C71G molar ratio	Mass of PhM for 1 tablet, mg	Mass of acyclovir for 1 tablet, mg	Na-bicarbonate mg	Total mass of 1 tablet, mg
1:2	50	100	10	160
1:2	50	100	15	165
1:2	50	100	20	170
1:1	50	100	10	160
1:1	50	100	15	165
1:1	50	100	20	170

Incorporation of Na-bicarbonate did not significantly affect the rapid drug release from PhMs matrices. This did not lead to acceleration of drug release by the effervescent action. However, it is worth noting that the drug release from matrices based on a PhM 1:1 is slightly higher than from a PhM 1:2 (Figures 9-10).

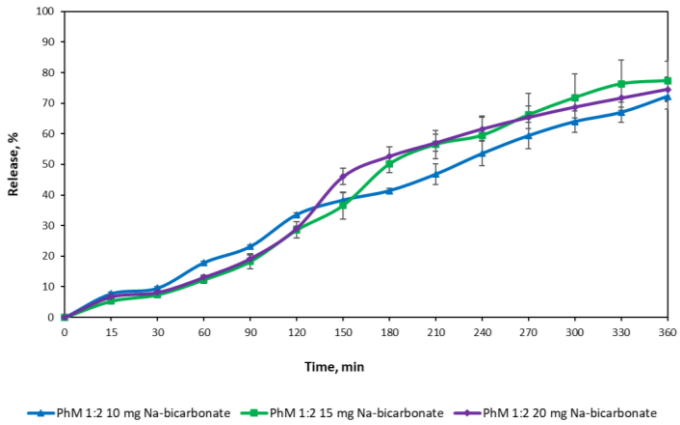

Figure 9. Effect of Na-bicarbonate level (mg/tablet) on Acyclovir release in 0.1 M HCl from PhM 1:2 tablet matrices (n = 3, mean ± SD)

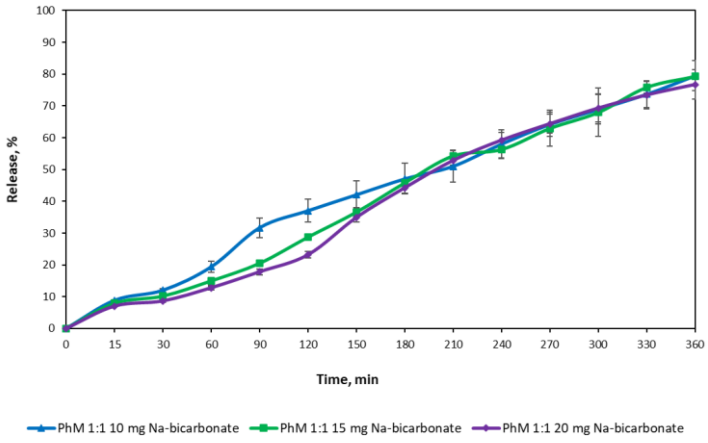

Figure 10. Effect of Na-bicarbonate level (mg/tablet) on Acyclovir release in 0.1 M HCl from PhM 1:1 tablet matrices (n = 3, mean ± SD)

This may be attributed to the erosion of the matrices due to existence of a soluble polymer (HPC) in them. The proportion of HPC in the PhM 1:2 is lower, which results in a reduced disruptive effect on the matrix. Conversely, the higher content of C71G allows the matrix to maintain its structure for a longer period due to the formation of a surface gel layer [47]. All compositions demonstrated a slower drug release, as no more than 85 % of the acyclovir was released within 6 hours. Release profile of acyclovir from all matrices, regardless of the concentration of Na-bicarbonate, can be characterized as prolonged with gradual drug release over 6 h.

Conclusions

Thus, according to the conducted studies, floating tablets based on a physical mixture of HPC and C71G were obtained. All matrices containing sodium bicarbonate showed a flotation time of less than 3 minutes, with the exception of a 2:1 PhM with 10 mg of sodium bicarbonate. The tablet matrices retained their shape during swelling and increased in size due to the swelling of Carbopol®. It is worth noting that with a polymer ratio in the PhM HPC/C71G (1:1 ratio) related to weight loss, greater matrix erosion was observed compared to a 1:2 due to the lower C71G content. Studies with methyl red indicator showed gradual penetration of the acidic media into the matrix and a color change from red to yellow. According to ATR-FTIR spectroscopy, a spectral shift is observed during matrix swelling, indicating the degree of hydrogen bonding between HPC and C71G in the samples. Thermal analysis revealed a somehow decrease in the glass transition temperatures in the DSC-thermograms, which is due to the formation of a polycomplex structure stabilized by an intermacromolecular hydrogen bonds.

The addition of sodium bicarbonate did not increase the release rate due to the effervescent effect. A slightly higher release rate was observed for matrices with a 1:1 polymer ratio, due to erosion of the soluble HPC polymer, while the higher C71G content maintains the structure due to the formation of a hydrogel layer. Thus, a PhMs of HPC/C71G with the addition of sodium bicarbonate can be used to produce floating tablets for the gastroretentive delivery of acyclovir.

Funding

The study was supported by a grant from the Russian Science Foundation (No. 23-15-00263, “Development polycomplex drug delivery systems for preparation of innovative dosage forms with modified release”, https://rscf.ru/en/project/23-15-00263/).

*Author Information**

**The authors' names are presented in the following order: First Name, Middle Name and Last Name*

Ulyana Nikolaevna Zabolotnaya — 3d year PhD Student, Institute of Pharmacy, Kazan State Medical University, Fatykha Amirkhan str., 16, Kazan, Republic of Tatarstan, 420126, Russia; e-mail: ulyana.zabolotnaya@kazangmu.ru, https://orcid.org/0009-0004-8058-8007

Venera Rasimovna Timergalieva — PhD, Institute of Pharmacy, Kazan State Medical University, Fatykha Amirkhan str., 16, Kazan, Republic of Tatarstan, 420126, Russia; e-mail: venera.timergalieva@kazangmu.ru, https://orcid.org/0000-0002-3690-8905

Shamil Flurovich Nasibullin — Lecturer, Institute of Pharmacy, Kazan State Medical University, Fatykha Amirkhan str., 16, Kazan, Republic of Tatarstan, 420126, Russia; e-mail: shamil.nasibullin@kazangmu.ru, https://orcid.org/0000-0002-7255-8041

Rouslan Ibragimovich Moustafine (*corresponding author*) — PhD, Director of Institute of Pharmacy, Institute of Pharmacy, Kazan State Medical University, Fatykha Amirkhan str., 16, Kazan, Republic of Tatarstan, 420126, Russia; e-mail: ruslan.mustafin@kazangmu.ru, https://orcid.org/0000-0002-0916-2853

Author Contributions

The manuscript was written through contributions of all authors. All authors have given approval to the final version of the manuscript. CRediT: **Ulyana Nikolaevna Zabolotnaya** conceptualization, data curation, investigation, methodology, visualization, writing-original draft; **Venera Rasimovna Timergalieva** conceptualization, methodology, visualization, writing-original draft; **Shamil Flurovich Nasibullin** assisted with thermal methods and advised on the experimental results; **Rouslan Ibragimovich Moustafine** conceptualization, data curation, formal analysis, funding acquisition, resources, supervision, validation, writing-original draft, writing-review & editing.

Conflicts of Interest

The authors declare no conflict of interest.

References

1 Vo, A. Q., Zhang, J., Nyavanandi, D., Bandari, S., & Repka, M. A. (2020). Hot melt extrusion paired fused deposition modeling 3D printing to develop hydroxypropyl cellulose based floating tablets of cinnarizine. *Carbohydrate Polymers*, *246*, 116519. https://doi.org/10.1016/J.CARBPOL.2020.116519

2 Alekseyev, K. V., Blynskaya, E. V., Karbusheva, E. Yu., Sedova, M. K., Tikhonova, N. V., & Uvarov, N. A. (2012). Production of Floating Medicinal Forms. *Pharmacy*, (6), 35–38 [in Russian].

3 Lin, X., Fu, H., Hou, Z., Si, Y., Shan, W., & Yang, Y. (2021). Three-dimensional printing of gastro-floating tablets using polyethylene glycol diacrylate-based photocurable printing material. *International Journal of Pharmaceutics*, *603*, 120674. https://doi.org/10.1016/j.ijpharm.2021.120674

4 Lopes, C. M., Bettencourt, C., Rossi, A., Buttini, F., & Barata, P. (2016). Overview on gastroretentive drug delivery systems for improving drug bioavailability. *International journal of pharmaceutics*, *510(1)*, 144–158. https://doi.org/10.1016/j.ijpharm.2016.05.016

5 Omidian, H. (2025). Gastroretentive drug delivery systems: A holy grail in oral delivery. *Drug Discovery Today*, 104340. https://doi.org/10.1016/j.drudis.2025.104340

6 Yuan, K. C., Chiang, Y. C., Li, P. H., & Chiang, P. Y. (2024). Physicochemical and release properties of anthocyanin gastric floating tablets colloidized with κ-carrageenan/metal ions. *Food Hydrocolloids*, *150*, 109674. https://doi.org/10.1016/j.foodhyd.2023.109674

7 Pinto, J. F. (2010). Site-specific drug delivery systems within the gastro-intestinal tract: from the mouth to the colon. *International journal of pharmaceutics*, *395(1-2)*, 44–52. https://doi.org/10.1016/j.ijpharm.2010.05.003

8 Shah, K., Singh, D., Agrawal, R., & Garg, A. (2025). Current developments in the delivery of gastro-retentive drugs. *American Association of Pharmaceutical Scientists PharmSciTech*, *26(2)*, 57. https://doi.org/10.1208/s12249-025-03052-4

9 Issarachot, O., Bunlung, S., Kaewkroek, K., & Wiwattanapatapee, R. (2023). Superporous hydrogels based on blends of chitosan and polyvinyl alcohol as a carrier for enhanced gastric delivery of resveratrol. *Saudi Pharmaceutical Journal*, *31(3)*, 335–347. https://doi.org/10.1016/j.jsps.2023.01.001

10 Charoenying, T., Opanasopit, P., Ngawhirunpat, T., Rojanarata, T., Akkaramongkolporn, P., & Patrojanasophon, P. (2023). Development of a novel tablet-shaped floating 3D-printed device with adjustable floating time as floating drug delivery systems provided zero-order release kinetics. *Journal of Drug Delivery Science and Technology*, *84*, 104506. https://doi.org/10.1016/j.jddst.2023.104506

11 Mustafin R. I., Protasova A. A., Bukhovets A. V., & Semina I. I. (2014). Issledovanie interpolymernykh sochetaniy na osnove (met)akrilatov v kachestve perspektivnykh nositeley v polikompleksnykh sistemakh dlya gastroretentivnoy dostavki [Investigation of interpolymers based on (meth)acrylates as promising carriers in multiplex gastroretentive drug delivery systems]. *Farmatsiya — Farmatsiya*, *5*, 3–5 [in Russian].

12 Blynskaya, E. V., Vinogradov, V. P., Tishkov, S. V., Suslina, S. N., & Alekseev, K. V. (2022). Modern Approaches to Obtaining Floating Drug Dosage Forms (A Review). *Pharmaceutical Chemistry Journal, 56(9)*, 1277–1284. https://doi.org/10.1007/s11094-022-02786-w

13 Raza, A., Hayat, U., Wang, H. J., & Wang, J. Y. (2020). Preparation and evaluation of captopril loaded gastro-retentive zein based porous floating tablets. *International Journal of Pharmaceutics, 579*, 119185. https://doi.org/10.1016/j.ijpharm.2020.119185

14 Tort, S., Han, D., & Steckl, A. J. (2020). Self-inflating floating nanofiber membranes for controlled drug delivery. *International Journal of Pharmaceutics, 579*, 119164. https://doi.org/10.1016/j.ijpharm.2020.119164

15 Rahim, S. A., Carter, P., & Elkordy, A. A. (2017). Influence of calcium carbonate and sodium carbonate gassing agents on pentoxifylline floating tablets properties. *Powder Technology, 322*, 65–74. https://doi.org/10.1016/j.powtec.2017.09.001

16 Yin, L., Qin, C., Chen, K., Zhu, C., Cao, H., Zhou, J., He, W., & Zhang, Q. (2013). Gastro-floating tablets of cephalexin: preparation and in vitro/in vivo evaluation. *International journal of pharmaceutics, 452(1-2)*, 241–248. https://doi.org/10.1016/j.ijpharm.2013.05.011

17 Chaudhary, S., Chandrika, A. M., Chaudhary, Y., Shahi, A., Sigdel, A., & Thapa, R. (2025). Formulation and Invitro Evaluation of Effervescent Floating Tablets of Hydrophilic Polymers Using Propranolol Hydrochloride as a Model Drug. *World Journal of Current Medical and Pharmaceutical Research, 7(1)*, 29–34. https://doi.org/10.37022/wjcmpr.v7i1.354

18 Tufail, M., Shah, K. U., Khan, I. U., Khan, K. A., Shah, S. U., Rashid, F., Khan, J., Alshammari, A., Alasmari, A. F., & Riaz, M. S. (2024). Controlled release bilayer floating effervescent and noneffervescent tablets containing levofloxacin and famotidine. *International Journal of Polymer Science, 2024(1)*, 1243321. https://doi.org/10.1155/2024/1243321

19 Siripruekpong, W., Wiwattanapatapee, R., Chambin, O., & Assifaoui, A. (2025). Structural and mechanistic exploration in the development of floating drug delivery systems using calcium-pectinate gels with sodium bicarbonate as CO_2 gas-forming agent. *Journal of Drug Delivery Science and Technology, 107*, 106729. https://doi.org/10.1016/j.jddst.2025.106729

20 Ahmad, S., Khan, J. A., Kausar, T. N., Mahnashi, M. H., Alasiri, A., Alqahtani, A. A., Alqahtani, T. S., Walbi, I. A., Alshehri, O. M., Elnoubi, O. A., Mahmood, F., & Sadiq, A. (2023). Preparation, characterization and evaluation of flavonolignan silymarin effervescent floating matrix tablets for enhanced oral bioavailability. *Molecules, 28(6)*, 2606. https://doi.org/10.3390/molecules28062606

21 Zhang, R., Shi, H., Li, S., Zhang, H., Zhang, D., Wu, A., Zhang, C., Li, C., Fu, X., Chen, S., Shi, J., Tian, Y., Wang, Y., & Liu, H. (2023). A double-layered gastric floating tablet for zero-order controlled release of dihydromyricetin: Design, development, and in vitro/in vivo evaluation. *International Journal of Pharmaceutics, 638*, 122929. https://doi.org/10.1016/j.ijpharm.2023.122929

22 Saady, M., Shoman, N. A., Teaima, M., Abdelmonem, R., El-Nabarawi, M. A., & Elhabal, S. F. (2024). Fabrication of gastro-floating sustained-release etoricoxib and famotidine tablets: design, optimization, in-vitro, and in-vivo evaluation. *Pharmaceutical Development and Technology, 29(5)*, 429–444. https://doi.org/10.1080/10837450.2024.2343320

23 Bellad, K., Nanjwade, B., Sarkar, A., Srichana, T., & Shetake, R. (2020). Development and evaluation of curcumin floating tablets. *Pharmaceutica Analytica Acta, 12*, 622. https://doi.org/10.35248/2153-2435.20.11.622

24 Bote, S., & Kolageri, S. (2022). Formulation and Evaluation of Floating Tablets of Pantoprazole. Journal of Drug Delivery and Therapeutics, 12(5), 34–45. https://doi.org/10.22270/jddt.v12i5.5577

25 Liu, H., Wang, S., Shi, H., Zhang, R., Qu, K., Hu, Y., Qu, X., Gan, C., Chen, J., Shi, X., Zhang, M., & Zeng, W. (2021). Gastric floating tablet improves the bioavailability and reduces the hypokalemia effect of gossypol in vivo. *Saudi Pharmaceutical Journal, 29(4)*, 305–314. https://doi.org/10.1016/j.jsps.2021.03.001

26 Wavhule, P., & Devarajan, P. V. (2021). Development and optimization of microballoons assisted floating tablets of Baclofen. *American Association of Pharmaceutical Scientists PharmSciTech, 22(8)*, 272. https://doi.org/10.1208/s12249-021-02139-y

27 Huh, H. W., Na, Y. G., Kang, H., Kim, M., Han, M., Pham, T. M. A., Lee, H., Baek, J. S., Lee, H. K., & Cho, C. W. (2021). Novel self-floating tablet for enhanced oral bioavailability of metformin based on cellulose. *International Journal of Pharmaceutics, 592*, 120113. https://doi.org/10.1016/j.ijpharm.2020.120113

28 Moustafine R. I., Bukhovets A. V., Protasova A. A., Shaykhramova R. N., Sitenkov A. Y., & Semina I. I. (2015). Sravnitel'noe issledovanie polikompleksnykh sistem dlya gastroretentivnoy dostavki metformina [Comparative investigation of polycomplex systems for gastroretentive metformin delivery]. *Razrabotka i registratsiya lekarstvennykh sredstv — Drug development & registration, 1(10)*, 48–50 [in Russian].

29 Khutoryanskiy, V. V., Dubolazov, A. V., & Mun, G. A. (2009). pH-and ionic strength effects on interpolymer complexation via hydrogen-bonding. *In Hydrogen-bonded interpolymer complexes: Formation, structure and applications*, 1-21. https://doi.org/10.1142/9789812709776_0001

30 Smyslov, R. Y., Gorshkova, Y. E., Nekrasova, T. N., Makhayeva, D. N., Mun, G. A., Irmukhametova, G. S., & Khutoryanskiy, V. V. (2025). Dynamic and structural insights into hydrogen-bonded interpolymer complexes of poly(2-alkyl-2-oxazolines) with poly(carboxylic acids). *Journal of Colloid and Interface Science, 699(1)*, 138185. https://doi.org/10.1016/j.jcis.2025.138185

31 Khutoryanskiy, V. V. (2007). Hydrogen-bonded interpolymer complexes as materials for pharmaceutical applications. *International Journal of Pharmaceutics, 334*(1-2), 15–26. https://doi.org/10.1016/j.ijpharm.2007.01.037

32 Bani-Jaber, A. K., Alkawareek, M. Y., Al-Gousous, J. J., & Helwa, A. Y. A. (2011). Floating and sustained-release characteristics of effervescent tablets prepared with a mixed matrix of Eudragit L-100-55 and Eudragit EPO. *Chemical and Pharmaceutical Bulletin, 59(2)*, 155–160. https://doi.org/10.1248/cpb.59.155

33 Zabolotnaya U.N., Timergalieva V.R., Nasibullin S.F., & Moustafine R.I. (2025). Development of polycomplex carriers based on hydroxypropyl cellulose and Carbopol® for gastroretentive drug delivery. *Drug development & registration, 14(4)*, 108–124 [in Russian]. https://doi.org/10.33380/2305-2066-2025-14-4-2148

34 Nurkeeva, Z. S., Mun, G. A., & Khutoryanskiy, V. V. (2003). Interpolymer complexes of water-soluble nonionic polysaccharides with polycarboxylic acids and their applications. *Macromolecular Bioscience, 3(6)*, 283–295. https://doi.org/10.1002/chin.200408305

35 Satoh, K., Takayama, K., Machida, Y., Suzuki, Y., Nakagaki, M., & Nagai, T. (1989). Factors affecting the bioadhesive property of tablets consisting of hydroxypropyl cellulose and carboxyvinyl polymer. *Chemical and pharmaceutical bulletin, 37(5)*, 1366-1368. https://doi.org/10.1248/cpb.37.1366

36 Mangazbaeva, R. A., Mun, G. A., Nurkeeva, Z. S., & Khutoryanskiy, V. V. (2006). Interpolymer complexes of hydroxypropylmethylcellulose with polycarboxylic acids in aqueous solutions. *Polymer international, 55(6)*, 668–674. https://doi.org/10.1002/pi.2012

37 Mun, G. A., Nurkeeva, Z. S., Khutoryanskiy, V., & Dubolazov, A. V. (2003). Effect of pH and ionic strength on the complex formation of poly(acrylic acid) with hydroxyethylcellulose in aqueous solutions. *Polymer Science, 45(12)*, 2091–2095.

38 Şakar-Deliormanli, A. (2012). Flow behavior of hydroxypropyl methyl cellulose/polyacrylic acid interpolymer complexes in aqueous media. *Polymer international, 61(12)*, 1751–1757. https://doi.org/10.1002/pi.4266

39 Negim, E. S. M., Nurpeissova, Z. A., Mangazbayeva, R. A., Khatib, J. M., Williams, C., & Mun, G. A. (2014). Effect of pH on the physico-mechanical properties and miscibility of methyl cellulose/poly(acrylic acid) blends. *Carbohydrate Polymers, 101*, 415–422. https://doi.org/10.1016/j.carbpol.2013.09.047

40 Fedorova, O. V., Ovchinnikova, I. G., Rusinov, G. L., Avdeeva, V. V., Zhdanov, A. P., Zhizhin, K. Yu., Kuznetsov, N. T., Zakharova, L. Ya., Kuznetsova, D. A., Razuvaeva, Yu. S., Zhiltsova, E. P., Sinyashin, O. G., Alekseeva, A. S., Vodovozova, E. L., Abdrakhmanova, I. I., Ibrahim, A., Solovyeva, V. V., Maltsev, A. V., Fisenko, V. P., Bachurin, S. O., Mikhailov, Yu. M., Aleksandrova, Yu. I., Shurpik, D. N., Stoikov, I. I., Ziganshina, A. Y., Solovieva, S. E., Antipin, I. S., Agafonov, M. A., Terekhova, I. V., Ilicheva, P. M., Pidenko, P. S., Burmistrova, N. A, Moustafine, R. I., Timergalieva, V. R., Zabolotnaya, Y. N., Khutoryanskiy, V. V., Demin, A. M., Levit, G. L., Charushin, V. N., Krasnov, V. P., Goryacheva, O. A., Mayorova, O. A., Mesheryakova, S. M., Goryacheva, I. Yu., Ayupova, A. I., Fattakhova, A. A., Rizvanov, A. A., Inozemtseva, O. A., Gusliakova, O. I., Gorin, D. A., Gerasimov, A. V., Zubaidullina, L. S., Ziganshin, M. A., Valiulin, S. V., Onischuk, A. A., Bezrukov, A. N., Galyametdinov, Yu. G., Padnya, P. L., Nazarova, A. A., Sultanova, E. D. & Burilov, V. A. (2025). Modern Strategies of Drug Therapy: Multi-Target Drug Delivery, Bioimaging, Diagnostics. *Russian Journal of General Chemistry, 95* (Suppl 1), S1-S448. https://doi.org/10.1134/S1070363225606726

41 Gordeeva D. S., Sitenkova (Bukhovets) A. V., Moustafine R. I. (2020). Interpolyelectrolyte Complexes Based On Eudragit® Copolymers As Carriers For Bioadhesive Gastroretentive Metronidazole Delivery System. *Drug development & registration, 9(2)*, 72–76 [in Russian]. https://doi.org/10.33380/2305-2066-2020-9-2-72-76

42 Viktorova A. S., Elizarova E. S., Romanova R. S., Timergalieva V. R., Khutoryanskiy V. V., Moustafine R. I. (2021). Interpolymer complexes based on Carbopol® and poly(2-ethyl-2-oxazoline) as carriers for buccal delivery of metformin. *Drug development & registration, 10(1)*, 48–55 [in Russian]. https://doi.org/10.33380/2305-2066-2021-10-1-48-55

43 Streubel, A., Siepmann, J., Dashevsky, A., & Bodmeier, R. (2000). pH-independent release of a weakly basic drug from water-insoluble and-soluble matrix tablets. *Journal of controlled release*, *67*(1), 101–110. https://doi.org/10.1016/S0168-3659(00)00200-5

44 Zhang X., Lin F., Yuan Q., Zhu L., Wang C., Yang S. (2019). Hydrogen-bonded thin films of cellulose ethers and poly(acrylic acid). *Carbohydrate Polymers, 215*, 58-62. https://doi.org/10.1016/j.carbpol.2019.03.066

45 Rao, G. K., Mandapalli, P. K., Manthri, R., & Reddy, V. P. (2013). Development and in vivo evaluation of gastroretentive delivery systems for cefuroxime axetil. *Saudi Pharmaceutical Journal, 21(1)*, 53–59. https://doi.org/10.1016/j.jsps.2012.01.003

46 Prajapati, P. H., Nakum, V. V., & Patel, C. N. (2012). Formulation and evaluation of floating matrix tablet of stavudine. *International Journal of pharmaceutical investigation, 2(2)*, 83. https://doi.org/10.4103/2230-973X.100047

47 Yusif R. M., Hashim I. I. A., Mohamed E. A., El Rakhawy M. M. (2016). Investigation and evaluation of an in situ interpolymer complex of carbopol with polyvinylpyrrolidone as a matrix for gastroretentive tablets of ranitidine hydrochloride. *Chemical and Pharmaceutical Bulletin, 64(1)*, 42–51. https://doi.org/10.1248/cpb.c15-00620

48 Priyanka, R., & Prabhu, R. (2020). Carbopol 71G-NF polymer–the next pillar of oral solid dosage form. *Magna Scientia Adv Res Rev, 1*, 010–017. https://doi.org/10.30574/msarr.2020.1.1.0018

49 Ozeki, T., Yuasa, H., & Kanaya, Y. (2000). Controlled release from solid dispersion composed of poly(ethylene oxide)–Carbopol® interpolymer complex with various cross-linking degrees of Carbopol®. *Journal of controlled release*, *63*(3), 287–295. https://doi.org/10.1016/S0168-3659(99)00202-3

50 Barman, S., Sarkar, A., Das, U., & Mandal, S. (2025). Double Target Strategy of Novel Floating Raft System Containing Metronidazole. *Journal of Pharmaceutical Innovation*, *20*(6), 1–25. https://doi.org/10.1007/s12247-025-10187-1

51 Thapa, P., & Jeong, S. H. (2018). Effects of formulation and process variables on gastroretentive floating tablets with a high-dose soluble drug and experimental design approach. *Pharmaceutics*, *10*(3), 161. https://doi.org/10.3390/pharmaceutics10030161

52 Jindal, S., Jindal, K., Gupta, G., Garg, R., & Awasthi, R. (2016). Gastroretentive floating tablets: An investigation of excipients effect on tablet properties. *Marmara Pharmaceutical Journal*, *20*(2), 100–110. https://doi.org/10.12991/mpj.20162018166

53 Moustafine, R. I., Viktorova, A. S., & Khutoryanskiy, V. V. (2019). Interpolymer complexes of carbopol® 971 and poly(2-ethyl-2-oxazoline): Physicochemical studies of complexation and formulations for oral drug delivery. *International journal of pharmaceutics*, *558*, 53–62. https://doi.org/10.1016/j.ijpharm.2019.01.002

54 Gómez-Carracedo, A., Alvarez-Lorenzo, C., Gomez-Amoza, J. L., & Concheiro, A. (2004). Glass transitions and viscoelastic properties of Carbopol® and Noveon® compacts. *International journal of pharmaceutics*, *274*(1-2), 233–243. https://doi.org/10.1016/j.ijpharm.2004.01.023

55 Khutoryanskiy, V. V., Cascone, M. G., Lazzeri, L., Barbani, N., Nurkeeva, Z. S., Mun, G. A., & Dubolazov, A. V. (2004). Morphological and thermal characterization of interpolymer complexes and blends based on poly(acrylic acid) and hydroxypropylcellulose. *Polymer International*, *53*(3), 307–311. https://doi.org/10.1002/pi.1408

56 Heda, P. K., Dollimore, D., Alexander, K. S., Chen, D., Law, E., & Bicknell, P. (1995). A method of assessing solid state reactivity illustrated by thermal decomposition experiments on sodium bicarbonate. *Thermochimica acta*, *255*, 255–272. https://doi.org/10.1016/0040-6031(94)02154-G

57 Sadik, T., Pillon, C., Carrot, C., & Ruiz, J. A. R. (2018). Dsc studies on the decomposition of chemical blowing agents based on citric acid and sodium bicarbonate. *Thermochimica Acta*, *659*, 74–81. https://doi.org/10.1016/j.tca.2017.11.007

How to Cite: Burkeyeva, G.K., Kovaleva, A.K., Zhumabek, N.M., & Nukin, N.A. (2026). Influence of External Factors on the Behavior of Polymer Materials Based on Polyethylene Glycol Maleate. *Eurasian Journal of Chemistry, 31, 1(121), 87–99.* https://doi.org/10.31489/2959-0663/1-26-6

Article

Received: 1 December 2025 | Revised: 27 February 2026
Accepted: 2 March 2026 | Published online: 11 March 2026

UDC 541.057.17

https://doi.org/10.31489/2959-0663/1-26-6

Gulsym K. Burkeyeva[1], Anna K. Kovaleva[2*], Nurken M. Zhumabek[1], Nurlan A. Nukin[1]

[1]*Department of Organic Chemistry and Polymers, Karaganda National Research University named after Academician Ye.A. Buketov, Karaganda, Kazakhstan;*
[2]*Research Institute of Chemical Problems, Karaganda National Research University named after Academician Ye.A. Buketov, Karaganda, Kazakhstan*
*(*Corresponding author's e-mail: cherry-girl1899@mail.ru)*

Influence of External Factors on the Behavior of Polymer Materials Based on Polyethylene Glycol Maleate

This study aims to evaluate the effect of external physicochemical factors on the behavior of hydrogels based on polyethylene glycol maleate (p-EGM) and to assess their potential applicability in sorption-active polymer matrices and biomedical hydrogel systems. This paper presents the results of an investigation into the physicochemical properties of polyethylene glycol maleate and acrylamide solutions in acrylic acid and their cured products. The degree of unsaturation of the initial unsaturated polyester was determined using the bromide–bromate method. The dynamic viscosity of the initial polymer–monomer mixtures was found to be in the range of 0.251–0.697 Pa·s, while the density of the solutions varied from 1.0554 to 1.0996 g/cm^3. The density of the cured terpolymers was calculated by the hydrostatic method, and the calculated total volumetric shrinkage did not exceed 15 %. The composition of the obtained terpolymers was confirmed by HPLC analysis. The synthesized hydrogels exhibited a high swelling degree (up to 2898 %) and pronounced sensitivity to environmental pH (4–8) and temperature (35–39 °C), as established by gravimetric measurements. Structural identification was performed using IR and NMR spectroscopy, and the surface morphology was analyzed by SEM. It was demonstrated that an increased acrylic acid content leads to the formation of a more porous polymer network with enhanced water absorption, controllable permeability and structural stability, indicating potential biomedical applicability of the developed materials. Overall, the obtained results suggest that the synthesized hydrogels may be considered promising candidates for potential use in sorption-active polymer matrices and hydrogel-based wound dressing systems.

Keywords: unsaturated polyester, terpolymer, hydrogel, "cold" curing, external factors, water absorption, swelling degree, acrylic acid, polyethylene glycol maleate

Introduction

Hydrogels are unique polymeric materials capable of retaining large amounts of water. This property makes them highly attractive for medical applications, including wound and burn treatment, as well as controlled drug delivery systems [1–3]. Due to their three-dimensional mesh structure, swollen hydrogels maintain optimal moisture levels, regulate the diffusion of active compounds and gas exchange, and protect damaged tissues from secondary infection [4, 5]. In addition, the ability of such materials to mimic the physicochemical properties of the extracellular matrix ensures their biocompatibility and contributes to the acceleration of tissue healing and regeneration processes [6].

Structural modification of polymer hydrogels allows their properties to be precisely tuned and enables the materials to perform targeted physiological functions [7]. The introduction of functional groups capable of ionization, thermosensitive or biocompatible segments into the polymer network allows the creation of materials with adjustable parameters of swelling, mechanical strength, moisture transfer and sorption activity [8]. Such modifications make it possible to adapt hydrogels to specific physiological conditions: regulating moisture in the wound coverage area, increasing sorption capacity during exudation or, conversely, retaining moisture in dry wounds [9].

Regulating the density of cross-linking and the composition of the polymer mesh allows control not only over mechanical properties, but also over the kinetics of active substance release [10]. In particular, looser networks with low cross-linking density ensure rapid release of drug compounds and effective sorption of exudate, while dense structures with a higher degree of cross-linking ensure prolonged release and stability

of form [11]. Thus, varying the degree of swelling, porosity, and elasticity makes it possible to adapt hydrogels to specific clinical tasks, including the treatment of burns, trophic ulcers, postoperative and chronic wounds [12, 13].

It is worth noting that modern research is focused on creating functional and stimulus-sensitive hydrogels capable of responding to external physicochemical factors — pH, temperature, ionic strength, light radiation or mechanical impact — and ensuring targeted drug release [14, 15]. Such "smart" materials change their degree of swelling and permeability in response to external stimuli, which makes it possible to accurately dose and spatially and temporally control the therapeutic effect [16].

Particular attention is paid to thermo- and pH-sensitive systems that function under conditions close to physiological conditions. Hydrogels that exhibit reversible "swelling-collapse" transitions at a temperature of ~35~39 °C and in the pH range of 5–8 are most promising for use as gel dressings and transdermal delivery systems. At body temperature (~37 °C), such materials can partially collapse, releasing moisture to the damaged surface and preventing over-moisturization, and when the acidity characteristic of an inflamed environment changes, they can swell again, actively absorbing exudate.

In addition, structural modification of such hydrogels allows additional functional components to be incorporated into their network, such as antiseptics, antibiotics, anti-inflammatory drugs, and metal or oxide nanoparticles to impart antibacterial properties [4, 8]. Thus, current trends in the development of polymer hydrogels are aimed at creating multifunctional adaptive materials that not only provide a comfortable moist environment and tissue protection, but are also capable of actively participating in the healing process [9, 14].

Taken together, these features make modified hydrogels a promising class of polymer systems for medicine and biotechnology. They can serve not only as a material for wound dressings, but also as a basis for intelligent local therapy systems, biosensors, cell matrices, and soft implants of a new generation [6, 15].

Despite significant progress in the development of polyethylene glycol maleate-based hydrogel systems, the combined effect of ionogenic acrylic acid and non-ionogenic acrylamide on the structure formation and stimulus sensitivity of polyethylene glycol maleate networks remains insufficiently clarified [6, 14]. In particular, the balance between polyelectrolyte swelling provided by acrylic acid and the hydrogen-bond-driven structuring introduced by acrylamide requires further systematic investigation. Understanding this interplay is essential for the rational design of hydrogels with controlled responsiveness under physiologically relevant conditions.

Compared to our previous studies focused primarily on related polyethylene glycol maleate systems, the present work provides a systematic investigation of ternary p-EGM–AA–AAm networks with controlled variation of ionogenic and non-ionogenic fragments. This approach makes it possible to elucidate the combined effect of electrostatic and hydrogen-bond interactions on the responsive behavior of the hydrogels under physiologically relevant conditions.

In view of this, systems based on terpolymers of unsaturated polyesters with vinyl monomers [17, 18], which combine hydrophilicity [19], biocompatibility and the ability to immobilize drug compounds [20], are of particular interest. Due to the presence of reactive double bonds, such systems are easily modified and allow varying the degree of cross-linking [21], and therefore controlling the swelling rate, porosity and stability of the hydrogel [22]. Such materials demonstrate high moisture retention capacity and structural stability, which is particularly important for dressings that are in prolonged contact with biological tissues [2, 7, 12].

In this regard, the present study is focused on elucidating the influence of external physicochemical factors on the behavior of hydrogels based on polyethylene glycol maleate–acrylic acid–acrylamide terpolymer systems obtained by "cold" curing. The novelty of this work lies in the systematic investigation of the relationship between monomer composition, network structure, and the responsive swelling behavior of the resulting hydrogels under physiologically relevant pH and temperature conditions. The main objective of the study is to establish the physicochemical regularities governing the formation, morphology, and stimulus sensitivity of the synthesized materials in order to assess their suitability for use in sorption-active polymer matrices and flexible hydrogel patch applications.

Experimental

The experimental work was carried out using the following reagents ("Sigma-Aldrich", USA):

– for the synthesis of the starting unsaturated polyester — polyethylene glycol maleate (p-EGM) — by polycondensation reaction: ethylene glycol and maleic anhydride; zinc chloride (catalyst for the synthesis);

– for the synthesis of p-EGM-based terpolymers: acrylic acid (AA, which is both a co-reagent and a solvent), acrylamide (AAm);

– for "cold" curing of the triple systems under study: an initiating system consisting of benzoyl peroxide (BP, initiator) and dimethylaniline (DMA, activator);

– for determining the molecular weight of p-EGM and washing the terpolymers after synthesis: dioxane (solvent).

– to study the effect of pH on the behaviour of the synthesized gels: buffer solutions with pH values from 4.0 to 8.0.

All reagents had a purity of 99.95 % and were used without additional purification.

The synthesis of the starting unsaturated polyester (p-EGM) was carried out by polycondensation of ethylene glycol with maleic anhydride in the presence of a zinc chloride catalyst (0.2 % of the mass of the reaction mixture). The ratio of reagents in the reaction mixture was 1.05:1.0 mol. Polycondensation was carried out according to the standard method [21]. The yield of the resulting polyester was 98 %. The molecular weight of p-EGM was determined using a VISCOTEK 270 DUAL DETECTOR gel permeation chromatograph (MALVERN Panalytical Ltd., UK) equipped with a four-capillary bridge viscometer detector and low-angle/right-angle light scattering detectors (LALS/RALS) using a 3 mW laser with a wavelength of 670 nm. Dust-free dioxane was used as the solvent. The molecular weight of the synthesized p-EGM was ~1232 Da (M_W).

In order to obtain polymer gels, solutions with different ratios of p-EGM, AA and AAm components were prepared: ~15:70:15 wt.%, 15:50:35 wt.% and 15:35:50 wt.%. The dynamic viscosity of the obtained solutions (T = 293 K) was measured using an SV-10 vibration viscometer (A&D Company, Japan) operating on the tuning fork vibration principle at 30 Hz. The instrument was equipped with a VT3 thermostat bath (TERMEX, Russia) with a capacity of 3 L and a temperature control range of +20 °C to +200 °C to ensure temperature stability during measurements. The density of the solutions was measured by the pycnometric method in accordance with ISO 1675:1985.

"Cold" curing was carried out using an optimised initiating system consisting of 1.0 wt.% benzoyl peroxide (initiator) and 0.15 wt.% dimethylaniline (activator) relative to the total mass of the reaction mixture. The polymerization process was carried out at 293 K.

The resulting p-EGM–AA–AAm terpolymers were washed with dioxane to remove unreacted residues. The mother liquors were analysed by high-performance liquid chromatography (HPLC) using an LC-20 Prominence system (Shimadzu, Japan) equipped with an SPD-20A UV–Vis absorbance detector and an SPD-M20A diode array detector. The results were used to determine the actual composition of the synthesised terpolymers. The yield of the products was calculated by gravimetric analysis.

The identification of the curing products was carried out by IR and NMR spectroscopy to establish the presence of characteristic functional groups. IR spectra were recorded in KBr pellets on an FSM 1201 spectrometer (Infraspek, Russia) with a spectral range of 400–7800 cm^{-1} and a pyroelectric detector module ($LiTaO_3$), and ^1H NMR spectra were recorded on a DX-90M instrument (Xiamen Dexing Magnet Tech. Co., Ltd., China) operating at a ^1H resonance frequency of 90 MHz with a resolution of 1 Hz.

The density of the cured terpolymers was evaluated by the hydrostatic method (ASTM D792-13). The volumetric shrinkage of terpolymers was calculated based on experimental values of the density of the initial solutions and cured samples, according to formula (1):

$$S_V = \frac{\rho_d - \rho_l}{\rho_l} \cdot 100\ \%, \quad (1)$$

where ρ_l — initial density of the solution, g/cm^3; ρ_d — density of the cured dry sample, g/cm^3.

The morphology of the polymer surface was studied using SEM on a MIRA 3 microscope (TESCAN, Czech Republic) at an accelerating voltage of 5.0 kV with an SE detector and a magnification of 57.6–57.7 thousand times (resolution 1024×1024 pixels).

The hydrophilicity of the cured materials was evaluated by the gravimetric method. The degree of swelling was measured after exposing a sample (~0.5 g) to water at 20 °C (pH 7) for 24 hours. The calculation was performed using formula (2):

$$\alpha = \frac{m - m_0}{m_0} \cdot 100\ \%, \quad (2)$$

where m — mass of the swollen sample, g; m_0 — dry sample mass, g.

The study of the influence of external factors on the behavior of synthesized hydrogels was carried out in the pH range of 4–8 and at a temperature of T = 35–39 °C using the gravimetric method. The calculation was performed using formula (2).

The temperature at which thermal deformation began was determined by TGA using the Labsys Evolution TG-DTA/DSC synchronous thermal analysis system (Setaram Instrumentation, France) with an operating temperature range up to 1600 °C.

All measurements were performed in triplicate (n = 3). The experimental data are presented as mean ± standard deviation. Statistical analysis included calculation of the arithmetic mean, standard deviation, and relative error using standard descriptive statistical methods.

Results and Discussion

For a systematic study of the physicochemical properties of hydrogel materials, three solutions based on p-EGM, AA, and AAm monomers were prepared in the first stage of the research. The ratios of 15:70:15 wt.%, 15:50:35 wt.%, and 15:35:50 wt.% were deliberately chosen to form systems that differ in the concentration of ionogenic fragments, the degree of hydration, and the nature of interchain interactions. Due to the variable content of AA and AAm, the polymer networks differed in the number of potential centers of electrostatic association, hydrogen bonding and the formation of hydrated domains — all these factors influence the viscosity of solutions, the swelling mechanism and the morphology of the final products — gels.

After preparation, the initial solutions were thoroughly homogenized until an optical clarity was achieved in all samples. At this stage, the primary organization of intermolecular contacts — hydrogen bonds, ion-dipole associations and hydration interactions — was established. The degree of optical homogeneity served as an important criterion for the absence of microphase separation and was critical for the further correct formation of the gel structure. After exposure, the system reached a pre-equilibrium configuration in which weak associative interactions stabilized and determined the conditions for the further curing process [18, 21].

After reaching the equilibrium configuration of the initial solutions using an SV-10 vibrating viscometer and a pycnometer, the dynamic viscosity and density values of the analyzed solutions were determined. The results are presented in Table 1.

Pycnometric determination of density showed a steady trend towards a decrease in the mass-volume density of solutions as the proportion of AA increased. Although the differences were small, their reproducibility confirmed the correctness of the observed pattern. Thus, an increase in the AA content in the initial mixture from ~35 wt.% to ~70 wt.% led to a decrease in the density of the solutions from 1.0996 g/cm^3 to 1.0554 g/cm^3. These differences can be explained by the fact that AA forms less compact intermolecular structures compared to the more polar and intensely intermolecularly interacting components p-EGM and AAm [17]. An increase in AA content leads to a weakening of interfragment associations in the liquid mixture, which is reflected in a slight increase in free intermolecular space and a decrease in density (Table 1).

Table 1

Physical and chemical properties of initial solutions of p-EGM (M_1) with AA (M_2) and AAm (M_3) T = 293К

Composition of prepared solution, wt.%			Density of solution value (ρ_l), g/cm^3	Dynamic viscosity value (η), Pa·s
M_1	M_2	M_3		
15.12	70.29	14.59	1.0554±0.0528	0.251±0.013
15.21	50.41	34.38	1.0787±0.0539	0.417±0.021
15.15	34.86	49.99	1.0996±0.0550	0.697±0.035

Rheological studies have revealed a similar trend: a solution with a higher AA content exhibits lower dynamic viscosity. In particular, a solution with the maximum AA content (~70 wt.%) has the lowest dynamic viscosity η, which is 0.251 Pa·s. Reducing the AA content in the solution to ~35 wt.% leads to an increase in its dynamic viscosity to 0.697 Pa·s. This is due to the fact that the presence of AA reduces the degree of intermolecular adhesion in p-EGM–AA–AAm mixtures and decreases the probability of branched associates forming. Thus, changes in density and dynamic viscosity are consistent with each other and reflect the same structural phenomenon — different degrees of intermolecular organization of components in a liquid mixture before gel formation occurs. It is worth noting that such differences in rheological characteristics determine the further kinetics of gel formation and the degree of accessibility of reactive fragments.

The introduction of a "cold" curing initiation system ensures copolymerization of the components under identical conditions. This allows the differences in the properties of the final gels to be unequivocally attributed exclusively to differences in chemical composition due to different co-reagent contents in the initial mixture. After the reaction was complete, the resulting hydrogels demonstrated high transparency and homogeneity, confirming the absence of macrophase separation and the effectiveness of terpolymerization. A schematic representation of the terpolymerization reaction is shown in Figure 1.

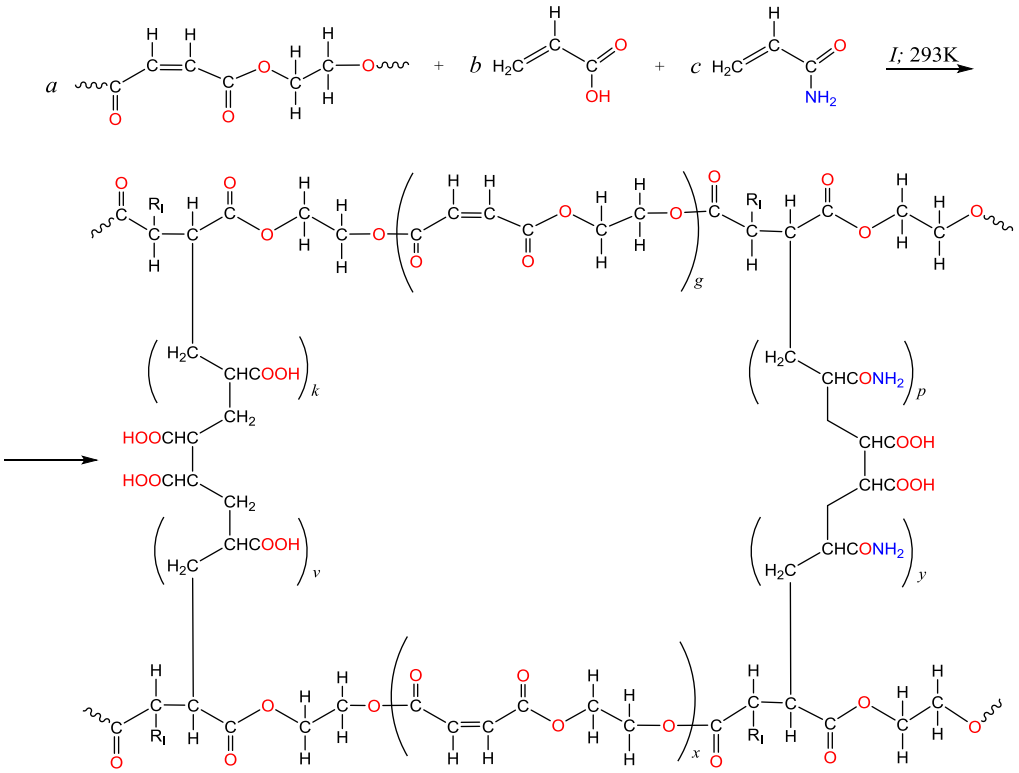

Figure 1. Terpolymer structural fragments of the p-EGM–AA–AAm

The synthesized terpolymers were then washed with dioxane and dried in an oven at T = 293 K until a constant mass was achieved. The yield of terpolymers is shown in Table 2. Using HPLC analysis of the mother liquors of the cured products in dioxane, the actual monomer content was found to correspond to the theoretical content. The results are also shown in Table 2. Determining the actual composition ensures correct interpretation of the differences between the synthesized gels, which are due to the different compositions of the initial reaction mixture.

Table 2

Dependence of terpolymers composition and other of their parameters on the composition of initial mixtures of p-EGM (M_1)–AA (M_2)–AAm (M_3)

Composition of the initial mixture, wt.%			Composition of the terpolymers, wt.%			Yield, %	Swelling degree (P), %
M_1	M_2	M_3	m_1	m_2	m_3		
15.12	70.29	14.59	13.9	72.2	13.9	90.4	2898
15.21	50.41	34.38	14.1	52.5	33.4	89.1	2114
15.15	34.86	49.99	15.4	35.8	48.8	88.7	1735

The data presented in Table 2 show that an increase in the acrylic acid content in the terpolymer leads to an increase in the degree of swelling from 1835 % (at the minimum AA content) to 2898 % (at its maximum value). Although AAm is also characterized by a high hydration capacity, its contribution is limited by local hydrogen interactions, which create predominantly compact hydrated regions.

Unlike AAm, AA forms regions with an increased concentration of negative charges in the network after partial dissociation. The accumulation of charge causes electrostatic repulsion between the anionic carboxylate groups within the polymer network, increasing the distance between the chains and leading to a significant expansion of the gel volume. At the same time, the resulting excess osmotic pressure promotes further water penetration into the porous structure and the formation of a powerful hydrate shell around the ionogenic fragments.

Thus, the main factor in the increase in the degree of swelling is the polyelectrolyte effect of AA, which provides significantly stronger osmotic swelling compared to the neutral amide groups of AAm [17].

IR spectroscopic analysis of dried samples allowed us to evaluate the degree of completion of the terpolymerization process. The corresponding IR spectra of the initial p-EGM and terpolymers with compositions of 13.9:72.2:13.9 wt.% and 15.4:35.8:48.8 wt.% are shown in Figure 2.

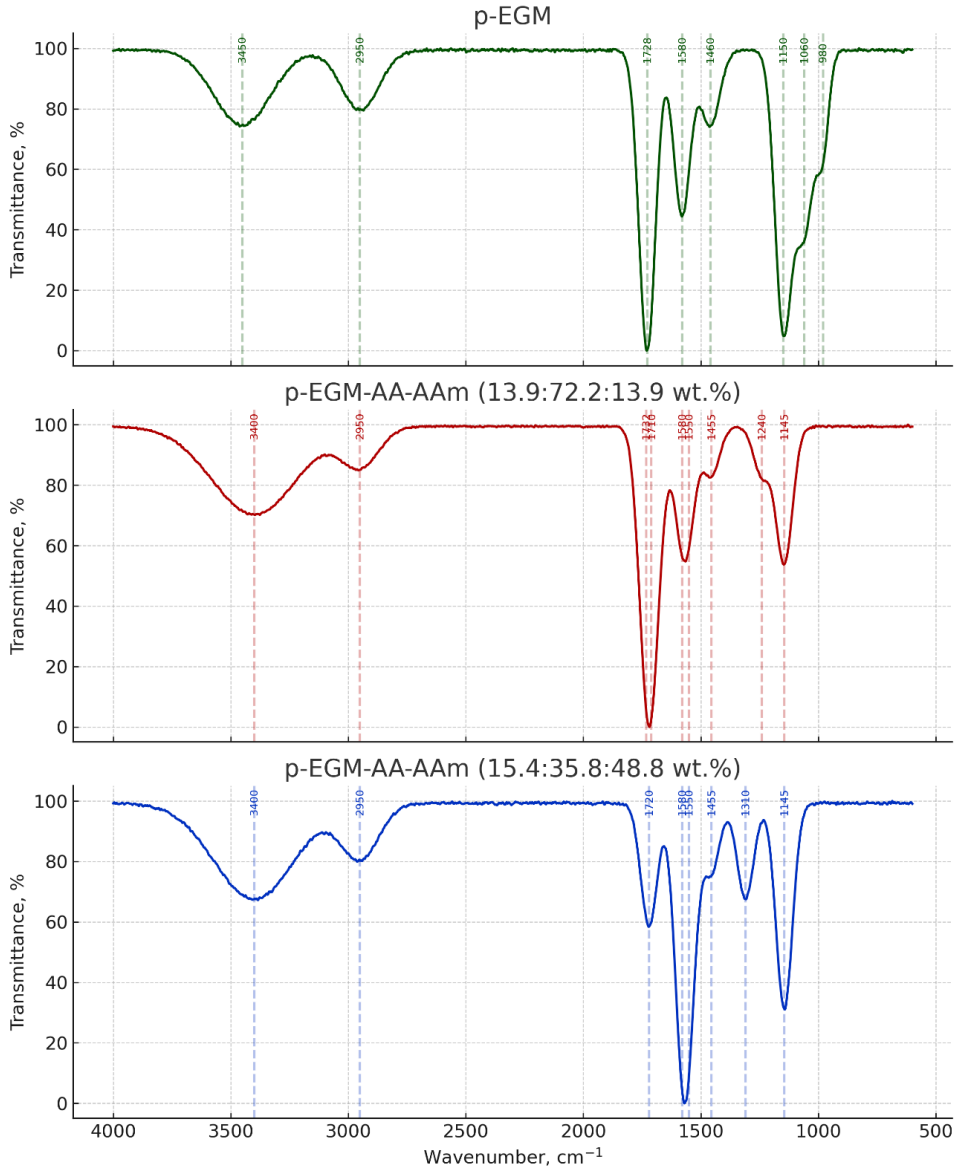

Figure 2. IR spectra of the initial p-EGM and p-EGM–AA–AAm terpolymers

The IR spectra of the initial p-EGM and p-EGM–AA–AAm terpolymers of various compositions show a characteristic set of bands confirming the formation of the corresponding structures. Thus, for the initial p-EGM, an intense band of valence vibrations of the carbonyl group of ester fragments is observed at 1725–1730 cm^{-1}, as well as a characteristic peak of unsaturated –C=C bonds of maleate units in the range of 1575–1590 cm^{-1}. The bands of $–CH_2$ deformation vibrations appear in the range 1455–1465 cm^{-1}, while the intense bands in the region 1140–1160 cm^{-1} correspond to the vibrations of the –C–O–C– polyester chain.

When containing a significant amount of AA (terpolymer p-EGM–AA–AAm with a composition of 13.9:72.2:13.9 wt.%), a broad absorption band appears in the spectrum in the 3100–3600 cm^{-1} region, caused by the superposition of the bands of the –OH carboxyl groups and hydrogen-bonded fragments. An important feature is the strengthening of the carboxyl vibration band –COOH at 1710–1715 cm^{-1}, the intensity of which exceeds that of the initial p-EGM and indicates an increase in the proportion of acrylic acid in the structure. The band of unsaturated double bonds at 1575–1585 cm^{-1} is preserved but noticeably decreases in intensity, which is characteristic of the partial conversion of –C=C bonds during terpolymerization.

In the terpolymer with a higher AAm content (p-EGM–AA–AAm composition 15.4:35.8:48.8 wt.%), further redistribution of band intensities is observed. A pronounced amide band appears in the spectrum at 1550–1555 cm^{-1}, as well as a band of amide vibrations in the region of 1305–1315 cm^{-1}. These bands become dominant, which is consistent with an increase in the proportion of amide fragments. Broad absorption in the 3200–3400 cm^{-1} region indicates the contribution of –NH amide groups, which form stable hydrogen bonds in the polymer structure. The –C=O band of ester groups shifts to 1720–1725 cm^{-1} and decreases slightly in intensity due to the dilution of polyester links with acrylamide (Figure 2).

Thus, a significant decrease in the intensity of the bands corresponding to the vibrations of unsaturated double –C=C bonds indicated a high degree of radical terpolymerization. The spectra showed characteristic bands of carboxyl, amide, and ether groups, confirming the presence of all functional fragments involved in the formation of a three-dimensional network. In samples with an increased AA content, an intensification of the carboxyl bands was observed, which corresponded to an increased number of ionogenic centres and a more pronounced polyelectrolyte character of the polymer network.

Further, by analyzing the cured samples based on p-EGM with AA and AAm, their densities and volume shrinkage index were determined, which for gel materials should not exceed 15 %.

The density of the cured products was measured by the hydrostatic method. Based on the results of the densities of the initial solutions and cured samples, the total volume shrinkage was calculated [21]. The results are presented in Table 3.

Table 3

Dependence of terpolymers properties on mass composition of p-EGM–AA–AAm, PB + DMA (1 % + 0.15 %), *T* = 293 K

Composition of initial mixture, wt.%			Density of the dried sample (ρ_d), g/cm^3	Volume shrinkage, %	Density of the swollen sample (ρ_s), g/cm^3
p-EGM	AA	AAm			
13.9	72.2	13.9	0.9128±0.0456	13.5	1.0254±0.0513
14.1	52.5	33.4	0.9512±0.0476	11.8	1.0361±0.0518
15.4	35.8	48.8	0.9841±0.0492	10.5	1.0408±0.0520

Based on the results obtained, it can be concluded that the density of the cured samples decreased relative to the initial solutions, which reflected the formation of internal porous volume. It should be noted that samples with an increased AA content were characterized by lower density (ρ_d = 0.9841 g/cm^3), which reflected the formation of a more sparse polymer network with increased internal volume and a higher degree of hydration. Table 3 also shows the densities of the synthesized gel samples after 24 hours of immersion in water. Considering that with an increase in the AAm content, the polymer fraction in the swollen gel volume is higher, this contributes to an increase in the density value of the studied sample p-EGM–AA–AAm with a composition of 15.4:35.8:48.8 wt.%.

Next, in order to establish the influence of external factors on the behavior of the studied hydrogels, studies were conducted on the effect of pH and temperature on them. When evaluating the prospects for the use of polymer gels as a basis for gel bandages and plasters, it is necessary to take into account conditions that are as close as possible to physiological ones. Thus, human skin and subcutaneous tissues are characterised by a slightly acidic surface reaction (pH 4.5–5.5) due to the lipid barrier and the presence of weak organic acids. When the skin is damaged, the pH shifts to neutral and slightly alkaline values (pH 6.0–8.0) due to the release of interstitial fluid and exudate containing proteins and salts.

The pH range of 4–8 covers all typical conditions of contact between the material and the skin and wound surface — from healthy epidermis to inflamed or infected tissues. More acidic (pH < 4) and more alkaline (pH > 8.5) conditions do not occur in physiological practice and can cause protein denaturation and destruction of the skin's barrier function, so they were not considered in this study.

The study of the degree of swelling of 0.5 g gel samples (Figure 3) in the pH range of 4–8 revealed a significant sensitivity of the structure to the acidity of the environment. When the pH was reduced to 4.0–5.5, gel compression (collapse) was observed, accompanied by a decrease in its volume and moisture content. This is due to the protonation of carboxyl groups, which reduces the charge repulsion between polymer chains and causes the network to compact [17]. This behavior is consistent with the acid–base properties of acrylic acid (pKa ≈ 4.25), which governs the degree of ionization of the carboxyl groups within the studied pH range. At pH values below the pKa, the –COOH groups remain predominantly protonated, resulting in reduced electrostatic repulsion and contraction of the polymer network. Conversely, at pH values above the pKa, progressive dissociation of the carboxyl groups occurs, leading to increased charge density and enhanced swelling of the hydrogel. This behavior may be advantageous for potential wound dressing applications, since in the acidic environment of healthy skin, the material retains its shape, does not over-moisten the surface and provides a barrier function.

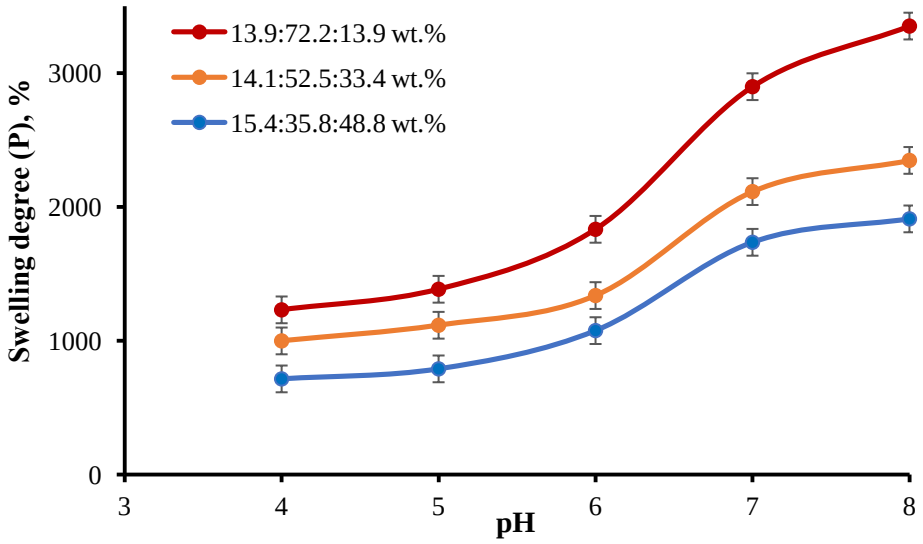

Figure 3. The influence of pH on the swelling of p-EGM–AA–AAm terpolymers

In the acidic range (pH 5–6), the carboxyl groups remained predominantly undissociated, the network remained compact, the internal porosity was minimal, and the degree of swelling was low. When the pH was increased to neutral and slightly alkaline values (pH 7–8), the carboxyl groups dissociated and negative charges accumulated, causing electrostatic repulsion between the macromolecules within the network. This led to its expansion and increase in volume, tending to minimize the free energy of the system, and, accordingly, to an increase in the sorption capacity of the material. For the samples analyzed, the degree of swelling at pH 8.0 reached its maximum value. This effect can be useful when the dressing comes into contact with wound exudate, which usually has a slightly alkaline reaction: in this case, the gel will actively absorb excess moisture, preventing tissue maceration.

It is also worth noting that the strongest increase in the degree of swelling was recorded in samples with a high AA content, where the proportion of ionogenic groups was significant. At the same time, analysing the dynamics of swelling of the analyzed gels, it is possible to conclude that water sorption is a two-stage process. Thus, in the first stage, large pores are quickly filled. The second stage consists of a slower rearrangement of the dense segments of the network. It is worth noting that in samples with a high AA content, the process of reaching equilibrium was faster, which indicated high structural fluctuation mobility. A slight acidification of the solution (pH ~6) was also observed during prolonged exposure of samples with a high AA content, caused by the release of some undissociated carboxyl groups.

Further investigation of the effect of temperature (35–39 °C) on the synthesized gels revealed a pronounced thermosensitive response, manifested in the form of a sharp, abrupt collapse (Figure 4). In particular, when the temperature was raised to ~37–38 °C, a partial collapse of the gel structure was observed, accompanied by intense water release from the polymer network. This effect is associated with a disturbance in the equilibrium between hydrophilic interactions and the internal cohesive forces of the polymer chains:

when heated, some of the hydrogen bonds are broken, the thickness of the hydrate shell decreases, which leads to a decrease in the volume of the gel and an increase in the proportion of hydrophobic interactions.

After the temperature was lowered, the structure of the gels was partially restored, but there was no complete return to the initial state. This is explained by the relaxation of the chains and partial fixation of new configurations during heating, as well as the possible redistribution of interchain bonds. The observed temperature memory effect indicates a shallow but significant redistribution of cross-link density in local areas of the gel.

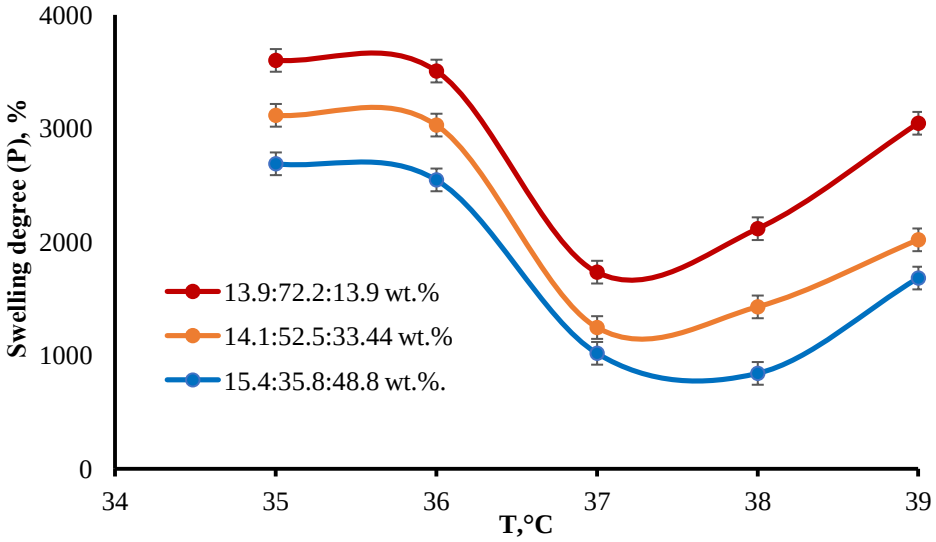

Figure 4. The influence of temperature on the swelling of p-EGM–AA–AAm terpolymers

Thus, gels with a high AA content (Figure 4) demonstrated a particularly strong thermal response. This is due to their polyelectrolyte nature: when heated, the degree of ionization of carboxyl groups decreases, reducing the electrostatic repulsion between polar fragments, which contributes to collapse. In addition, large hydrate shells around –COOH fragments are more sensitive to temperature changes, which increases the rate of dehydration and leads to a more pronounced change in volume.

An additional factor that enhances thermosensitivity is the difference in the mechanical flexibility of reactive segments: more mobile chains in gels with a high AA content are more easily rearranged under the influence of temperature, which leads to a more pronounced volume transition. At the same time, systems with a high AAm content retain residual hydration when heated due to the presence of amide groups, which makes their thermal response less pronounced [6, 14]. Thus, the thermosensitivity of the gels under study is the result of a complex combination of hydration, ionic interactions, chain configurational mobility, and local crosslink density. These features are particularly important for the use of materials as gel dressings and thermosensitive delivery systems: controlled moisture release upon heating helps maintain optimal wound surface hydration, and partial volume transition can promote prolonged drug release.

Subsequently, scanning electron microscopy (SEM) examination (Figure 5) of the structure of the synthesized hydrogels revealed significant differences in the morphology of the samples depending on their composition. An increase in AA content (Figure 5*a*) contributed to the formation of a looser, porous structure with well-defined channels and local cavities of various sizes. This structure is characterized by increased pore space openness, which facilitated water penetration and accelerated the swelling process. The presence of partially branched pore clusters also indicates less dense packing of chains during the formation of the polymer network. In contrast, the gel with an increased AAm content of ~50 wt.% (Figure 5*b*) is characterized by a more compact structure with fewer large pores. The SEM image of this sample (Figure 5*b*) shows small, isolated pores without a pronounced channel system, and the structure itself appears denser. This indicates a tighter packing of macromolecules and a higher local cross-link density, which limits the inflow and retention of water in the material volume and leads to a decrease in the degree of swelling.

The morphological data obtained are consistent with the results of studies of sorption characteristics: loose structures with a large number of macro- and mesopores demonstrated higher water absorption capacity, while compact structures with a predominance of micropores provided limited swelling. Thus, the identi-

fied relationship between the chemical composition of terpolymers and the structure of the three-dimensional polymer network allows for targeted regulation of the morphology, porosity, and functional properties of hydrogels by varying the ratio of AA and AAm.

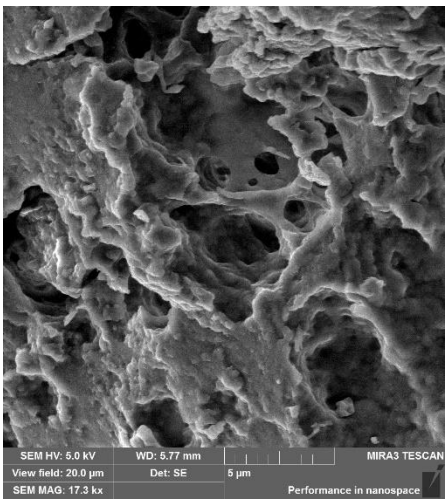

p-EGM–AA–AAm (13.9:72.2:13.9 wt.%)

a

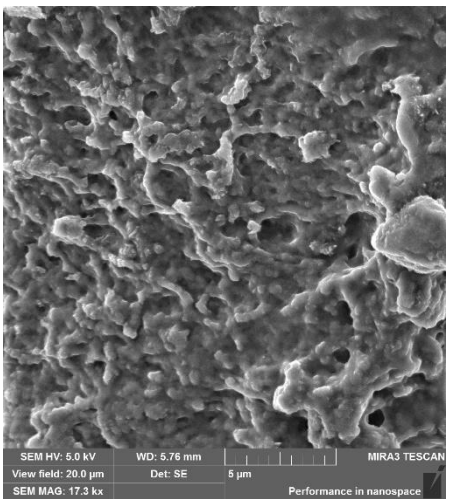

p-EGM–AA–AAm (15.4:35.8:48.8 wt.%)

b

Figure 5. SEM-images of the p-EGM–AA–AAm terpolymers

It is worth noting that the observed differences may be related to the peculiarities of the terpolymerization mechanism. Thus, AA, with its strong hydrophilicity and ionization ability, contributes to the formation of a more sparse three-dimensional network, while AAm, on the contrary, forms smoother and more densely packed structures due to amide groups capable of multiple interchain interactions. These results highlight the key role of monomer composition in the formation of the final morphology and allow us to predict the operational properties of the resulting gels in real-world conditions [14].

Furthermore, TG analysis data showed that the thermal decomposition of the studied hydrogels proceeds in two main stages. The first stage corresponds to the removal of weakly bound and partially adsorbed water. In this section (Figure 6), samples with a higher AA content showed a more pronounced peak in mass loss, which is associated with the increased hydrating ability of the polyelectrolyte network and the large number of ionogenic groups that retain water.

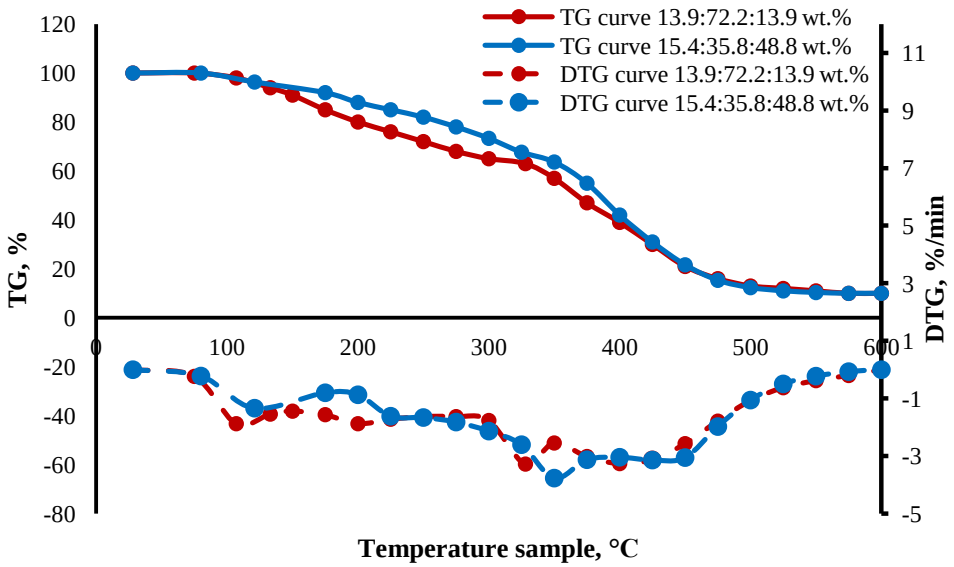

Figure 6. TG-analysis of the p-EGM–AA–AAm terpolymers

The decomposition onset temperature depended significantly on the chemical composition of the terpolymers. For the p-EGM–AA–AAm composition of 13.9:72.2:13.9 wt.%, decomposition began at ~107 °C, while the sample with a composition of 15.4:35.8:48.8 wt.% showed a higher heat distortion temperature of ~121 °C. This behavior may be attributed to differences in intermolecular interactions and network organization associated with the monomer composition.

The second stage, corresponding to the destruction of the organic polymer backbone, was also characterized by a shift in the maximum decomposition temperature. For the p-EGM–AA–AAm terpolymer with a composition of 13.9:72. 2:13.9 wt.%, the maximum decomposition occurred at ~328 °C, while for the composition with a ratio of 15.4:35.8:48.8 wt.%, it shifted to a higher temperature range of ~348 °C, confirming the more thermally stable and rigid structure of the polymer with an increase in AAm content.

Complete carbonization of the samples was completed at ~585~590 °C, after which the remaining inorganic residue was about 7 % for the system with a composition of 13.9:72.2:13.9 wt.% and about 9 % for the p-EGM–AA–AAm terpolymer with a composition of 15.4:35. 8:48.8 wt.%. The increase in residue also reflects a denser spatial network and a higher degree of structural organization of samples with increased AAm content.

Conclusions

The physicochemical properties of p-EGM–AA–AAm terpolymer hydrogels obtained by "cold" curing were systematically investigated. It was established that increasing the acrylic acid content promotes the formation of polyelectrolyte-type networks characterized by a high swelling degree (up to 2898 %), developed porosity, and pronounced sensitivity to external stimuli.

At the same time, acrylamide was shown to act primarily as a structure-forming non-ionogenic component that enhances network compactness and thermal stability through hydrogen-bond interactions. The synthesized materials exhibited controlled volumetric shrinkage not exceeding 10.5–13.5 %, indicating the formation of structurally stable three-dimensional networks.

The hydrogels demonstrated clear responsiveness in the physiologically relevant pH range of 4–8 and at temperatures of 35–39 °C, confirming their adaptive behavior under conditions close to biological environments. Among the studied compositions, the p-EGM–AA–AAm system with a ratio of ~15:70:15 wt.% showed the most balanced combination of swelling capacity, structural integrity, and porous morphology.

Overall, the obtained results indicate that the developed hydrogels may be considered promising candidates for potential use in sorption-active polymer matrices and hydrogel-based wound dressing systems.

Funding

This research is funded by the Science Committee of the Ministry of Science and Higher Education of the Republic of Kazakhstan (Grant No. AP23488036).

*Author Information**

**The authors' names are presented in the following order: First Name, Middle Name and Last Name*

Gulsym Kabayevna Burkeyeva — PhD, Associate Professor of Chemical Sciences, Karaganda National Research University named after Academician Ye.A. Buketov, Universitetskaya street, 28, 100024, Karaganda, Kazakhstan; e-mail: guls_b@mail.ru; https://orcid.org/0000-0003-1993-7648

Anna Konstantinovna Kovaleva (*corresponding author*) — PhD, Senior Researcher, Karaganda National Research University named after Academician Ye.A. Buketov, Universitetskaya street, 28, 100024, Karaganda, Kazakhstan; e-mail: cherry-girl1899@mail.ru; https://orcid.org/0000-0001-9758-648X

Nurken Meiramuly Zhumabek — 1st year Master student, Karaganda National Research University named after Academician Ye.A. Buketov, Universitetskaya street, 28, 100024, Karaganda, Kazakhstan; e-mail: zhumabek2003@list.ru; https://orcid.org/0009-0004-5318-0110

Nurlan Aleksandrovich Nukin — 1st year Master student, Karaganda National Research University named after Academician Ye.A. Buketov, Universitetskaya street, 28, 100024, Karaganda, Kazakhstan; e-mail: nukinnurlan3@gmail.com; https://orcid.org/0009-0004-5468-0846

Author Contributions

The manuscript was written through contributions of all authors. All authors have given approval to the final version of the manuscript. CRediT: **Gulsym Kabayevna Burkeyeva** validation, visualization & supervision, **Anna Konstantinovna Kovaleva** conceptualization, data curation, methodology, validation, visualization, writing-original draft, writing-review & editing, **Nurken Meiramuly Zhumabek** data curation & investigation; **Nurlan Aleksandrovich Nukin** data curation & investigation.

Acknowledgments

Authors thank Karaganda National Research University named after academician Ye.A. Buketov for access to library facilities.

Conflicts of Interest

The authors declare no conflict of interest.

References

1 Yu, P., Wei, L., Yang, Z., Liu, X., Ma, H., Zhao, J., Liu, L., Wang, L., Chen, R., & Cheng, Y. (2024). Hydrogel wound dressings accelerating healing process of wounds in movable parts. *International Journal of Molecular Sciences, 25*(12), 6610. https://doi.org/10.3390/ijms25126610

2 Demeter, M., Scărișoreanu, A., & Călina, I. (2023). State of the art of hydrogel wound dressings developed by ionizing radiation. *Gels, 9*(1), 55. https://doi.org/10.3390/gels9010055

3 Sulastri, E., Zubair, M.S., Lesmana, R., Mohammed, A.F.A., & Wathoni, N. (2021). Development and characterization of ulvan polysaccharides-based hydrogel films for potential wound dressing applications. *Drug Design, Development and Therapy, 15*, 4213–4226. https://doi.org/10.2147/DDDT.S331120

4 Ahmed, E.M. (2015). Hydrogel: Preparation, characterization, and applications: A review. *Journal of Advanced Research, 6*(2), 105–121. https://doi.org/10.1016/j.jare.2013.07.006

5 Boateng, J.S., Matthews, K.H., Stevens, H.N.E., & Eccleston, G.M. (2008). Wound healing dressings and drug delivery systems: A review. *Journal of Pharmaceutical Sciences, 97*(8), 2892–2923. https://doi.org/10.1002/jps.21210

6 Liang, Y., He, J., & Guo, B. (2021). Functional hydrogels as wound dressing to enhance wound healing. *ACS Nano, 15*(8), 12687–12722. https://doi.org/10.1021/acsnano.1c04206

7 Caló, E. & Khutoryanskiy, V.V. (2015). Biomedical applications of hydrogels: A review of patents and commercial products. *European Polymer Journal*, 65, 252–267. https://doi.org/10.1016/j.eurpolymj.2014.11.024

8 Koetting, M.C., Peters, J.T., Steichen, S.D., & Peppas, N.A. (2015). Stimulus-responsive hydrogels: Theory, modern advances, and applications. *Materials Science and Engineering: R: Reports*, 93, 1–49. https://doi.org/10.1016/j.mser.2015.04.001

9 Li, J. & Mooney, D.J. (2016). Designing hydrogels for controlled drug delivery. *Nature Reviews Materials*, 1, 16071. https://doi.org/10.1038/natrevmats.2016.71

10 Pan, Z., Ye, H. & Wu, D. (2021). Recent advances on polymeric hydrogels as wound dressings. *APL Bioengineering, 5*(1), 011504. https://doi.org/10.1063/5.0038364

11 Tavakoli, S. & Klar, A.S. (2020). Advanced hydrogels as wound dressings. *Biomolecules, 10*(8), 1169. https://doi.org/10.3390/biom10081169

12 Alberts, A., Bratu, A. G., Niculescu, A.-G., & Grumezescu, A. M. (2025). New Perspectives of Hydrogels in Chronic Wound Management. *Molecules, 30*(3), 686. https://doi.org/10.3390/molecules30030686

13 Liang, Y., Chen, B., Li, M., He, J., Yin, Z., & Guo, B. (2020). Injectable Antimicrobial Conductive Hydrogels for Wound Disinfection and Infectious Wound Healing. *Biomacromolecules, 21*(5), 1841–1852. https://doi.org/10.1021/acs.biomac.9b01732

14 Xu, Z., Shou, D., Cai, W., Li, J., Wu, D., Jiang, T., & Kong, Y. (2025). Dynamically self-degradable, injectable and self-healing 6-deoxy-6-arginine grafted chitosan hydrogels for wounds healing. *European Polymer Journal*, 233, 113986. https://doi.org/10.1016/j.eurpolymj.2025.113986

15 Kapusta, O., Jarosz, A., Stadnik, K., Giannakoudakis, D.A., Barczyński, B., & Barczak, M. (2023). Antimicrobial Natural Hydrogels in Biomedicine: Properties, Applications, and Challenges—A Concise Review. *International Journal of Molecular Sciences, 24*(3), Art. 2191. https://doi.org/10.3390/ijms24032191

16 Jaiswal, R., & Sherje, A.P. (2024). Recent advances in biopolymer-based smart hydrogel for wound healing. *Journal of Drug Delivery Science and Technology*, 99, 105990. https://doi.org/10.1016/j.jddst.2024.105990

17 Burkeyev, M.Z., Kovaleva, A.K., Burkeyeva, G.K., Tazhbayev, Y.M., & Plocek, J. (2020). Polypropylene Glycol Maleate Phthalate Terpolymerization with Acrylamide and Acrylic Acid. *Polymer Korea, 2*(44), 123–131. https://doi.org/10.7317/pk.2020.44.2.123

18 Burkeyev, M., Kudaibergen, G., Tazhbayev, Y., Burkeyeva, G., Omasheva, A., Yesentayeva, N., & Bolatbay, A. (2018). The number average and mass average molar masses of polyethylene (propylene) glycol fumarates. *Bulletin of the Karaganda University. "Chemistry" Series*, *90*(2), 17–22. https://doi.org/10.31489/2018ch2/17-22

19 Burkeev, M., Zhunissova, M., Tazhbayev, Y., Fomin, V., Sarsenbekova, A., Burkeyeva, G., Kazhmuratova, A., Zhumagalieva, T., Zhakupbekova, E., & Khamitova, T. (2022). Influence of RAFT Agent on the Mechanism of Copolymerization of Polypropylene Glycol Maleinate with Acrylic Acid. *Polymers*, *14*(9), 1884. https://doi.org/10.3390/polym14091884

20 Akhmetkarimova, Z.S., Kudaibergen, G.K., Kaukabaeva, G.K., Abeldenov, S.K., & Rysbek, A.B. (2023). Thiol-Ene Click Synthesis of Alginate Hydrogels Loaded with Silver Nanoparticles and Cefepime. *Eurasian Journal of Chemistry*, *28*(2(110)), 14–23. https://doi.org/10.31489/2959-0663/2-23-14

21 Burkeyeva, G.K., Kovaleva, A.K., Muslimova, D.M., Havlicek, D., Zhumabek, N.M., & Nukin, N.A. (2025). Investigation of Physical and Chemical Properties of Thermosetting Copolymers of Polyethylene Glycol Maleate with Acrylic Acid During their "Cold" Curing. *Eurasian Journal of Chemistry*, *30*, 2(118), 52–61. https://doi.org/10.31489/2959-0663/2-25-9

22 Singh, B. & Singh, J. (2021). Application of tragacanth gum and alginate in hydrogel wound dressings formed by radiation-induced copolymerization. *Carbohydrate Polymer Technologies and Applications*, 2, 100058. https://doi.org/10.1016/j.carpta.2021.100058

How to Cite: Kareem, D.W., & Ways, T.M. (2026). Comparative Development and Characterization of Itraconazole-Loaded Solid Lipid Nanoparticles Incorporating Myristic Acid and Pluronic F127 for Oral Delivery. *Eurasian Journal of Chemistry, 31, 1(121), 100–120.* https://doi.org/10.31489/2959-0663/1-26-11

Article

Received: 13 December 2025 | Revised: 03 March 2026 | Accepted: 10 March 2026 | Published online: 17 March 2026

UDC 541.1; 66.095.2

https://doi.org/10.31489/2959-0663/1-26-11

Darya Wahhab Kareem, Twana Mohammed M. Ways*

Department of Pharmaceutics, College of Pharmacy, University of Sulaimani, Sulaymaniyah, Iraq
*(*Corresponding author's e-mail: twana.mohammed@univsul.edu.iq)*

Comparative Development and Characterization of Itraconazole-Loaded Solid Lipid Nanoparticles Incorporating Myristic Acid and Pluronic F127 for Oral Delivery

This study developed itraconazole-loaded solid lipid nanoparticles (SLNs) to enhance the solubility of this poorly water-soluble antifungal drug and evaluate key physicochemical properties. SLNs were prepared using the microemulsion technique with solid lipids stearic acid, palmitic acid, and myristic acid, and surfactants Tween 80 and Pluronic F127. The synthesized SLNs were characterized using dynamic light scattering (DLS) and electrophoretic light scattering (ELS) for size and zeta potential determination, while transmission electron microscopy (TEM) and field emission scanning electron microscopy (FESEM) were employed to examine surface morphology. Furthermore, the structural and thermal properties of the formulation were analyzed via Fourier transform infrared (FTIR) spectroscopy, X-ray diffraction (XRD), and differential scanning calorimetry (DSC). Among the formulations, SLN3 (containing stearic acid–Pluronic F127) and SLN9 (containing myristic acid–Tween 80) exhibited the smallest particle sizes and lowest polydispersity indices. Encapsulation efficiency was 97.04 ± 0.004 % for SLN3 and 42.69 ± 0.02 % for SLN9, with drug loading capacities of 3 ± 0.1 % and 1.8 ± 0.17 %, and yields of 50.03 ± 3.55 % and 57.9 ± 6.6 %, respectively. Solubility of ITZ increased to 2900 µg/mL (SLN3) and 3369 µg/mL (SLN9). *In vitro* release studies demonstrated controlled and sustained drug release, with SLNs exhibiting formulation- and pH-dependent behavior; SLN3 provided more prolonged release under acidic conditions, whereas SLN9 showed relatively higher release at intestinal pH, reflecting differences in lipid chain length and surfactant type. These results indicate that the optimized SLNs improve ITZ solubility and exhibit favorable physicochemical characteristics, supporting their potential as oral delivery systems for poorly soluble antifungal agents.

Keywords: itraconazole, solid lipid nanoparticles, solubility enhancement, stearic acid, myristic acid, Pluronic F127, Tween 80, controlled drug release

Introduction

Itraconazole (ITZ) is a triazole antifungal agent with a broad spectrum of activity against a wide range of dermal and systemic fungal infections. It is commonly prescribed for both immunocompromised and non-immunocompromised patients and is often preferred in cases where amphotericin B therapy is contraindicated due to its comparatively favorable safety profile [1]. Despite its clinical efficacy, the therapeutic performance of ITZ following oral administration is limited by significant formulation-related challenges [2]. One major limitation of ITZ is its poor aqueous solubility, which results from its highly lipophilic nature. Accordingly, ITZ is classified as a Biopharmaceutics Classification System (BCS) class II drug, characterized by low solubility and high membrane permeability. This poor solubility leads to slow and incomplete dissolution in gastrointestinal fluids, contributing to low and highly variable oral bioavailability among patients. [3]. In addition to solubility-related issues, uncontrolled or rapid drug release from certain oral formulations may result in high peak plasma concentrations, which have been associated with concentration-dependent adverse effects, including hepatotoxicity, elevations in hepatic enzymes and cardiotoxicity. ITZ is a potent inhibitor of cytochrome P450 3A4 (CYP3A4), and concomitant use with other CYP3A4 substrates can lead to elevated plasma concentrations of co-administered drugs, significantly increasing the risk of serious toxicities including QT prolongation [4]. Thus, while enhancing solubility is necessary to improve oral absorption, excessive or rapid release of ITZ can increase the risk of systemic toxicity. Therefore, an optimal oral formulation should not only improve solubility and dissolution but also provide controlled drug release to maintain plasma concentrations within the therapeutic window [5]. Therefore, the development of novel delivery systems with features such as reduced particle size, protection of the drug from degradation, improved drug solubility and the ability to provide sustained drug release is essential for the successful administration of ITZ. Nanoparticulate drug delivery systems have emerged as promising approaches to overcome the limitations

associated with conventional formulations. Example includes solid lipid nanoparticles (SLNs), colloidal carriers with particle size ranging from 50–1000 nm, first developed at the beginning of 1990s [6]. SLNs-based formulations have since been investigated for several routes of administration, including parenteral, oral, ocular, pulmonary, and rectal [7]. SLNs have attracted considerable attention as a potential drug carrier as they offer many advantages compared to other carrier systems. Compared with polymeric nanoparticles, SLNs are generally prepared from physiological lipids, which are biodegradable and biocompatible, reducing concerns of long-term toxicity [8]. Unlike liposomes, SLNs exhibit greater physical stability and lower risk of rapid leakage of incorporated drug [9]. Compared with nanoemulsions, SLNs are typically composed of solid lipids (e.g., fatty acids, waxes, or triglycerides) stabilized with surfactants and co-surfactants. The solid lipid matrix can improve drug stability, which in some cases, enables sustained or controlled drug release [10]. Despite the advantages of SLNs, ITZ has not been comprehensively investigated in such formulations. Previous attempts have largely been limited to general SLN systems without systematic evaluation of lipid type and surfactant composition. Although previous studies focused on topical and ocular delivery of ITZ-loaded SLNs, their potential for oral delivery has not been explored [11]. In particular, there is a lack of detailed studies examining the effects of different long-chain fatty acids such as stearic acid, palmitic acid, and myristic acid as lipid matrices, in combination with surfactants like Tween 80 and Pluronic F127, on the physicochemical properties, the solubility of ITZ, and release behavior of ITZ-loaded SLNs. This gap limits the ability to optimize formulations for enhanced solubility and stability of ITZ-loaded SLNs. Although Mukherjee et al. [12] demonstrated the feasibility of encapsulating ITZ into SLNs using palmitic acid as the lipid matrix and a combination of Pluronic F127 and Tween 80 as surfactants, systematic studies exploring alternative lipid matrices and surfactant systems for ITZ-loaded nanoparticles remain limited. In this study, we report the formulation and characterization of ITZ-loaded SLNs prepared using stearic acid, palmitic acid, and myristic acid as lipid carriers, stabilized with Tween 80 and Pluronic F127. Stearic acid, palmitic acid, and myristic acid were selected as solid lipids based on their well-established safety, biocompatibility, and suitability for oral drug delivery [13]. These lipids are naturally occurring saturated fatty acids that are widely used as pharmaceutical excipients and are metabolized through normal lipid metabolic pathways [14]. The selected lipids possess melting points above physiological temperature, ensuring that the lipid matrix remains in the solid state after administration, which is essential for the structural integrity and controlled drug release behavior of SLNs. Additionally, their hydrophobic nature promotes efficient drug incorporation and contributes to high entrapment efficiency [15]. To the best of our knowledge, this is the first comprehensive study systematically comparing the influence of different lipid, surfactant and cosurfactant combinations on the physicochemical properties of the ITZ SLNs including the particle size, polydispersity index, zeta potential, entrapment efficiency, and in vitro drug release of ITZ-loaded SLNs. Additionally, although myristic acid offers a favorable melting point, biocompatibility, and the potential to form stable lipid matrices, its use as a lipid matrix in combination with Pluronic F127 as a nonionic surfactant in ITZ SLNs has not been reported previously. By addressing this gap, this study provides important insights into the rational design of lipid-based nanocarriers for enhancing the solubility, stability and controlled release behavior of ITZ.

Experimental

Materials

ITZ was purchased from Kemprotec Limited (UK). Stearic acid, palmitic acid, myristic acid, Pluronic F127 (MWt ≈ 12,600 g/mol) and Tween 80 were purchased from Sigma-Aldrich (UK). Dimethyl sulfoxide (DMSO) was purchased from BIOCHEM Chemopharma (France). All other chemicals were of analytical grade and were used as received.

Methods

Solubility of ITZ in Lipids

The solubility of ITZ in three lipids — stearic acid, palmitic acid, and myristic acid — was determined quantitatively using a lipid-addition method according to Kumar and Goindi [11] with some modifications. Briefly, 10 mg of pure ITZ was placed in a tube, and 200 mg of molten lipid was added under continuous stirring at 70–75 °C using a hotplate stirrer (IKA® RCT Basic, Germany). Additional portions of lipid were sequentially added with continuous stirring until the mixture became turbid, indicating saturation. The total weight of lipid required to completely solubilize ITZ was recorded. A fixed amount of ITZ (10 mg) was selected to allow comparative evaluation of the lipid solubilization capacity under standardized conditions. The

initial amount of molten lipid (200 mg) was chosen to ensure complete immersion and adequate mixing of the drug at elevated temperature. Additional lipid was incrementally added until turbidity was observed, indicating the solubility limit had been reached. Solubility was calculated based on the total mass of lipid required to dissolve the fixed amount of ITZ and was expressed as mg of drug per gram of lipid. All experiments were performed in triplicate to ensure reproducibility and accuracy.

Preparation of ITZ Loaded SLN

Blank and ITZ loaded SLNs were prepared by a microemulsion technique as described by Gasco (1997) [16] with some modifications. The composition of the formulations is shown in Table 2 and Table S1. Solid lipids (stearic acid, palmitic acid and myristic acid) were melted at 70–75 °C by placing the solid lipid in a beaker within a water bath. Then ITZ was added to the molten lipid and stirred using a magnetic stirrer at 800 rpm until the drug was dispersed in the molten lipid. Then, to prepare aqueous phase, the surfactant (Tween 80 or Pluronic F127) was added to 4 mL distilled water and stirred until completely dispersed or dissolved in distilled water at the same temperature as the lipid phase. Following the preparation of both phases, the hot aqueous phase was added to the hot lipid phase and stirred at 800 rpm until an optically transparent system (warm microemulsion) was obtained. The warm microemulsion was immediately dispersed in cold water (15 °C), under high-speed homogenization (Ultra-Turrax T25 basic, Germany) at 8000 rpm for 15 min to trigger the SLNs formation. The volume ratio of warm microemulsion to cold water was 1:20.

Table 1

Composition of ITZ loaded SLNs formulations

S. No.	ITZ, mg	Stearic acid, g	Palmitic acid, g	Myristic acid, g	Tween 80, %	Pluronic F127, %	Ethanol, mL	Distilled water, mL
SLN 1	25	1			1			4
SLN 2	25	1			1.5			4
SLN 3	25	1				1		4
SLN 4	25	1				1.5		4
SLN 5	25		1		1			4
SLN 6	25		1		1.5			4
SLN 7	25		1			1		4
SLN 8	25		1			1.5		4
SLN 9	25			1	1			4
SLN10	25			1	1.5			4
SLN11	25			1		1		4
SLN12	25			1		1.5		4
SLN13	25	1			1.5		0.5	4
SLN14	25		1		1.5		0.5	4
SLN15	25			1	1.5		0.5	4
SLN16	12.5	1			1.5		0.5	4
SLN17	25	0.5		0.5	1.5			4

Turbidimetric Analysis

The turbidity of the ITZ-SLNs dispersions was measured at room temperature using a UV/visible spectrophotometer (PharmaSpec, UV-1700, Japan) at a maximum wavelength (λ_{max}) of 600 nm. The turbidity was determined from the absorbance of the dispersions, with distilled water was used as a blank.

pH Analysis

The pH of all ITZ-SLNs formulations was measured using a calibrated digital pH meter (Eutech instrument pH 700, Singapore). The electrode was directly immersed in each SLN dispersion, and the pH value was recorded upon stabilization. Measurements were performed at ambient temperature, and each formulation was assessed in triplicate.

Size, Size Distribution and Zeta Potential

A Zetasizer Nano ZS (Malvern Instruments Ltd., UK) was used to determine the particle size and size distribution of the SLNs by dynamic light scattering (DLS), and zeta potential by the electrophoretic light scattering (ELS). The SLNs dispersions were diluted with distilled water at a 1:100 ratio. Particle size meas-

urements were performed at a constant scattering angle of 90° and a controlled temperature of 25 °C. Each sample was analyzed in triplicate, with a 60-second equilibration period preceding measurement, utilizing 12 μL quartz cuvettes. The polydispersity index (PDI), indicating the measure of the distribution of nanoparticle population (size distribution), was also determined. Zeta potential measurements were conducted utilizing a disposable cell packed with carbon-coated electrodes. The electrophoretic mobility data were transformed into zeta potential utilizing the Smoluchowski model (Fκa = 1.5).

Effects of SLNs on ITZ Solubility

After preparing and evaluating all ITZ-SLN formulations, SLN3 and SLN9 were determined to be the optimum formula based on particle size and PDI data acquired using DLS. To evaluate the effect of SLN encapsulation on the aqueous solubility of ITZ, the solubility of the chosen formulations was measured using the shake-flask method.

An excess amount of pure ITZ and ITZ-loaded SLNs (SLN3 and SLN9) was individually introduced to 0.1 M simulated gastric fluid (SGF, pH 1.2; consisted of NaCl and HCl) and 0.1 M phosphate-buffered saline (PBS, pH 6.8; formulated from NaOH and KH_2PO_4). Each sample was made in three replicates. The suspensions were agitated continuously at 100 rpm for 48 hours at ambient temperature to achieve equilibrium. Following incubation, the mixtures were subjected to filtration through a 0.22 μm syringe filter to eliminate undissolved drug/particles. The filtrates were spectrophotometrically examined at a wavelength of 265 nm utilizing a UV-Visible spectrophotometer (PharmaSpec, UV-1700, Japan). The concentration of ITZ in each sample was determined using a standard calibration curve established in ethanol and distilled water, spanning a concentration range of 0.78–100 μg/mL.

Determination of Yield, Encapsulation Efficiency (EE), and Loading Capacity (LC)

To precipitate the SLNs and separate them from free ITZ, samples of the optimized formulations were centrifuged for 1 hour using a (Maanlab, HC 02R, Sweden, at 25 °C and 15,000 rpm). The resultant precipitates were collected, moved to a round-bottom flask with a thin neck, and then lyophilized using a Biobase BK-FD10P freeze dryer (China). The lyophilized SLNs were then collected, weighed and stored for further studies. Then the yield, encapsulation efficiency and drug loading capacity of the nanoparticles were calculated as follows:

The yield of the NPs was calculated using equation (1):

$$\text{Yield}\ (\%) = \frac{\text{Weight of dried SLNs obtained}}{\text{Total weight of drug+lipid+surfactant used}} \times 100\,\%, \tag{1}$$

After collecting the precipitated SLNs, the supernatant obtained from centrifugation (15,000 rpm, 1 hour, 25 °C) was analyzed spectrophotometrically using a UV/visible spectrophotometer at 265 nm (PharmaSpec, UV-1700, Japan) to quantify the amount of free ITZ based on a calibration curve prepared in ethanol/water (0.78–100 μg/mL). The encapsulated ITZ was then determined indirectly by subtracting the free drug in the supernatant from the total drug initially added. Encapsulation efficiency (EE%) and drug loading (DL%) were subsequently calculated using Equations (2) and (3).

$$\text{EE}\,(\%) = \frac{\text{Total drug-Free drug}}{\text{Total drug}} \times 100\,\%, \tag{2}$$

$$\text{DL}\ (\%) = \frac{\text{Amount of drug encapsulated}}{\text{Total weight of SLNs}} \times 100\,\%. \tag{3}$$

Fourier Transform Infrared (FTIR) Spectroscopy

FTIR spectroscopy was conducted using a Shimadzu FTIR-8400S spectrometer (Shimadzu Corporation, Japan). The analysis was performed on the pure ITZ, stearic acid, myristic acid, SLN3 and SLN9. The materials were mixed with potassium bromide (KBr) pellets using a mortar and pestle and then compressed using a hydraulic press to form a transparent pellet. The FTIR spectra were collected over the wavenumber range of 4000-400 cm^{-1}, using 3 scans with a resolution of 2 cm^{-1}.

Transmission Electron Microscopy (TEM)

TEM was used to examine the morphology of the ITZ-loaded SLNs at a 100 kV accelerating voltage using a transmission electron microscope (Carl Zess_EM1OC, Germany). One drop of SLN dispersions was applied on a copper grid coated with carbon and allowed to dry at room temperature for one minute. The

sample was then stained with uranyl acetate solution and left to air dry. Then, TEM imaging was conducted, and the particle size was measured from the TEM images using ImageJ 1.54 g software. The size distribution graphs were plotted using OriginPro software (version 2018 SR1, b9.51.195, OriginLab Corporation, Northampton, MA, USA).

Field Emission Scanning Electron Microscopy (FESEM)

The shape and surface texture of the SLNs were studied using a scanning electron microscope (TESCAN MIRA3 FESEM, Brno, Czech Republic). One drop of the optimized SLN dispersion was placed on an aluminum stub (TAAB Laboratories Equipment, Aldermaston, UK) utilizing a double-sided sticky tab (TAAB Laboratories Equipment) and, following drying, was vacuum-coated with gold–palladium in an argon atmosphere for 60 seconds. Imaging was conducted at an accelerating voltage of 15 kV, with magnifications of between 5000× and 135,000×, and a working distance of 4.91 mm.

Powder X-Ray Diffraction (PXRD)

The X-ray diffraction patterns for ITZ, stearic acid, myristic acid, SLN3 and SLN9 were recorded using an X-ray diffractometer (Bruker, Model No: D8 advance, Germany). The investigation was conducted using a diffractometer with a Cu Kα radiation source (λ = 1.5406 Å for Kα1 and λ = 1.5444 Å for Kα2), operating at 35 kV and 30 mA. The diffraction patterns were obtained between the 2θ range of 5° to 80°, with a step size of 0.02° and a scan speed of 411.2 seconds per step in continuous mode. The goniometer radius measured 240 mm, while the specimen length was kept at 10 mm. A fixed turning slit of 1.0° and a receiving slit of 0.1 mm were employed.

Differential Scanning Calorimetry (DSC)

The thermal characteristics of ITZ, stearic acid, myristic acid, SLN3 and SLN9 were determined using a DSC instrument (DSC TA, Q600, USA). Samples were crimped in a standard aluminum pan and heated from 40 to 400 °C at a heating rate 10 °C/min under constant purging of nitrogen at 20 mL/min.

Stability Study

Physical stability of the optimized ITZ-loaded SLNs was evaluated by assessing both the visual appearance of the nanoparticle formulation for the freshly prepared nanoparticles and those stored at room temperature (25 °C) for one month to detect any changes in physical appearance, such as color change or precipitation. In addition, the size and PDI of the optimized formulations were measured using DLS (Malvern Instruments, UK) for both the fresh and stored formulations to assess any potential changes in size distribution over time.

Drug Release Study

The in vitro drug release from free ITZ solution, and the freeze-dried SLN3 and SLN9 was performed using a dialysis membrane method. An amount of the freeze-dried SLN3 and SLN9 (66.6 mg and 111 mg, respectively) was dispersed in 2 mL of a 1:1 mixture of DMSO and 0.1 M simulated gastric fluid (SGF, pH 1.2) or 0.1 M phosphate-buffered saline (PBS, pH 6.8) containing 1 % v/v Tween 80, which was equivalent to 2 mg/mL of free ITZ solution. The nanoparticles dispersion was then placed in a cellulose dialysis membrane (MWCO 14 kDa, Membra-Cell, USA), which had been pre-soaked overnight in water and washed repeatedly with the release medium before use. The dialysis membrane was firmly tied at both ends using a clamp, and its center part was immersed in 40 mL of the release medium (1:1 DMSO and 0.1 M SGF, pH 1.2 or PBS, pH 6.8, with 1 % Tween 80), kept at 37 ± 1 °C under constant stirring at 100 rpm. At predetermined time intervals, 5 mL of the external dialysis medium was removed and replaced with an equal amount of fresh release medium to keep sink conditions. The concentration of ITZ in the collected samples was measured using UV-visible spectrophotometry at a maximum wavelength (λ_{max}) of 265 nm, based on a calibration curve constructed using a 3:1 ethanol: water mixture over the concentration range of 100 μg/mL to 0.78 μg/mL. An ITZ solution at 2 mg/mL in a liquid mixture of water and DMSO (1:3 v/v) was used as a reference. The experiment was performed in triplicate. The in vitro drug release patterns of solid lipid nanoparticles formulations were compared quantitatively using the similarity factor (f_2). The f_2 value is a logarithmic equivalent square root transformation of the sum of squared differences between two dissolution profiles, as specified by the following equation:

$$f_2 = 50 * \log\left\{\left[1+\frac{1}{n}\sum_{t=1}^{n}\left(R_t - T_t\right)^2\right]^{-0.5} * 100\right\}, \quad (4)$$

where n is the number of sampling time points; R_t is the cumulative percentage of drug released from the reference formulation at time t; and T_t is the cumulative percentage of drug released from the test formulation at the same time point. An f_2 value between 50 and 100 shows similarity between two release patterns, but values below 50 suggest dissimilarity [17].

Statistical Analysis

All tests were performed in triplicate, and the results are reported as mean ± standard deviation, which were calculated using Microsoft Excel software 2021 (version 2503). Statistical analysis was carried out with one-way ANOVA with post hoc Tukey test using IBM SPSS Statistics (version 25). When comparisons involved two independent groups, statistical differences were evaluated using an independent-samples *t*-test. A *p*-value of < 0.05 was considered statistically significant.

Ethical Approval

This study was performed according to the standard procedures and institutional guidelines, and the study protocol was reviewed and approved by the Ethics and Research Registration Committee at the College of Pharmacy, University of Sulaimani (approval number PH143-24, Kurdistan Region, Iraq).

Results and Discussion

Solubility of ITZ in Lipids

Lipid solubility is crucial in the development of lipid-based nanoparticles, especially for hydrophobic drugs like ITZ. Solubility of drug in lipid is one of the most important factors for determining drug loading capacity of the SLNs as well as influencing their release characteristics and bioavailability. Therefore, prior to the formulation of the nanoparticles, the solubility of ITZ in the selected lipids was determined. The results of the solubility studies are shown in Table 2.

Table 2

Solubility of pure ITZ in different solid lipids used to prepare the ITZ loaded SLNs
Data are expressed as mean ±SD, n=3

Lipids	Solubility (mg/g)
Stearic acid	8.72 ± 0.04
Palmitic acid	8.38 ± 0.28
Myristic acid	8.40 ± 0.36

ITZ exhibited comparable solubility in all tested lipids. Stearic acid showed a marginally higher solubilization capacity; however, the differences among the lipids were minimal, indicating a broadly similar affinity of ITZ toward saturated fatty acids with varying carbon chain lengths. Overall, all three lipids appear suitable for ITZ incorporation, with stearic acid offering a slight advantage. Previous research has shown that increased drug solubility in the lipid phase correlates with enhanced encapsulation efficiency and prolonged release capability [18].

Turbidimetric Analysis

The turbidity measurements were used as a rapid and indirect indicator of particle size, aggregation behavior, and dispersion stability of the ITZ-loaded SLNs. Changes in turbidity reflect differences in lipid chain length, surfactant type, and concentration, thereby supporting and complementing the particle size and dispersion stability of the SLNs. Figure 1 showed the results of the turbidity measurements for the prepared ITZ –loaded SLNs. Formulations contained stearic acid with Tween 80 (SLN1, SLN2) exhibited highest turbidity, which can be related to the stiff structure of long-chain lipids (C18) and limited stabilization, resulting in large aggregates [19]. The substitution with Pluronic F127 (in SLN3, SLN4) significantly diminished turbidity, indicating improved steric stability and the production of smaller particles [20]. Palmitic acid formulations exhibited moderate turbidity, with Pluronic F127 (SLN7, SLN8) exceeding Tween 80 (SLN5, SLN6). Myristic acid nanoparticles (SLN9–SLN12) demonstrated the least turbidity due to their shorter chain length (C14) and reduced melting point, which facilitated the formation of smaller, more translucent dispersions, especially in conjunction with Pluronic F127. The increase in surfactant quantity from 1 % to 1.5 % typically reduced turbidity in all formulations [21]. These data collectively indicate that shorter-chain lipids, high sur-

factant concentrations, and the application of Pluronic F127 improve particle dispersion and stability reflected by the reduced turbidity.

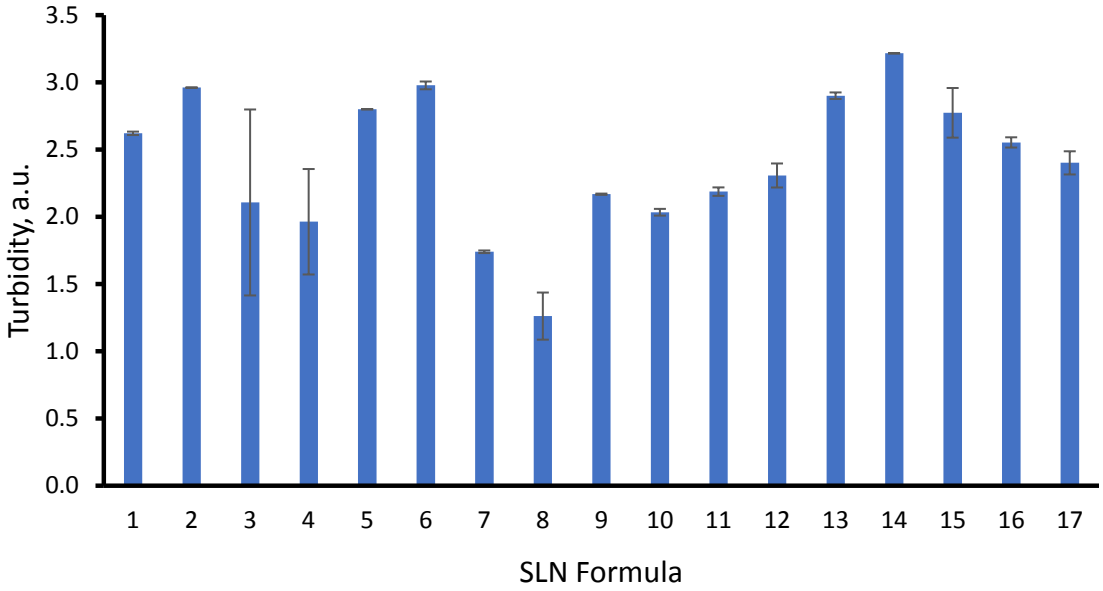

Figure 1. Turbidimetric analysis of ITZ-loaded solid lipid nanoparticle formulations

pH Analysis

Figure 2 showed the pH of the prepared ITZ-loaded SLN formulations. The measured pH values of the formulations varied from 4.7 to 6.1, indicating the impact of lipid and surfactant content. Formulations containing stearic acid (SLN1–SLN4) demonstrated slightly higher pH values. This finding corresponds with the decreased water solubility and increased hydrophobicity of stearic acid, resulting from its long-chain saturated fatty acid structure (C18), which reduces the ionization of its carboxyl groups into the aqueous phase [22]. Conversely, formulation containing myristic acid (C14) SLN9–SLN12 showed the lowest pH values (SLN11 and SLN12, below 4.8), likely due to the increased release of carboxylate ions caused by higher solubility and shorter chain length. Formulations including palmitic acid (C16; SLN5–SLN8) showed intermediate pH values in comparison with stearic and myristic acid-based systems, often varying between 5.2 and 5.8. The pH range indicates a moderate ionization of the carboxyl groups into carboxylate ions in aqueous media, which is associated with the chain length and solubility of palmitic acid in water. Palmitic acid, a medium-chain saturated fatty acid, exhibits lower solubility than myristic acid but higher solubility than stearic acid, resulting in moderate acidity of the dispersion [23].

The type and concentration of surfactants considerably influenced the pH. In all lipid matrices, formulations containing Tween 80 (SLN1, 2, 5, 6, 9, 10) consistently exhibited higher pH values relative to those containing Pluronic F127 (SLN3, 4, 7, 8, 11, 12). Tween 80, a non-ionic surfactant characterized by a polyoxyethylene structure, is recognized for sustaining a relatively neutral pH and facilitating emulsion stabilization without inducing acidification. Conversely, Pluronic F127, a block copolymer of polyethylene and polypropylene oxide, may facilitate the solubilization of lipid components, hereby promoting the ionization of fatty acid carboxyl groups into the aqueous phase and consequently lowering the pH [24]. Additionally, a slight concentration-dependent impact was also observed. In Tween 80 formulations, elevating the content from 1 % to 1.5 % slightly raised the pH, likely due to enhanced micelle formation that sequesters free fatty acids. In contrast, within Pluronic F127 systems, elevated concentrations sometimes resulted in reduced pH values, particularly when combined with myristic acid (SLN 12), which may adversely affect acid-labile drugs [25].

All formulations consistently maintained pH values within the appropriate physiological range for oral administration (pH 4.5–7), indicating their compatibility with the gastrointestinal tract and suggesting a reduced risk of mucosal irritation [22]. Furthermore, formulations with a pH around neutrality are seen as more stable, particularly for pH-sensitive pharmaceuticals such as ITZ, which demonstrates pH-dependent solubility and dissolution [26].

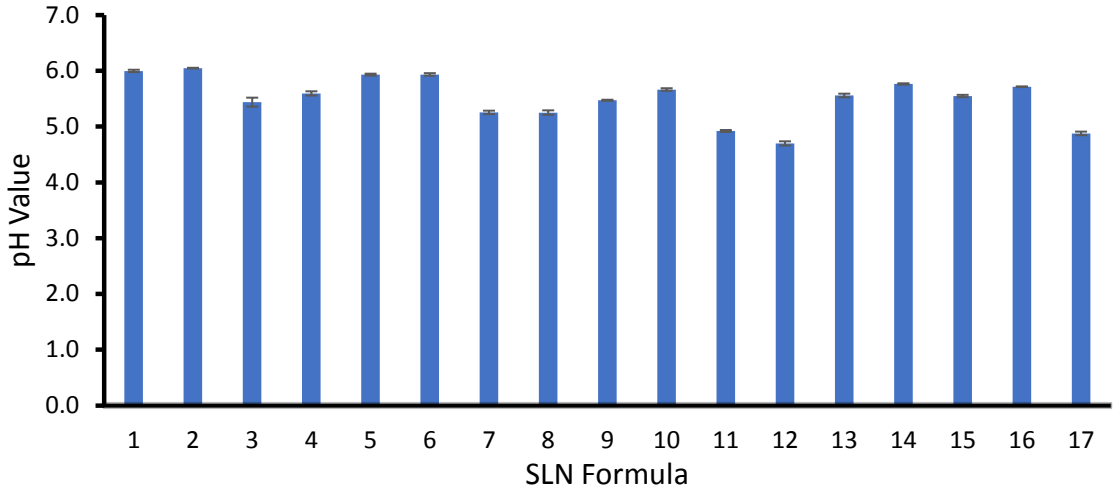

Figure 2. pH of the prepared ITZ-loaded solid lipid nanoparticle formulations

Particle Size, PDI, and Zeta Potential

The particle size and polydispersity of SLNs were significantly affected by the type of lipid, surfactant, and their concentrations. Table 3 shows the Z-average, PDI and zeta potential of the SLN formulations. Formulations based on stearic acid (SLN1–4) produced comparatively smaller particles (550–975 nm) with moderate uniformity, attributed to the rigid crystalline nature of stearic acid, leading to restricted molecular rearrangement during particle formation and thereby limiting particle coalescence and growth. Increased Tween 80 concentration (in SLN2) enhanced size homogeneity, whereas Pluronic F127 (SLN4) produced wider distributions, indicating diminished stabilization with stearic acid [26]. Palmitic acid formulations (SLN5–8) produced larger particles (up to approximately 1975 nm), with Tween 80 resulting in narrower peaks compared to Pluronic F127, especially at a concentration of 1.5 %. Myristic acid-containing SLNs (SLN9–12) exhibited enhanced emulsification with Tween 80 at 1.5 % (SLN10), whereas Pluronic systems maintained greater polydispersity [27]. Figure 3-Panel A shows stearic acid-based SLNs (SLN1–4) exhibited moderately uniform size distributions ranging from 550–975 nm. Figure 3-Panel B shows myristic acid-based SLNs (SLN9–12) displayed slightly broader but well-defined peaks between 600–1500 nm which highlights the influence of lipid type on particle size distribution, allowing direct comparison of lipid-dependent effects. The post-hoc analysis indicated substantial differences in the particle size of different lipid-based SLNs (p = 0.002). Independent samples t-tests indicated a significant effect of surfactant type on the particle size, with Tween 80- and Pluronic F127-stabilized systems having statistically different particle sizes (p = 0.042), indicating changes in interfacial adsorption behavior. SLN13 which contained stearic acid and ethanol remained significantly polydisperse, while SLN14 which contained palmitic acid and ethanol attained monomodal distributions, thereby indicating ethanol's efficacy in improving dispersion. Based on these data, the optimum formulations were determined primarily for having the smallest particle size and the lowest PDI of all formulations, showing excellent nanoscale features and size homogeneity. These formulations were thus regarded the best candidates for further physicochemical and performance evaluation.

Zeta potential analysis demonstrated consistently negative surface charges (−14.4 to −23.5 mV), indicating colloidal stability. Stearic acid-based SLNs demonstrated the greatest negative values, indicating enhanced surface packing and ionization. Tween 80 generally revealed a greater number of charged groups compared to Pluronic F127, hence augmenting surface charge in certain instances (e.g., SLN1 versus SLN3). Increasing surfactant concentration occasionally diminished zeta potential, presumably due to adsorption masking lipid head groups [28]. The addition of ethanol marginally reduced the magnitude of zeta potential, which is ascribed to alterations in interfacial organization. Formulations attaining zeta potentials of approximately −20 mV or lower, specifically stearic acid–Tween 80 and myristic acid–Pluronic F127 systems, exhibited advantageous electrostatic stabilization. Overall, although the absolute zeta potential values were moderate, the presence of non-ionic surfactants indicated that steric stabilization, in addition to electrostatic repulsion, helped to preserve colloidal stability. Surface-adsorbed surfactant chains create a hydrated barrier that reduces particle–particle interactions and helps stabilize nanoparticles, even when zeta potentials are

below ±30 mV. As a result, the observed stability of selected formulations is most likely due to a mixed electrostatic-steric stabilization mechanism, similar to that described for SLNs stabilized with Tween 80 or Pluronic surfactants [29].

Table 3

Physicochemical properties of the prepared ITZ loaded SLNs. Data are expressed as mean ±SD, *n* = 3

Formulation	Size (Z-average), nm	PDI	Zeta potential, mV
SLN1	591 ± 40	0.680 ± 0.120	–23.53 ± 0.85
SLN2	676 ± 7	0.497 ± 0.039	–16.83 ± 0.37
SLN3	550 ± 30	0.615 ± 0.075	–14.56 ± 0.41
SLN4	975 ± 52	0.759 ± 0.036	–21.40 ± 0.70
SLN5	1763 ± 350	0.922 ± 0.134	–20.46 ± 0.80
SLN6	1975 ± 66	0.606 ± 0.030	–16.96 ± 0.68
SLN7	1054 ± 33	0.522 ± 0.037	–15.36 ± 0.56
SLN8	955 ± 13	0.558 ± 0.075	–17.26 ± 0.37
SLN9	664 ± 78	0.634 ± 0.069	–20.20 ± 0.36
SLN10	1562 ± 161	0.705 ± 0.021	–19.76 ± 0.49
SLN11	1546 ± 71	0.705 ± 0.021	–21.76 ± 0.15
SLN12	1403 ± 35	0.490 ± 0.051	–21.46 ± 0.55
SLN13	939 ± 34	0.575 ± 0.030	–16.10 ± 0.26
SLN14	4008 ± 517	0.755 ± 0.147	–14.40 ± 0.43
SLN15	1748 ± 185	1 ± 0.000	–18.13 ± 0.41
SLN16	2745 ± 131	1 ± 0.000	–17.26 ± 0.57
SLN17	968 ± 42	0.371 ± 0.036	–17.50 ± 0.55

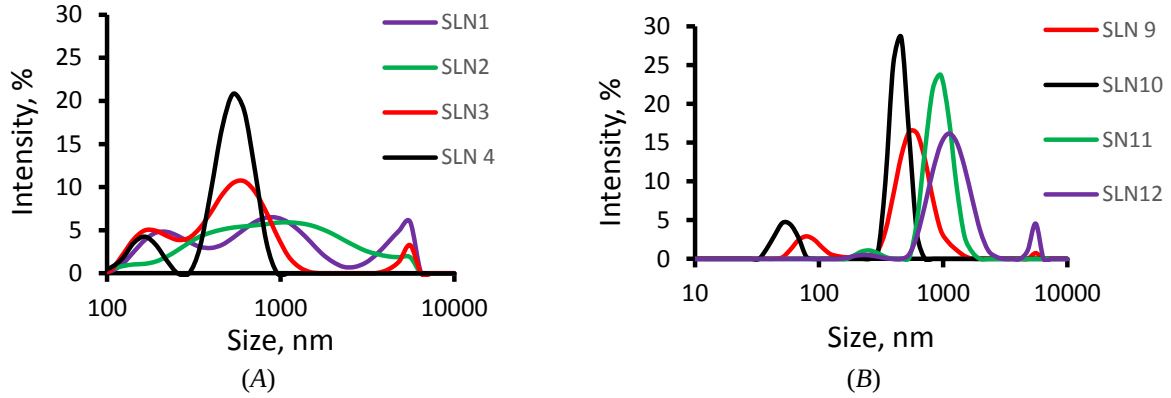

Figure 3. Dynamic light scattering size distribution curves of the ITZ loaded SLNs.
(*A*) SLN 1, 2, 3 and 4 were formulated with stearic acid as the lipid carrier;
(*B*) SLN 9, 10, 11, and 12 were formulated with myristic acid as the lipid carrier

Among the prepared ITZ-loaded SLN formulations, SLN3 and SLN9 were selected as the optimum formulations based on their smaller particle size as determined by DLS and the lowest PDI indicating uniform and stable nanoparticles. Notably, SLN9 incorporated myristic acid, an unexplored lipid for ITZ SLNs, highlighting its potential as a novel lipid matrix for enhancing formulation performance, warranting further in-depth evaluation as a promising oral delivery system for ITZ.

Effects of SLNs on ITZ Solubility

ITZ exhibits poor aqueous solubility, which is further influenced by its pH-dependent ionization behavior. As show in Figure 4, the shake-flask solubility study demonstrated extremely low solubility for pure ITZ at both pH 1.2 and pH 6.8, with concentrations remaining in the range of 67.067 µg/mL at pH 1.2 and 0.306 µg/mL at pH 6.8. The solubility was slightly higher under acidic conditions, consistent with ITZ being a weakly basic drug (pKa ≈ 3.7), which favors protonation and partial dissolution in gastric-like environments [30]. However, even at pH 1.2, the solubility of pure ITZ was negligible compared to its therapeutic

requirements, confirming the need for solubility-enhancing formulations. Encapsulation of ITZ into SLNs markedly enhanced its solubility at both tested pH conditions. At pH 1.2, SLN3 achieved solubility values close to 2900 µg/mL, while SLN9 reached 3369 µg/mL. At pH 6.8, the solubility improvement was even more remarkable compared to the pure drug. SLN3 achieved 10.59 µg/mL, and SLN9 showed the highest solubility 26.94 µg/mL. These enhancements reflect a multifactorial effect of lipid type and surfactant characteristics. The superior performance of SLN9 over SLN3 may be attributed to the formulation differences which are the lipid chain length; Myristic acid (C14) in SLN9 possesses a shorter hydrocarbon chain than stearic acid (C18) used in SLN3. Shorter-chain fatty acids generally form less-ordered crystalline lattices with lower melting points, enhancing solubilization of lipophilic drugs within the lipid matrix [31]. Tween 80 in SLN9 is a nonionic surfactant with a high hydrophilic-lipophilic balance (HLB ≈ 15), facilitating stronger interfacial stabilization and promotes solubilization of poorly water-soluble drugs. In contrast, Pluronic F127, a block copolymer, often stabilizes particles through steric mechanisms but may provide lower solubilization capacity in the aqueous phase [11]. These differences likely explain the higher solubility observed for SLN9 at both acidic and near-physiological pH.

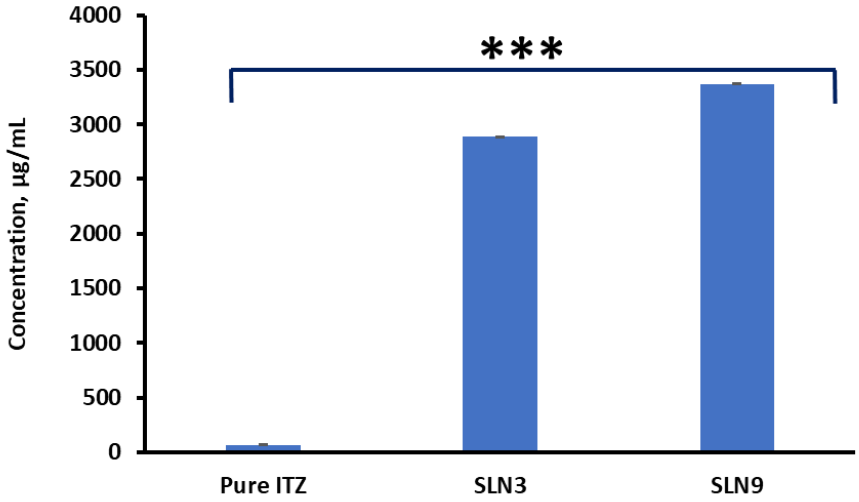

(*A*)

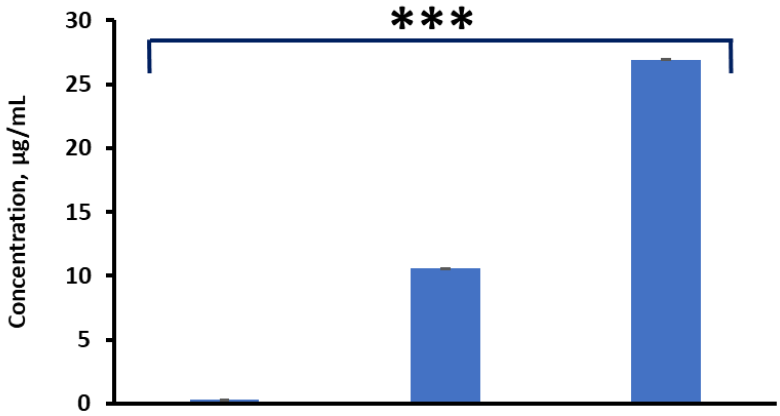

(*B*)

Figure 4. Saturation solubility of ITZ in its pure form as well as in SLN formulations (SLN3 and SLN9) (*A*) in simulated gastric fluid (pH 1.2) and (*B*) in phosphate-buffered saline (pH 6.8).
*** indicates statistically significant difference in solubility ($p < 0.001$). Statistically significant differences were observed between pure ITZ and SLN3, pure ITZ and SLN9, as well as between SLN3 and SLN9

Determination of Yield, Encapsulation Efficiency (EE), and Loading Capacity (LC)

The lyophilized SLNs appeared as a fine, white powder with a slightly fluffy texture, with no visible signs of aggregation or caking immediately after freeze-drying, suggesting good preservation of particle integrity. Upon reconstitution in simulated gastric fluid (pH 1.2) and phosphate-buffered saline (pH 6.8), the powders readily dispersed, yielding suspensions with a uniform and colloidally stable appearance. The yield of the freeze-dried SLNs was modest, with SLN9 (57.9 ± 6.6 %) indicating some higher recovery than SLN3 (50.03 ± 3.55 %), likely attributable to variations in lipid and surfactant composition influencing particle aggregation and collection. SLN3 had a markedly higher encapsulation efficiency (97.04 ± 0.004 %) compared to SLN9 (42.69 ± 0.02 %), indicating enhanced drug encapsulating capability. This can be due to the superior compatibility of ITZ with stearic acid and the denser lipid matrix in SLN3. Additionally, SLN3 exhibited superior drug loading (3 ± 0.1 %) compared to SLN9 (1.8 ± 0.17 %), underscoring its potential as a more effective drug delivery system for poorly water-soluble drugs. These findings correlate with prior studies indicating that lipid type and surfactant concentration significantly affect EE and LC [32].

FTIR Spectroscopy

FTIR spectroscopy was utilized to examine possible interactions between ITZ and solid lipids (stearic acid, myristic acid) in SLN3 and SLN9 formulations. As shown in Figure 5, pure ITZ displayed distinct peaks at 3120 cm^{-1} (aromatic C–H stretching), 2970 cm^{-1} (aliphatic C–H stretching), 1700 cm^{-1} (C=O stretching), 1600 cm^{-1} and 1500 cm^{-1} (aromatic C=C stretching), along with a pronounced band near 1045 cm^{-1} attributed to C–O stretching. The observed bands correlate with previously documented FTIR spectra of ITZ, signifying its stable chemical structure [33].

Stearic acid (SA) and myristic acid (MA) exhibited significant peaks at 2850–2920 cm^{-1}, indicative of symmetric and asymmetric C–H stretching vibrations, along with a distinct peak at approximately 1700 cm^{-1}, corresponding to the C=O stretching of carboxylic acid. These characteristics are indicative of long-chain saturated fatty acids, consistent with prior research [34]. The SLN3 formulation, comprising stearic acid and Pluronic F127, preserved the significant C–H stretching peaks at 2850 and 2920 cm^{-1}, accompanied by a considerable expansion of the O–H stretching area (~3000–3500 cm^{-1}), suggesting potential hydrogen bonding. The C=O peak exhibited a modest shift and diminished intensity, indicating interaction between ITZ and the lipid matrix [34]. Likewise, SLN9 (composed of myristic acid and Tween 80) exhibited retained C–H and C=O peaks of the lipid; however, the ITZ peaks at 1600–1500 cm^{-1} and 1045 cm^{-1} were slightly reduced. This indicates that ITZ was molecularly diffused within the lipid matrix, resulting in an altered crystalline structure, as evidenced by the reduced intensity of typical ITZ peaks [35].

The lack of significant ITZ-specific peaks in the SLN spectra, along with the observation of shifted or widened bands, suggests possible encapsulation and molecular interaction between the drug and lipids. The alteration or absence of specific ITZ peaks during the formulation of SLNs has been documented by others as a sign of effective drug entrapment and conversion from crystalline to amorphous state [36].

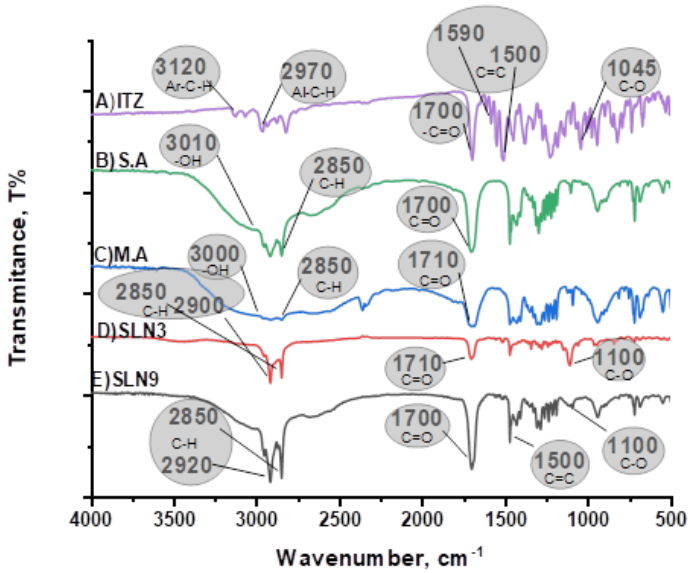

Figure 5. FTIR spectra for ITZ, stearic acid (S.A), myristic acid (M.A), SLN3 and SLN9

Transmission Electron Microscopy (TEM)

Transmission Electron Microscopy (TEM) was utilized to investigate the internal structure and morphology of the optimized SLN3 and SLN9 formulations. The TEM micrographs of ITZ-loaded SLNs (SLN3 and SLN9) (Figure 6) reveal discrete nanoparticles with a predominantly spherical to quasi-spherical morphology. Individual SLNs appear as relatively light, rounded features, consistent with the expected morphology of lipid-based nanoparticles. The darker contrast regions observed in the images do not represent the morphology of single nanoparticles; instead, they arise from overlapping particles and localized thickening of the lipid matrix during sample deposition and drying on the TEM grid. Such contrast variations are inherent to TEM imaging of soft lipid nanocarriers and reflect differences in electron density rather than particle irregularity [37].

The mean particle size detected using TEM (Figure 7 and 8) were 102 nm and 244 nm for SLN3 and SLN9, respectively and was slightly smaller than those derived from DLS measurements. The discrepancy between particle sizes determined by DLS and TEM should be interpreted in light of the fundamentally different physical principles governing these techniques [38]. DLS provides an ensemble-averaged, intensity-weighted hydrodynamic diameter, which is highly sensitive to polydispersity, minor populations of larger particles, transient aggregation, concentration-dependent diffusion, and electrostatic double-layer effects. In contrast, TEM yields number-based, projection-dependent particle dimensions obtained under dry-state and high-vacuum conditions, which may underestimate soft, hydrated or low-density surface structures [39]. Furthermore, particle shape anisotropy, contrast limitations, and sample-preparation artefacts can further amplify apparent size mismatches. As emphasized by Filippov et al. [39], substantial DLS–TEM size discrepancies arise primarily from methodological bias rather than experimental inconsistency, and therefore the observed size difference in the present study is consistent with the expected ensemble-scattering nature of DLS compared with the single-particle visualization of TEM.

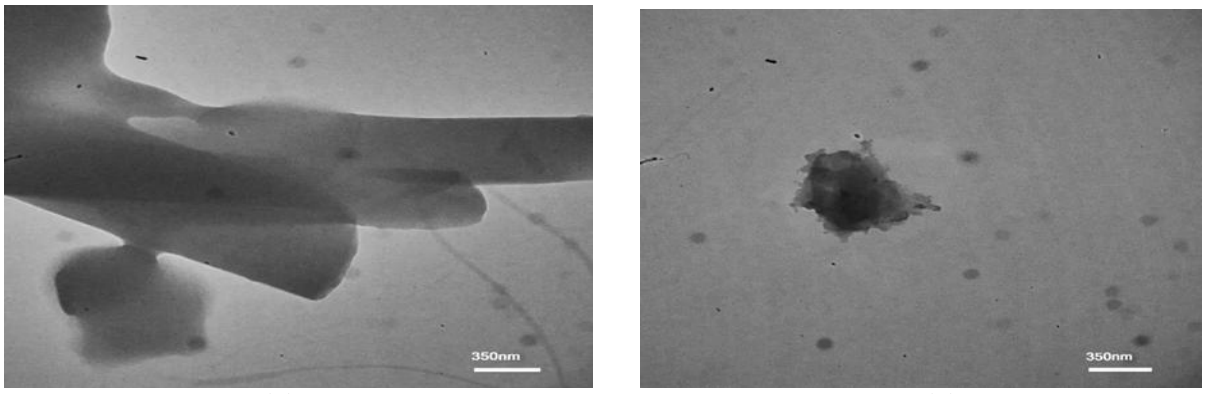

(*A*) (*B*)

Figure 6. Transmission electron microscopy (TEM) images of ITZ loaded SLNs, (*A*) SLN3 and (*B*) SLN9

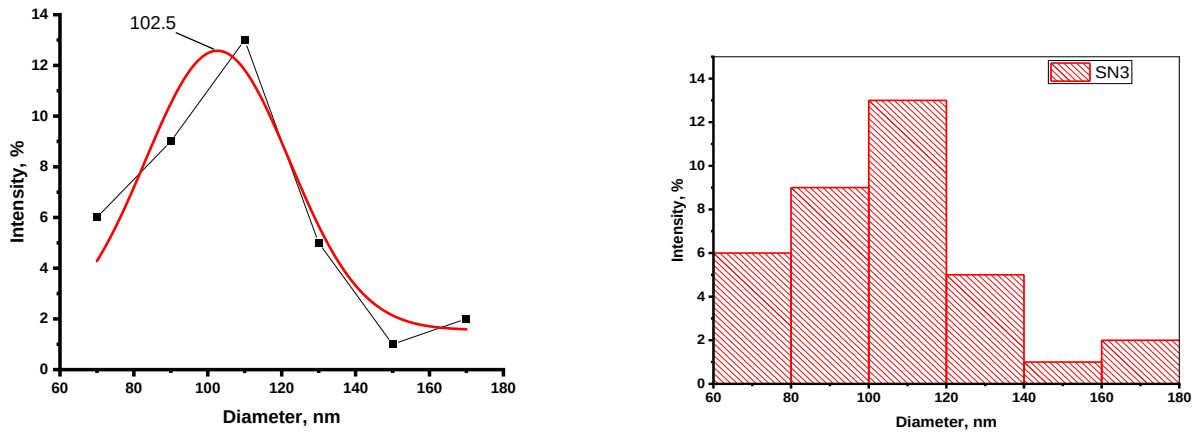

(*A*) (*B*)

Figure 7. Transmission electron microscopy (TEM) derived size distribution curve (*A*) and histogram (*B*) of SLN3 based on TEM analysis

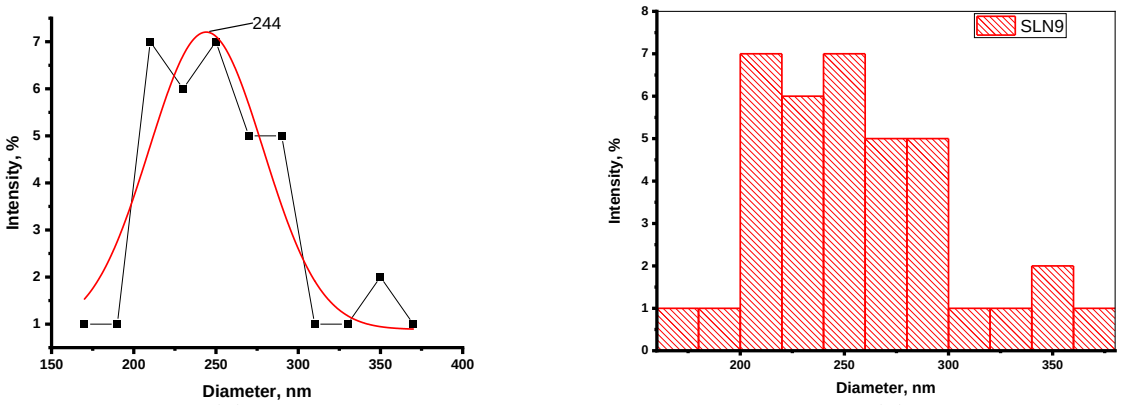

(*A*) (*B*)

Figure 8. Transmission electron microscopy (TEM) derived size distribution curve (*A*) and histogram (*B*) of SLN9 based on TEM analysis

Field Emission Scanning Electron Microscopy (FESEM)

Field Emission Scanning Electron Microscopy (FESEM) was employed to examine the morphological characteristics and surface properties of SLN3 and SLN9. Figure 9 illustrates that SLN3, synthesized using stearic acid and Pluronic F127, had primarily spherical particles with a relatively uniform distribution. The image displayed a certain level of surface roughness, likely due to the utilization of stearic acid as the principal lipid matrix. Conversely, the FESEM images of SLN9, composed of myristic acid and Tween 80, exhibited more distinct and well-separated spherical particles with smoother surfaces. This may be due to the shorter carbon chain length of myristic acid, leading to reduced cohesive interactions within the lipid matrix, resulting in more uniformly distributed particles. Prior research has indicated that the lipid type significantly influences the particle morphology of SLNs [40]. The differences in SLN morphology observed between TEM and FESEM images are mainly attributed to differences in sample preparation and imaging mechanisms. TEM requires drying and high-vacuum conditions, which may induce particle deformation, aggregation, or partial collapse of the solid lipid matrix, leading to irregular morphologies [38]. In contrast, FESEM primarily provides surface-topographical information and generally preserves external morphology more effectively, although some aggregation may still occur during solvent evaporation and conductive coating. Together, the TEM and FESEM data provide complementary information, supporting the successful formation of nanosized, predominantly spherical lipid nanoparticles [41]. From the FESEM study, it was revealed that the size of optimal ITZ-loaded SLNs was 69 ± 22 nm and 45 ± 19 nm for SLN3 and SLN9, respectively. The FESEM-derived particle size distribution curve and histogram are illustrated in Figure 10 and 11.

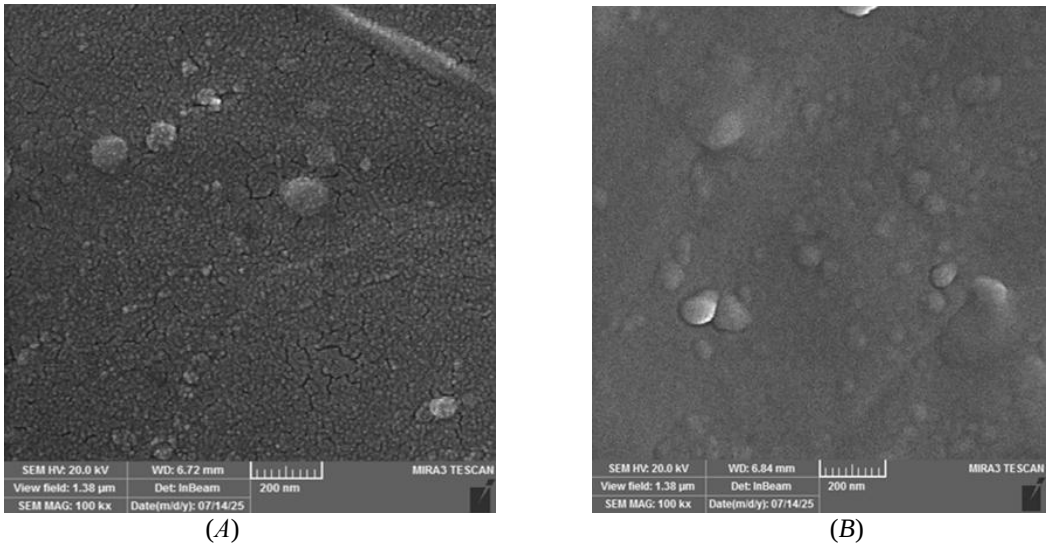

(*A*) (*B*)

Figure 9. Field Emission Scanning Electron Microscopy (FESEM) images of the optimal ITZ-loaded SLNs (*A*) SLN3 and (*B*) SLN9

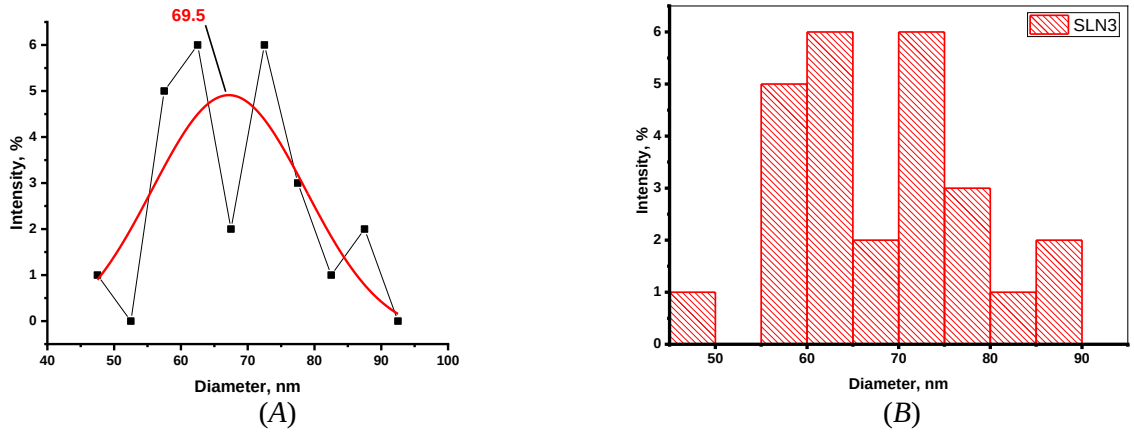

Figure 10. FESEM-derived particle size distribution curve (*A*) and histogram (*B*) of SLN3

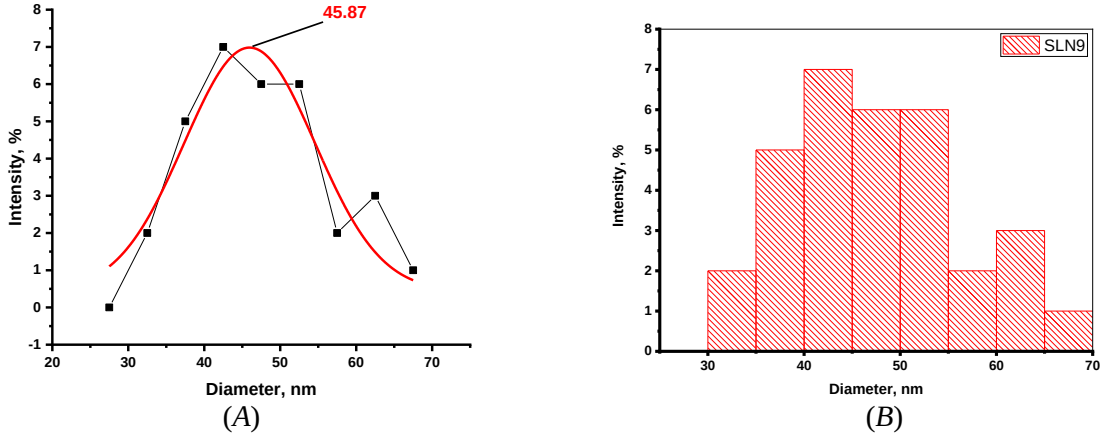

Figure 11. FESEM-derived particle size distribution curve (*A*) and histogram (*B*) of SLN9

Powder X-Ray Diffraction (PXRD)

Powder X-ray diffraction (XRD) was performed to evaluate the crystalline properties of pure ITZ, stearic acid (SA), myristic acid (MA), and their respective solid lipid nanoparticle formulations (SLN3 and SLN9). Figure 12 shows that pure ITZ exhibited characteristic sharp and intense peaks within the 2θ range of 10° to 30°, a pattern indicative of its extremely crystalline characteristics. These results correspond with previously documented diffractograms of pure ITZ, which often display characteristic polymorphism attributes [42].

Stearic acid and myristic acid exhibited distinct diffraction peaks around 2θ = 21°–24°, stearic acid showing reflections at about 21.66° and 24.26°. Likewise, myristic acid was shown to display strong broad-but-sharp peaks around 20.51°, 21.85°, and 24.34° [43]. Conversely, the XRD patterns of SLN3 and SLN9 demonstrated a significant decrease in peak intensity and sharpness, with broad bands substituting the distinct sharp peaks which could indicate a change from a crystalline to an amorphous state, signifying the effective encapsulation of ITZ within the lipid matrix [11]. The absence or considerable attenuation of distinctive peaks in both ITZ and the lipids indicates a loss of long-range molecular order, possibly resulting from high-energy emulsification processes followed by rapid cooling during SLN synthesis. This transition is advantageous for poorly soluble drugs such as ITZ, as the amorphous state typically correlates with increased dissolution rates and greater bioavailability [44]. PXRD results demonstrated that the crystalline peaks of ITZ and lipids were significantly broadened or attenuated in SLN3 and SLN9, indicating the molecular embedding of ITZ within a solid lipid matrix. Importantly, the presence of broad lipid diffraction peaks confirms that the lipid phase remained solid, which differentiates these formulations from liquid lipid-based systems such as nanoemulsions or microemulsions, which lack solid-state diffraction patterns. The notable change in the diffraction patterns of SLN3 and SLN9, in contrast to the pure drug and lipid components, clearly indicates effective molecular embedding and diminished crystallinity, which is a favorable result in nanocarrier-based drug delivery.

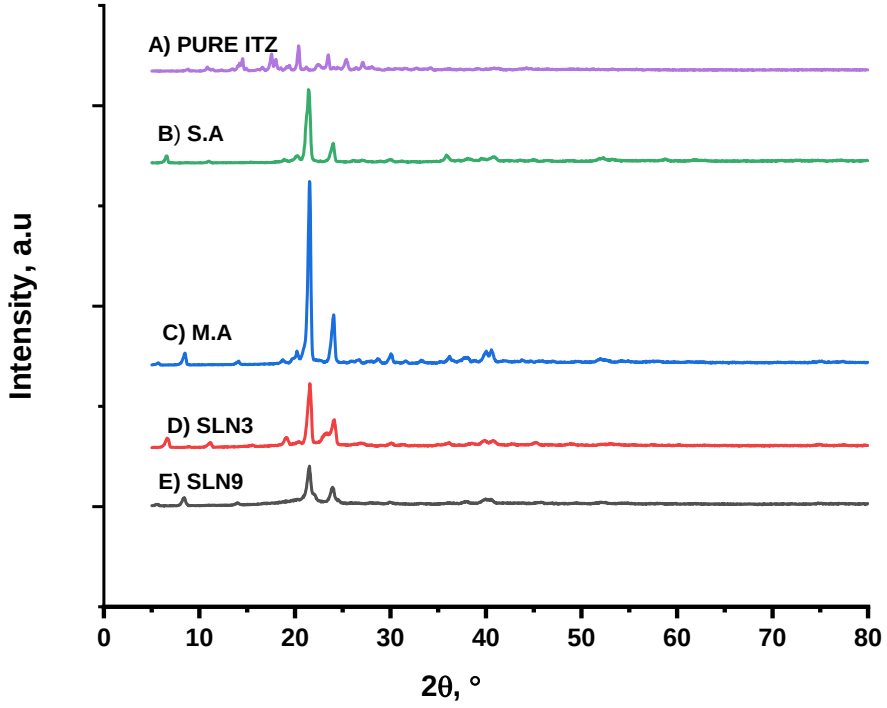

Figure 12. Powder X-ray diffractograms of Pure ITZ, stearic acid (S.A), myristic acid (M.A), SLN3 and SLN9

Differential scanning calorimetry (DSC)

The DSC analysis showed that pure ITZ exhibited a sharp endothermic peak at approximately 167 °C, corresponding to its melting point and confirming its crystalline nature [45]. Figure 13 shows that stearic acid (SA) and myristic acid (MA) exhibited distinct endothermic peaks at roughly 69 °C and 54 °C, respectively, indicative of their melting temperatures. These results correspond with literature values for the melting transitions of SA and MA, signifying their pure and crystalline forms [46].

The SLN formulations (SLN3 and SLN9) demonstrated unique thermal characteristics in contrast to their pure constituents. SLN3, consisting of stearic acid and Pluronic F127, exhibited a broad and diminished endothermic peak at approximately 60–65 °C, whilst SLN9, comprising of myristic acid and Tween 80, demonstrated a similarly broadened peak around 52 °C. The distinctive melting peak of ITZ was either absent or markedly diminished in the thermograms of both SLN3 and SLN9. The absence or alteration of the drug's melting peak in the SLNs indicates that ITZ was either molecularly dispersed within the lipid matrix or present in an amorphous state, rather than in a crystalline form. Such modifications are frequently reported in lipid-based nanoparticle systems and signify effective drug encapsulation and amorphization, potentially improving dissolution rates and bioavailability [47].

The observed decrease in peak intensity and enthalpy values in the lipid matrix of the SLNs may be due to the disruption of the lipid crystal structure caused by the inclusion of drugs and surfactants. The interplay between lipid chains and surfactants like Tween 80 or Pluronic F127 can create defects in the lipid matrix, diminishing crystallinity and enhancing drug loading capacity [48]. DSC analysis further supported the solid nature of the lipid nanoparticles, showing defined melting transitions of the lipids in SLN3 and SLN9, while the characteristic melting peak of ITZ was absent or markedly diminished. These results are consistent with the amorphization and molecular incorporation of ITZ into a solid lipid core, confirming the formation of SLNs rather than liquid lipid-based systems. The DSC data robustly indicates a successful integration of ITZ into the SLN systems and demonstrates a decrease in drug crystallinity, a favorable attribute for improving solubility and release profiles of poorly soluble drugs.

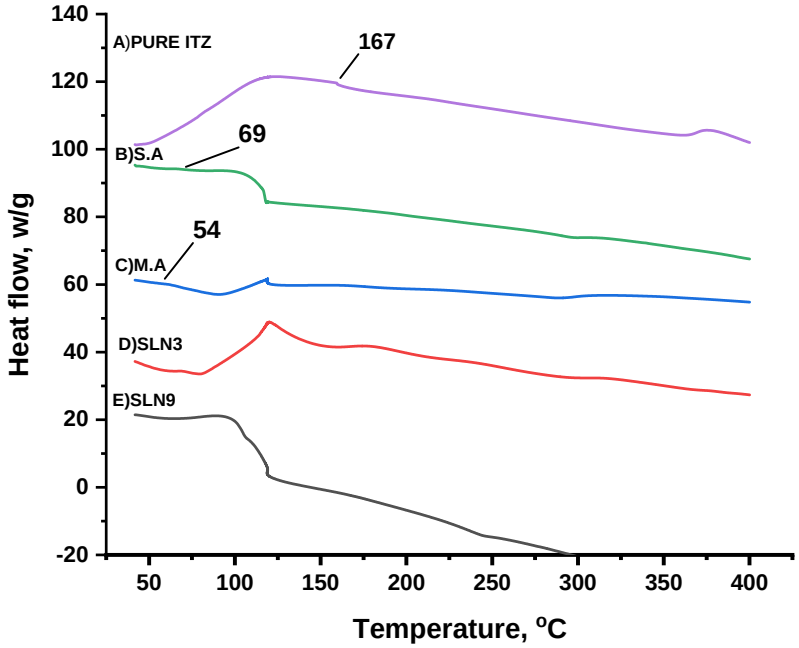

Figure 13. DSC thermograms of Pure ITZ, stearic acid (S.A), myristic acid (M.A), SLN3 and SLN9

Stability Study

The physical stability study revealed marked differences in particle size and PDI between the two formulations, SLN3 and SLN9. SLN3, composed of stearic acid and Pluronic F127, demonstrated a particle size of 550 ± 30 nm and a PDI of 0.61 ± 0.0367 immediately post-preparation (Table S3). After one month, the particle size exhibited a marginal rise to 583 ± 41 nm, while the PDI significantly decreased to 0.533 ± 0.082, while after six months the particle size exhibited a marginal rise to 835 ± 27 nm, PDI decreased to 0.519 ± 0.081 indicating a relatively steady particle dispersion [49]. Conversely, SLN9, comprising myristic acid and Tween 80, exhibited a gradual increase in particle size from 664 ± 78 nm to 2856 ± 102 nm during the six month-storage, accompanied by an elevation in PDI from 0.634 ± 0.069 to 1, signifying some aggregations and a decline in physical stability. The instability may be ascribed to the shorter carbon chain of myristic acid, which likely results in diminished van der Waals interactions and reduced structural rigidity relative to longer-chain fatty acids such as stearic acid [50]. The slight fluctuations in SLN3's particle size and PDI values indicate that it preserved colloidal stability during the specified storage conditions. The observed changes in SLN9 highlight the importance of lipid selection and surfactant type in formulating stable SLNs, suggesting that shorter-chain lipids or particular surfactant type can lead to moderate alterations in particle size and dispersion without necessarily compromising functional performance [51].

Drug Release Study

The *in vitro* release study conducted at pH 1.2, demonstrated notable variations in the release profiles of pure ITZ, SLN3 and SLN9 (Figure 14, A). DMSO was added to the release medium due to its strong solubilizing ability for the highly hydrophobic drug ITZ, ensuring complete dispersion and accurate quantification. Tween 80, a non-ionic surfactant, was included in the release medium to enhance ITZ solubility and maintain sink conditions. Although these conditions do not fully replicate the gastrointestinal environment, they are commonly employed in *in vitro* release studies of poorly soluble drugs to provide reproducible and reliable measurements of formulation performance [52]. Pure ITZ exhibited a gradual and limited release, achieving roughly 25 % after 2880 minutes. This corresponds with the established low aqueous solubility and pH-dependent dissociation characteristics of ITZ, which has a pKa of around 3.7, demonstrating diminished solubility at neutral pH but enhanced solubility in extremely acidic environments [31]. Nonetheless, even in acidic environments, its crystalline structure and lipophilicity result in dissolution-limited release, explaining the level that was seen following the initial stages [53]. Conversely, SLN3, formulated with stearic acid and Pluronic F127, exhibited a markedly superior release profile, attaining nearly 55 % within the same timeframe. The improved and sustained release can be attributable to important formulation features; Pluronic F127 enhances wetting and drug stability in the medium, whereas stearic acid produces a stiff lipid

matrix that regulates release via erosion and diffusion [27]. Notably, SLN9 containing myristic acid and Tween 80 demonstrated a moderate release of around 22 % at 1440 minutes, which decreased marginally by 2880 minutes. The enhanced efficacy of SLN3 relative to SLN9 highlights the essential influence of lipid composition and surfactant choice. Pluronic F127, a block copolymer with a hydrophilic-lipophilic balance, may provide superior drug retention and extended release compared to Tween 80 in acidic environments [27]. The data robustly indicate that SLNs, particularly those composed of stearic acid and Pluronic F127, effectively enhance the release of poorly soluble drug such as ITZ under gastric conditions, potentially leading to increased oral bioavailability.

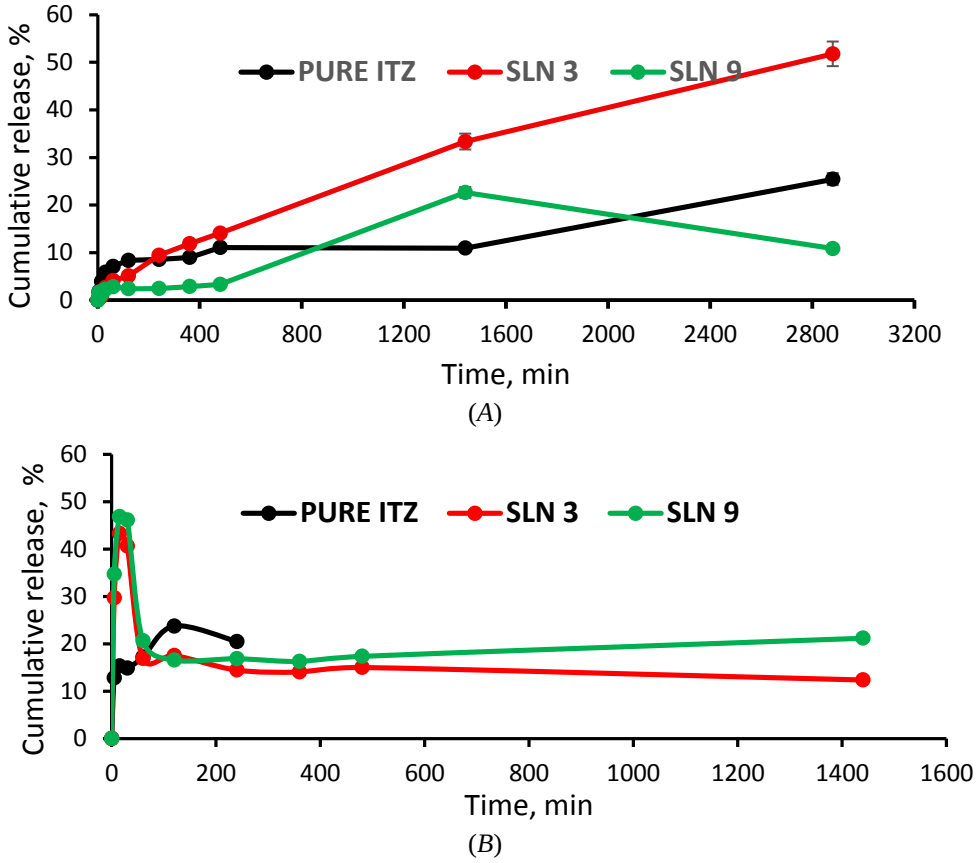

Figure 14. *In vitro* drug release profiles of pure ITZ, SLN 3 and SLN 9 (*A*) in simulated gastric fluid (pH 1.2), and (*B*) in phosphate buffered saline (pH 6.8), $n = 3 \pm SD$

The *in vitro* release profile of pure ITZ, SLN3 and SLN9 at pH 6.8 (Figure 14, B), demonstrated significantly distinct behaviors relative to acidic circumstances. All formulations exhibited an initial burst release during the first 30 minutes, subsequently transitioning to either an equilibrium or a gradual progressive release over 24 hours. Pure ITZ exhibited an initial release of roughly 25 %, subsequently stabilizing with negligible further increase. This trend underscores the notably inadequate aqueous solubility of ITZ at neutral to alkaline pH, which can be due to its weakly basic properties (pKa ~3.7). At pH levels exceeding 6, the drug remains unionized and demonstrates diminished solubility, hence restricting its dissolution in the intestinal milieu [54]. SLN3 demonstrated an initial rapid release within the first few minutes, succeeded by a gradual decrease, indicating potential recrystallization or drug re-adsorption onto the lipid surface, a phenomenon sometimes noted in lipid-based systems due to precipitation from supersaturation. The inadequate solubility of stearic acid-based carriers in intestinal fluid, coupled with the reduced solubility of ITZ at this pH, may lead to drug entrapment within the matrix and restricted diffusion [55]. Conversely, SLN9 had the largest cumulative release at pH 6.8, with sustained release exceeding 20 % by 1500 minutes. This effect may be ascribed to the shorter fatty acid chain of myristic acid [56]. The decrease in release at pH 6.8 can be attributed to ITZ's poor solubility under near-neutral conditions, leading to precipitation. SLN3 shows a more pronounced decline due to the rigid stearic acid matrix, whereas SLN9 maintains higher release owing to

greater matrix fluidity from myristic acid [57]. Overall, the pH-responsive release reflects both ITZ solubility and lipid matrix properties, including crystallinity, chain length, and fluidity. Thus, the differences between SLN3 and SLN9 arise from combined drug–matrix interactions rather than solubility alone. The disparity in performance between SLNs and pure ITZ emphasizes the significance of lipid-surfactant synergy and pH responsiveness. Although SLNs are typically formulated to improve solubility and extend release, their efficacy at intestinal pH is significantly dependent on matrix fluidity, drug-lipid compatibility, and surfactant activity. The data indicate that SLN9 may provide a superior release profile under intestinal conditions compared to SLN3, rendering it a more suitable option for releasing the drug at intestinal pH (around 6–7.4) which could allow drug targeting to the intestine. To assess the *in vitro* release behavior of lipid-based formulations, a similarity factor (f_2) study was done between SLN3 and SLN9. At pH 1.2, the computed f_2 value was less than 50, indicating different release profiles due to lipid chain length and surfactant type. SLN3, containing stearic acid-Pluronic F127, provided more prolonged release under acidic conditions than SLN9, containing myristic acid-Tween 80. At pH 6.8, the f_2 value remained under 50, indicating formulation-dependent and pH-responsive release behavior. The relatively larger release of SLN9 at intestinal pH may be due to increased matrix fluidity caused by myristic acid's shorter fatty acid chain [58].

Conclusions

The successful development of ITZ-loaded SLNs illustrates their promise as a novel drug delivery technology for improving the solubility and bioavailability of ITZ. This study showed that the selection of lipids and surfactants markedly affects the physicochemical characteristics of SLNs, such as particle size, stability, and encapsulation efficiency. The results indicated that formulations including stearic acid and Pluronic F127 produced smaller particle sizes and enhanced stability over time, demonstrating their appropriateness for oral delivery. The solubility experiments indicated a significant enhancement in ITZ solubility when encapsulated in SLNs, with solubility efficiencies markedly above those of pure ITZ. This improvement is due to the nanoscale dimensions of the particles, which increase the surface area for dissolving, and the establishment of a molecularly dispersed state within the lipid matrix that inhibits recrystallization. Furthermore, the physical stability of the formulations over time demonstrates their suitability for pharmaceutical applications, with SLN3 showing negligible alterations in particle size and dispersion after one month of storage. The research indicates that SLNs markedly improve the release of poorly soluble ITZ in different pH levels. SLN3, comprising stearic acid and Pluronic F127, demonstrates superior performance in acidic environments, whereas SLN 9, which includes myristic acid and Tween 80, exhibits enhanced release in intestinal circumstances. In conclusion, the study confirms the usefulness of SLNs in enhancing the solubility, controlling drug release and stability of ITZ while also opening the way for additional research into the *in vivo* performance and therapeutic effectiveness of these formulations. Future studies should concentrate on refining SLN formulations for targeted therapeutic uses and performing pharmacokinetic assessments to evaluate their efficacy in clinical environments.

Supporting Information

The Supporting Information is available free at https://ejc.buketov.edu.kz/ejc/article/view/652/359

*Author Information**

**The authors' names are presented in the following order: First Name, Middle Name and Last Name*

Darya Wahhab Kareem — MSc Student, Department of Pharmaceutics, College of Pharmacy, University of Sulaimani, Sulaymaniyah, Zanko Street, 46001, Kurdistan Region, Iraq; e-mail: darya.kareem@univsul.edu.iq

Twana Mohammed M. Ways (*corresponding author*) — Assistant Professor, Department of Pharmaceutics, College of Pharmacy, University of Sulaimani, Sulaymaniyah, Zanko Street, 46001, Kurdistan Region, Iraq; e-mail: twana.mohammed@univsul.edu.iq; https://orcid.org/0000-0002-7595-2159

Author Contributions

The manuscript was written through contributions of all authors. All authors have given approval to the final version of the manuscript. CRediT: ***Darya Wahhab Kareem*** conceptualization, data curation, investigation, methodology, validation, visualization, formal analysis, writing-original draft, writing-review & edit-

ing; **Twana Mohammed M. Ways** conceptualization, data curation, investigation, formal analysis, resources, supervision, validation, writing-original draft, writing-review & editing.

Acknowledgments

The authors gratefully acknowledge the University of Sulaimani for its support and for providing the facilities necessary to carry out this study.

Conflicts of Interest

The authors declare no conflict of interest.

References

1 Alam, S., Iqbal, Z., Ali, A., Khar, R. K., Ahmad, F. J., Akhter, S., & Talegaonkar, S. (2009). Microemulsion as a Potential Transdermal Carrier for Poorly Water Soluble Antifungal Drug Itraconazole. *Journal of Dispersion Science and Technology*, *31*(1), 84–94. https://doi.org/10.1080/01932690903107265

2 Chhatbar, M., Borkhataria, C., Patel, O., Raichura, K., Pethani, T., Parmar, G., Mori, D., & Manek, R. (2025). Enhancing the solubility and bioavailability of itraconazole through pharmaceutical cocrystallization: A promising strategy for drug formulation. *Journal of Pharmaceutical Sciences*, *114*(6), 103770. https://doi.org/10.1016/j.xphs.2025.103770

3 Pardeike, J., Weber, S., Haber, T., Wagner, J., Zarfl, H. P., Plank, H., & Zimmer, A. (2011). Development of an itraconazole-loaded nanostructured lipid carrier (NLC) formulation for pulmonary application. *International Journal of Pharmaceutics*, *419*(1–2), 329–338. https://doi.org/10.1016/j.ijpharm.2011.07.040

4 Osborn, M. R., Zuniga-Moya, J. C., Mazi, P. B., Rauseo, A. M., & Spec, A. (2025). Side effects associated with itraconazole therapy. *The Journal of Antimicrobial Chemotherapy*, *80*(2), 503–508. https://doi.org/10.1093/jac/dkae437

5 Cheng, Y., Xu, Z., Ma, M., & Xu, T. (2008). Dendrimers as drug carriers: Applications in different routes of drug administration. *Journal of Pharmaceutical Sciences*, *97*(1), 123–143. https://doi.org/10.1002/jps.21079

6 Hu, L., Tang, X., & Cui, F. (2004). Solid lipid nanoparticles (SLNs) to improve oral bioavailability of poorly soluble drugs. *The Journal of Pharmacy and Pharmacology*, *56*(12), 1527–1535. https://doi.org/10.1211/0022357044959

7 Xie, S., Zhu, L., Dong, Z., Wang, Y., Wang, X., & Zhou, W. (2011). Preparation and evaluation of ofloxacin-loaded palmitic acid solid lipid nanoparticles. *International Journal of Nanomedicine*, *6*, 547–555. https://doi.org/10.2147/IJN.S17083

8 Severino, P., Andreani, T., Macedo, A. S., Fangueiro, J. F., Santana, M. H. A., Silva, A. M., & Souto, E. B. (2012). Current State-of-Art and New Trends on Lipid Nanoparticles (SLN and NLC) for Oral Drug Delivery. *Journal of Drug Delivery*, *2012*, 750891. https://doi.org/10.1155/2012/750891

9 Dattani, S., Li, X., Lampa, C., Lechuga-Ballesteros, D., Barriscale, A., Damadzadeh, B., & Jasti, B. R. (2023). A comparative study on micelles, liposomes and solid lipid nanoparticles for paclitaxel delivery. *International Journal of Pharmaceutics*, *631*, 122464. https://doi.org/10.1016/j.ijpharm.2022.122464

10 Wissing, S. A., & Müller, R. H. (2003). The influence of solid lipid nanoparticles on skin hydration and viscoelasticity — *In vivo* study. *European Journal of Pharmaceutics and Biopharmaceutics: Official Journal of Arbeitsgemeinschaft Fur Pharmazeutische Verfahrenstechnik e.V*, *56*(1), 67–72. https://doi.org/10.1016/s0939-6411(03)00040-7

11 Kumar, N., & Goindi, S. (2021). Development and Optimization of Itraconazole-Loaded Solid Lipid Nanoparticles for Topical Administration Using High Shear Homogenization Process by Design of Experiments: *In Vitro*, *Ex Vivo* and *In Vivo* Evaluation. *AAPS PharmSciTech*, *22*(7), 248. https://doi.org/10.1208/s12249-021-02118-3

12 Mukherjee, S., Ray, S., & Thakur, R. S. (2009). Design and evaluation of itraconazole loaded solid lipid nanoparticulate system for improving the antifungal therapy. *Pakistan Journal of Pharmaceutical Sciences*, *22*(2), 131–138.

13 Müller, R. H., Shegokar, R., & Keck, C. M. (2011). 20 years of lipid nanoparticles (SLN and NLC): Present state of development and industrial applications. *Current Drug Discovery Technologies*, *8*(3), 207–227. https://doi.org/10.2174/157016311796799062

14 Mehnert, W., & Mäder, K. (2012). Solid lipid nanoparticles: Production, characterization and applications. *Advanced Drug Delivery Reviews*, *64*, 83–101. https://doi.org/10.1016/j.addr.2012.09.021

15 Mishra, V., Bansal, K. K., Verma, A., Yadav, N., Thakur, S., Sudhakar, K., & Rosenholm, J. M. (2018). Solid Lipid Nanoparticles: Emerging Colloidal Nano Drug Delivery Systems. *Pharmaceutics*, *10*(4), 191. https://doi.org/10.3390/pharmaceutics10040191

16 Cassano, R., Ferrarelli, T., Mauro, M. V., Cavalcanti, P., Picci, N., & Trombino, S. (2016). Preparation, characterization and *in vitro* activities evaluation of solid lipid nanoparticles based on PEG-40 stearate for antifungal drugs vaginal delivery. *Drug Delivery*, *23*(3), 1047–1056. https://doi.org/10.3109/10717544.2014.932862

17 Shah, V., Lesko, L., Fan, J., Fleischer, N., Handerson, J., Malinowski, H., Makary, M., Ouderkirk, L., Roy, S., Sathe, P., Singh, G., Tillman, L., Tsong, Y., & Williams, R. (1997). fDA Guidance for Industry 1 Dissolution Testing of Immediate Release Solid Oral Dosage Forms. *Dissolution Technologies*, *4*, 15–22. https://doi.org/10.14227/DT040497P15

18 Zoubari, G., Staufenbiel, S., Volz, P., Alexiev, U., & Bodmeier, R. (2017). Effect of drug solubility and lipid carrier on drug release from lipid nanoparticles for dermal delivery. *European Journal of Pharmaceutics and Biopharmaceutics: Official Journal of Arbeitsgemeinschaft Fur Pharmazeutische Verfahrenstechnik e.V*, *110*, 39–46. https://doi.org/10.1016/j.ejpb.2016.10.021

19 Gaba, B., Fazil, M., Khan, S., Ali, A., Baboota, S., & Ali, J. (2015). Nanostructured lipid carrier system for topical delivery of terbinafine hydrochloride. *Bulletin of Faculty of Pharmacy, Cairo University*, *53*(2), 147–159. https://doi.org/10.1016/j.bfopcu.2015.10.001

20 Khalil, R. M., Abd El-Bary, A., Kassem, M. A., Ghorab, M. M., & Basha, M. (2013). Influence of formulation parameters on the physicochemical properties of meloxicam-loaded solid lipid nanoparticles. *Egyptian Pharmaceutical Journal*, *12*(1), 63. https://doi.org/10.7123/01.EPJ.0000428643.74323.d9

21 Elmowafy, M., & Al-Sanea, M. M. (2021). Nanostructured lipid carriers (NLCs) as drug delivery platform: Advances in formulation and delivery strategies. *Saudi Pharmaceutical Journal*, *29*(9), 999–1012. https://doi.org/10.1016/j.jsps.2021.07.015

22 Zimmermann, E., & Müller, R. H. (2001). Electrolyte- and pH-stabilities of aqueous solid lipid nanoparticle (SLN^{TM}) dispersions in artificial gastrointestinal media. *European Journal of Pharmaceutics and Biopharmaceutics*, *52*(2), 203–210. https://doi.org/10.1016/S0939-6411(01)00167-9

23 Sanna, V., Gavini, E., Cossu, M., Rassu, G., & Giunchedi, P. (2007). Solid lipid nanoparticles (SLN) as carriers for the topical delivery of econazole nitrate: In-vitro characterization, ex-vivo and in-vivo studies. *The Journal of Pharmacy and Pharmacology*, *59*(8), 1057–1064. https://doi.org/10.1211/jpp.59.8.0002

24 Younus, M., Hawley, A., Boyd, B. J., & Rizwan, S. B. (2018). Bulk and dispersed aqueous behaviour of an endogenous lipid, selachyl alcohol: Effect of Tween 80 and Pluronic F127 on nanostructure. *Colloids and Surfaces. B, Biointerfaces*, *169*, 135–142. https://doi.org/10.1016/j.colsurfb.2018.05.013

25 Karjiban, R. A., Basri, M., Rahman, M. B. A., & Salleh, A. B. (2012). Structural Properties of Nonionic Tween80 Micelle in Water Elucidated by Molecular Dynamics Simulation. *APCBEE Procedia, 2nd International Conference on Chemistry and Chemical Process (ICCCP 2012) May 5-6, 2012*, *3*, 287–297. https://doi.org/10.1016/j.apcbee.2012.06.084

26 Kumar, M., Tiwari, A., Asdaq, S. M. B., Nair, A. B., Bhatt, S., Shinu, P., Al Mouslem, A. K., Jacob, S., Alamri, A. S., Alsanie, W. F., Alhomrani, M., Tiwari, V., Devi, S., Pathania, A., & Sreeharsha, N. (2022). Itraconazole loaded nano-structured lipid carrier for topical ocular delivery: Optimization and evaluation. *Saudi Journal of Biological Sciences*, *29*(1), 1–10. https://doi.org/10.1016/j.sjbs.2021.11.006

27 Ebrahimi, H. A., Javadzadeh, Y., Hamidi, M., & Jalali, M. B. (2015). Repaglinide-loaded solid lipid nanoparticles: Effect of using different surfactants/stabilizers on physicochemical properties of nanoparticles. *Daru: Journal of Faculty of Pharmacy, Tehran University of Medical Sciences*, *23*(1), 46. https://doi.org/10.1186/s40199-015-0128-3

28 Garud, A., Singh, D., & Garud, N. (2012). Solid Lipid Nanoparticles (SLN): Method, Characterization and Applications. *International Current Pharmaceutical Journal*, *1*(11), 384–393. https://doi.org/10.3329/icpj.v1i11.12065

29 Pizzol, C. D., Filippin-Monteiro, F. B., Restrepo, J. A. S., Pittella, F., Silva, A. H., Alves de Souza, P., Machado de Campos, A., & Creczynski-Pasa, T. B. (2014). Influence of Surfactant and Lipid Type on the Physicochemical Properties and Biocompatibility of Solid Lipid Nanoparticles. *International Journal of Environmental Research and Public Health*, *11*(8), 8581–8596. https://doi.org/10.3390/ijerph110808581

30 Mellaerts, R., Mols, R., Jammaer, J. A. G., Aerts, C. A., Annaert, P., Van Humbeeck, J., Van den Mooter, G., Augustijns, P., & Martens, J. A. (2008). Increasing the oral bioavailability of the poorly water soluble drug itraconazole with ordered mesoporous silica. *European Journal of Pharmaceutics and Biopharmaceutics: Official Journal of Arbeitsgemeinschaft Fur Pharmazeutische Verfahrenstechnik e.V*, *69*(1), 223–230. https://doi.org/10.1016/j.ejpb.2007.11.006

31 Mohanty, B., Majumdar, D. K., Mishra, S. K., Panda, A. K., & Patnaik, S. (2015). Development and characterization of itraconazole-loaded solid lipid nanoparticles for ocular delivery. *Pharmaceutical Development and Technology*, *20*(4), 458–464. https://doi.org/10.3109/10837450.2014.882935

32 Pandey, S., Shaikh, F., Gupta, A., Tripathi, P., & Yadav, J. S. (2022). A Recent Update: Solid Lipid Nanoparticles for Effective Drug Delivery. *Advanced Pharmaceutical Bulletin*, *12*(1), 17–33. https://doi.org/10.34172/apb.2022.007

33 Nesseem, D. I. (2001). Formulation and evaluation of itraconazole via liquid crystal for topical delivery system. *Journal of Pharmaceutical and Biomedical Analysis*, *26*(3), 387–399. https://doi.org/10.1016/s0731-7085(01)00414-9

34 Subroto, E., Afifah, T. N., Harlina, P. W., Indiarto, R., Pangawikan, A. D., Huda, S., Wiguna, B., & Geng, F. (2025). Solid lipid nanoparticles of mangosteen peel extract based on monoacylglycerol-diacylglycerol-rich fat and stearic acid: Study on physicochemical properties and encapsulation efficiency. *Future Foods*, *12*, 100719. https://doi.org/10.1016/j.fufo.2025.100719

35 Tao, T., Zhao, Y., Wu, J., & Zhou, B. (2009). Preparation and evaluation of itraconazole dihydrochloride for the solubility and dissolution rate enhancement. *International Journal of Pharmaceutics*, *367*(1–2), 109–114. https://doi.org/10.1016/j.ijpharm.2008.09.034

36 Triboandas, H., Pitt, K., Bezerra, M., Ach-Hubert, D., & Schlindwein, W. (2022). Itraconazole Amorphous Solid Dispersion Tablets: Formulation and Compaction Process Optimization Using Quality by Design Principles and Tools. *Pharmaceutics*, *14*(11), 2398. https://doi.org/10.3390/pharmaceutics14112398

37 Franken, L. E., Boekema, E. J., & Stuart, M. C. A. (2017). Transmission Electron Microscopy as a Tool for the Characterization of Soft Materials: Application and Interpretation. *Advanced Science*, *4*(5), 1600476. https://doi.org/10.1002/advs.201600476

38 Nogueira, S. S., Samaridou, E., Simon, J., Frank, S., Beck-Broichsitter, M., & Mehta, A. (2024). Analytical techniques for the characterization of nanoparticles for mRNA delivery. *European Journal of Pharmaceutics and Biopharmaceutics*, *198*, 114235. https://doi.org/10.1016/j.ejpb.2024.114235

39 Filippov, S. K., Khusnutdinov, R., Murmiliuk, A., Inam, W., Zakharova, L. Ya., Zhang, H., & Khutoryanskiy, V. V. (2023). Dynamic light scattering and transmission electron microscopy in drug delivery: a roadmap for correct characterization of nanoparticles and interpretation of results. *Materials Horizons*, 10(12), 5354–5370. https://doi.org/10.1039/d3mh00717k

40 Subroto, E., Andoyo, R., Indiarto, R., Wulandari, E., & Wadhiah, E. F. N. (2022). Preparation of Solid Lipid Nanoparticle-Ferrous Sulfate by Double Emulsion Method Based on Fat Rich in Monolaurin and Stearic Acid. *Nanomaterials*, *12*(17), 3054. https://doi.org/10.3390/nano12173054

41 Naseri, N., Valizadeh, H., & Zakeri-Milani, P. (2015). Solid Lipid Nanoparticles and Nanostructured Lipid Carriers: Structure, Preparation and Application. *Advanced Pharmaceutical Bulletin*, *5*(3), 305–313. https://doi.org/10.15171/apb.2015.043

42 Chen, W., Gu, B., Wang, H., Pan, J., Lu, W., & Hou, H. (2008). Development and evaluation of novel itraconazole-loaded intravenous nanoparticles. *International Journal of Pharmaceutics*, *362*(1–2), 133–140. https://doi.org/10.1016/j.ijpharm.2008.05.039

43 Das, S., Ng, W. K., Kanaujia, P., Kim, S., & Tan, R. B. H. (2011). Formulation design, preparation and physicochemical characterizations of solid lipid nanoparticles containing a hydrophobic drug: Effects of process variables. *Colloids and Surfaces. B, Biointerfaces*, *88*(1), 483–489. https://doi.org/10.1016/j.colsurfb.2011.07.036

44 Lang, B., McGinity, J. W., & Williams, R. O. (2014). Dissolution enhancement of itraconazole by hot-melt extrusion alone and the combination of hot-melt extrusion and rapid freezing — Effect of formulation and processing variables. *Molecular Pharmaceutics*, *11*(1), 186–196. https://doi.org/10.1021/mp4003706

45 Salah, E., Abouelfetouh, M. M., Pan, Y., Chen, D., & Xie, S. (2020). Solid lipid nanoparticles for enhanced oral absorption: A review. *Colloids and Surfaces. B, Biointerfaces*, *196*, 111305. https://doi.org/10.1016/j.colsurfb.2020.111305

46 Silva, A. C., González-Mira, E., García, M. L., Egea, M. A., Fonseca, J., Silva, R., Santos, D., Souto, E. B., & Ferreira, D. (2011). Preparation, characterization and biocompatibility studies on risperidone-loaded solid lipid nanoparticles (SLN): High pressure homogenization versus ultrasound. *Colloids and Surfaces. B, Biointerfaces*, *86*(1), 158–165. https://doi.org/10.1016/j.colsurfb.2011.03.035

47 Ghasemiyeh, P., & Mohammadi-Samani, S. (2018). Solid lipid nanoparticles and nanostructured lipid carriers as novel drug delivery systems: Applications, advantages and disadvantages. *Research in Pharmaceutical Sciences*, *13*(4), 288–303. https://doi.org/10.4103/1735-5362.235156

48 Zainol, S., Basri, M., Basri, H. B., Shamsuddin, A. F., Abdul-Gani, S. S., Karjiban, R. A., & Abdul-Malek, E. (2012). Formulation Optimization of a Palm-Based Nanoemulsion System Containing Levodopa. *International Journal of Molecular Sciences*, *13*(10), 13049–13064. https://doi.org/10.3390/ijms131013049

49 Andonova, V., & Peneva, P. (2017). Characterization Methods for Solid Lipid Nanoparticles (SLN) and Nanostructured Lipid Carriers (NLC). *Current Pharmaceutical Design*. https://doi.org/10.2174/1381612823666171115105721

50 Martins, S., Tho, I., Ferreira, D. C., Souto, E. B., & Brandl, M. (2011). Physicochemical properties of lipid nanoparticles: Effect of lipid and surfactant composition. *Drug Development and Industrial Pharmacy*, *37*(7), 815–824. https://doi.org/10.3109/03639045.2010.545414

51 Stahl, M. A., Lüdtke, F. L., Grimaldi, R., Gigante, M. L., & Ribeiro, A. P. B. (2024). Characterization and stability of solid lipid nanoparticles produced from different fully hydrogenated oils. *Food Research International (Ottawa, Ont.)*, *176*, 113821. https://doi.org/10.1016/j.foodres.2023.113821

52 Kawakami, K., Oda, N., Miyoshi, K., Funaki, T., & Ida, Y. (2006). Solubilization behavior of a poorly soluble drug under combined use of surfactants and cosolvents. *European Journal of Pharmaceutical Sciences: Official Journal of the European Federation for Pharmaceutical Sciences*, *28*(1–2), 7–14. https://doi.org/10.1016/j.ejps.2005.11.012

53 Segale, L., Giovannelli, L., Mannina, P., & Pattarino, F. (2015). Formulation and characterization study of itraconazole-loaded microparticles. *Pharmaceutical Development and Technology*, *20*(2), 153–158. https://doi.org/10.3109/10837450.2013.852572

54 Lee, J.-H., Park, C., Weon, K.-Y., Kang, C.-Y., Lee, B.-J., & Park, J.-B. (2021). Improved Bioavailability of Poorly Water-Soluble Drug by Targeting Increased Absorption through Solubility Enhancement and Precipitation Inhibition. *Pharmaceuticals (Basel, Switzerland)*, *14*(12), 1255. https://doi.org/10.3390/ph14121255

55 Parikh, T., Sandhu, H. K., Talele, T. T., & Serajuddin, A. T. M. (2016). Characterization of Solid Dispersion of Itraconazole Prepared by Solubilization in Concentrated Aqueous Solutions of Weak Organic Acids and Drying. *Pharmaceutical Research*, *33*(6), 1456–1471. https://doi.org/10.1007/s11095-016-1890-8

56 Kim, J.-K., Park, J.-S., & Kim, C.-K. (2010). Development of a binary lipid nanoparticles formulation of itraconazole for parenteral administration and controlled release. *International Journal of Pharmaceutics*, *383*(1–2), 209–215. https://doi.org/10.1016/j.ijpharm.2009.09.008

57 Khan, J., Rades, T., & Boyd, B. J. (2016). Lipid-Based Formulations Can Enable the Model Poorly Water-Soluble Weakly Basic Drug Cinnarizine To Precipitate in an Amorphous-Salt Form During In Vitro Digestion. *Molecular Pharmaceutics*, *13*(11), 3783–3793. https://doi.org/10.1021/acs.molpharmaceut.6b00594

58 Das, S., & Chaudhury, A. (2011). Recent advances in lipid nanoparticle formulations with solid matrix for oral drug delivery. *AAPS PharmSciTech*, *12*(1), 62–76. https://doi.org/10.1208/s12249-010-9563-0

How to Cite: Mulyukina, S.M., Dzeranov, A.D., Pankratov, D.A., Bondarenko, L.S., Kugabaeva, G.D., Prokofiev, M.V., & Kydralieva, K.A. (2026). Engineering Biocompatible Goethite Nanoparticles: Microstructural Tuning through Controlled Ferrihydrite Conversion Routes. *Eurasian Journal of Chemistry, 31, 1(121), 121–136.* https://doi.org/10.31489/2959-0663/1-26-9

Article

Received: 2 December 2025 | Revised: 2 February 2026 | Accepted: 12 February 2026 | Published online: 19 February 2026

UDC 544.42+519.242.7

https://doi.org/10.31489/2959-0663/1-26-9

Sofia M. Mulyukina[1]*, Artur A. Dzeranov[2, 3], Denis A. Pankratov[4, 5], Lyubov S. Bondarenko[2], Gulsara D. Kugabaeva[2, 3], Mikhail V. Prokofiev[2], Kamila A. Kydralieva[2]

[1]*Surgut State University, Surgut, Russia;*
[2]*Moscow Aviation Institute (National Research University), Moscow, Russia;*
[3]*Federal Research Center of Problems of Chemical Physics and Medicinal Chemistry, Russian Academy of Sciences, Moscow Region, Russia;*
[4]*Lomonosov Moscow State University, Moscow, Russia;*
[5]*Moscow Institute of Physics and Technology (National Research University), Moscow region, Russia*
*(*Corresponding author's e-mail: sbolotskaya@inbox.ru)*

Engineering Biocompatible Goethite Nanoparticles: Microstructural Tuning through Controlled Ferrihydrite Conversion Routes

The goethite (α-FeOOH) nanoparticles (NPs) are highly attractive material with a broad spectrum of applications, including biomedicine thanks to a high thermodynamical stability. The formation and strict control of the phase-pure goethite NPs remain a challenging task due to the high sensitivity of the particles to the synthesis conditions. This study presents for the first time effect of the iron source (nitrate vs. chloride) and alkaline medium (NaOH vs. NH_4OH) on three known distinct post-synthesis transformation pathways for preparing goethite NPs from ferrihydrite suspensions: aging, ultrasonic-assisted conversion, and hydrothermal crystallization. We observed that ferrihydrite NPs precursor generated from $FeCl_3$ with NaOH facilitated the formation of phase-pure goethite through both aging and ultrasonic transformation under ambient conditions. In contrast, synthesis at 90 °C promoted the formation of larger crystals, often accompanied by significant phase impurities. For the first time, comprehensive characterization of the synthesized materials was performed in addition to previously used methods as X-ray diffraction, the ^{57}Fe Mössbauer spectroscopy, transmission electronic microscopy, and low-temperature nitrogen adsorption/desorption enabling in-depth assessment of crystallinity, phase purity, and morphological features. These findings highlight the potential of iron-based goethite nanomaterials as safe, functional, and versatile platforms for future biomedical and technological applications.

Keywords: goethite nanoparticles, ferrihydrite precursor, aging, ultrasonic-assisted conversion, hydrothermal crystallization, post-synthesis transformation, iron source, alkaline medium, crystal structure

Introduction

Goethite (α-FeOOH) is one of the most thermodynamically stable. Owing to its chemical robustness, non-toxicity, low cost, and the abundance of reactive hydroxyl groups on its surface, goethite is a highly attractive material with a broad spectrum of applications [1]. These include bioinspired and biomimetic scaffolds for biomedical use [2, 3]. For example, a recent study [2] employed spongin extracted from the marine demosponge *Hippospongia communis* as a microporous template for constructing a 3D goethite-based composite with enhanced electrochemical performance for dopamine sensing in human urine. Nano-sized goethite exhibits significant antibacterial properties against E. coli O157:H7 by damaging bacterial membranes, mediated by both ROS-dependent RNA damage and cell membrane destruction [5]. The exposure to nano-sized goethite increased the levels of ribonucleoside-related substances, phenylalanine and adenosine 5′-triphosphate, while decreased those of glycogen, protein and lipopolysaccharide & outer membrane porins (LPS & OMPs). Goethite shows promising anti-parasitic effects, particularly against the protozoan Toxoplasma gondii, with studies revealing that goethite nanoparticles can significantly reduce parasite viability, potentially offering new therapeutic avenues, especially when combined with surface modifications like L-tryptophan for improved targeted toxicity, addressing the need for better treatments for diseases like toxoplasmosis [6]. Furthermore, α-FeOOH has emerged as a promising functional material in photocatalytic systems [6–10], for oxidation of other toxicants [11].

Numerous synthetic strategies have been developed for the preparation of α-FeOOH nanoparticles (NPs), including Fe(III) coprecipitation [1, 12, 13], rapid ferrihydrite transformation via ultrasonic irradiation, sol–gel methods, and microemulsion techniques [14, 15]. However, the synthesis and structural control of iron (oxyhydr)oxides remains a significant challenge since there is no single synthesis protocol. Varying the conditions of NPs synthesis in order to find scientifically sound methods is associated with the impossibility of achieving the formation of monophasic NPs with specified properties for various potential target applications within the framework of the same synthesis conditions. The hydrolysis of Fe^{2+} and Fe^{3+} in aqueous systems can yield a complex mixture of hydroxides, oxyhydroxides, and oxides, as their formation is highly sensitive to parameters such as pH, ionic strength, temperature, and precursor identity [16]. Thus, precise control over synthesis conditions is critical to direct the formation of a desired phase. Synthesis approaches often used lead to the production of a mixture of several phases rather than a monophase product. So obtaining goethite by the hydrothermal method, declare a mixture of phases of 70, 21.6 magnetite and 8.4 % hematite [17]. The authors [18] using wet synthesis approaches, according to X-ray phase analysis data, a mixture is obtained Hematite 47(3) %; Goethite 19(2) %; Magnetite 1.7(13) %; Quartz 6(2) %. Interestingly, the authors [19], obtaining goethite by co-precipitation with further aging overnight at 14 °C, declare the preservation of the goethite phase in the XRD analysis and the appearance of the hematite phase in the analysis by Mossbauer spectroscopy.

The morphological and structural properties of goethite are highly dependent on the chosen synthetic pathway [1, 16, 20]. For instance, Kosmulski et al. [19] demonstrated that parameters such as the Fe(III) : OH^- ratio, titration rate, and crystallization temperature and duration markedly influence the specific surface area and overall particle characteristics. Similarly, Meret et. al. [22] showed that the low-temperature transformation of ferrihydrite into goethite proceeds slowly under mild conditions, and its final phase composition is sensitive to both pH and thermal input. Ristic et al. [23] demonstrated that variations in parameters such as pH, weight of the initial precursor sample, temperature, and retention time during co-precipitation in a highly alkaline medium led, for example, to partial conversion of goethite to hematite. In the study Xu et al. [24], E. coli adapted to goethite at a concentration of 1 mg/mL did not acquire antibiotic resistance even after 13 generations, probably due to its poor biofilm-formation capacity. In the article Agresti [25], the electrorheological properties of suspensions of lamellar goethite (α-FeOOH) nanoparticles in silicone oil are investigated. The particles were synthesized and functionalized with urea to increase polarizability. Electrorheological characterization has shown that urea functionalization enhances rheological properties (limiting shear stress and viscosity) under the action of an electric field up to 5 kV/mm, which allows achieving similar characteristics at a lower filler concentration. The results demonstrate the potential of functionalized goethite as an efficient and economical material for smart electrorheological fluids. Cabral-Prieto et al. [26] showed that low oxygen flow rates (0.025, 0.017, 0.013, 0.01 cm^3/s) during the oxidation of $Fe(OH)_2$ to obtain goethite led to the secondary production of magnetite and maghemite, registered by the XRD. In general, varying the oxygen flow rate led to a change in particle size and specific surface area. Other studies using hydrothermal methods revealed that the choice of iron precursor has a pronounced impact on phase evolution: ferric nitrate tends to favor goethite formation, while ferric chloride and ferric sulfate may result in akaganéite, lepidocrocite, or mixed-phase nanocomposites such as goethite/parabutlerite [27–29]. Goethite NPs could be used as T_2 MRI contrasting agents with unique properties which are not suffering from upper size limitations [30–33].

In this study, we systematically investigated the hydrolysis of Fe(III) at pH 12 to selectively promote the formation of monophasic goethite, following the thermodynamic framework proposed by Cudennec and Lecerf [16].

The aim of this study was to determine synthesis conditions that would yield goethite nanoparticles while avoiding secondary phases that could affect reactivity, using a wider range of methods, including Mössbauer spectroscopy, a more powerful technique than X-ray diffraction. To achieve this, we employed a comparative analysis of several known distinct synthesis routes: ferrihydrite aging, ultrasonic-assisted conversion, and hydrothermal crystallization by variation for the first time key parameters within these routes, including the iron source (nitrate vs. chloride), alkaline medium (NaOH vs. NH_4OH). The resulting nanostructures were comprehensively characterized in addition to previously used methods as X-ray diffraction, the ^{57}Fe Mössbauer spectroscopy, transmission electronic microscopy, and low-temperature nitrogen adsorption/desorption enabling enabling us to correlate synthesis conditions (iron source and alkaline medium) with the phase composition, morphology, and textural properties of the goethite NPs prepared.

Experimental

Materials

In this work, the following reagents were used: iron(III) nitrate nonahydrate $Fe(NO_3)_3 \cdot 9H_2O$ (extra pure grade; Prime Chemicals Group, Russia); iron(III) chloride hexahydrate $FeCl_3 \cdot 6H_2O$ (extra pure grade; Krasnaya Zvezda Trading House, Russia); sodium hydroxide NaOH (analytical grade; Reachim, Russia); and ammonium hydroxide solution 25 % NH_4OH (extra pure grade; SigmaTek, Russia).

All the dry substances used were previously dissolved in deionized water with a certain molarity for subsequent syntheses.

Synthesis of Goethite NPs

Goethite (α-FeOOH) NPs were synthesized using three distinct approaches for the conversion of ferrihydrite suspensions: 1) Aging of ferrihydrite suspensions obtained by coprecipitation (Samples A-N and A-C); 2) Rapid transformation of ferrihydrite via ultrasonic irradiation (Samples U-N and U-C) [1]; 3) Hydrothermal treatment (Samples H-N and H-C) [34]. In all procedures, the pH was adjusted and maintained during all process at approximately 12 to ensure the dominance of hydroxo ions, which are essential for goethite formation. The iron precursors used were iron(III) nitrate ($Fe(NO_3)_3 \cdot 9H_2O$) and iron(III) chloride ($FeCl_3 \cdot 6H_2O$) [1], with specific precursors corresponding to different samples (e.g., Sample A-N used iron(III) nitrate, while Sample A-C used iron(III) chloride, and similar variations applied to other sample pairs).

Method 1.1 — Aging (Iron(III) Nitrate)

Goethite nanoparticles were prepared by the dropwise addition of 45 mL of 1.5 M NaOH to 5 mL of 0.06 M $Fe(NO_3)_3 \cdot 9H_2O$ at room temperature under constant stirring (100 rpm), while maintaining the pH at 12 during all process. The resulting ferrihydrite suspension was aged for 3 days at ambient conditions. The precipitate was then washed with deionized water until it reached a neutral pH, centrifuged (10 min, 3000 rpm), and dried in a desiccator at 60 °C for 24 hours. The final yield was 0.64 g.

Method 1.2 — Aging (Iron(III) Chloride)

This sample was synthesized following the same protocol as Method 1.1, but with $FeCl_3 \cdot 6H_2O$ used as the iron source. The yield was 0.75 g.

Method 2.1 — Ultrasonic Conversion (Iron(III) Nitrate)

A 5.625 M NaOH solution was added to 20 mL of 0.1 M $Fe(NO_3)_3 \cdot 9H_2O$ under continuous stirring (100 rpm) until the pH reached 12. The mixture was then subjected to ultrasonic treatment (30 kHz, 60 W, ultrasound bath, complete immersion of sample in a test tube in water) for 1 hour at 30 °C, pH was maintained during all process. The precipitate was washed with deionized water to neutral pH, centrifuged (10 min, 3000 rpm), and dried in a desiccator at 60 °C for 10 hours. The yield was 0.93 g.

Method 2.2 — Ultrasonic Conversion (Iron(III) Chloride)

This sample followed the same procedure as Method 2.1, using $FeCl_3 \cdot 6H_2O$ as the iron precursor. The final yield was 0.297 g.

Method 3.1 — Hydrothermal (Iron(III) Nitrate)

A total of 47 mL of 0.33 M $Fe(NO_3)_3 \cdot 9H_2O$ was mixed with 80 mL of 25 % NH_4OH, and the pH was adjusted to 12. The reaction mixture was heated at 90 °C for 2 hours without allowing vigorous boiling, pH was maintained during all process, then cooled to room temperature and left undisturbed for 24 hours. The solid was washed with deionized water until pH 6, centrifuged (15 min, 6000 rpm), and dried in a desiccator at 60 °C for 24 hours. The yield was 2.23 g.

Method 3.2 — Hydrothermal (Iron(III) Chloride)

This sample was synthesized using the same procedure as Method 3.1, replacing the nitrate salt with $FeCl_3 \cdot 6H_2O$. The yield was 2.95 g.

Table 1

Designations of samples and corresponding synthesis parameters

Method	Type of iron precursor	
	Cl^-	NO_3^-
Aging	A-C	A-N
Ultrasonic Conversion	U-C	U-N
Hydrothermal	H-C	H-N

Characteristics of Samples

X-ray Diffraction (XRD)

The crystal structure and phase composition of the synthesized NPs were analyzed by X-ray diffraction (XRD) using a Thermo Fisher Scientific ARL X'TRA diffractometer equipped with $Cu_{K\alpha}$ radiation (λ=1.54184 Å). Measurements were conducted over a 2θ range of 10–95° at a scanning speed of 5 deg/min and a temperature of 25 °C. The full width at half maximum (FWHM) was used for particle size determination with the Scherrer equation [29]. The diffraction patterns were processed using the Rietveld method in the Match! software. The final diffraction patterns were constructed in OriginPro software.

Mössbauer Spectroscopy

^{57}Fe Mössbauer absorption spectra (MS) were recorded in transmission geometry with a moving source and triangular velocity reference signal using an MS1104EM Mössbauer spectrometer (CJSC Kordon, Rostov-on-Don, Russia). Measurements were performed at 296(3) K and 77.7(3) K using a cryogen-free closed-cycle cryostat (CFPR-221-MESS). The γ-radiation source consisted of ^{57}Co in a metallic rhodium matrix (10 mCi activity; Cyclotron Co., Ltd, Obninsk, Russia) and was maintained at room temperature. An α-Fe foil was used as a reference absorber for velocity calibration. The signal-to-noise ratio did not exceed 2 %. High-resolution spectra (1024 channels) were processed using the SpectRelax 3.4 software package (Lomonosov Moscow State University, Russia). Isomer shifts are reported relative to α-Fe at 296 K.

Transmission Electron Microscopy (TEM)

The morphology of the NPs was examined using transmission electron microscopy (TEM). Prior to imaging, samples were dispersed in deionized water and sonicated with an ultrasonic processor (Fisherbrand, USA) at 75 % amplitude to promote homogenization and prevent aggregation. A 10 μL droplet of the suspension was deposited onto a 200-mesh carbon-coated copper grid (Ted Pella Inc., USA), which had been pretreated via glow discharge (PELCO Inc., USA) to enhance particle adhesion. After 1 minute of incubation at room temperature, excess liquid was blotted off with filter paper. The grids were mounted on the TEM stage, and imaging was performed using a Tecnai G2-20 transmission electron microscope (FEI Company, Hillsboro, OR, USA) operated at 120 kV. Particle size distributions were determined by analyzing at least 100 particles per image using ImageJ software (National Institutes of Health, USA).

Specific Surface Area and Porosity Analysis (BET/BJH)

The specific surface area (SSA) and porous structure characteristics of the samples were evaluated using a Sorbtometer-M instrument (Katakon, Russia). Measurements relied on nitrogen adsorption-desorption isotherms obtained at liquid nitrogen temperature (77 K). During testing, a stationary flow of a helium–nitrogen gas mixture (with the nitrogen volume fraction ranging from 0 to ≈1) was passed over the sample. Desorption isotherms were constructed by measuring the volume of nitrogen released upon heating (approximately −100 °C), while adsorption isotherms were obtained as the nitrogen volume fraction decreased from ≈1 to 0. SSA and pore structure parameters were calculated using the Brunauer–Emmett–Teller (BET) method and the Barrett–Joyner–Halenda (BJH) method, respectively. Prior to analysis, all samples underwent degassing ("thermoregulation") at 150 °C under vacuum in a stationary nitrogen flow to remove adsorbed gases and vapors.

Results and Discussion

Phase Composition (XRD)

The crystalline structure and phase composition of the synthesized NPs were comprehensively evaluated via X-ray diffraction (XRD). Representative diffractograms for all samples are presented in Figure 1. XRD analysis revealed that the final phase composition was highly sensitive to synthesis parameters, including the identity of the iron precursor, the nature of the alkaline medium, and the applied thermal conditions. Samples A-C and U-C were found to consist predominantly of goethite (α-FeOOH) [37], demonstrating that these specific synthesis routes effectively favored the crystallization of a monophasic product. In contrast, alternative conditions yielded more complex or multiphase systems. Sample A-N yielded primarily goethite with a minor secondary phase. This secondary component was identified by Mössbauer spectroscopy as a paramagnetic Fe^{3+} octahedral species (Fe^{3+}_{Oh}), typical of superparamagnetic iron oxyhydroxides.

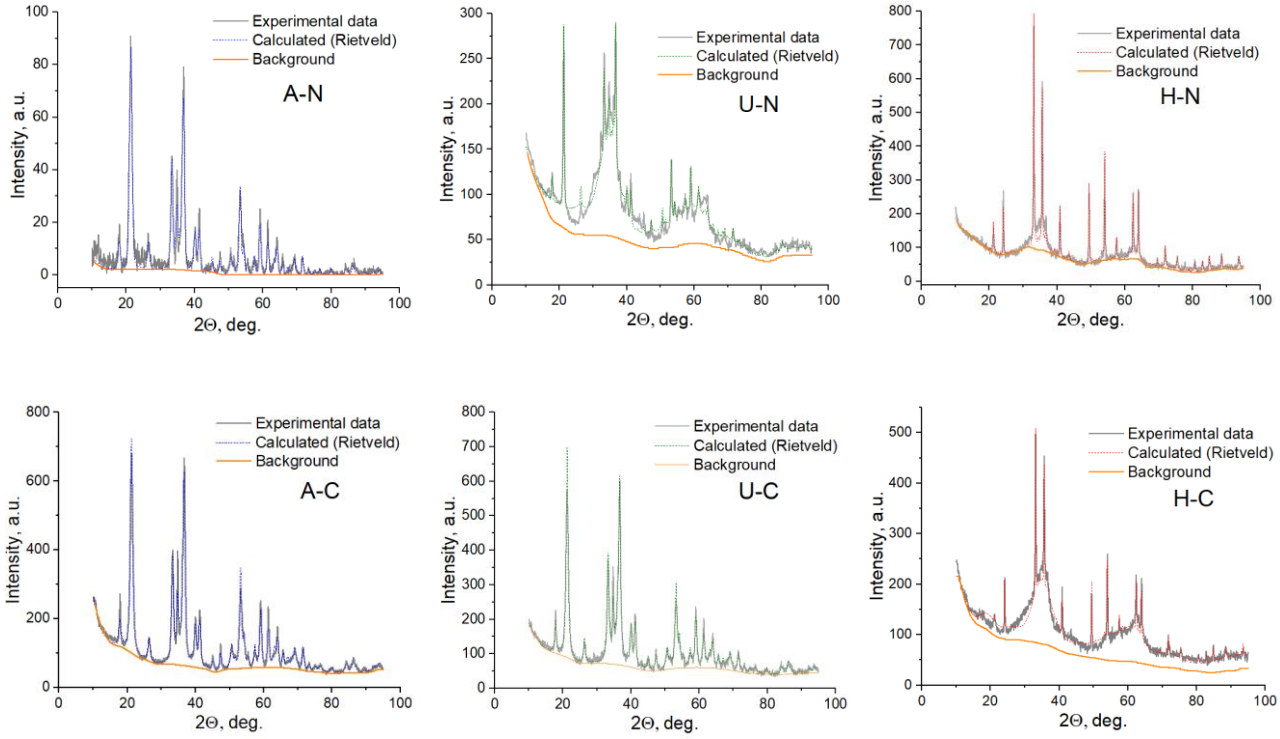

Figure 1. X-ray diffraction of synthesized iron (oxyhydr)oxide NPs

Sample U-N was dominated by ferrihydrite ($5Fe_2O_3 \cdot 9H_2O$), [38, 39] a poorly crystalline iron oxyhydroxide, as evidenced by its broad diffraction hump centered near 62° 2θ (Fig. 1), a hallmark of bilayer-type ferrihydrite [40]. Sample H-N displayed a well-defined crystalline pattern characteristic of hematite (α-Fe_2O_3), as indicated by sharp peaks near 32° 2θ (Fig. 1) [17]. Although minor goethite reflections were also detected around 20° 2θ, these were less pronounced, suggesting it formed as a secondary product under hydrothermal conditions [41]. Sample H-C exhibited the most complex phase composition. Its diffractogram revealed a mixture of ferrihydrite, hematite, and goethite, with the latter present only in minor quantities (Fig. 1). Collectively, these findings emphasize the pivotal role of synthesis design, particularly the iron salt identity, base selection, and thermal regime, in governing the crystallization and final properties of iron oxyhydroxide NPs.

Table 2

X-ray diffraction data for synthesized goethite NPs

Sample	*a*, Å	*b*, Å	*c*, Å	$(GoF)^2$	Composition	Amount, %	*D*, nm	No COD
A-N	4.607	9.945	3.019	1.2	α-FeOOH	79	13±4	9003078
A-C	4.616	9.945	3.021	0.8	α-FeOOH	96	15±5	1008768
U-N	6.175	–	9.205	0.9	$5Fe_2O_3 \cdot 9H_2O$	79	28±2	2211652
	4.606	9.971	3.023		α-FeOOH	20		9011571
U-C	4.617	9.996	3.024	0.9	α-FeOOH	96	18±6	9002158
H-N	5.037	–	13.765	1.1	α-Fe_2O_3	76	31±5	9000139
	4.671	9.392	3.028		α-FeOOH	18		9003079
H-C	6.118	–	9.062	0.9	$5Fe_2O_3 \cdot 9H_2O$	84	41±10	9011573
	5.038	–	13.778		α-Fe_2O_3	14		9000139
	4.603	10.098	3.022		α-FeOOH	1		9003077

Note: *GoF — goodness of fit, COD — Crystallography Open Database.

Phase Composition and Magnetic Properties (Mössbauer Spectroscopy)

To complement the crystallographic insights provided by XRD, detailed phase composition and magnetic behavior of the synthesized iron (oxyhydr)oxide NPs were examined using ^{57}Fe Mössbauer spectroscopy. Representative spectra for all samples are presented in Figure 2.

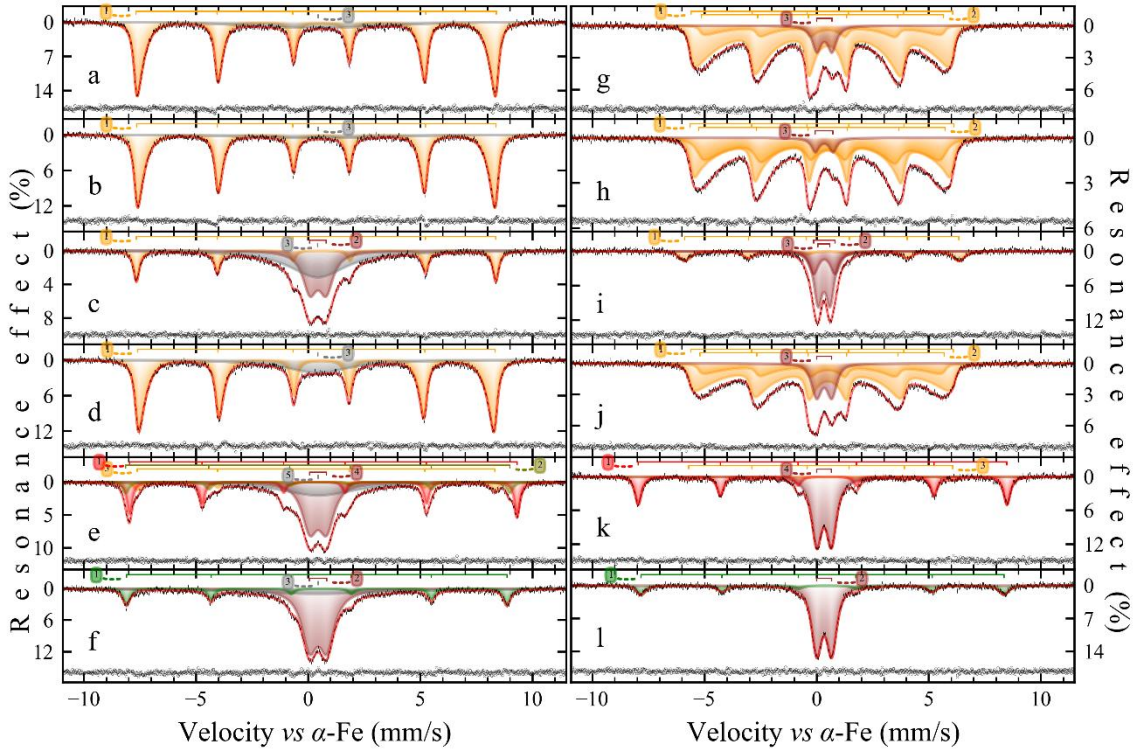

Figure 2. Mössbauer spectra of samples recorded at 78 K (*a*–*f*) and 296 K (*g*–*l*): A-N (*a*, *g*), A-C (*b*, *h*), U-N (*c*, *i*), U-C (*d*, *j*), H-N (*e*, *k*), and H-C (*f*, *l*). Subspectra are labeled in accordance with Table 3. Error bars for the experimental data points are shown; residuals obtained by subtracting the fitted model from the experimental spectra are displayed beneath each corresponding plot

The Mössbauer spectra exhibit pronounced temperature-dependent features, consistent with the known behavior of iron (oxyhydr)oxides [42–44] and nanostructured iron-containing phases [45–47]. In particular, Samples A-N, A-C, U-C, all of which were confirmed by XRD to consist primarily of goethite (79.4 %, 96.4 %, and 96 %, respectively), display sextets characteristic of magnetically ordered α-FeOOH. At 296 K (room temperature) (Fig. 2*f*, *h*), the spectra of these samples are dominated by heavily distorted sextets with broadened inner resonance lines, indicative of partial magnetic relaxation typical of nanocrystalline goethite.

Upon cooling to 78 K (liquid nitrogen temperature), these spectra evolve into more well-resolved, weakly distorted sextets with narrower lines (Fig. 2*a*, *c*), reflective of reduced thermal fluctuation and stronger magnetic ordering at low temperature. The observed behavior conforms to the many-state superparamagnetic relaxation model, [48] and the spectra were successfully fitted using two correlated relaxation sextets at 296 K and a single relaxation sextet at 78 K. The extracted hyperfine parameters align closely with literature values for goethite, [49–51] reinforcing its dominant presence in these samples. From these relaxation spectra, the ratio of magnetic anisotropy energy to thermal energy (α) was calculated using the relation:

$$\alpha = \frac{KV}{k_B T}, \tag{1}$$

where K is the magnetic anisotropy constant (assumed at 1×10^5 J m^{-3} at room temperature [52]), V is the magnetic domain volume, k_B is the Boltzmann constant, and T is the absolute temperature. Based on this model, estimated domain volumes were 114.9 nm^3 for Sample A-N and 100.5 nm^3 for Sample U-N, suggesting nanoscale magnetic domains typical of weakly interacting goethite NPs. In contrast, Samples U-N, H-N, H-C identified by XRD as mixed-phase systems, exhibited Mössbauer spectra at 296 K dominated by broad doublets superimposed on low-intensity sextets (Fig. 2*g*, *i*, *j*).

Upon cooling to 78 K (Fig. 2*b*, *d*, *e*), sextet intensity increased modestly while the doublets became broader and less distinct. These complex spectra were accurately fitted using a combination of singlets, doublets, and sextets modelled with pseudo-Voigt line shapes (Table 3). For Sample U-N, the sextet component, accounting for over 20 % of the total spectral area, was again attributed to goethite, consistent with its identification as the sole ferromagnetic phase. Sample H-N exhibited a lower goethite content (~7 %) but also revealed a distinct hematite (α-Fe_2O_3) contribution of at least 20 %, corroborated by its characteristic hyperfine field values [47, 51, 53]. In addition, at low temperature, an extra sextet emerged in Sample H-N whose parameters match those reported for ferroxyhite (δ-FeOOH), [42, 54, 55] indicating the presence of this metastable intermediate. Sample H-C presented a unique spectral profile. The dominant sextet observed at 78 K displayed hyperfine parameters that deviate from those of goethite or hematite, and were instead consistent with maghemite (γ-Fe_2O_3) [55–57]. The accompanying doublets and singlets, attributed to Fe^{3+} in octahedral coordination, are indicative of superparamagnetic or magnetically collapsed states, characteristic of nanosized ferrihydrite or disordered phases. Overall, the Mössbauer data affirm the strong influence of synthesis conditions not only on phase composition but also on magnetic domain properties, underscoring the intricate interplay between chemical environment, thermal treatment, and NPs magnetism.

Table 3

Hyperfine parameters derived from Mössbauer spectra of iron (oxyhydr)oxide samples recorded at different temperatures

Temperature, K		77.7(3)							296(3)							
Sample	№	*δ	ε {Δ=2ε}	Γ_{exp}	H_{eff}	S	α	Site/Phase	№	δ	ε {Δ=2ε}	Γ_{exp}	H_{eff}	S	α	Site/Phase
		mm s^{-1}			kOe	%				mm s^{-1}			kOe	%		
A-N	1	0.48	–0.11	0.30	498.23	83.6	16.9	α-FeOOH	1	0.37	–0.13	0.29	361.8	75.8	2.81	α-FeOOH
									2	0.38	–0.12	0.29	334.6	16.2		
	3	0.45		6.98		16.4		Fe^{3+}_{Oh}	3	0.34	{0.67}	0.483		7.95		Fe^{3+}_{Oh}
A-C	1	0.48	–0.11	0.31	496.85	87.9	17.9	α-FeOOH	1	0.37	–0.13	0.24	364.9	56	3.135	α-FeOOH
									2	0.36	–0.13	0.52	340.6	40		
	3	0.45		7.2		12.1		Fe^{3+}_{Oh}	3	0.34	{0.79}	0.42		3.72		Fe^{3+}_{Oh}
U-N	1	0.48	–0.12	0.32	496.96	21.31		α-FeOOH	1	0.37	–0.13	0.617	379.2	26.5		α-FeOOH
	2	0.44	{0.73}	0.772		32.6		Fe^{3+}_{Oh}	2	0.34	{0.96}	0.51		24		Fe^{3+}_{Oh}
	3	0.426		3.09		46.1		Fe^{3+}_{Oh}	3	0.33	{0.532}	0.452		49		Fe^{3+}_{Oh}
U-C	1	0.48	–0.11	0.31	494.54	75.1	15.74	α-FeOOH	1	0.37	–0.12	0.31	363.3	64.9	2.459	α-FeOOH
									2	0.36	–0.12	0.31	337.6	23.1		
	3	0.436		3.52		24.9		Fe^{3+}_{Oh}	3	0.33	{0.67}	0.54		12.0		Fe^{3+}_{Oh}
H-N	1	0.48	0.20	0.30	535.96	20.1		α-Fe_2O_3	1	0.37	–0.10	0.36	509.90	34.5		α-Fe_2O_3
	2	0.48	–0.05	0.354	531.0	8.1		δ-FeOOH								
	3	0.47	–0.12	0.388	494.5	6.7		α-FeOOH	3	0.35	–0.17	0.76	364.8	7.0		α-FeOOH
	4	0.44	{0.75}	0.826		37.2		Fe^{3+}_{Oh}	4	0.33	{0.66}	0.55		58.5		Fe^{3+}_{Oh}
	5	0.453		4.03		27.9		Fe^{3+}_{Oh}								
H-C	1	0.48	–0.10	0.384	526.07	16.1		γ-Fe_2O_3	1	0.37	–0.10	0.520	501.8	21.4		γ-Fe_2O_3
	2	0.44	{0.77}	0.839		57.4		Fe^{3+}_{Oh}	2	0.34	{0.67}	0.54		78.6		Fe^{3+}_{Oh}
	3	0.45		7.8		26.5		Fe^{3+}_{Oh}								

* δ is the isomer shift, ε (Δ=2ε) is the quadrupole shift (splitting), Γ_{exp} is the line width, H_{eff} is the hyperfine magnetic field, S is the relative area of the subspectrum, α is as (1)

Structural Evolution and Morphological Features of Synthesized NPs

The results of the XRD and Mössbauer spectroscopy data processing confirms that controlled synthesis through the dissolution–recrystallization of thermodynamically unstable ferrihydrite leads predominantly to goethite (α-FeOOH) NPs formation under suitable conditions. Ferrihydrite, a poorly crystalline iron oxide typically approximated by the formula $5Fe_2O_3 \cdot 9H_2O$, [8] is widely recognized as the first-formed phase during iron(III) hydrolysis. However, its exact stoichiometry remains debated. The physicochemical parameters governing its transformation have been thoroughly investigated by Schwertmann et al., [14, 16] who demonstrated that the final phase (goethite vs. hematite) is strongly dependent on pH and can proceed via either a dissolution–precipitation mechanism or solid-state transformation.

Cudennec et al. [16] provided further mechanistic insights into goethite formation by comparing the crystallographic frameworks of relevant intermediates. In our study, the role of precursor chemistry emerged as a significant factor influencing both phase composition and morphology. For instance, in Sample A-N, an additional phase, identified as a paramagnetic Fe^{3+} component, was observed alongside goethite (79.4 %), likely resulting from the slower dissociation kinetics of $Fe(NO_3)_3$ compared to $FeCl_3$. This delay in hydrolysis could favor the formation of metastable iron oxyhydroxide phases.

Temperature also exerted a profound influence on phase evolution. In hydrothermal syntheses, elevated temperatures not only accelerated hydrolysis and crystallization kinetics but also altered the redox dynamics of Fe species and facilitated active oxygen species generation, especially under ultrasonic irradiation [1]. These thermal conditions favored the formation of hematite (α-Fe_2O_3), [16] particularly in systems using the weaker base NH_4OH, which may suppress the formation of strongly basic iron hydroxides and thus shift the equilibrium toward oxide phases. Collectively, these parameters shaped not only the phase composition but also the particle morphology.

Morphological Analysis by TEM

Transmission Electron Microscopy (TEM) imaging (Fig. 3) revealed strong correlations between synthesis conditions and NPs morphology.

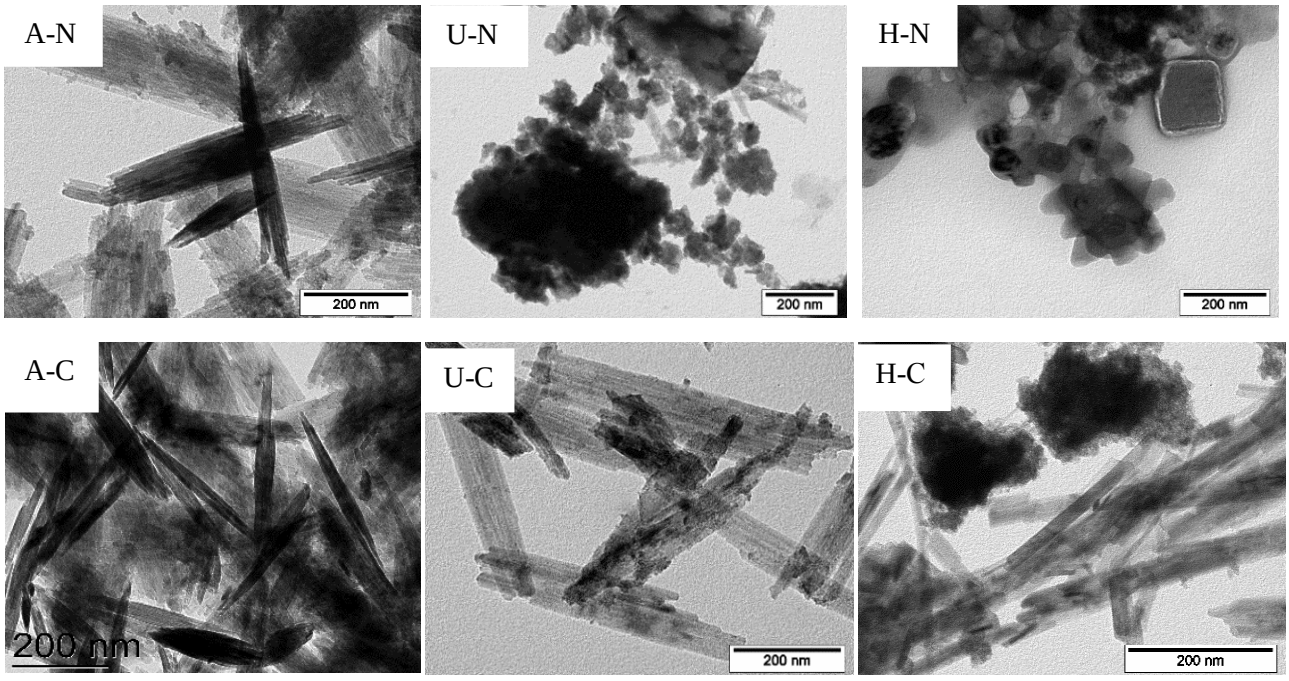

Figure 3. Transmission electron microscopy (TEM) images of iron (oxyhydr)oxide NPs samples

Samples A-N, A-C, and U-C, which were identified as predominantly goethite by XRD and Mössbauer spectroscopy, exhibited the characteristic acicular (needle-like) or rod-like morphologies typical of α-FeOOH [58–61]. These results are consistent with the observations of Maria et al. [1] (particularly for aging and hydrothermal pathways, despite our use of ferric (III) chloride hexahydrate instead of ferric (III) nitrate nonahydrate) and Mira et al. [20], who also reported needle-shaped goethite NPs formed via comparable synthesis routes. Sample U-C, although morphologically similar to A-N and A-C, displayed slightly less-defined

crystallinity and structural uniformity. This effect is likely attributable to the mechanical stresses induced by ultrasonic treatment, which may introduce lattice defects or disrupt ordered growth.

Interestingly, Sample H-C, despite containing only 1 % goethite according to XRD and being primarily composed of ferrihydrite (84.3 %) and hematite (14.7 %), also exhibited rod-like structures. This suggests that even minor amounts of goethite may dictate the overall particle morphology, either through templated growth or preferential aggregation within mixed-phase systems.

Sample U-N presented a markedly different appearance. As shown in Figure 3, it consists mainly of disordered aggregates resembling amorphous or nanocrystalline ferrihydrite, [38] consistent with its high ferrihydrite content (79.7 % by XRD) and the presence of broad doublets in its Mössbauer spectrum.

The morphology of Sample H-N (Fig. 3) closely resembles that of hematite, typically reported as rhombohedral or diamond-like in shape [62]. This observation correlates well with the high α-Fe_2O_3 content determined by XRD (76.7 %) and Mössbauer analysis. Previous studies [63, 64] have shown that mixed goethite–hematite systems often form agglomerates in which distinct phases are not easily differentiated, particularly at elevated synthesis temperatures (e.g., 90 °C). Similar dual-phase morphologies were reported by Combes et al. [65] and observed again by Vu et al. [66], supporting the inference that hematite dominates the particle shape in these hybrid systems.

Consistent with these findings, the morphology of Sample H-N reflects its dual composition, 7 % goethite and >20 % hematite. Despite this complexity, nanocrystalline domains with an average length of 78 ± 28 nm were readily distinguished via TEM imaging (Fig. 3), suggesting partial phase separation and crystallite coarsening within the sample.

Particle Size Distribution and Polydispersity

Although Samples A-N (79.4 % goethite), A-C (96.4 % goethite), and U-C (96 % goethite) share a predominantly goethite composition, their particle size distributions reveal notable differences influenced by synthesis conditions, particularly the application of ultrasonic treatment. Sample U-C, synthesized via ultrasonic conversion, exhibited the broadest size distribution, with an average particle length of 560 ± 105 nm and width of 85 ± 24 nm. In contrast, Sample A-N yielded particles with a length of 476 ± 83 nm and width of 113 ± 27 nm, while Sample A-C produced more compact particles, averaging 389 ± 75 nm in length and 93 ± 28 nm in width (Fig. 4).

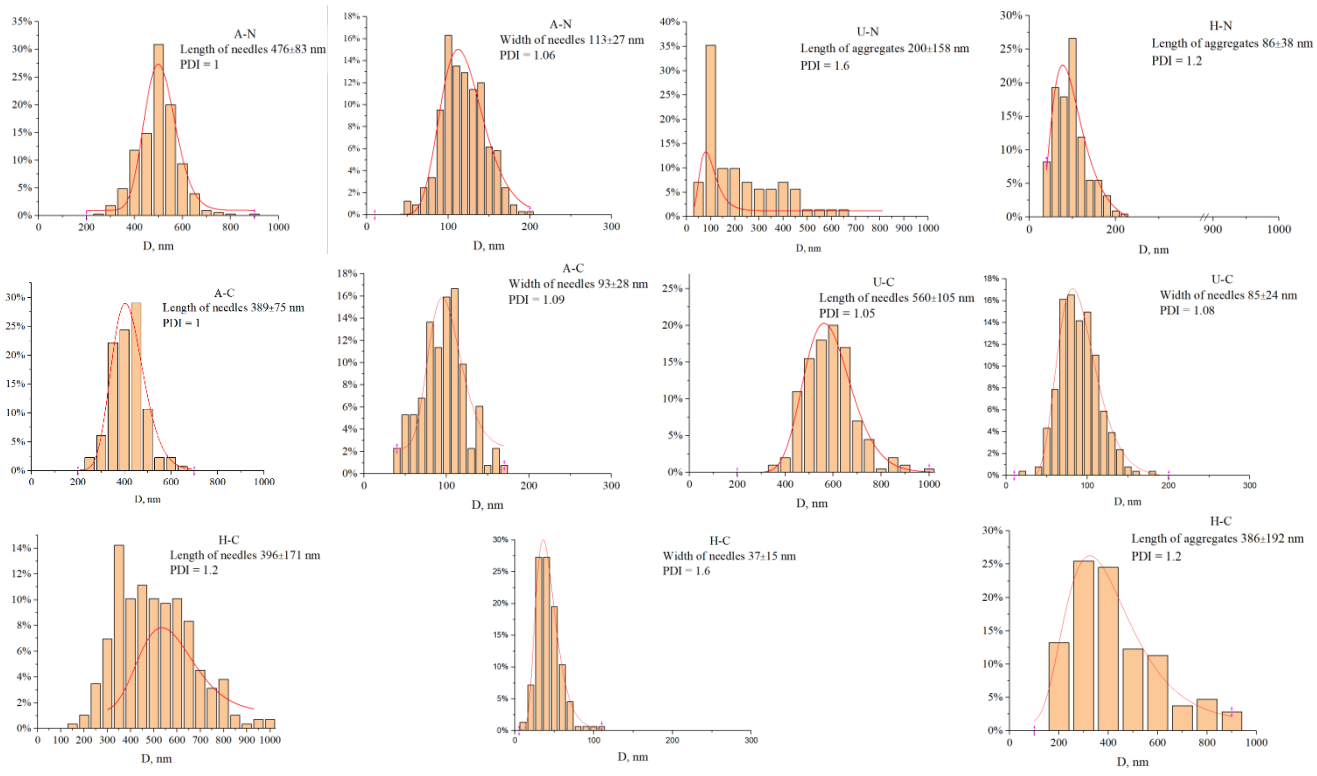

Figure 4. Particle size distribution of iron (oxyhydr)oxide NPs

The broader distribution in Sample U-C likely reflects the cavitation-driven fragmentation and nucleation associated with ultrasonic treatment, which can both promote particle refinement and introduce heterogeneity. Interestingly, Sample U-N, also prepared under ultrasonic conditions, exhibited a markedly narrower size distribution. This observation suggests that the nature of the precipitated phase plays a critical role in determining the effect of ultrasound on particle dispersion and growth kinetics. The homogeneity of particle size distribution was assessed by calculating the polydispersity index:

$$K_p = \frac{\partial}{\Delta}, \quad (2)$$

where K_p is the polydispersity index (PDI), ∂ is the weighted average particle radius (accounting for the relative abundance of each particle size), and Δ is the arithmetic mean radius. A PDI value near 1 indicates a highly monodisperse population, whereas values approaching or exceeding 2 signify broader and more heterogeneous distributions.

Considering the effect of iron salt ions (Cl^- and NO_3^-) on the polydispersity of goethite NPs, it can be assumed that the use of nitrate ions leads to the formation of monodisperse needle-shaped forms (PDI = 1.0–1.2). Chloride ions observe the aggregation of particles with PDI = 1.6. Samples A-N and A-C, obtained via low-temperature aging of ferrihydrite, exhibited PDI values of 1.0, indicating exceptional homogeneity and monodispersity.

The most uniform particle populations were still obtained under room-temperature aging conditions (Samples A-N and A-C), reinforcing the value of controlled, low-energy precipitation pathways in producing well-defined goethite nanocrystals.

Conversely, broader distributions were observed in Samples U-N (PDI = 1.6), H-N (PDI = 1.2), and H–C (PDI = 1.6), corresponding to syntheses involving elevated temperatures and/or hydrothermal treatment. These higher PDI values reflect not only greater size variability but also increased morphological and compositional heterogeneity, emphasizing the cumulative influence of precursor type, basic agent, temperature, and reaction time on NPs uniformity.

Textural Characteristics (BET/BJH Analysis)

The textural properties of the synthesized NPs were investigated using nitrogen adsorption–desorption isotherms at liquid nitrogen temperature, with results summarized in Figure 5.

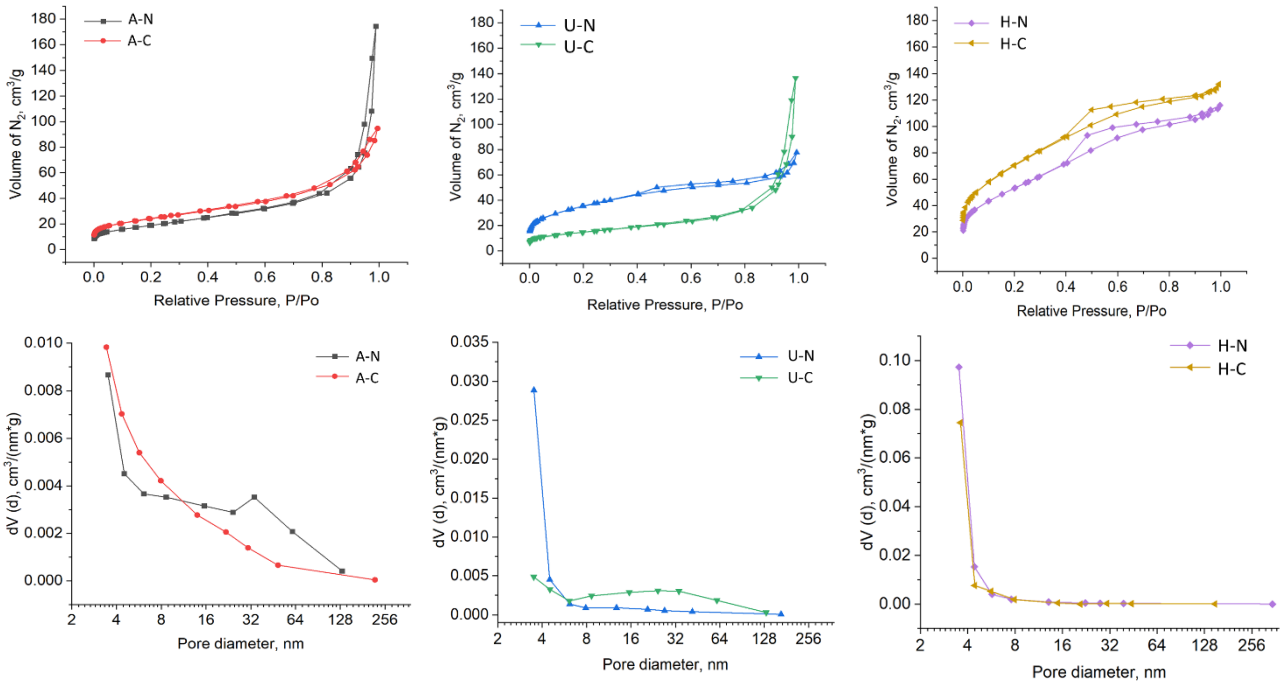

Figure 5. Low-temperature (77 K) nitrogen adsorption/desorption isotherms and corresponding pore size distribution of iron (oxyhydr)oxide samples

According to the International Union of Pure and Applied Chemistry (IUPAC) classification, all samples exhibit Type IV isotherms, characteristic of mesoporous materials, indicating multilayer adsorption and the occurrence of capillary condensation within mesopores.

Distinct hysteresis loop types were observed across different synthesis methods, reflecting variations in pore structure. Samples A-N and U-C displayed H3-type hysteresis loops, typically associated with cavitation-controlled evaporation processes and slit-like pores formed between non-rigid aggregates of plate-like particles. In contrast, Samples U-N, H-N, and H-C demonstrated H4-type hysteresis, also indicative of slit-shaped pores but more commonly associated with narrow, micropore-like structures within porous solids.

In several samples, a pronounced uptake at low relative pressures ($P/P_0 < 0.1$) suggests the presence of micropores. Moreover, the absence of a plateau near $P/P_0 \approx 1$ implies an open pore network with interparticle voids, lacking closed porosity. The SSA values calculated using the Brunauer–Emmett–Teller (BET) method, and average pore diameters, determined via the Barrett–Joyner–Halenda (BJH) model (Table 4), further elucidate the differences among samples. The goethite-dominant samples (A-N, A-C and U-C) exhibited moderately high SSA values ranging from 53 to 88 $m^2 g^{-1}$. These values are consistent with samples demonstrating the needle-like morphology observed in TEM micrographs and are typical of well-crystallized goethite NPs with defined mesoporosity.

Table 4

Textural properties of samples

Sample	BET		BJH	
	SSA, $m^2 g^{-1}$	Pore volume, $cm^3 g^{-1}$	Pore volume, $cm^3 g^{-1}$	Pore diameter, nm
A-N	69.0	0.27	0.26	3.51
A-C	87.8	0.15	0.12	3.40
U-N	127.8	0.12	0.07	3.52
U-C	52.5	0.21	0.20	3.44
H-N	198.5	0.18	0.12	3.52
H-C	260.5	0.20	0.11	3.60

In contrast, the heterophase samples (U-N, H-N, and H-C), which contain various combinations of ferrihydrite, hematite (H-N and H-C) in addition to goethite, showed more variable SSA values. Notably, Sample H-C exhibited the highest SSA (260 $m^2 g^{-1}$) among all samples, which can be attributed to its ferrihydrite-rich composition and greater contribution of microporous features.

As reported by Kail et al. [68], while high SSA generally offers more sites, goethite with a relatively lower SSA can sometimes exhibit increased surface roughness or defects, which may enhance sorption efficiency by providing highly accessible active sites for adsorbate interaction. Conversely, high SSA values (as observed in Samples A-C, U-N, H-N, and H-C) often stem from microporous structures, which can impose diffusional constraints. The slow diffusion kinetics within narrow pores may, in certain applications, limit sorption efficiency despite the higher available SSA [69].

These findings underscore the importance of not only maximizing SSA in sorptive materials but also tailoring pore architecture and morphology to optimize accessibility and transport within the porous network.

Conclusions

This study provides a comprehensive framework for understanding the physicochemical principles that govern the controlled synthesis of biocompatible, phase-pure goethite (α-FeOOH) nanoparticles with tunable structural and morphological features. By systematically exploring multiple synthesis routes, including variations in temperature, reaction time, and ultrasonic treatment, and for the first time, precursor type (iron nitrate vs. chloride), alkalizing agent (NH_4OH vs. NaOH), we have elucidated the critical parameters that dictate nanoparticle formation pathways and final properties.

Our results highlight that the choice of iron source and alkali was found to be equally consequential: $FeCl_3$ and NaOH facilitated rapid hydrolysis and crystallization, promoting goethite formation, whereas NH_4OH, particularly under hydrothermal conditions, often led to multiphase systems involving ferrihydrite and hematite.

Regardless of iron source and alkalizing agent, temperature emerged as a dominant factor in driving crystal growth and phase transitions. Hydrothermal treatments at 90 °C resulted in markedly increased parti-

cle sizes and more complex phase compositions, underscoring the importance of kinetic control in phase-selective synthesis.

Collectively, these findings advance the rational design of iron (oxyhydr)oxide nanoparticles by providing actionable insights into how synthesis variables, namely iron and alkali source translate into structural and functional outcomes. The ability to tailor goethite nanomaterials with predictable microstructures positions them as promising candidates for a wide spectrum of applications, including biomedical scaffolds, catalysis, nanoscale sorbents. This work thus lays the groundwork for the future development of safe, functionally optimized iron-based nanomaterials with high application relevance.

Funding

The study was supported by a grant from the Russian Science Foundation (No. 24-14-20030, "Assessment of the negative impact of oil pollution on natural microbiocenoses by methods of bioassay and molecular dynamics", https://rscf.ru/en/project/24-14-20030/).

*Author Information**

**The authors' names are presented in the following order: First Name, Middle Name and Last Name*

Sofia Magomadaevna Mulyukina (*corresponding author*) — 3th year PhD Student, Department of Chemistry — Surgut State University, 628403, Surgut, Russia; e-mail: sbolotskaya@inbox.ru; https://orcid.org/0009-0003-9530-4241

Artur Albertovich Dzeranov — Assistant Professor, Department 903 ―Advanced Materials and Technologies for Aerospace Applications, Moscow Aviation Institute (National Research University), 125993, Moscow, Russia; Junior Research Fellow of Laboratory of metal polymers, Federal Research Center of Problems of Chemical Physics and Medicinal Chemistry, Russian Academy of Sciences, Semenov avenue, 1, 142432, Chernogolovka, Moscow region, Russia; e-mail: arturdzeranov99@gmail.com; https://orcid.org/0000-0003-3240-9321

Denis Alexandrovich Pankratov — PhD in Chemical Sciences, Department of Chemistry, Lomonosov Moscow State University, 119991, Moscow, Russia; Moscow Institute of Physics and Technology (National Research University), Institutskii per. 9, 141701, Dolgoprudny, Russia; e-mail: pankratov@radio.chem.msu.ru, https://orcid.org/0000-0001-6557-2753

Lyubov Sergeevna Bondarenko — PhD in Chemical Sciences, Associate Professor, Department 903 ―Advanced Materials and Technologies for Aerospace Engineering, Moscow Aviation Institute (National Research University), 125993, Moscow, Russia; e-mail: l.s.bondarenko92@gmail.com; https://orcid.org/0000-0002-3107-0648

Gulsara Damirovna Kugabaeva — 4th year PhD Student, Moscow Aviation Institute (National Research University), 125993, Moscow, Russia, Federal Research Center of Problems of Chemical Physics and Medicinal Chemistry, Russian Academy of Sciences, Moscow Region, Russia; e-mail: gulsara_kugabaev@mail.ru, https://orcid.org/0009-0006-7749-6384

Mikhail Vladimirovich Prokofiev — PhD in Chemical Sciences, Department 903 ―Advanced Materials and Technologies for Aerospace Applications, Moscow Aviation Institute (National Research University), 125993, Moscow, Russia; e-mail: mikepro1953@rambler.ru

Kamila Asylbekovna Kydralieva — Doctor of Chemical Sciences, Department 903 ―Advanced Materials and Technologies for Aerospace Applications, Moscow Aviation Institute (National Research University), 125993, Moscow, Russia; e-mail: kamila.kydralieva@gmail.com; https://orcid.org/0000-0002-4596-4140

Author Contributions

The manuscript was written through contributions of all authors. All authors have given approval to the final version of the manuscript. CRediT: **Sofia Magomadaevna Mulyukina**: Investigation, Software; **Artur Albertovich Dzeranov**: Investigation, Writing, Editing; **Denis Alexandrovich Pankratov**: Investigation, Writing; **Lyubov Sergeevna Bondarenko**: Writing, Software; **Gulsara Damirovna Kugabaeva**: Investiga-

tion; **Mikhail Vladimirovich Prokofiev**: Investigation; **Kamila Asylbekovna Kydralieva**: Conceptualization, Data curation, Methodology, Writing — Reviewing and Editing.

Acknowledgments

The Mössbauer spectroscopy analysis was conducted as part of the state assignment of *Lomonosov Moscow State University*, "Solving problems of nuclear energy and environmental safety, as well as diagnostics of materials using ionizing radiation" (No. 122030200324-1). Low-temperature nitrogen adsorption measurements were performed in accordance with the state research assignments registered under No. 124013000757-0. These experiments were carried out using the facilities of *the Multi-User Analytical Center of the Federal Research Center of Problems of Chemical Physics and Medicinal Chemistry of the Russian Academy of Sciences*.

Declaration of Generative AI and AI-Assisted Technologies in the Writing Process

During the preparation of this work, the authors used grammar-checking tools (Grammarly and equivalent standard proofreading instruments) only to refine the language of the manuscript. After using these tools, the authors thoroughly reviewed and edited the text as needed and take full responsibility for the content of the publication.

Conflicts of Interest

The authors declare no conflict of interest.

References

1 Martina, M. R., Zoli, L., Sani, E. (2022). Synthesis and characterization of goethite (α-FeOOH) magnetic nanofluids. *International Journal of Thermofluids*, *15*, 100169. https://doi.org/10.1016/j.ijft.2022.100169

2 Kubiak, A., Voronkina, A., & Jesionowski, T. (2023). Creation of a 3D Goethite–Spongin Composite Using an Extreme Biomimetics Approach. *Biomimetics*, *8*, 533. https://doi.org/10.3390/biomimetics8070533

3 Nowacki, K., Kubiak, A., & Jesionowski, T. (2024). 3D Spongin Scaffolds as Templates for Electro-Assisted Deposition of Selected Iron Oxides. *Biomimetics*, *9*, 387. https://doi.org/10.3390/biomimetics9070387

4 Shi, Z., Zachara, J.M., & Fredrickson, J.K. (2012). Redox Reactions of Reduced Flavin Mononucleotide (FMN), Riboflavin (RBF), and Anthraquinone-2,6-disulfonate (AQDS) with Ferrihydrite and Lepidocrocite. *Environmental Science & Technology*, *46* (21), 11644–11652. https://doi.org/10.1021/es301544b

5 Zhourui, L., Manisha, M., Yichao, W., Qiaoyun, H., Peng C. (2021). Increased particle size of goethite enhances the antibacterial effect on human pathogen Escherichia coli O157:H7: A Raman spectroscopic study. Journal of Hazardous Materials, 405, 124174. https://doi.org/10.1016/j.jhazmat.2020.124174

6 Kosei, I., Eiji, A., Oluyomi, S. A. & (2024). Goethite and Hematite Nanoparticles Show Promising Anti-Toxoplasma Properties. *Pharmaceutics*, *16* (3), 413. https://doi.org/10.3390/pharmaceutics16030413

7 Dulnee, S., Scheinost, A.C. (2014). Surface Reaction of SnII on Goethite (α-FeOOH): Surface Complexation, Redox Reaction, Reductive Dissolution, and Phase Transformation. *Environmental Science & Technology*, *48* (16), 9341–9348. https://doi.org/10.1021/es501923z

8 Lin, Y.L., Wei, Y., Sun, Y.H. (2012). Room-temperature synthesis and photocatalytic properties of lepidocrocite by monowavelength visible light irradiation. *Journal of Molecular Catalysis A: Chemical*, *353–354*, 67–73. https://doi.org/10.1016/j.molcata.2011.11.006

9 Tiar, K., Soualah, A., Bisio, C., Guidotti, M. (2024). Effect of initial solution pH on 4-nitrophenol oxidation through homogeneous/heterogeneous photo-Fenton process using goethite/H_2O_2 system. *Journal of Photochemistry and Photobiology A: Chemistry*, *447*, 115184. https://doi.org/10.1016/j.jphotochem.2023.115184

10 Li, X., Niu, A., Yang, S. (2024). The reduction of nitrobenzene by Fe(II)-goethite-hematite heterogeneous systems: Insight from thermodynamic parameters of reduction potential. *Journal of Environmental Management*, *370*, 122404. https://doi.org/10.1016/j.jenvman.2024.122404

11 Liu, G., Yu, H., Zhou, T. (2022). Activation of peroxydisulfate by biogenic nanocomposites of reduced graphene oxide and goethite for non-radical selective oxidation of organic contaminants: Production of singlet oxygen and direct electron transfer. *Chemical Engineering Journal*, *430*, 133177. https://doi.org/10.1016/j.cej.2021.133177

12 Montes-Hernandez, G., Beck, P., & Findling, N. (2011). Fast precipitation of acicular goethite from ferric hydroxide gel under moderate temperature (30 and 70 C degrees). *Crystal Growth & Design*, *11* (6), 112264–2272. https://doi.org/10.1021/cg1016802

13 Gilbert, F., Refait, P., C., & Conforto, E. (2008). Synthesis of goethite from $Fe(OH)_2$ precipitates: Influence of Fe(II) concentration and stirring speed. *Journal of Physics and Chemistry of Solids*, *69* (8), 2124-2130. https://doi.org/10.1016/j.jpcs.2008.03.010

14 Oulego, P., Villa-García, M.A., Lacaa, A., Diaz, M. (2016). Effect of the synthetic route on the structural, textural, morphological and catalytic properties of Iron (III) oxides and oxyhydroxides. *Dalton Transactions*, 45, 9446–9459. 10.1039/C6DT00247A

15 Kuncser, A.C., Vlaicu, I.D., Pavel, O.D., Olar, R. (2021). Soft synthesis and characterization of goethite-based nanocomposites as promising cyclooctene oxidation catalysts. *RSC Advances*, *11*, 27589-27602. https://doi.org/10.1039/D1RA04211D

16 Cudennec, Y., Lecerf, A. (2006). The transformation of ferrihydrite into goethite or hematite, revisited. *Journal of Solid State Chemistry*, *179* (3), 716–722. https://doi.org/10.1016/j.jssc.2005.11.030

17 Alves, C.A.P., Palharim, P.H., & Ramos, B. (2025). Photocatalytic ammonia synthesis from nitrogen in water using iron oxides: Comparative efficiency of goethite, magnetite, and hematite. *Journal of Photochemistry and Photobiology A: Chemistry*, *460*, 116159. https://doi.org/10.1016/j.jphotochem.2024.116159

18 Adeoye A. O., Quadri, R. O., Lawal, O. S. (2023). Wet synthesis, characterization of goethite nanoparticles and its application in catalytic pyrolysis of palm kernel shell in TGA. *Results in Surfaces and Interfaces*, *11*, 100118. https://doi.org/10.1016/j.rsurfi.2023.100118

19 Kosmulski, M., Maczka, E., Jartych, E., Rosenholm, J. B. (2003). Synthesis and characterization of goethite and goethite–hematite composite: experimental study and literature survey. *Advances in Colloid and Interface Science*, *103* (1), 57–76. https://doi.org/10.1016/S0001-8686(02)00083-0

20 Hinrichs, S., Grossmann, L., & Hankiewicz, B. (2020). Goethite Nanorods: Synthesis and Investigation of the Size Effect on Their Orientation within a Magnetic Field by SAXS. *Nanomaterials*, *10* (12), 2526. https://doi.org/10.3390/nano10122526

21 Mohapatra M., Gupta S., & Mishra B.K. (2010). pH and temperature dependent facile precipitation of nano-goethite particles in $Fe(NO_3)_3$–NaOH–$NH_3NH_2HSO_4$–H_2O medium. *Colloids and Surfaces A: Physicochemical and Engineering Aspects*, 355 (1-3), 53–60. https://doi.org/10.1016/j.colsurfa.2009.11.029

22 Meret, A., Ralf, K., & Ruben, K. (2019). Electrochemical Analysis of Changes in Iron Oxide Reducibility during Abiotic Ferrihydrite Transformation into Goethite and Magnetite. *Environmental Science & Technology*, *53* (7), 3568–3578. https://doi.org/10.1021/acs.est.8b07190

23 Mira, R., Ivana, O., Svetozar, M. (2013). The synthesis and microstructure of goethite particles precipitated in highly alkaline media. *Journal of Alloys and Compounds*, *559*, 49–56. https://doi.org/10.1016/j.jallcom.2013.01.027

24 Xu, Y., Wang, H., Ye, S., et al. (2024). Goethite adaptation prompts alterations in antibiotic susceptibility and suppresses development of antibiotic resistance in bacteria. *Science of The Total Environment*, *916*, 170248. https://doi.org/10.1016/j.scitotenv.2024.170248

25 Agresti, F., Isopi, J., Scattareggia Marchese, S., et al. (2025). Electrorheology of urea-functionalized lathlike goethite particles in silicone oil. *Colloids and Surfaces A: Physicochemical and Engineering Aspects*, *704*, 135509. https://doi.org/10.1016/j.colsurfa.2024.135509

26 Lyane, M.D., Gustavo, R.G., Miguel, A.S. Jr. (2022). Synthesis of nanostructured iron oxides and study of the thermal crystallization process using DSC and in situ XRD experiments. *Materials Chemistry and Physics*, *285*, 126065. https://doi.org/10.1016/j.matchemphys.2022.126065

27 Zhang, Y-X., Jia, Y. (2014). A facile solution approach for the synthesis of akaganéite (β-FeOOH) nanorods and their ion-exchange mechanism toward As (V) ions. *Applied Surface Science*, *290*, 102-106. https://doi.org/10.1016/j.apsusc.2013.11.007

28 Jia, Y., Luo, T., & Huang, X.J. (2013). Facile one-pot synthesis of lepidocrocite (γ-FeOOH) nanoflakes for water treatment. *New Journal of Chemistry*, *37* (8), 2551–2556. doi: http://dx.doi.org/10.1039/c3nj00509g

29 Fang F., Jia Y., Wu P-Y., & Peng D-Y. (2015). Facile one-pot preparation of goethite/parabutlerite nanocomposites and their removal properties and mechanism toward As(V) ions. *Applied Surface Science Journal*, *324*, 355–362. https://doi.org/10.1016/j.apsusc.2014.10.174

30 Ma, J., Zhang, X., He, Y., et al. (2015). Non-superparamagnetic iron-oxide architectures with controlled T_2 contrast ability in magnetic resonance imaging. *Applied Physics Letters*, *107*, 073701. https://doi.org/10.1063/1.4928914

31 Kang, S., Kim, G., Cheon, J. (2025). Corrugated-Surface Goethite Nanoparticles with Reduced Magnetization and Increased Surface Area for Enhanced T_1 MRI Contrast Effect. *ACS Applied Materials & Interfaces*, *17*(49), 66450–66459. https://doi.org/10.1021/acsami.5c18713

32 Serup, J., Alsing, K.K., Olsen, O., et al. (2023). On the mechanism of painful burn sensation in tattoos on magnetic resonance imaging (MRI). Magnetic substances in tattoo inks used for permanent makeup (PMU) identified: Magnetite, goethite, and hematite. *Skin Research and Technology*, *29*(3), e13281. https://doi.org/10.1111/srt.13281

33 Gulzar, A., Ayoub, N., Mir, J.F., et al. (2022). In vitro and in vivo MRI imaging and photothermal therapeutic properties of Hematite (α-Fe2O3) Nanorods. *Journal of Materials Science: Materials in Medicine*, *33* (10). https://doi.org/10.1007/s10856-021-06636-1

34 Lunin, A.V., Kolychev, E.L., & Nikitin, M.P. (2019). Synthesis of highly-specific stable nanocrystalline goethite-like hydrous ferric oxide nanoparticles for biomedical applications by simple precipitation method. *Journal of Colloid and Interface Science*, *541*, 143–149. https://doi.org/10.1016/j.jcis.2019.01.065

35 Balzar, D., Audebrand, N., Daymond, M. R., Toby, B. H. (2004). Size-strain line-broadening analysis of ceria round-robin sample. *Journal of Applied Crystallography*, *37*, 911–924. https://doi.org/10.1107/S0021889804022551

36 Nikolaeva, O.V., Terekhov, V.A. (2017). Improvement of laboratory phytotest for the ecological evaluation of soils. *Eurasian Soil Science*, *50*, 1105-1114. 10.1134/S1064229317090058

37 Skalny, M., Rokowska, A., & Bajda, T. (2024). Nanoscale surface defects of goethite governing DNA adsorption process and formation of the Goethite-DNA conjugates, *Chemosphere*, *362*, 142602. https://doi.org/10.1016/j.chemosphere.2024.142602

38 Gomez, M.A., Jiang, R., & Jia, Y. (2020). Further insights into the Fe(II) reduction of 2-line ferrihydrite: a semi in situ and in situ TEM study. *Nanoscale Advances*, *2*, 4938-4950. https://doi.org/10.1039/d0na00643b

39 Smith, S.J., Page, K., & Woodfield, B.F. (2012). Novel synthesis and structural analysis of ferrihydrite. *Inorganic Chemistry*, *51* (11), 6421–6424. https://doi.org/10.1021/ic300937f

40 Su, R., Li, C., & Lan, S. (2024). Catalytic oxidation of Mn(II) on ferrihydrite and goethite surfaces and the subsequent oxidation and immobilization of coexisting Cr(III). *Applied Geochemistry*, *175*, 106195. https://doi.org/10.1016/j.apgeochem.2024.106195

41 Okada, S., Takagi, K., Ozaki, K. (2016). Synthesis of submicron-sized acicular goethite and platelet-like hematite particles and dependence of magnetic properties of α-Fe particles on their shape and size. *Materials Chemistry and Physics*, *171*, 171–177. https://doi.org/10.1016/j.matchemphys.2016.01.002

42 Polyakov, A.Y., Sorkina, T.A., & Goodilin, E.A. (2013). Mössbauer spectroscopy of frozen solutions as a stepwise control tool in preparation of biocompatible humic-stabilized feroxyhyte nanoparticles. *Hyperfine Interactions*, *219*, 113–120. https://doi.org/10.1007/s10751-013-0812-y

43 Pankratov, D.A., Dolzhenko, V.D., & Severin, A.V. (2017). Properties of iron-containing nanohydroxyapatite-based composites. *Inorganic Materials*, *53* (1), 115–124. https://doi.org/10.1134/S0020168517010125

44 Kulikova N.A., Polyakov A.Y., & Perminova I.V. (2017). Key roles of size and crystallinity of nanosized iron hydr (oxides) stabilized by humic substances in iron bioavailability to plants. *Journal of Agricultural and Food Chemistry*, *65* (51), 11157–11169. https://doi.org/10.1021/acs.jafc.7b03955

45 Yurkov, G.Y., Shashkeev, K.A., & Koksharov, Y.A. (2016). Synthesis and magnetic properties of cobalt ferrite nanoparticles in polycarbosilane ceramic matrix. Journal of Alloys and Compounds, *686*, 421–430. https://doi.org/10.1016/j.jallcom.2016.06.025

46 Pankratov, D.A., Anuchina, M.M., Spiridonov, F.M., Krivtsov, G.G. (2020). $Fe_{3-\delta}O_4$ Nanoparticles Synthesized in the Presence of Natural Polyelectrolytes. *Crystallography Reports*, *65* (3), 393–397. https://doi.org/10.1134/S1063774520030244

47 Chernavskiy, P.A., Novakova, A.A., & Petrovskaya, G.A. (2023). Synthesis and Characterization of Hematite, Magnetite and Maghemite Supported on Silica Gel. *Magnetochemistry*, *9* (11), 228. https://doi.org/10.3390/magnetochemistry9110228

48 Jones, D.H., Srivastava, K.K.P. (1986). Many-state relaxation model for the Mössbauer spectra of superparamagnets. *Physical Review B*, *34* (11), 7542–7548. https://doi.org/10.1103/PhysRevB.34.7542

49 Zharkynbaeva, R., Dzeranov, A., & Kydralieva, K. (2024). Exploring the synergistic effects of goethite intercalated coal in the presence of humic acids for enhanced growth of Sinapis alba. *Chemical and Biological Technologies in Agriculture*, *14*, 1354. https://doi.org/10.1186/s40538-023-00530-4

50 Pankratov, D.A., Dovletyarova, E.A., & Neaman, A. (2024). Deciphering the corrosion puzzle: Nano-iron-biochar composite — Not a quick fix for metal immobilization in peat soils. *Applied Geochemistry*, *166*, 105982. https://doi.org/10.1016/j.apgeochem.2024.105982

51 Shoppert, A., Valeev, D., & Pankratov, D. (2022). High-Iron Bauxite Residue (Red Mud) Valorization Using Hydrochemical Conversion of Goethite to Magnetite. *Materials*, *15* (23), 8423. https://doi.org/10.3390/ma15238423

52 Brok, E., Frandsen, C., & Berhe, A. A. (2014). Magnetic properties of ultra-small goethite nanoparticles. *Journal of Applied Physics D: Applied Physics*, *47* (36), 365003. 10.1088/0022-3727/47/36/365003

53 Shoppert, A., Valeev, D., Loginova, I., Pankratov, D. (2023). Low-Temperature Treatment of Boehmitic Bauxite Using the Bayer Reductive Method with the Formation of High-Iron Magnetite Concentrate. *Materials*, *16* (13), 4678. https://doi.org/10.3390/ma16134678

54 Polyakov, A.Y., Goldt, A.E., & Tretyakov, Y.D. (2012). Constrained growth of anisotropic magnetic δ-FeOOH nanoparticles in the presence of humic substances. *CrystEngComm*, *14* (23), 8097. https://doi.org/10.1039/C2CE25886B

55 Dzeranov, A., Bondarenko, L., & Kydralieva, K. (2023). Iron Oxides Nanoparticles as Components of Ferroptosis-Inducing Systems: Screening of Potential Candidates. *Magnetochemistry*, *9* (1), 3. https://doi.org/10.3390/magnetochemistry9010003

56 Rostovshchikova, T.N., Korobov, M.S., & Gubin, S.P. (2005). Catalytic conversions of chloroolefins over iron oxide nanoparticles 2. Isomerization of dichlorobutenes over iron oxide nanoparticles stabilized on the surface of ultradispersed poly(tetrafluoroethylene). *Russian Chemical Bulletin*, *54* (6), 1425–1432. https://doi.org/10.1007/s11172-005-0422-1

57 Klygach, D.S., Vakhitov, M.G., & Trukhanov, A.V. (2021). MCC: Specific of preparation, correlation of the phase composition and electrodynamic properties. Journal of Magnetism and Magnetic Materials. *526*, 167694. https://doi.org/10.1016/j.jmmm.2020.167694

58 Campo, B.C., Rosseler, O., & Volp M.A. (2008). On the nature of goethite, Mn-goethite and Co-goethite as supports for gold nanoparticles Mater. *Materials Chemistry and Physics*, *109*, 448-454. https://doi.org/10.1016/j.matchemphys.2007.12.014

59 Tartaj, P., Amarilla, J.M. (2011). Iron oxide porous nanorods with different textural properties and surface composition: Preparation, characterization and electrochemical lithium storage capabilities. *Journal of Power Sources*, *196* (4), 2164–2170. https://doi.org/10.1016/j.jpowsour.2010.09.116

60 Maiti, D., Aravindan, V., Madhavi, S., Sujatha, P. D. (2015). Electrochemical performance of hematite nanoparticles derived from spherical maghemite and elongated goethite particles. *Journal of Power Sources*, *276*, 291–298. https://doi.org/10.1016/j.jpowsour.2014.11.097

61 Harris, R.A. (2024). Phase transformation of magnetite and goethite nanoparticles controlled by pH: Experimental and simulation study of cuboid magnetic nanoparticles prepared with NaOH. *Solid State Sciences*, *148*, 107416. https://doi.org/10.1016/j.solidstatesciences.2023.107416

62 Zhu, M., Wang, Y., Meng, D., Qin, X., Diao G. (2012). Hydrothermal Synthesis of Hematite Nanoparticles and Their Electrochemical Properties. *The Journal of Physical Chemistry C*, *116* (30), 16276–16285. https://doi.org/10.1021/jp304041m

63 Chen, S.A., Heaney, P.J., & Stubbs, J.E. (2022). Hematite-goethite ratios at pH 2–13 and 25–170 °C: A time-resolved synchrotron X-ray diffraction study. *Chemical Geology*, *606*, 120995. https://doi.org/10.1016/j.chemgeo.2022.120995

64 Akinwekomi, V., Maree, J.P., & Chatzisymeon, E. (2020). Beneficiation of acid mine drainage (AMD): A viable option for the synthesis of goethite, hematite, magnetite, and gypsum — Gearing towards a circular economy concept. *Minerals Engineering*, *148*, 106204. https://doi.org/10.1016/j.mineng.2020.106204

65 Combes, J.M., Manceau, A., Calas, G. (1990). Formation of ferric oxides from aqueous solutions: A polyhedral approach by X-ray Absorption Spectroscopy: II. Hematite formation from ferric gels. *Geochimica et Cosmochimica Acta*, *54*, 1083–1091. https://doi.org/10.1016/0016-7037(90)90440-V

66 Vu, H.P., Shaw, S., Brinza, L., Benning, L.G. (2013). Partitioning of Pb(II) during goethite and hematite crystallization: Implications for Pb transport in natural systems. *Applied Geochemistry*, *39*, 119-128. https://doi.org/10.1016/j.apgeochem.2013.10.001

67 De La Vega, J.C., Elischer, P., Schneider, T., Häfeli, U.O. (2013). Uniform polymer microspheres: monodispersity criteria, methods of formation and applications. *Nanomedicine*, *8*, 265–285. https://doi.org/10.2217/nnm.12.210

68 Chen, K., Guo, C., & Dang Z. (2024). Using machine learning to explore oxyanion adsorption ability of goethite with different specific surface area. *Environmental Pollution*, *343*, 123162. https://doi.org/10.1016/j.envpol.2023.123162

69 Belloni, C., Korving, L., & Dugulan, A.I. (2024). Zn induced surface modification of stable goethite nanoparticles for improved regenerative phosphate adsorption. *Colloids and Surfaces A: Physicochemical and Engineering Aspects*, *687*, 133476. https://doi.org/10.1016/j.colsurfa.2024.133476

How to Cite: Dzeranov, A.A., Bondarenko, L.S., Prokofiev, M.V., Bondarenko, R.A., Abramov, D.R., Dzhardimalieva, G.I. & Kydralieva, K.A. (2026). Size and Magnetization Control of Magnetite NPs via Ethylene Glycol and Temperature for Ferrofluid and Magnetotargeting: Model Experiments. *Eurasian Journal of Chemistry, 31, 1(121), 137–150.* https://doi.org/10.31489/2959-0663/1-26-10

Article

Received: 11 December 2025 | Revised: 27 February 2026 | Accepted: 2 March 2026 | Published online: 19 March 2026

UDC 544.42+519.242.7

https://doi.org/10.31489/2959-0663/1-26-10

Artur A. Dzeranov[1, 2*], Lyubov S. Bondarenko[1], Michail V. Prokofiev[1], Roman A. Bondarenko[3], Danil R. Abramov[1], Gulzhian I. Dzhardimalieva[1, 2], Kamila A. Kydralieva[1]

[1]*Moscow Aviation Institute (National Research University), Moscow, Russia;*
[2]*Federal Research Center of Problems of Chemical Physics and Medicinal Chemistry, Chernogolovka, Russia;*
[3]*Institute of Applied Mechanics, Russian Academy of Sciences, Moscow, Russia*
*(*Corresponding author's e-mail: arturdzeranov99@gmail.com)*

Size and Magnetization Control of Magnetite NPs via Ethylene Glycol and Temperature for Ferrofluid and Magnetotargeting: Model Experiments

Magnetic nanoparticles (NPs) are highly promising materials for diverse biomedical applications, particularly in magnetotargeting, owing to their tunable magnetic properties. Achieving precise control over their synthesis parameters is critical for optimizing these properties and ensuring their efficacy. This study investigates the impact of synthesis the impact of synthesis conditions on the properties of magnetite (Fe_3O_4) nanoparticles. A set of magnetite NPs were prepared via co-precipitation of ferrous and ferric ions by a base in ambient conditions, systematically varying the ratio of ethylene glycol/water (EG/water) solvents and temperatures (4, 20, and 70 °C). Crystal structure, morphology and magnetic parameters were analyzed. Additionally, rheological experiments were conducted to study the dynamic viscosity of ferrofluids containing varying sizes and concentrations NPs in polyglucinum. Results showed that Fe_3O_4 NPs size linearly increased with the EG/water volume ratio only at 70 °C. Increasing EG from 0 % to 50 % elevated magnetite stoichiometry from $Fe_{2.72}O_4$ to $Fe_{2.912}O_4$ with higher concentrations reducing it. The effect of temperature on stoichiometry varied depending on the ethylene glycol (EG) content. At low EG content, stoichiometry decreased with increasing temperature. But, at higher EG content, maximum stoichiometry was observed at 20 °C. Increasing polydispersity of NPs (0.07–0.13) decreased viscosity in polyglucinum from ~10 to ~4 mPa s (1–5 % EG). Evaluation tests of the magnetic induction gradient on NPs capture in a flow-through setup were also performed. A sigmoidal relationship ($R^2 = 0.97$) was established between the NPs capture efficiency and the magnetic induction gradient. These findings provide valuable insights for optimizing the synthesis and suspension performance for magnetic fluids for magnetotargeting applications.

Keywords: Synthesis of magnetic NPs, Ethylene glycol, Synthesis temperature, Oxidation, Size control, Saturation magnetization, Rheology, Magnetic capture

Introduction

Magnetite (Fe_3O_4) is among the most extensively studied magnetic NPs due to its unique combination of various properties making it highly attractive for numerous biomedical applications, such as magnetic resonance imaging [1], drug/gene delivery [2–5], in catalysis [6–8], in ferroptosis therapy due to Fe^{2+}/Fe^{3+} mediators of Fenton and Fenton-like reactions [9–11] as well as ferrofluids [12]. Uniformity of magnetite NPs size, shape, and crystalline structure is crucial in biomedical applications [13] that require the design and synthesis of NPs with the perfectly controlled features such as magnetization of NPs. The latter is a size dependent property, so, it can utilize its size-in dependent version that is called saturation magnetization (σ_s) [14]. Many reports of solution-phase synthesis of monodisperse magnetite nanocrystals (MNCs) have been published [15–17]. However, lack of reproducibility of MNC synthesis is a persistent problem, and the keys to producing monodisperse MNCs remain elusive [18]. The structural characteristics and subsequently magnetic properties of materials are greatly originated from their synthesis process [19–23]. In recent studies of coprecipitation synthesis, there have been many reports on changing various experimental parameters to control the size of Fe_3O_4 NPs, such as altering the reaction temperature and reaction time in synthesis [24, 25], varying the Fe^{2+}/Fe^{3+} cation ratio, and pH [26], stirring velocity [27], etc. Interfacial tension of the medium is also expected to be one factor in controlling the size NPs. Ethylene glycol (EG) is a solvent miscible with water at any composition [28]. Besides, EG have a high boiling point (246 °C) and a

low interfacial tension (47.99 mN m^{-1}) [29]. It can be therefore expected that EG becomes a useful additive for controlling the size of magnetite produced by a forced hydrolysis reaction at an elevated temperature. Moreover, EG being a polyol capable of acting as a reducing and stabilizing agent, influencing stoichiometry of magnetite as well as nucleation and growth processes. Recent mechanistic work also shows that, in alcohol-based systems, the water fraction and oxygen access can be decisive for iron nanoparticle oxidation pathways and kinetics, underscoring why solvent composition must be treated as a primary control parameter [30]. This paper demonstrates a synthesis of magnetite NPs via co-precipitation of ferrous and ferric ions by a base in ambient conditions of 10 to 34 nm in diameter regulated by changing the ratio of EG/water and temperature from 4 to 70 °C. We investigated in this paper the influence of both EG and temperature on the size, polydispersity, stoichiometry and saturation magnetization (σ_s) of NPs. Selected NPs samples were tested under model conditions to assess their effect on the dynamic viscosity of polyglucinum-based ferrofluids, as well as the influence of magnet induction on NPs capture in a model flow-through setup.

Experimental

Preparation of Fe_3O_4 NPs

Magnetite NPs Fe_3O_4 with different sizes were synthesized using the co-precipitation method by Elmore reaction [31] by changing the volume ratio of ethylene glycol/water (EG/water) and temperature while keeping the other experimental conditions the same. 150 mL of a 0.05 M $FeSO_4 \cdot 7H_2O$ and 0.1 M $FeCl_3 \cdot 6H_2O$ solution was poured in a beaker in ambient (air) conditions for technological reason and the solution's temperature was maintained at 4, 20 or 70 °C. 1 M NaOH was added dropwise into the solution in order to reach pH 9 and stirred at 300 rpm for 30 min. pH control was over time. The product was harvested by magnetic separation, washed repeatedly with deionized water 3 times with a hydromodulus of 1:50 and then dried at 70 °C. Storage conditions was in a sealed container in a dark place. Synthesis conditions and cipher of NPs are presented in Table 1.

Table 1

Synthesis conditions and cipher of NPs

T, °C	EG, volume ratio			
	0	25	50	75
4	4/0*	4/25	4/50	4/75
20	20/0	20/25	20/50	20/75
70	70/0	70/25	70/50	70/75
*the code in the name of the samples indicates the temperature (first index) and the volumetric content of EG.				

Characterization of NPs

NPs samples were characterized using X-ray diffraction (XRD) analysis, transmission electron microscopy (TEM), and vibrating sample magnetometer (VSM) analysis. Method descriptions are provided in Supporting Information (SI).

Results and Discussion

The Influence of Ethylene Glycol Concentration and Temperature on the Morphology of NPs

The TEM images taken to determine the morphology, shape and size distribution for the selected NPs produced at the different volume ratios EG/water and temperature are shown in Fig. 1. The resulting magnetite nanoparticle samples are found to be nearly of spherical/cubic shape. For samples 4/25, 20/25 and 70/25, the average particle size was 16.7, 19.1 and 14.1 nm, respectively; for samples 70/0, 70/50 and 70/75, it was 9.8, 22.6 and 33.6 nm, respectively. The size particle distribution histograms constructed from TEM images show that with increasing EG in the synthesized solution, the range of particle sizes increases. The electron diffraction patterns in the selected region obtained by TEM are shown in Fig. S1 (SI). The ring diameters of the corresponding atomic planes indicate that the main phase of the NPs is magnetite [AMCSD 0002400, Supplementary Materials].

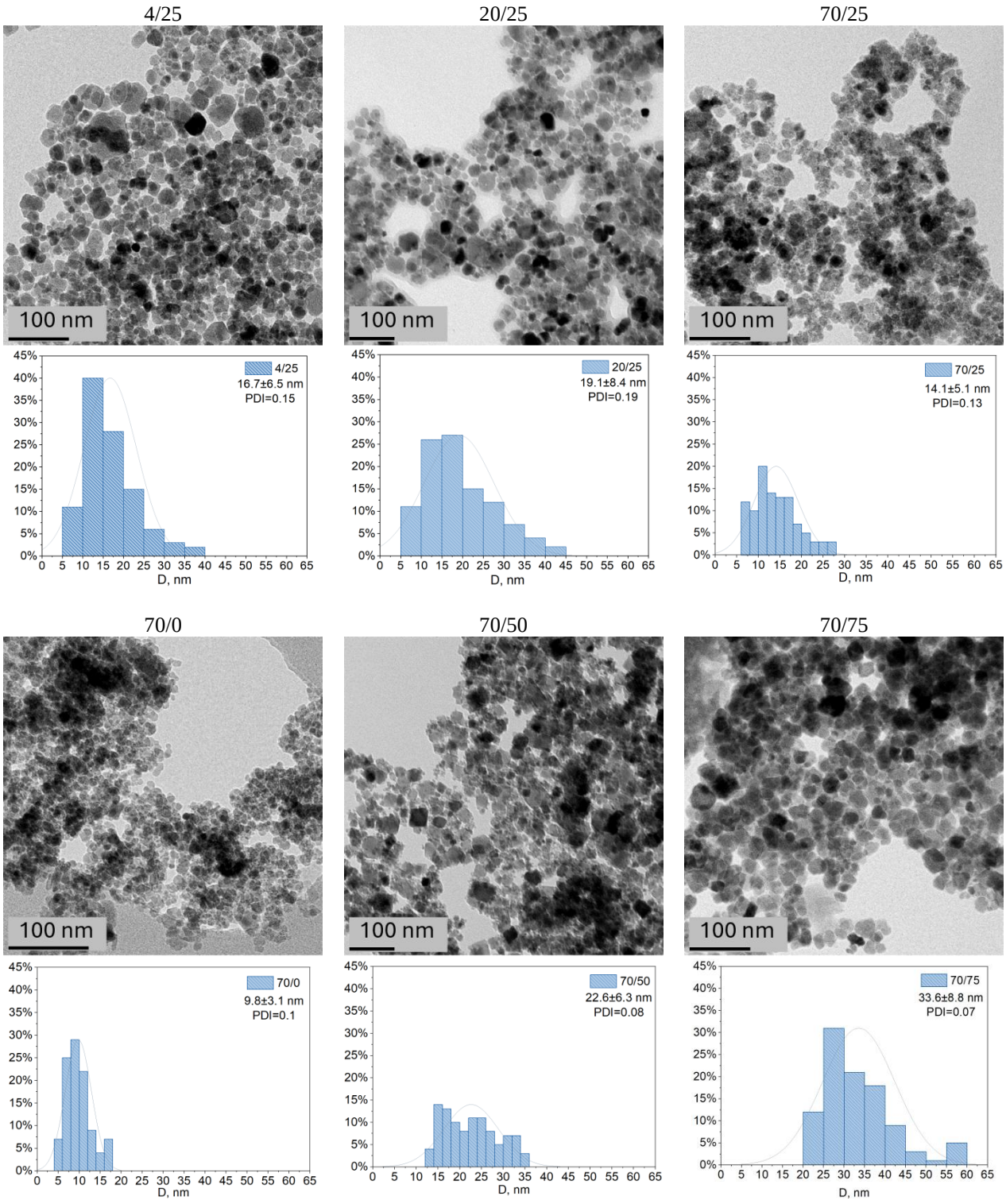

Figure 1. TEM images and plotted particle size distribution histograms

For these samples, graphs were constructed showing the dependence of NPs size on the EG content in the solution and the synthesis temperature. The results are presented in Figure 1*a*, *b*.

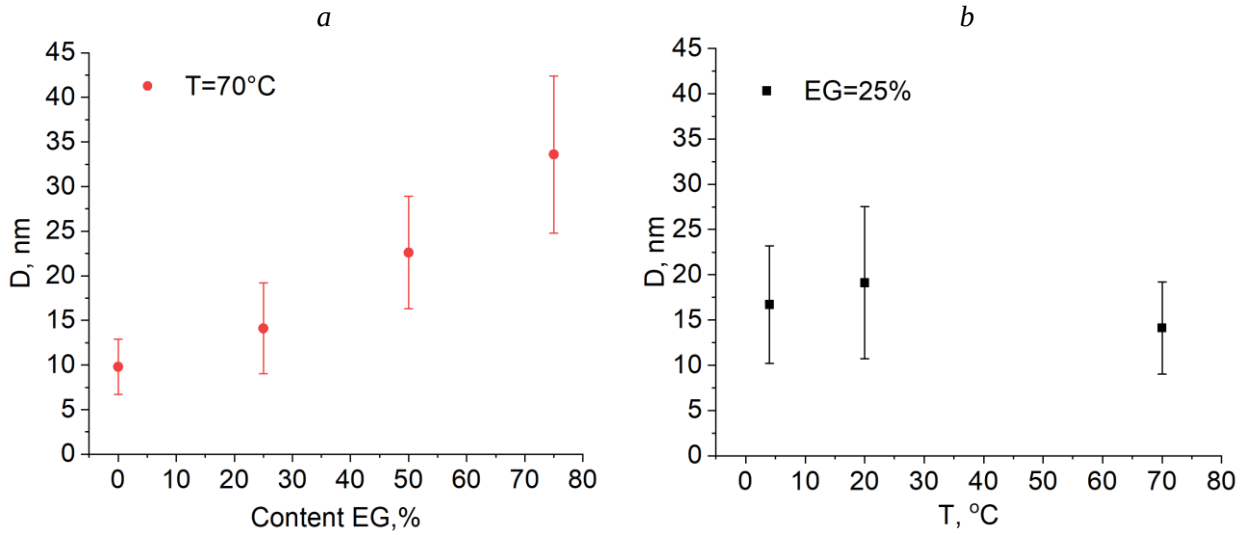

Figure 2. Dependence of NPs size on the EG content (*a*) and the synthesis temperature (*b*)

Although size distribution NPs with irregular shapes (Fig. 1) could be found due to the inevitable fluctuations in a coprecipitation system, the trend that the size and shape of the NPs controlled by the synthesis conditions was obvious. Figure 2*a* shows that with increasing EG content, the particle size increases, which is due to an increase in the viscosity of the solution, since the density of EG is higher than the density of water, and the density of the solution increases with increasing EG concentration (from 0.41 to 2.3 mPa s for water and 75 % EG, respectively, at 70 °C). A statistically significant difference exists only between samples 70/0 and 70/75, p-value = 0.009. Xu et al. found that anisotropic octahedral Fe_3O_4 NPs vary the particle sizes from 30 to 115 nm by changing the volume ratios of ethylene glycol/diethylene glycol in hydrothermal synthesis [32].

Temperature can play a crucial role in the phase formation in process, e.g. due to the increased loss of ammonia (in case of NH_4^+ present in the system) with increased temperature and its implications for the phase formation kinetics [33]. According to [33] in aqueous solution, synthesis at the lowest temperature of 5 °C exhibit magnetite phase, while increase in the growth temperature to 95 °C leads to pure maghemite phase. Authors noted that since the temperatures used here are too small for solid state transformations, the observed changes should occur primarily in the particle formation process itself where the role of precursor radicals can be temperature sensitive. Moreover, the grains in the case of the 27 °C sample are much smaller (6–8 nm), in the case of the 95 °C sample, the grains are somewhat bigger than the 27 °C case and they are again better faceted though smaller than the 5 °C case. But, in our experiments no dependence of NPs size is observed on the temperature of EG-assisted synthesis. The above phenomena about the influence of temperature on the size of Fe_3O_4 particle can be interpreted by thermophysical properties of EG: heat capacity and thermal conductivity decrease (compared to water) by up to 20 % with increasing EG concentration and decreasing operating temperatures in the low zone; kinematic and dynamic viscosity are 2–3 times higher than that of water at positive temperatures and increase by 8–10 times as the concentration increases to the practical limit of 65 %.

X-Ray Diffraction Analysis

The phase composition of magnetic NPs was also investigated by XRD (Figure 13). A typical diffraction pattern was observed, confirming the presence of the magnetite phase (Fe_3O_4). The content of magnetite and maghemite was calculated using the Rietveld method (Fig. 3). The obtained unit cell parameter values for all samples were smaller than those of magnetite (8.396–8.400 Å according to ICDD-PDF 19–629), but larger than those of maghemite (8.33–8.34 Å according to ICDD-PDF 39–1346). This is explained by partial oxidation of Fe^{2+} ions during drying and/or storage and modification, leading to the formation of non-stoichiometric magnetite with the formula $Fe_{3-\delta}O_4$, where δ can vary from zero (stoichiometric magnetite) to 1/3 (fully oxidized).

4/0

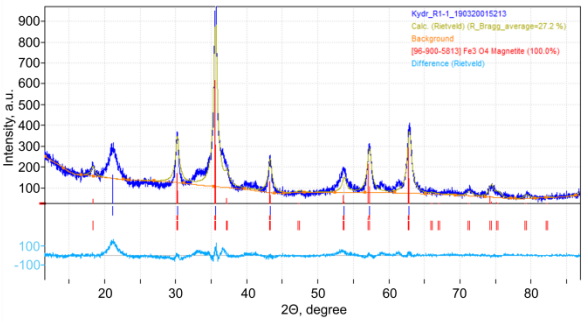

4/25

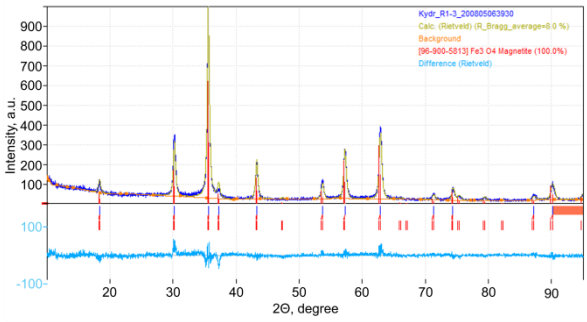

4/50

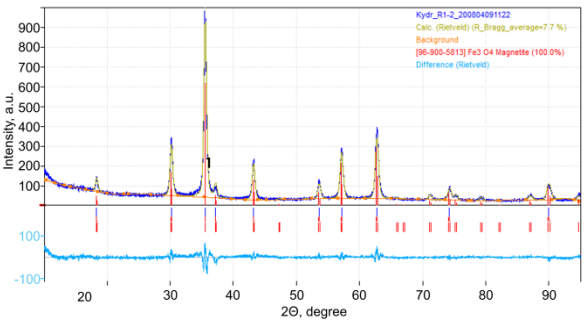

4/75

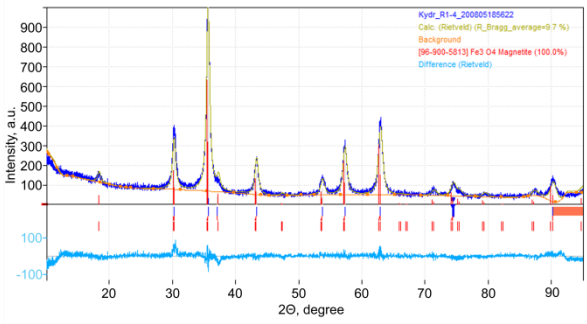

20/0

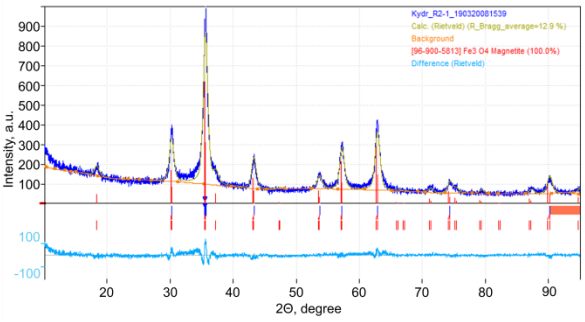

20/25

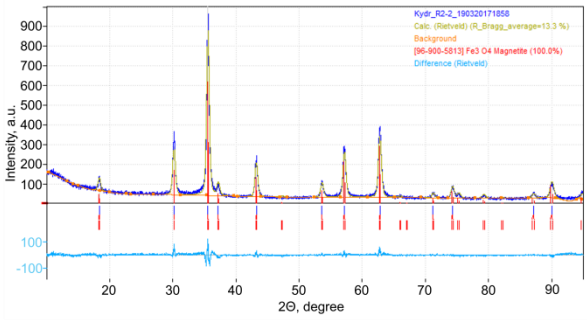

20/50

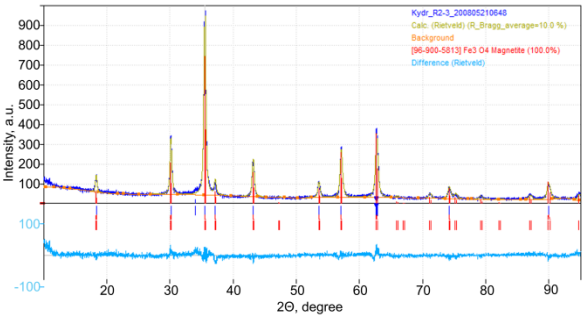

20/75

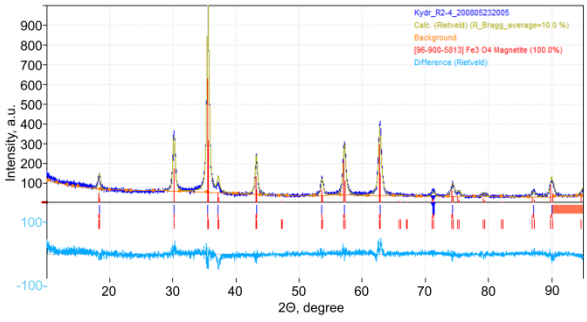

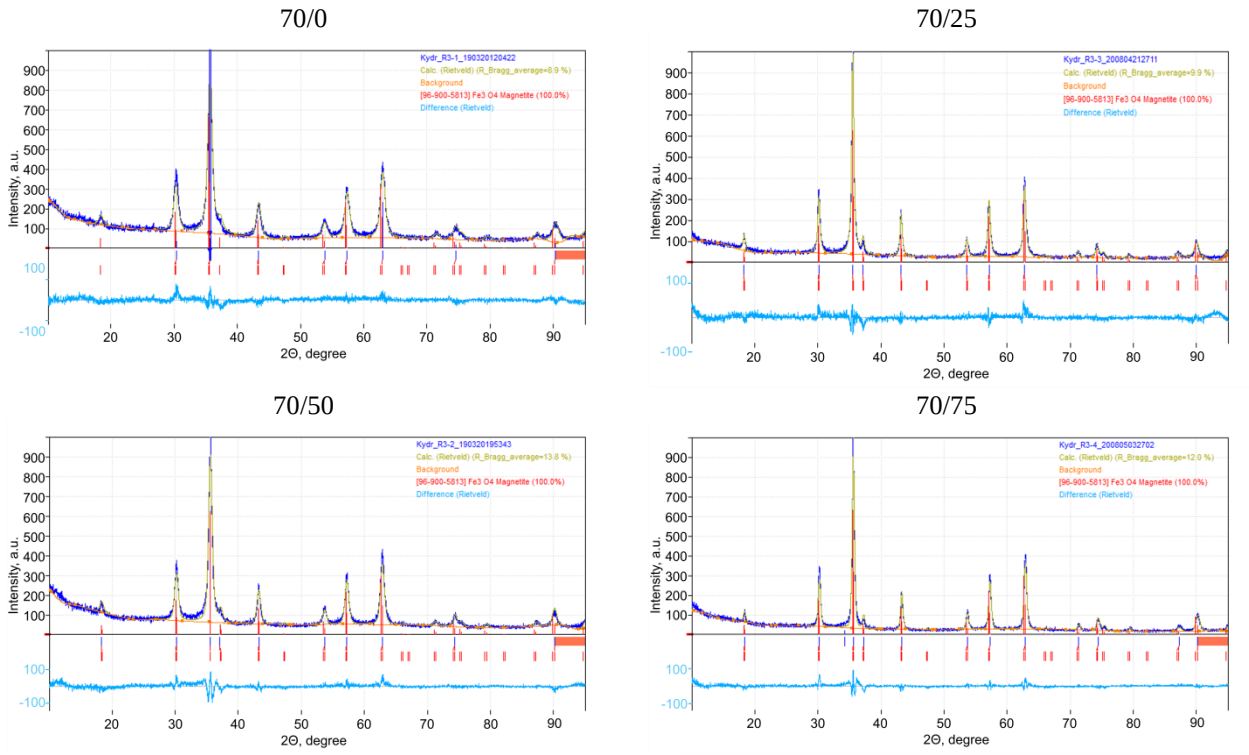

Figure 3. Diffraction patterns of NPs

The calculated stoichiometric formulas of magnetite samples and crystallite sizes calculated using the Williamson-Hall method [34] are presented in Table 2.

Table 2

Formula and crystallite size of iron oxide NPs

Sample	*a*, Å	$(GoF)^2$	Composition	Amount, %	*D*, nm	No. COD
4/0	8.363	0.7	$Fe_{2.83}O_4$	88.1	8.40	9005838
4/25	8.374	1.1	$Fe_{2.90}O_4$	96.1	22.20	9005838
4/50	8.358	1.6	$Fe_{2.80}O_4$	92.6	29.00	9005838
4/75	8.354	0.9	$Fe_{2.77}O_4$	96.2	18.40	9005838
20/0	8.361	0.8	$Fe_{2.82}O_4$	96.4	12.50	9007706
20/25	8.373	0.8	$Fe_{2.89}O_4$	96.5	26.00	9005839
20/50	8.378	1.0	$Fe_{2.912}O_4$	96.5	31.50	2101926
20/75	8.368	1.1	$Fe_{2.86}O_4$	96.4	24.40	9005839
70/0	8.345	1.0	$Fe_{2.72}O_4$	96.2	11.80	9002319
70/25	8.359	0.9	$Fe_{2.81}O_4$	96.5	20.80	9005842
70/50	8.376	0.6	$Fe_{2.91}O_4$	96.1	27.90	2101926
70/75	8.357	0.6	$Fe_{2.79}O_4$	95.9	28.20	9005839

The average size of NPs for the 70/0, 70/25, 70/50 and 70/75 samples are close to the results obtained using TEM. According to X-ray diffraction data, the presence of EG in the reaction mixture, compared to temperature and solution viscosity, is the most significant factor influencing crystallite size (Fig. 4*a*). The maximum magnetite content and its most stoichiometric form (with a 3-δ parameter in the range of 2.89–2.91) were observed at a solution viscosity of 1.3–4.5 mPa s and an EG content of 25–50 % (Fig. 4*b*). This confirms the active participation of EG in the reduction of iron (III) salts in an alkaline medium. A further increase in the EG concentration to 70 % and the observed decrease in the stoichiometry of magnetite are associated with a decrease in the equivalent water content in the system required for coprecipitation methods where the hydrolysis of ferrous and ferric ions, ferrous hydroxide ($Fe(OH)_2$) and goethite

(-FeOOH), are coprecipitated as precursors in an alkaline solution according to Elmore reaction. For the samples synthesized at 20 and 70 °C, the peak stoichiometry was achieved at a content of 50 % EG and amounted to $Fe_{2.912}O_4$ and $Fe_{2.91}O_4$, respectively, while at 4 °C the peak stoichiometry was achieved at a content of 25 % EG and amounted to $Fe_{2.9}O_4$ (i.e. mixture 60 % magnetite and 31 % maghemite) [35]. Our previous studies showed that a change in the stoichiometry of magnetite, associated with the partial transformation to maghemite phase, leads to a change in the biological activity of NPs compared to stoichiometric magnetite [36, 37].

The stoichiometry of magnetite is important and essential parameter because the Fe^{3+}/Fe^{2+} ions pair mediates Fenton oxidation-reduction reactions, which are the primary mechanism triggering ferroptosis [38]. The magnetite stoichiometry in samples prepared at volume ratios of 0/100 and 25/75 (EG/water) steadily decreases with increasing synthesis temperature, likely due to the oxidation of iron ions. In contrast, samples prepared at 50/50 and 75/25 (EG/water) exhibited a peak at 20 °C of coprecipitation conditions followed by decline. This behavior is explained by the fact that, at this temperature, the reducing potential of EG outweighs the oxidizing effect of increasing temperature.

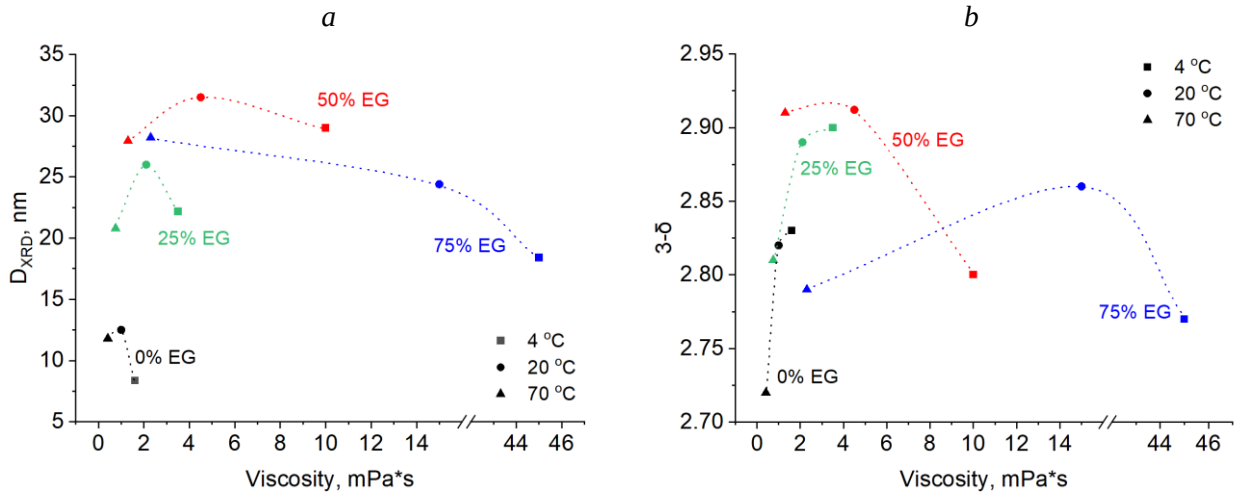

Figure 4. Dependence of crystallite size (*a*) and magnetite stoichiometry (*b*) on solution viscosity and synthesis temperature

The optimal EG content facilitates controlled synthesis due to two factors: firstly, as a reducing agent, it determines the kinetics of magnetite nucleation; secondly, by modifying the viscosity of the medium, it influences the diffusion coefficient of the reactants, slowing the growth rate and promoting the formation of larger, more perfect crystals with a minimum of defects.

Magnetic Properties of Magnetite NPs

The results of the analysis of the magnetic properties of magnetite are presented as hysteresis loops (Fig. 5). Table 3 presents the values of saturation magnetization (σ_s), remanent magnetization (σ_r), and coercivity (H_c) for magnetite NPs.

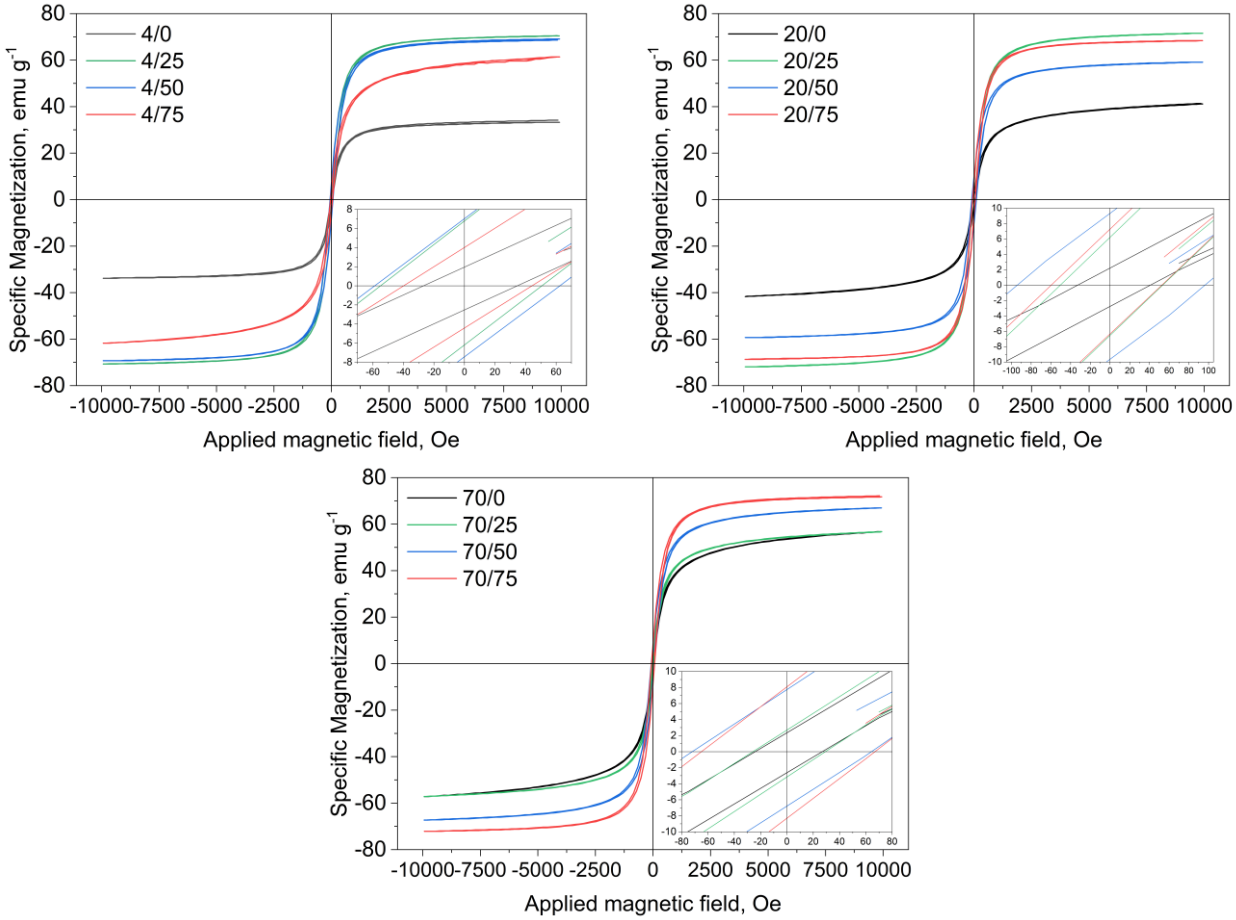

Figure 5. Hysteresis loops of magnetite samples

Table 3

Magnetic characteristics of magnetite samples

Sample	σ_s, emu g^{-1}	σ_r, emu g^{-1}	H_c, Oe
4/0	33.5	2.5	30.0
4/25	70.5	8.0	58.0
4/50	68.7	7.0	55.0
4/75	61.8	4.0	41.0
20/0	41.2	2.5	36.5
20/25	71.9	6.5	45.5
20/50	59.5	9.3	98.0
20/75	68.3	6.7	55.0
70/0	56.7	2.5	25.5
70/25	58.7	2.9	35.5
70/50	67.0	7.7	65.0
70/75	72.0	7.2	70.0

The saturation magnetization (σ_S) of magnetite NPs demonstrates variations influenced synthesis temperature (Fig. 5). Specifically: at a synthesis temperature of 4 °C and 25 % EG content, the saturation magnetization reaches a peak of 70.5 emu g^{-1} before subsequently decreasing. At 20 °C, σ_S does not show a clear correlation with increasing EG content. At 70 °C, σ_S increases from 56.7 to 72 emu g^{-1} as EG content changes. When EG content is 0 % and 75 % in the synthesis solution, σ_S increases from 33.5 and 61.8 emu g^{-1} to 56.7 and 72 emu g^{-1}, respectively. At 25 % EG, σ_S decreases from 70.5 to 56.7 emu g^{-1}, at 50 % EG, σ_S does not exhibit a clear dependence on increasing synthesis temperature (Fig. 6).

The samples exhibiting the highest σ_S values are those synthesized at 20 °C with 25 EG (20/25) and at 70 °C with 75 % EG (70/75).

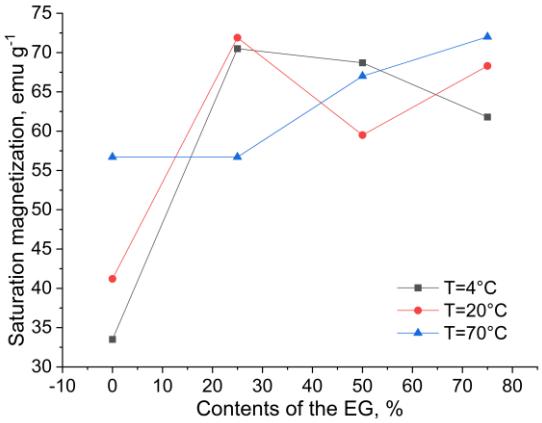

Figure 6. Dependence of saturation magnetization on the EG content in the synthesis solution

As a result, the key factors determining the magnetic characteristics of the synthesized NPs were identified as follows: 1) crystallite size: larger NPs have a smaller specific surface area, which reduces the proportion of disordered spins in the surface layer and leads to an increase in the total magnetic moment; 2) magnetite stoichiometry ($Fe_{3-\delta}O_4$): the saturation magnetization of magnetite directly depends on maintaining the balance between Fe^{2+} and Fe^{3+} ions in the octahedral positions of the crystal lattice, since their electron exchange ensures ferrimagnetic order.

Optimal conditions for synthesizing magnetite NPs with high Fe^{2+} content (Fig. 4*b*) and saturation magnetization (Fig. 6), suitable for ferroptosis-inducing applications were determined to be 25 % EG at 4 °C and 25 °C, and 50 % EG at 70 °C.

Changes in the Viscosity of Nanofluids at NPs Different Concentrations in Polyglucinum

To investigate the influence of NPs on viscosity, samples synthesized at 70 °C were selected. TEM data revealed a linear increase in NPs size from 10 to 34 nm with increasing EG concentration. The intrinsic dynamic viscosity of the PG base fluid, measured at room temperature, was 3.952 mPa s. Figure 7 presents the dynamic viscosity values of PG suspensions containing varying volumes and average particle sizes of Fe_3O_4 NPs with different PDI.

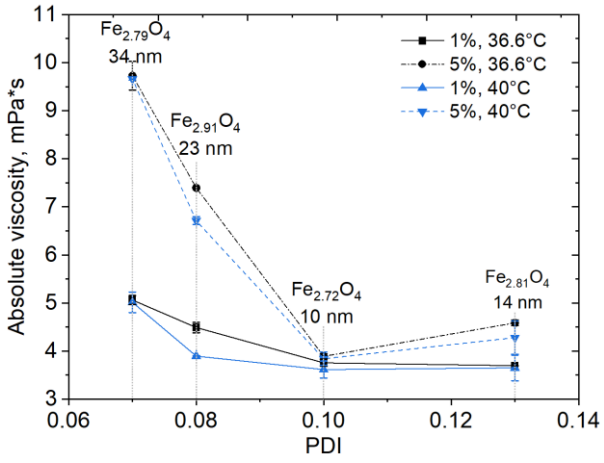

Figure 7. Influence of volume concentration, size and dispersion on the absolute viscosity in Fe_3O_4-PG suspensions (EG/water ratios, vol.%: 70/0, 70/25, 70/50, 70/75)

As shown in Figure 7, the volume concentration of NPs in the PG suspensions ranged from 1 % to 5 %. An increase in NPs content was observed to correlate with an increase in viscosity. At a constant particle size, increasing the NPs concentration causes the flow behavior to transition from Newtonian to shear-

thinning, and subsequently to shear-thickening. In Newtonian regime, low NPs interaction predominates. Shear-thinning arises as weak particle interactions are disrupted at higher shift deformations. At higher particle concentrations, physical collisions and aggregation lead to shear-thickening behavior.

The nanofluid's viscosity increased with larger NPs sizes and decreasing polydispersity index (from 0.13 to 0.07). This is due to the fact that NPs with a wider size span (PDI = 0.13) pack more efficiently than monodisperse particles (PDI = 0.07), creating more free space for NPs movement. Consequently, the fluid flows more easily, resulting in lower viscosity.

Model Experiments: Influence of Magnet Induction on NPs Capture in a Flow-Through Setup

The NPs test sample was synthesized via coprecipitation with EG/water volume ratio of 70/50. This sample exhibited minimal viscosity change in PG, a monodisperse particle size distribution (PDI = 0.08), and high stoichiometry (3–δ = 2.91). These characteristics are crucial for the efficient occurrence of Fenton and Fenton-like processes.

An experimental setup was assembled, considering both hydrodynamic and magnetic parameters (Fig. S2). The setup parameters included: distance from the magnet (0; 0.5; 1; 2; 3; 5 cm); a flow velocity of 9.5 mm s^{-1} (appr. 56.61 cm min^{-1}); introduced NPs masses (0.02, 0.04, 0.08, 0.1, 0.2, 0.3, 0.5 g), and a Neodymium disk magnet (50×20 mm, NbFeB, N42, 298 g) with axial magnetization. The conversion of the distance (*r*) from the magnetite surface to the NPs localization site into magnetic field induction (B) is detailed in SI. Experiments were conducted at room temperature using distilled water as the liquid medium. Gravimetric data analysis, aimed at determining the optimal fixed mass of magnetite NPs on a magnet based on external magnetic field induction, is presented in Table S3 and Figure S4. A mathematical model describing the dependence of NPs capture efficiency on magnetic field parameters and target distance is proposed in Table S4.

A sigmoidal relationship (R^2 = 0.97) was established between the NPs capture efficiency and the magnetic induction (based on the gradient of distance from the target) (Fig. 8). The injection mass at which the proportion of captured NPs reaches its maximum corresponds to the injection mass that maximizes particle capture efficiency. This is defined as the optimal injection mass for maximum injection efficiency (Fig. S5*b* and Table S5).

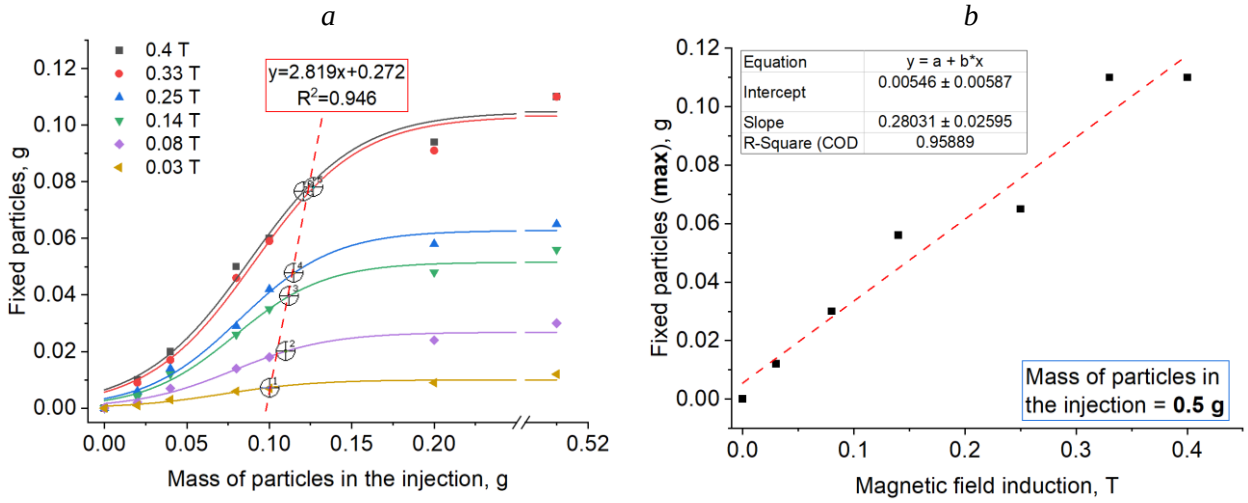

Figure 8. Sigmoid models illustrating the dependence of optimal captured NPs masses (*a*) and the dependence of the saturation mass on magnetic induction (*b*)

Figure 8*a* presents an approximation of the optimal captured NPs masses. Additionally, the maximum capacity line, shown in Figure 8*b*, is significant as it allows for the estimation of the maximum NPs mass reaching the target organ at a given magnetic induction.

Conclusions

In summary, NPs size regulation of Fe_3O_4 can be effectively achieved by adjusting the volume ratio of EG to water. X-ray diffraction data demonstrated that the presence of EG in the reaction mixture, compared to temperature and solution viscosity, is the most significant factor influencing crystallite size. Increasing the

EG concentration to 50 % enhances the Fe_3O_4 stoichiometry, indicating improved oxidation states, while higher concentration beyond this point lead to a decline likely due to restricted hydrolysis pathways that impede Fe_3O_4 NPs formation. Temperature variations influence the magnetite's composition differently depending on EG content with optimal stoichiometry achieved at specific combinations, which correlates directly with saturation magnetization. Additionally, rheological studies with Fe_3O_4-polyglucinum suspensions revealed that viscosity decreases as the particle size distribution broaden from 0.07 to 0.13. This is due to the fact that NPs with a wider size span pack more efficiently than monodisperse particles, creating more free space for NPs movement. Consequently, the fluid flows more easily, resulting in lower viscosity. A mathematical model is proposed to describe the dependence of NPs capture efficiency. A sigmoidal relationship (R^2 = 0.97) was established between the NPs capture efficiency and the magnetic induction gradient. These findings provide insights into controlling NPs synthesis parameters in ambient conditions and suspension properties for advanced magnetic fluid applications.

Supporting Information

The Supporting Information is available free at https://ejc.buketov.edu.kz/ejc/article/view/641/365

Funding

The study was supported by a grant from the Russian Science Foundation (No. 22-73-10222-P, "Preparation, physicochemical characterization and pro-oxidant properties of new iron-containing mesoporous materials", https://rscf.ru/en/project/22-73-10222/).

*Author Information**

**The authors' names are presented in the following order: First Name, Middle Name and Last Name*

Artur Albertovich Dzeranov — Assistant Lecturer, Advanced Materials and Technologies for Aerospace Applications Department, Moscow Aviation Institute (National Research University), Volokolamskoe shosse, 4, 125080, Moscow, Russia; Junior Research Fellow of Laboratory of Metal Polymers, Federal Research Center of Problems of Chemical Physics and Medicinal Chemistry, Russian Academy of Sciences, Semenov avenue, 1, 142432, Chernogolovka, Moscow region, Russia; e-mail: arturdzeranov99@gmail.com; https://orcid.org/0000-0003-3240-9321

Lyubov Sergeevna Bondarenko — PhD (Chemistry), Associate Professor, Advanced Materials and Technologies for Aerospace Applications Department, Moscow Aviation Institute (National Research University), Volokolamskoe shosse, 4, 125080, Moscow, Russia; e-mail: l.s.bondarenko92@gmail.com; https://orcid.org/0000-0002-3107-0648

Michail Vladimirovich Prokofiev — PhD (Chemistry), Associate Professor, Advanced Materials and Technologies for Aerospace Applications Department, Moscow Aviation Institute (National Research University), Volokolamskoe shosse, 4, 125080, Moscow, Russia; e-mail: mikepro1953@rambler.ru

Roman Alexandrovich Bondarenko — PhD Student, Institute of Applied Mechanics of the Russian Academy of Sciences, Leningradsky Prospekt, 7, 125040, Moscow, Russia; e-mail: bondarenko.romaa@yandex.ru; https://orcid.org/0009-0007-8400-5229

Danil Romanovich Abramov — MSc Student, Moscow Aviation Institute (National Research University), Volokolamskoe shosse, 4, 125080, Moscow, Russia; e-mail: dizox13@mail.ru; https://orcid.org/0009-0000-3278-9876

Dzhardimalieva Gulzhian Iskakovna — PhD, DSc (Chemistry), Head of Laboratory of Metallopolymers, Federal Research Center of Problems of Chemical Physics and Medicinal Chemistry, Russian Academy of Sciences, Chernogolovka, Moscow region, 142432, Russia; Professor, Advanced Materials and Technologies for Aerospace Applications Department, Moscow Aviation Institute (National Research University), Volokolamskoe shosse, 4, 125080, Moscow, Russia; e-mail: dzhardim@icp.ac.ru; https://orcid.org/0000-0002-4727-8910

Kamila Asylbekovna Kydralieva — PhD, DSc (Chemistry), Professor, Advanced Materials and Technologies for Aerospace Applications Department, Moscow Aviation Institute (National Research Uni-

versity), Volokolamskoe shosse, 4, 125080, Moscow, Russia; e-mail: kamila.kydralieva@gmail.com; https://orcid.org/0000-0002-4596-4140

Author Contributions

The manuscript was written through contributions of all authors. All authors have given approval to the final version of the manuscript. CRediT: **Artur Albertovich Dzeranov**: Investigation, Writing, Editing; **Lyubov Sergeevna Bondarenko**: Writing, Software; **Michail Vladimirovich Prokofiev**: Investigation; **Roman Alexandrovich Bondarenko**: Investigation; **Danil Romanovich Abramov**: Investigation; **Dzhardimalieva Gulzhian Iskakovna:** Data curation, Conceptualization; **Kamila Asylbekovna Kydralieva**: Conceptualization, Data curation, Methodology, Writing — Reviewing and Editing.

Acknowledgments

Magnetic measurements were performed in accordance with the state research assignments registered under No. 124013000757-0. These experiments were carried out using the facilities of *the Multi-User Analytical Center of the Federal Research Center of Problems of Chemical Physics and Medicinal Chemistry of the Russian Academy of Sciences*.

Conflicts of Interest

The authors have no conflicts of interest to declare.

References

1 Tian, Y., Yu, B., Li, X., & Li, K. (2011). Facile solvothermal synthesis of monodisperse Fe3O4 nanocrystals with precise size control of one nanometre as potential MRI contrast agents. *Journal of Materials Chemistry*, *21*(8), 2476–2481. https://doi.org/10.1039/C0JM02913K

2 Turrina, C., Oppelt, A., Mitzkus, M., Berensmeier, S., & Schwaminger, S. P. (2022). Silica-coated superparamagnetic iron oxide nanoparticles: New insights into the influence of coating thickness on the particle properties and lasioglossin binding. *MRS Communications*, *12*(5), 632–639. https://doi.org/10.1557/s43579-022-00228-y

3 Ulbrich, K., Hola, K., Subr, V., Bakandritsos, A., Tucek, J., & Zboril, R. (2016). Targeted drug delivery with polymers and magnetic nanoparticles: covalent and noncovalent approaches, release control, and clinical studies. *Chemical reviews*, *116*(9), 5338–5431. https://doi.org/10.1021/acs.chemrev.5b00589

4 Reindl, M., Zach, V., & Schwaminger, S. P. (2025). Biocompatible Poly(acrylic acid-co-methacrylic acid)-Coated Iron Oxide Nanoparticles for Enhanced Adsorption and Antimicrobial Activity of Lasioglossin-III. *ACS Applied Materials & Interfaces*, *17*(11), 16644-16657. https://doi.org/10.1021/acsami.4c22603

5 Eigenfeld, M., Reindl, M., Sun, X., & Schwaminger, S. P. (2024). Exploring Multi-Parameter Effects on Iron Oxide Nanoparticle Synthesis by SAXS Analysis. *Crystals*, *14*(11), 961. https://doi.org/10.3390/cryst14110961

6 Pham, A. L. T., Lee, C., Doyle, F. M., & Sedlak, D. L. (2009). A silica-supported iron oxide catalyst capable of activating hydrogen peroxide at neutral pH values. *Environmental science & technology*, *43*(23), 8930–8935. https://doi.org/10.1021/es902296k

7 Saman, D., Bondarenko, L. S., Baimuratova, R. K., Dzeranov, A. A., Dzhardimalieva, G. I., Tropskaya, N. S., & Kydralieva, K. A. (2024). A Statistical Design Approach for an Effective Catalyst in the Fenton Reaction in Case of Fe_3O_4-MOF MIL-88b (Fe) in Methylene Blue Degradation Kinetics. *Eurasian Journal of Chemistry*, *29*(115), 16–29. https://doi.org/10.31489/2959-0663/3-24-15

8 Dzeranov, A., Pankratov, D., Bondarenko, L., Telegina, L., Dzhardimalieva, G., Saman, D., & Kydralieva, K. (2024). Humic acids-modified mesoporous silica encapsulating magnetite: crystal and surface characteristics. *CrystEngComm*, *26*(24), 3250–3262. https://doi.org/10.1039/D4CE00281D

9 Bondarenko, L., Baimuratova, R., Dzeranov, A., Pankratov, D., Kicheeva, A., Sushko, E., ... & Kydralieva, K. (2024). Fenton reaction-driven pro-oxidant synergy of ascorbic acid and iron oxide nanoparticles in MIL-88B (Fe). *New Journal of Chemistry*, *48*(22), 10142–10160. https://doi.org/10.1039/D4NJ00963K

10 Bondarenko, L., Baimuratova, R., Reindl, M., Zach, V., Dzeranov, A., Pankratov, D., ... & Schwaminger, S. P. (2024). Designed magnetic nanoparticles for ferroptosis: Release of iron ions from metal-organic frameworks modified with iron oxides. *Materials Today Chemistry*, *42*, 102332. https://doi.org/10.1016/j.mtchem.2024.102332

11 Dzeranov, A., Bondarenko, L., Pankratov, D., Prokof`ev, M., Dzhardimalieva, G., Jorobekova, S., ... & Kydralieva, K. (2022). Iron oxides nanoparticles as components of ferroptosis-inducing systems: screening of potential candidates. *Magnetochemistry*, *9*(1), 3. https://doi.org/10.3390/magnetochemistry9010003

12 Sahoo, Y., Goodarzi, A., Swihart, M. T., Ohulchanskyy, T. Y., Kaur, N., Furlani, E. P., & Prasad, P. N. (2005). Aqueous ferrofluid of magnetite nanoparticles: fluorescence labeling and magnetophoretic control. *The Journal of Physical Chemistry B*, *109*(9), 3879–3885. https://doi.org/10.1021/jp045402y

13 Lee, N., & Hyeon, T. (2012). Designed synthesis of uniformly sized iron oxide nanoparticles for efficient magnetic resonance imaging contrast agents. *Chemical Society Reviews*, *41*(7), 2575–2589. https://doi.org/10.1039/C1CS15248C

14 Jurgons, R., Seliger, C., Hilpert, A., Trahms, L., Odenbach, S., & Alexiou, C. (2006). Drug loaded magnetic nanoparticles for cancer therapy. *Journal of Physics: Condensed Matter*, *18*(38), S2893. https://doi.org/10.1088/0953-8984/18/38/S24

15 Pankhurst, Q. A., Connolly, J., Jones, S. K., & Dobson, J. J. J. (2003). Applications of magnetic nanoparticles in biomedicine. *Journal of physics D: Applied physics*, *36*(13), R167. https://doi.org/10.1088/0022-3727/36/13/201

16 Laurent, S., Forge, D., Port, M., Roch, A., Robic, C., Vander Elst, L., & Muller, R. N. (2008). Magnetic iron oxide nanoparticles: synthesis, stabilization, vectorization, physicochemical characterizations, and biological applications. *Chemical reviews*, *108*(6), 2064–2110. https://doi.org/10.1021/cr068445e

17 Spicher, M. T., Schwaminger, S. P., Von Der Haar-Leistl, D., Peralta, M. M., Mikacevic, G., Wagner, F. E., & Berensmeier, S. (2024). Pilot-scale co-precipitation synthesis of a novel active ingredient made of ultrasmall iron (oxyhydr) oxide nanoparticles for the treatment of hyperphosphatemia. *RSC advances*, *14*(23), 16117–16127. https://doi.org/10.1039/D4RA02719A

18 Qiao, L., Fu, Z., Li, J., Ghosen, J., Zeng, M., Stebbins, J., ... & Swihart, M. T. (2017). Standardizing size-and shape-controlled synthesis of monodisperse magnetite (Fe_3O_4) nanocrystals by identifying and exploiting effects of organic impurities. *ACS nano*, *11*(6), 6370–6381. https://doi.org/10.1021/acsnano.7b02752

19 Mathew, D. S., & Juang, R. S. (2007). An overview of the structure and magnetism of spinel ferrite nanoparticles and their synthesis in microemulsions. *Chemical engineering journal*, *129*(1-3), 51–65. https://doi.org/10.1016/j.cej.2006.11.001

20 Lu, A. H., Salabas, E. E., & Schüth, F. (2007). Magnetic nanoparticles: synthesis, protection, functionalization, and application. *Angewandte Chemie International Edition*, *46*(8), 1222–1244. https://doi.org/10.1002/anie.200602866

21 Peng, S., & Sun, S. (2007). Synthesis and characterization of monodisperse hollow Fe_3O_4 nanoparticles. *Angewandte Chemie International Edition*, *46*(22), 4155–4158. https://doi.org/10.1002/anie.200700677

22 Schwaminger, S. P., Syhr, C., & Berensmeier, S. (2020). Controlled synthesis of magnetic iron oxide nanoparticles: magnetite or maghemite? *Crystals*, *10*(3), 214. https://doi.org/10.3390/cryst10030214

23 Reindl, M., Zach, V., Cvirn, G., & Schwaminger, S. P. (2025). Influence of coprecipitation synthesis parameters on the physicochemical properties and biological effects of iron oxide nanoparticles. *Nanoscale Advances*, *7*(22), 7395–7407. https://doi.org/10.1039/d5na00632e

24 Schwaminger, S. P., Bauer, D., Fraga-García, P., Wagner, F. E., & Berensmeier, S. (2017). Oxidation of magnetite nanoparticles NanoNPs: impact on surface and crystal properties. *CrystEngComm*, *19*(2), 246–255. https://doi.org/10.1039/C6CE02421A

25 Siregar, N., Indrayana, I. P. T., Suharyadi, E., Kato, T., & Iwata, S. (2017). Effect of synthesis temperature and NaOH concentration on microstructural and magnetic properties of $Mn_{0.5}Zn_{0.5}Fe_2O_4$ nanoparticles. In *IOP Conference Series: Materials Science and Engineering*, *202*(1), 012048. https://doi.org/10.1088/1757-899X/202/1/012048

26 Ghazanfari, M. R., Kashefi, M., & Jaafari, M. R. (2016). Optimizing and modeling of effective parameters on the structural and magnetic properties of Fe_3O_4 nanoparticles synthesized by coprecipitation technique using response surface methodology. *Journal of Magnetism and Magnetic Materials*, *409*, 134–142. https://doi.org/10.1016/j.jmmm.2016.02.094

27 Valenzuela, R., Fuentes, M. C., Parra, C., Baeza, J., Duran, N., Sharma, S. K., ... & Freer, J. (2009). Influence of stirring velocity on the synthesis of magnetite nanoparticles (Fe_3O_4) by the co-precipitation method. *Journal of Alloys and Compounds*, *488*(1), 227–231. https://doi.org/10.1016/j.jallcom.2009.08.087

28 Huang, Z., Tang, F., & Zhang, L. (2005). Morphology control and texture of Fe_3O_4 nanoparticle-coated polystyrene microspheres by ethylene glycol in forced hydrolysis reaction. *Thin Solid Films*, *471*(1-2), 105–112. https://doi.org/10.1016/j.tsf.2004.04.042

29 Furusawa, K., Norde, W. & Lyklema, J. (1972). A method for preparing surfactant-free polystyrene latices of high surface charge. *Kolloid-Zeitschrift & Zeitschrift für Polymere*, *250*(9), 908–909. https://doi.org/10.1007/BF01506246

30 Sobenin, D.V., Solovov, R.D. & Ershov B.G. (2026). Transformation of zerovalent iron nanoparticles in isopropanol into oxide particles: effect of water and air on mechanism and kinetics. *Journal of Molecular Liquids*, *447*, 129333. https://doi.org/10.1016/j.molliq.2026.129333

31 Elmore, W.C. (1938). Ferromagnetic colloid for studying magnetic structures. *Physical Review*, *54*(4), 309–310. https://doi.org/10.1103/PhysRev.54.309

32 Xu, N., Yan, H., Jiao, X., Jiang, L., Zhang, R., Wang, J., Liu, Z., Liu, Z., Gu, Y., Gang, F., Wang, X., Zhao, L., & Sun, X. (2020). Effect of OH^- concentration on Fe_3O_4 nanoparticle morphologies supported by first principle calculation. *Journal of Crystal Growth*, *547*, 125780. https://doi.org/10.1016/j.jcrysgro.2020.125780

33 Bhagwat, S., Singh, H., Athawale, A., Hannoyer, B., Jouen, S., Lefez, B., Kundaliya, D., Pasricha, R., Kulkarni, S., & Ogale, S. (2007). Low temperature synthesis of magnetite and maghemite nanoparticles. *Journal of Nanoscience and Nanotechnology*, *7*(12), 4294–4302. https://doi.org/10.1166/jnn.2007.873

34 Vinila, V.S.; Isac, J. (2022). Chapter 14 — Synthesis and structural studies of superconducting perovskite $GdBa_2Ca_3Cu_4O_{10.5+\delta}$ nanosystems. *Design, Fabrication, and Characterization of Multifunctional Nanomaterials*, 319–341. https://doi.org/10.1016/B978-0-12-820558-7.00022-4

35 Frison, R., Cernuto, G., Cervellino, A., Zaharko, O., Colonna, G. M., Guagliardi, A., Masciocchi, N. (2013). Magnetite–Maghemite Nanoparticles in the 5–15 Nm Range: Correlating the Core–Shell Composition and the Surface Structure to the Magnetic Properties. A Total Scattering Study. *Chemistry of Materials*, *25*(23), 4820–4827. https://doi.org/10.1021/cm403360f.

36 Dzeranov, A., Bondarenko, L., Saman, D., Prokof'ev, M., Terekhova, V., Telegina, L., Dzhardimalieva, G., Bolotskaya, S., Kydralieva, K. (2024). Effects of water-induced aging on iron (oxyhydr)oxides nanoparticles: linking crystal structure, iron ion release, and toxicity. *Chemical Papers*. https://doi.org/10.1007/s11696-024-03373-x.

37 Bondarenko, L., Kahru, A., Terekhova, V., Dzhardimalieva, G., Uchanov, P., Kydralieva, K. (2020). Effects of Humic Acids on the Ecotoxicity of Fe_3O_4 Nanoparticles and Fe-Ions: Impact of Oxidation and Aging. *Nanomaterials*, *10*(10), 2011. https://doi.org/10.3390/nano10102011

38 Chen, L., Ma, J., Li, X., Zhang, J., Fang, J., Guan, Y., & Xie, P. (2011). Strong enhancement on fenton oxidation by addition of hydroxylamine to accelerate the ferric and ferrous iron cycles. *Environmental science & technology*, *45*(9), 3925–3930. https://doi.org/10.1021/es2002748

How to Cite: Bondarenko, L.S., Dzeranov, A.A., Tropskaya, N.S., & Kydralieva, K.A. (2026). Dispersion Technique May Change Structure and Bio-Oxidative Activity of Magnetic MOF Nanoparticles. *Eurasian Journal of Chemistry, 31, 1(121), 151–163.* https://doi.org/10.31489/2959-0663/1-26-8

Article

Received: 2 December 2025 | Revised: 2 March 2026 | Accepted: 5 March 2026 | Published online: 13 March 2026

UDC 544.42+519.242.7

https://doi.org/10.31489/2959-0663/1-26-8

Lyubov S. Bondarenko[1], Artur A. Dzeranov[1], Nataliya S. Tropskaya[1, 2], Kamila A. Kydralieva[1*]

[1]*Moscow Aviation Institute (National Research University), Moscow, Russia;*
[2]*Sklifosovsky Research Institute for Emergency Medicine, Moscow, Russia*
*(*Corresponding author's e-mail: kamila.kydralieva@gmail.com)*

Dispersion Technique May Change Structure and Bio-Oxidative Activity of Magnetic MOF Nanoparticles

The overlooked influence of routine operations on hydrophobic nanosuspensions can induce polymorphic transformation, a critical factor that contributes to their instability and significantly limits their applications. Techniques such as ultrasonication are commercially employed for producing nanosuspensions. However, the impact of routine operations, including mechanical grinding and ultrasound, on obtaining stable suspensions has not received sufficient attention, despite their potential to alter microstructure, morphology, and consequently, functional properties. In this study, Fe_3O_4-ascorbic acid/ metal-organic coordination polymer (MOF) MIL-88b (Fe_3O_4-AA-MOF) nanoparticles (NPs) were subjected to grinding in a mortar (GM). Subsequently, 1.0 wt.% of aqueous suspensions were ultrasonicated (GM+US) for 3 min at 30 kHz and 37 °C. The structure and oxidative properties of the homogenized suspensions were investigated using X-ray diffraction technique, dynamic light scattering (DLS), and scanning electronic microscope (SEM), with native NPs serving as a control. Homogenization treatment significantly affected the microstructure and oxidative behavior of Fe_3O_4-AA-MOF NPs. The combination of milling and ultrasound led to a change in the stoichiometry of magnetite, partial destruction of MOF, and simultaneously, an acceleration of the Fenton reaction and increased stability of NPs in suspension. These findings underscore that the influence of routine sample preparation operations on the functional properties of NPs cannot be underestimated.

Keywords: metal organic framework, MOF, magnetic iron oxide nanoparticles, nanosuspensions, sample preparation operations, grinding in the mortar, ultrasonication, structure, oxidative properties

Introduction

The reproducibility crisis of scientific experiments can stem from various factors affecting chemical reactions, including solvent variability, temperature fluctuations, vessel configuration, heat and mass transfer within the reaction mixture, challenges with thorough mixing, reagent and intermediates purity, and contamination or phantom reactivity, as highlighted by [1]. However, another often-overlooked factor significantly impacting the reproducibility of biological experiments, particularly those involving insoluble chemical compounds like magnetite nanoparticles (NPs), is the mandatory sample preparation. These routine operations, justified by the logic of *in vitro* and *in vivo* experiments, include grinding samples and dispersing them to achieve the required sizes for administration, such as intravenous injection. Such operations are frequently considered so routine and insignificant that they are often omitted from experimental methodology. Nevertheless, they can induce changes not only in particle size but also in their microstructure and, consequently, their functional properties.

In a recent Nanofocus paper [2], the authors identified the need for improved nanotechnology tools and methods as one of 33 key questions in nanoscience and nanotechnology. As a crucial characteristic of NPs, size profoundly influences the efficiency of passive or active targeted drug delivery and other biomedicine applications. This influence extends to circulation time, biodistribution, accumulation, and penetration, cellular uptake, and subcellular distribution [3, 4]. While the preferred size for intravenous injection typically ranges from 2 to 200 nm, as larger NPs (>200 nm) are prone to phagocytosis by macrophages and thus cannot leverage the enhanced permeability and retention effect [5, 6]. NPs generally range from 10 to 1000 nm in size [7]. Furthermore, numerous properties, including size, dictate their *in vivo* behavior, encompassing stability in blood and other body fluids, biodistribution, margination, circulation time, phagocytic uptake, organ-specific accumulation, drug release, attachment and penetration into target cells, excretion and toxicity

[3, 5, 6, 8–12]. Stability is a critical prerequisite for most of the biopreparations, as it ensures predictable and controllable behavior. Consequently, nanofluids are desired to possess thermodynamic, kinetic, chemical, and dispersion stabilities. Due to inter-particle adhesion forces, NPs tend to agglomerate, and their settlement can occur due to the gravitational forces [13]. Concurrently, an increasing number of newly developed drugs exhibit poorly solubility, leading to bioavailability challenges. A promising alternative approach to overcome these issues is the production of stable nanosuspensions with controlled size or post-production processing of NPs [14]. To prepare stable nanofluids, extensive investigations into colloidal dispersions have been conducted, focusing on particle motion analysis under various flow conditions and sedimentation characteristics of suspended NPs in base fluids [15]. Two primary methods exist for producing nanofluids; (i) the one-step direct evaporation method, which involves the direct formation of NPs within the base fluids, and (ii) the two-step method, which entails forming NPs and subsequently dispersing them in the base fluids [15]. In the latter approach, various dispersion techniques are employed, including stirrers, ultrasonic baths, ultrasonic disruptors, high-pressure homogenizers, and modified magnetron sputtering systems, to prepare nanofluids. Among these techniques, ultrasonication is widely used [13] due to its technical simplicity and cost effectiveness. During homogenization, particle fracture is achieved through cavitation, high-shear forces, and inter-particle collisions [16]. It is commonly assumed that longer ultrasonication durations are more beneficial for nanofluid preparation [13]. However, no standardized protocols have been established to nanofluid preparation, particularly regarding optimal homogenization duration, sonicator power amplitude, or the type and duration of pulse mode operation. Nevertheless, the National Institute of Standards and Technology (NIST, Gaithersburg, MD), in collaboration with the Center for the Environmental Implications of Nanotechnology (CEINT of Duke University), has initiated efforts to develop standardized and validated protocols for NPs dispersion [17]. Proposed guidelines include the use of cooling baths, pulse mode operation, and cylindrical flat-bottom beakers. It is important to note that ultrasonication is a complex physicochemical process that can both break down agglomeration and induce further aggregation, alongside other effects together and chemical reactions [17]. For iron-containing nanoparticles, even trace water and dissolved oxygen can shift the oxidation pathway and kinetics, as shown for zerovalent iron nanoparticles in isopropanol where the presence of water and air governs the transformation into oxide particles [18]. Ultrasonic dispersion is also frequently employed to obtain stable nanosuspensions for biomedicine [19–21]. Despite its routine use, authors often overlook the state of NPs microstructure after dispersion. The harsh effect of cavitation can not only lead to re-aggregation [17], but also cause a change in the sample's microstructure and surface chemistry [22]. According to Li et al [22], ultrasonic irradiation can alter the dealloying process, activate particles by removing the oxide layer, and influence the morphology and structure of the products. Li et al. demonstrated that ultrasonic irradiation leads to chemical dealloying of Co-Al NPs. Similarly, Zhang et al [23] showed that extensive sonication severely damages the crystal structures of carbon nanotubes, thereby degrading the mechanical properties of carbon nanotube films and their composites. However, we have found no studies investigating the structure and functional properties of NPs after ultrasonic dispersion specifically for injection applications.

Iron-based metal-organic coordination frameworks (MOFs) serve as efficient catalysts for heterogeneous Fenton reactions due to their high porosity, large specific surface area, and numerous, uniformly distributed unsaturated iron sites [24, 25]. We utilized, MIL-88b (Fe), a three-dimensional porous MOF composed of 1,4-benzenedicarboxylic acid and octahedral trinuclear Fe clusters (Fe_3-μ_3-oxo) with vacant coordination sites accessible to hydrogen peroxide (H_2O_2) molecules. The resulting MIL-88b was modified with ascorbic acid (AA) to accelerate the Fe^{2+}/Fe^{3+} redox cycle and iron oxides, particularly magnetite Fe_3O_4, for localized drug delivery [26]. In this study, an aqueous suspension of Fe_3O_4-AA-MOF was homogenized using a mechanical grinding and ultrasound treatment as a routine procedure for injection. The effect of this homogenization, as a sample preparation step for injection, on both the crystal structure and oxidative characteristics of NP_S was investigated.

Experimental

Preparation of the Fe_3O_4-AA-MOF

The Fe_3O_4-AA-MOF complex was synthesized following a procedure as described in [26]. Briefly, The Fe_3O_4–MOF complex was prepared in an inert atmosphere (argon) in two steps. In the first step, magnetite NPs were obtained by coprecipitation of aqueous solutions of iron(II) and iron(III) salts with a base using the Elmore method [27] in an inert atmosphere (argon). Briefly, 3.07 g $FeCl_3 \times 6H_2O$ and 1.13 g $FeSO_4 \times 7H_2O$ were dissolved in 0.35 L of deionized water and stirred using a mechanical stirrer (1400–1500 rpm). Then

6.8 mL of 25 % NH_4OH solution were slowly added with stirring, adjusting the pH to 9. Then, ascorbic acid (0.1 g AA per 1 g MOF), 5.90 g (0.035 mol) terephthalic acid (TPA) and 8.70 g (0.0118 mol) $[Fe_3O(C_8H_4O_4)_3(H_2O)_3]Cl$ were added to the suspension containing magnetite NPs. The mixture was continuously stirred with a mechanical stirrer (900 rpm) for 60 min. The precipitate was filtered off on a paper filter and washed repeatedly with degassed distilled water and 96.5 % ethanol. The resulting sample was dried in a dynamic vacuum at low heating (60 °C). Elemental analysis revealed an iron content of 44.4 %. Infrared spectroscopy (KBr pellet) confirmed the expected structure, with characteristic peaks observed at 3423 cm^{-1} (O–H), 2925 cm^{-1} (CH), 1564 and 1392 cm^{-1} (COO–), 1155 cm^{-1}, and 1018, 822, 749, 613, and 551 cm^{-1} (Fe–O).

Pretreatment

Intravenous administration of NPs requires their dispersion to reduce their size: dispersion was carried out sequentially by the gentle manual grinding in an agate mortar using agate pestle for 10 min in air-ambient conditions and/or treatment in an ultrasonic bath (30 kHz, 50 W) for 3 min at 37 °C. Thus, three samples were selected for subsequent analysis of structure and morphology: initial Fe_3O_4-AA-MOF (IN), after grinding in the mortar (GM) and after both grinding and ultrasonication (GM+US).

X-Ray Diffraction Analysis

Transmission geometry was used for X-ray diffraction (XRD) analysis on a Philips X-pert diffractometer (Philips Analytical, Eindhoven, The Netherlands) with Cr-Ka radiation (λ = 2.29106 Å) and a step size of 0.0121. Quantitative analyses were performed by refinement of the total multiphase spectrum method (the Rietveld method) with a fundamental parameters approach, using the Profex software. Background was handly calculated and a fixed seven-line K_α plus an intensity-refined K_β emission profile was adopted.

Fourier Transform Infrared Spectroscopy

The functional groups present in the samples were analyzed using Fourier transform infrared (FTIR) spectroscopy. Measurements were performed on an FTIR IR-200 spectrometer (ThermoNicolet, Waltham, MA, USA) in the range of 4000 to 400 cm^{-1}. For analysis, powdered samples were mixed with high purity potassium bromide (KBr) at a ratio of 1 mg sample to 150 mg KBr. The mixture was then pressed into pellets with a diameter of 13 mm using a force of 6 tons.

Scanning Electron Microscopy

To examine the size and shape of the particles, we used scanning electron microscopy (SEM). First, a double-sided sticky tape was attached to small sample holders (SEM stubs), and the particles were placed onto the stubs. To enhance image quality, a thin layer of platinum (10 nm thick) was sputtered onto the samples. Finally, the particles were observed using a Tescan Vega 3 microscope operating at 20 kV, equipped with a specialized detector for secondary electrons.

Determining the Degree of Methylene Blue Decolorization.

The degree of methylene blue decolorization was assessed as an indirect indicator of OH-radicals production during the Fenton reaction (H_2O_2 decomposition) using UV-Vis spectroscopy. This method relies on the colour change of MB caused by these radicals. The experiments were carried out under conditions simulating the microenvironment of tumor cells 0.1 M buffers (NaAc for pH 4.5) [28, 29]. Briefly, 10 mg of the sample was suspended in 1.5 mL of 0.1 M buffers (NaAc for pH 4.5) and MB. The mixture was heated to 37 °C and stirred at 700 rpm. 30 % H_2O_2 (100 mM) was then added to initiate the Fenton reaction. To enable comparison of the experimental results with literature data, the H_2O_2 concentration was chosen in accordance with model experiments by other authors [30, 31]. At specific points in time (0, 30, 90, and 180 min), the reaction was stopped, and the supernatant was separated by centrifugation at 6000 rpm for 2 min. The absorbance of the supernatant was measured at 652 nm using a Cary UV-Vis-NIR Spectrophotometer (Agilent Technologies).

Determination of the Equilibrium Concentration of Fe^{2+} and Fe^{3+} in Solution

To detect iron ions, the powder was suspended in 0.1 M buffers (NaAc for pH 4.5) then subjected to centrifugation (6000 rpm, 5 min) after 0, 30, 90, 180 min, and 24 h. Appropriate ion detection reagents were added to the supernatant after separation. To detect Fe^{3+}, 200 μL of potassium thiocyanate KSCN (50 % solution) and 200 μL of HCl (18.25 % solution) were added to 5 mL of supernatant since the reaction between Fe^{3+} and KSCN proceeded in a strongly acidic medium at pH close to 2. The solution was then kept for

20 min to reach equilibrium, and the absorption spectrum in the region of 480 nm was measured. In order to detect Fe^{2+} ions, 2 mL o-phenanthroline $C_{12}H_8N_2$ H_2O (2.5 % solution) and 600 μL of ammonium acetate buffer solution (250 mL of NH_4OH and 900 mL of glacial acetic acid) were also added to 5 mL of the supernatant. The solution was also kept for 20 min to reach equilibrium (no color change) and examined in the region of 510 nm. The absorbance was detected by UV-Vis-NIR spectrophotometry (Cary UV-Vis-NIR Spectrophotometer, Agilent Technologies).

Results and Discussion

Effect of Sample Preparation on the Crystal Structure and Morphology of NPs

The NPs powder underwent sample preparation, which involved grinding in a mortar followed by dispersion in deionized water using an ultrasonic bath for 3 min at 30 kHz and 37 °C. Our primary interest was to determine whether this sample preparation alters the structure and morphology of the NPs, as such changes could subsequently affect their functional properties. The Fe^{2+} located at tetrahedral sites on the surface of magnetite NPs are highly susceptible to rapid oxidation under ambient conditions, leading to alterations in composition and properties [32]. This sensitivity to oxygen often restricts their application, as distinct magnetic properties and particle size can be compromised. To accurately determine the Fe^{2+}/Fe^{3+} ratio in our samples, employed X-ray diffraction (XRD) analysis (Figure 1), which can reveal changes in the crystal structure indicative of a complete atomic rearrangement that occurs during the oxidation process. As evident from the diffraction pattern, peaks observed at 2θ values of 30.14, 35.53, 43.32, 53.51, 57.20, and 62.69 correspond to those of magnetite (ICDD-PDF 19–629). Additionally, peaks at 17.37, 25.20, and 27.91 correspond to an impurity phase, specifically unreacted TPA ligand (CCDC 1269122). This impurity may be attributed to the entrapment of ligand molecules within the pores of MOF. Low intensity peaks at 39.6° and 41.1° are highly likely due to NH_4Cl (ICDD 34-0710), which was formed as a by-product of the reaction between ferric chloride and ammonia.

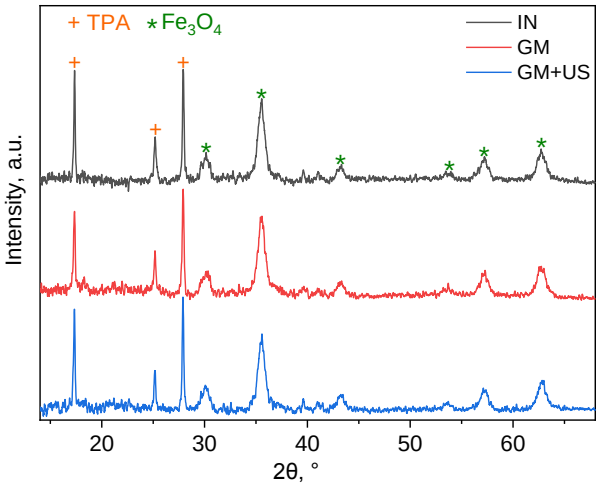

Figure 1. XRD of initial sample (IN), after grinding in the mortar (GM) and after both grinding and ultrasonication (GM+US)

Rietveld analysis, performed using Profex 2.5.4 program (goodness of fit, GoF) values are presented in Table 1), was used to determine the lattice parameters for samples containing iron oxide NPs. Interestingly, all samples displayed lower lattice parameters compared to standard magnetite (8.396–8.400 Å according to ICDD-PDF 19–629), yet higher values than those of maghemite (8.330–8.340 Å according to ICDD-PDF 39-1346). This observation suggests partial oxidation of Fe^{2+} during drying, storage, or modification, leading to the formation of non-stoichiometric magnetite. Stoichiometric magnetite refers to the mineral phase with an ideal Fe^{2+} content, corresponding to the Fe_3O_4 formula. As magnetite undergoes oxidation, its Fe^{2+}/Fe^{3+} ratio changes, resulting in a nonstoichiometric or partially oxidized form, represented by the formula $Fe_{3-\sigma}O_4$ (where σ ranges from zero for stoichiometric magnetite to 1/3 for fully oxidized maghemite) [33].

Table 1

XRD and statistical parameters of Rietveld refinement

	Unit lattice, Å	GOF	Formula
IN	8.3756±0.0002	1.06	$Fe_{2.89}O_4$
GM	8.3742±0.0004	1.07	$Fe_{2.89}O_4$
GM+US	8.3574±0.0001	1.09	$Fe_{2.79}O_4$

This analysis confirms the formation of non-stoichiometric magnetite $Fe_{2.89}O_4$ within the MOF matrix, which contains both magnetite and maghemite NPs (Figure 1). This is likely due to the oxidation of Fe^{2+} ions in the pre-synthesized magnetite. The synthesis, storage, and use of iron oxide NPs can lead to oxidation and phase transformations. The mechanism for this process involves: (1) adsorption of oxygen: oxygen adsorbs onto the NPs surface, where it is ionized by the electrons released during the oxidation of Fe^{2+} to Fe^{3+}, (2) concentration gradient and diffusion: further surface oxidation creates a concentration gradient, promoting diffusion of iron ions to the surface and the formation of vacancies [34]. Gentle manual grinding of NPs in a mortar does not significantly alter the elementary cell parameter or magnetite content (Table 1). In contrast, ultrasonic dispersion results in a notable change in the unit cell parameter, indicating partial oxidation of Fe^{2+} to Fe^{3+} and the subsequent transformation of Fe_3O_4 to γ-Fe_2O_3. This partial oxidation of divalent iron ions may be attributed to the unique conditions of ultrasonic irradiation, such as the acoustic cavitation process, which generates localized hot spots with temperature up to 5000 K, pressures up to 2000 atm, cooling rates of 1010 K s^{-1}. In addition to these hot spots, sonochemical processes also produce shock waves and microjets [35]. Interestingly, while US-exposure can lead to magnetite oxidation, possibly due to the mechanical effects of cavitation, it can also induce the reduction of iron ions depending on the specific conditions. For example, Stolyar et al [36] reported the formation of α-Fe metal phase from iron oxide and iron oxyhydroxide NPs when exposed to ultrasound, but only in the presence of albumin.

As revealed by Infrared (IR) spectroscopy (Figure 2), all three samples exhibited identical absorption bands before and after pretreatment, which demonstrates the stability of the sample's microstructure to both mechanical and ultrasound treatment. In all samples, a broad absorption band in the 2800–3600 cm^{-1} region was observed. This band is attributed to the stretching vibrations of hydroxyl (OH) groups, originating from both physically adsorbed and crystallizing water molecules.

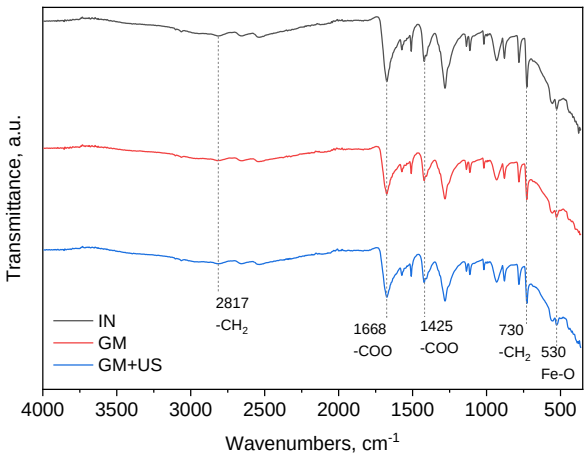

Figure 2. IR-spectra of initial sample (IN), after grinding in the mortar (GM) and after both grinding and ultrasonication (GM+US)

The IR-spectra dispayed stretching vibration peaks correspondimg to the =C–H bonds of the terephtaluic acid (TPA) molecules between 2950 and 2640 cm^{-1}, with the most prominent at 2817 cm^{-1}). Additionally, peaks approximately 1600 cm^{-1} and ~1400 cm^{-1} are assigned to the asymmetric and symmetric stretching vibrations of the carboxylate anion (–COO) within the MOF. A vibration peak located at approximately 530 cm^{-1} correspond to the Fe–O bond, which is present in both the MOF and the iron oxide components.

SEM analysis (Figure 3) confirmed that the morphology of Fe_3O_4-AA-MOF was preserved after grinding in a mortar. As shown in Figures 3*a* and *b*, the characteristic bipyramidal shape of the MIL-88B component remained intact [37–39].

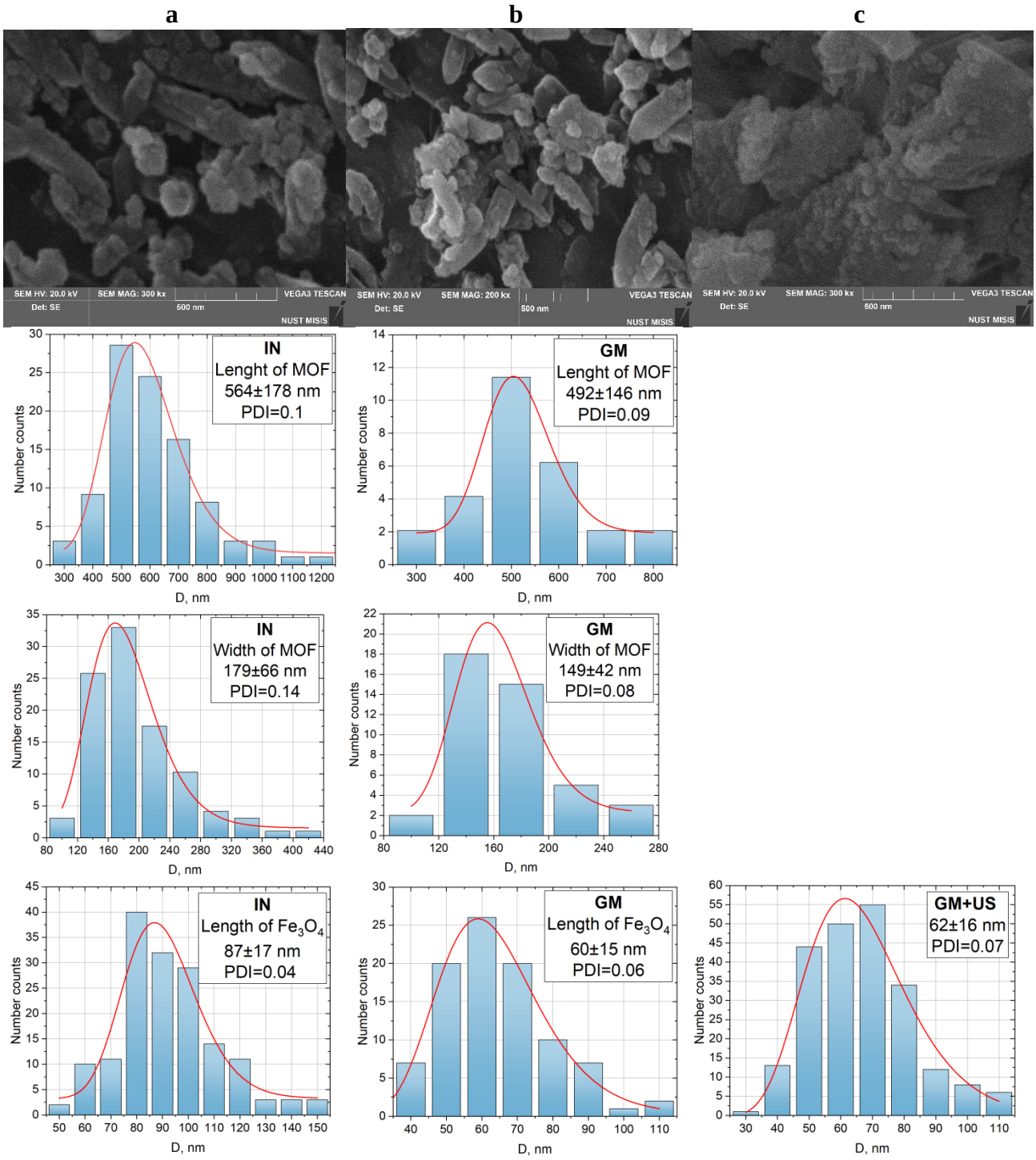

Figure 3. SEM images of IN (*a*) [26], GM (*b*) and GM+US (*c*).
The size distribution for MOF length and width is based on the analysis
of at least 100 particles per image, with at least three images used for each calculation.
(PDI=0 — monodisperse distribution; PDI=1 — polydisperse distribution)

Following the mechanical dispersion, the average particle length decreased from 564 to 492 nm, and the width decreased from 179 to 149 nm. In contrast, subsequent dispersion in an ultrasonic bath resulted in the

partial destruction of the MOF structures (Figure 3*c*), although the iron oxide immobilized on its surface was preserved. The size of these Fe_3O_4 particles was measured to be 62 nm.

To evaluate the stability of the Fe_3O_4-AA-MOF in 0.9 % NaCl solution following the treatments, the concentration of TPA was monitored. The samples were suspended for 180 min with continuous shaking at 300 rpm (Figures 4*a* and *b*).

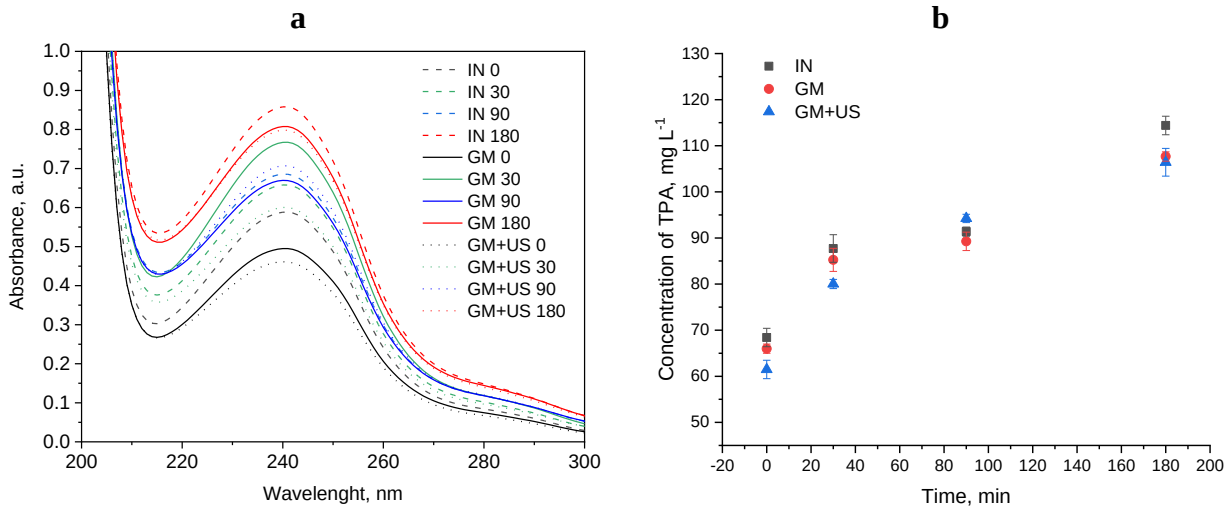

Figure 4. UV-Vis spectra of the samples after grinding in a mortar and dispersion in an ultrasonic bath during 180 min (*a*); Concentration of TPA in IN, GM, GM + US samples during 180 min (*b*)

As shown in Figure 4*b*, the concentration of TPA increased by a factor of approximately 1.7 over the three-hour period. This increase is likely attributable to the release of unreacted TPA from the pores of the MOF, a funding that is consistent with the X-ray diffraction data. Concurrently, the variation in TPA concentration between the untreated and treated samples did not exceed 20 %. This limited variation indicates the sample's stability against both mechanical and ultrasound exposure, which corroborates the findings from IR spectroscopy and X-ray diffraction analyses.

Study of Prooxidant Properties of the Sample Before and After Treatment

In this study, methylene blue (MB) was selected as a model dye to systematically investigate the degradation mechanism and reactive oxygen species (ROS) generation in iron-containing systems. A reduction in absorbance at λ_{max} is typically associated with the oxidation of the chromophore group by hydroxyl radicals (•OH). Dye decolorization was monitored by measuring the decrease in absorbance at its characteristic wavelength of λ_{max} (652 nm) under the experimental conditions. suggesting that the dye was likely converted into colorless, smaller molecules [40]. To correlate the model data with the *in vivo* experimental results, sample concentrations of 7.5 and 15 g L^{-1} were chosen, corresponding to doses of 25 and 50 mg kg^{-1}.

An investigation into the effect of sample preparation method used in *in vivo* experiments revealed that mechanical grinding in a mortar, or mechanical treatment followed by ultrasonic dispersion, led to a two-fold increase in the reaction rate. Complete decolorization occurred within 90 min, compared to 180 min for the native sample (Figure S1, SI).

Mechanical dispersion in a mortar resulted in a statistically significant 1.4-fold increase in the Fenton reaction rate. The rate constant increased from 0.015 min^{-1} for the native sample to 0.02 min^{-1} for the ground sample (Figure 5). Conversely, additional dispersion in an ultrasonic bath did not lead to statistically significant changes in the prooxidant properties or any deterioration compared to the original preparation.

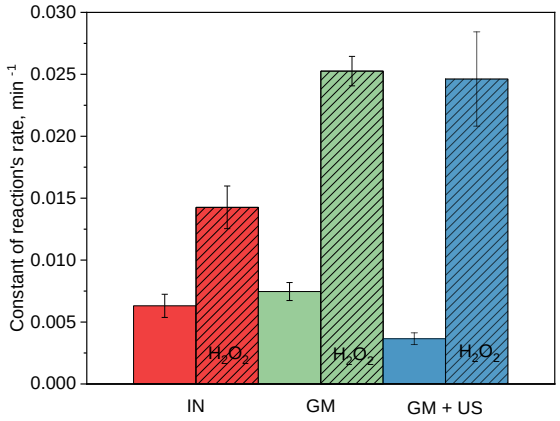

Figure 5. Fenton reaction rate constant of samples in the presence of hydrogen peroxide

The contribution of the Fenton reaction to MB degradation was estimated by calculating the difference between the supernatant absorbance after sorption without H_2O_2 and its absorbance after the Fenton reaction in the presence of H_2O_2. It was observed that both mechanical grinding and a combination of grinding with ultrasonic dispersion resulted in a statistically significant acceleration of the Fenton reaction. It is well-documented that coupling the Fenton reaction with external energy sources like ultraviolet (UV) or ultrasound (US) is of great interest due to a higher yield of hydroxyl •OH radicals or the ability to use lower concentrations of Fenton reagents [41, 41]. Accordingly, the oxidation rate of a process like UV/Fenton is accelerated through generation of additional radical •OH radicals within the system [42, 43].

To elucidate the mechanism underlying the effect of sample preparation on the prooxidant properties of the Fe_3O_4-AA-MOF sample, the release of Fe^{2+} and Fe^{3+} ions was investigated. As illustrated in the corresponding graph, sample preparation generally leads to an increased concentration of both released Fe^{2+} and Fe^{3+} ions over the course of the experiment. Figure 6 shows an estimate of the Fe^{2+}/Fe^{3+} ion ratios for different sample preparation methods 90 minutes after the experiment began. The data indicate that mechanical grinding, as well as its combination with ultrasonic dispersion, leads to a decrease in the relative Fe^{2+} concentration. This is presumably due to the oxidation of these ions in localized hot spots generated by the sonochemical process. Nevertheless, despite the oxidation of Fe^{2+} ions during sample preparation, the net increase in the total concentration of released ions leads to the observed acceleration of the Fenton reaction (Figure 6).

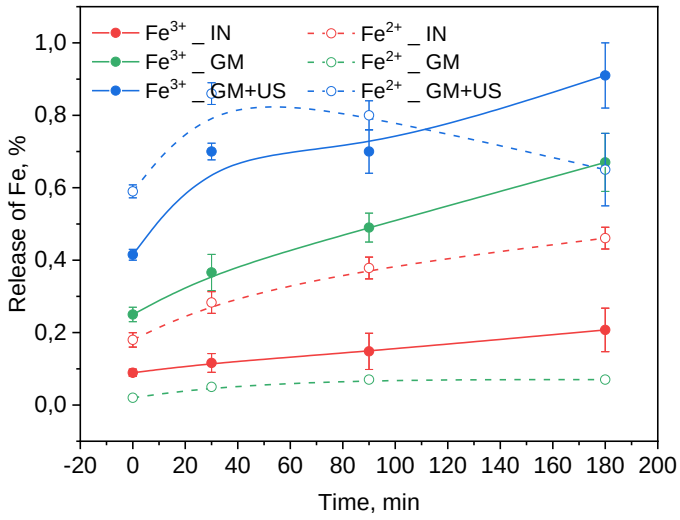

Figure 6. Kinetics of Fe^{2+} and Fe^{3+} release from Fe_3O_4-AA-MOF before and after sample preparation

Several additional reasons for the increased catalytic activity of magnetite NPs are highlighted in the literature. Changes in the catalytic activity of the modified magnetite have been attributed to the existence of thermodynamically favorable redox pairs of cations on the catalysts surface. These pairs are reported to en-

hance Fenton degradation of probe molecules through three primary pethways (i) direct involvement in the Fenton oxidation cycle and generation of •OH radicals via the Haber-Weiss mechanism; (ii) the regeneration of Fe^{2+} cations; and (iii) the acceleration of electron transfer during the oxidation reaction within the magnetite structure [44, 45]. Futhermore, Costa et al. proposed the generation of oxygen vacancies as another possible reason for enhanced catalytic activities [46]. These vacancies, which arise from adjustments for unequal replacements or cationic deficiency in the modified iron oxide structure, can act as active sites. They may contribute either directly to the degradation of probe molecules or indirectly by facilitating the decomposition of H_2O_2 [47]. Additional factors, such as enlarged surface area and consequently higher concentrations of hydroxyl groups on the catalyst surface, have also been reported in numerous studies [48]. Regarding the MOF component, under ultrasonic conditions, MIL-88B can be stimulated to produce electron-hole (e^-h^+) pairs. The resulting electrons can react with O_2 to generate superoxide radicals ($•O_2^-$), while the holes can react with OH^- or H_2O to generate hydroxyl radicals (•OH), also leading to an acceleration of the Fenton reaction [49].

It can be concluded that the observed enhancement of iron ions release and functional properties is caused by the samples preparation steps of mortar grinding and subsequent dispersion. This outcome is likely the result of a decrease in particle size and a corresponding increase in surface area, or the partial destruction of the MOF. These changes would create more active sites on the surface for contact with H_2O_2 and promote the release of Fe^{2+}/Fe^{3+} ions.

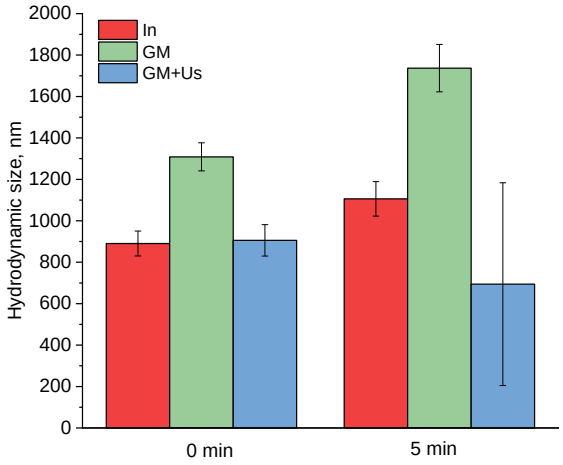

Figure 7. Change in hydrodynamic diameter of NPs before and after treatment for 5 min

The hydrodynamic diameter of NPs was evaluated by DLS in 0.9 % NaCl medium, as shown in Figure 7. A particle size distribution analysis in deionized water confirmed that all prepared samples were polydisperse, exhibiting polydispersity indices between 0.004 and 0.007. The initial average particle diameters at time zero were measured as 890±60 nm for the initial NPs (IN), 1308±83 nm for particles subjected to grinding in a mortar (GM), and 906±76 nm for particles that were ground and subsequently treated with ultrasonication (GM+US). The untreated NPs consisted of two primary fractions with sizes around 800 nm and 4000 nm. The process of grinding in a mortar lead to a statistically significant decrease in the proportion of the micron-sized fraction from 13.9±9.2 to 1.9±0 (Figure S1, SI). This fraction was further reduced to 0 % in samples with ultrasonication.

To assess their suitability for animal studies, the aggregation stability of NPs was investigated over a 5-minute period, mimicking the time from suspension to administration. This study revealed that after 5 minutes of storage, the hydrodynamic diameter of the initial (IN) and ground (GM) particles increased by approximately 200 nm and 400 nm, respectively. Conversely, for particles prepared by grinding and ultrasonication (GM+US), the hydrodynamic diameter decreased by about 200 nm, a change attributed to contribution of newly observed 204 nm fraction (5.5 %). Importantly, holding the ultrasonically dispersed particles for 5 minutes did not result in the appearance of a micron fraction. This observation suggest that these samples are sufficiently stable for use in *in vivo* applications.

Conclusions

This work investigated the effect of homogenization treatment on the crystal structure and oxidative performance of NPs. The results revealed that the NPs initially formed within MOF-cylinder as surface Fe_3O_4-spheric samples. However, after homogenization treatment involving mortar grinding and ultrasonication (3 min at 30 kHz and 37 °C), these particles transformed into compact, near-spherical structures. Crucially, the oxidative behavior of NPs was remarkably improved by both milling and ultrasonic homogenization. The enhanced oxidative oxidative performance of the homogenized samples is primarily attributed to the increased release of Fe^{2+}/Fe^{3+} ions. Furthermore, the ultrasonically-treated samples exhibited sufficiently low hydrodynamic diameters and higher stability compared to the initial samples. These findings underscore that the influence of routine sample preparation operations on the structure and functional properties of NPs cannot be underestimated.

Supporting Information

The Supporting Information is available free at https://ejc.buketov.edu.kz/ejc/article/view/606/355

Funding

The study was supported by a grant from the Russian Science Foundation (No. 22-73-10222-P, "Preparation, physicochemical characterization and pro-oxidant properties of new iron-containing mesoporous materials", https://rscf.ru/en/project/22-73-10222/).

*Author Information**

**The authors' names are presented in the following order: First Name, Middle Name and Last Name*

Lyubov Sergeevna Bondarenko — PhD (Chemistry), Associate Professor, Advanced Materials and Technologies for Aerospace Applications Department, Moscow Aviation Institute (National Research University), Volokolamskoe shosse, 4, 125080, Moscow, Russia; e-mail: l.s.bondarenko92@gmail.com; https://orcid.org/0000-0002-3107-0648

Artur Albertovich Dzeranov — Assistant Lecturer, Advanced Materials and Technologies for Aerospace Applications Department, Moscow Aviation Institute (National Research University), Volokolamskoe shosse, 4, 125080, Moscow, Russia; e-mail: arturdzeranov99@gmail.com; https://orcid.org/0000-0003-3240-9321

Natalya Sergeevna Tropskaya — PhD, DSc (Biology), Professor, Advanced Materials and Technologies for Aerospace Applications Department, Moscow Aviation Institute (National Research University), Volokolamskoe shosse, 4, 125080, Moscow, Russia; Head of Experimental Pathology Laboratory, Sklifosovsky Research Institute for Emergency Medicine, Bolshaya Sukharevskaya Square, 3/21, 107045, Moscow, Russia; e-mail: tropskayans@gmail.com; https://orcid.org/0000-0001-5870-9483

Kamila Asylbekovna Kydralieva (*corresponding author*) — PhD, DSc (Chemistry), Professor, Advanced Materials and Technologies for Aerospace Applications Department, Moscow Aviation Institute (National Research University), Volokolamskoe shosse, 4, 125080, Moscow, Russia; e-mail: kamila.kydralieva@gmail.com; https://orcid.org/0000-0002-4596-4140

Author Contributions

The manuscript was written through contributions of all authors. All authors have given approval to the final version of the manuscript. CRediT: **Lyubov Sergeevna Bondarenko:** Investigation, Writing — original draft; **Artur Albertovich Dzeranov:** Investigation, Formal analysis; **Natalya Sergeevna Tropskaya:** Resources; **Kamila Asylbekovna Kydralieva:** Writing — review & editing, Supervision, Conceptualization.

Acknowledgments

Special thanks to Professor Gulzhian Dzhardimalieva and Roza Baimuratova from the Federal Research Center for Problems of Chemical Physics and Medicinal Chemistry of the Russian Academy of Sciences for providing the samples.

Conflicts of Interest

The authors declare no conflict of interest.

References

1 Cherepanova, V.A., Gordeev, E.G., & Ananikov, V.P. (2025). Magnetic Stirring May Cause Irreproducible Results in Chemical Reactions. *JACS Au*, *5*(8), 3789–3798. https://doi.org/10.1021/jacsau.5c00412

2 Mirkin, C.A., Petrosko, S.H., Artzi, N., Aydin, K., Biaggne, A., Brinker, C.J., Bujold, K.E., Cao, Y.C., Chan, R.R., Chen, C., Chen, P.C., Chen, X., Chevalier, O.J.G.L., Choi, C.H.J., Crooks, R.M., Dravid, V.P., Du, J.S., Ebrahimi, S.B., Fan, H., Farha, O.K., Figg, C.A., Fink, T.D., Forsyth, C.M., Fuchs, H., Geiger, F.M., Gianneschi, N.C., Gibson, K.J., Ginger, D.S., Guo, S.S., Hanes, J.S., Hao, L., Huang, J., Hunter, B.M., Huo, F., Hwang, J., Jin, R., Kelley, S.O., Kempa, T.J., Kim, Y., Kudruk, S., Kumari, S., Landy, K.M., Lee, K.B., Leon, N.J., Li, J., Li, Y., Li, Z., Liu, B., Liu, G., Liu, X., Liz-Marzán, L.M., Lorch, J.H., Luo, T., Macfarlane, R.J., Millstone, J.E., Mrksich, M., Murphy, C.J., Naik, R.R., Nel, A.E., Oetheimer, C., Hedlund Orbeck, J.K., Park, S.J., Partridge, B.E., Peppas, N.A., Personick, M.L., Raj, A., Ramani, N., Ross, M.B., Ross, S.B., Sargent, E.H., Sengupta, T., Schatz, G.C., Seferos, D.S., Seideman, T., Seo, S.E., Shen, B., Shim, W., Shin, D., Simon, U., Sinegra, A.J., Smith, P.T., Spokoyny, A.M., Stang, P.J., Stegh, A.H., Stoddart, J.F., Swearer, D.F., Tan, W., Teplensky, M.H., Thaxton, C.S., Walt, D.R., Wang, M.X., Wang, Z., Wei, W.D., Weiss, P.S., Winegar, P.H., Xia, Y., Xie, Y., Xu, X., Yang, P., Yang, Y., Ye, Z., Yoon, K.R., Zhang, C., Zhang, H., Zhang, K., Zhang, L., Zhang, X., Zhang, Y., Zheng, Z., Zhou, W., Zhu, S. & Zhu, W. (2025). 33 Unresolved Questions in Nanoscience and Nanotechnology. *ACS Nano*, 19, 36, 31933–31968. https://doi.org/10.1021/acsnano.5c12854

3 Babayevska, N., Przysiecka, L., Iatsunskyi, I., Nowaczyk, G., Jarek, M., Janiszewska, E., & Jurga, S. (2023). Author Correction: ZnO size and shape effect on antibacterial activity and cytotoxicity profile. *Scientific reports*, *13*(1), 12465. https://doi.org/10.1038/s41598-023-39615-3

4 Zhang, B., Sai Lung, P., Zhao, S., Chu, Z., Chrzanowski, W., & Li, Q. (2017). Shape dependent cytotoxicity of PLGA-PEG nanoparticles on human cells. *Scientific reports*, *7*(1), 7315. https://doi.org/10.1038/s41598-017-07588-9

5 Subhan, M.A., Yalamarty, S.S.K., Filipczak, N., Parveen, F., & Torchilin, V.P. (2021). Recent Advances in Tumor Targeting via EPR Effect for Cancer Treatment. *Journal of personalized medicine*, *11*(6), 571. https://doi.org/10.3390/jpm11060571

6 Rizvi, S.A.A., & Saleh, A.M. (2018). Applications of nanoparticle systems in drug delivery technology. *Saudi pharmaceutical journal: SPJ: the official publication of the Saudi Pharmaceutical Society*, *26*(1), 64–70. https://doi.org/10.1016/j.jsps.2017.10.012

7 Öztürk, K., Kaplan, M., & Çalış, S. (2024). Effects of nanoparticle size, shape, and zeta potential on drug delivery. *International journal of pharmaceutics*, *666*, 124799. https://doi.org/10.1016/j.ijpharm.2024.124799

8 Bhatia, S. (2016). Natural Polymer Drug Delivery Systems. *Springer International Publishing*. https://doi.org/10.1007/978-3-319-41129-3

9 Bhardwaj, V., Kaushik, A., Khatib, Z.M., Nair, M., & McGoron, A.J. (2019). Recalcitrant Issues and New Frontiers in Nano-Pharmacology. *Frontiers in pharmacology*, *10*, 1369. https://doi.org/10.3389/fphar.2019.01369

10 Honary, S., & Zahir, F. (2013). Effect of Zeta Potential on the Properties of Nano-Drug Delivery Systems — A Review (Part 2). *Tropical Journal of Pharmaceutical Research*, *12*(2), 265–273. https://doi.org/10.4314/tjpr.v12i2.20

11 Ding, S., Khan, A. I., Cai, X., Song, Y., Lyu, Z., Du, D., Dutta, P., & Lin, Y. (2020). Overcoming blood-brain barrier transport: Advances in nanoparticle-based drug delivery strategies. *Materials today (Kidlington, England)*, *37*, 112–125. https://doi.org/10.1016/j.mattod.2020.02.001

12 Clogston, J.D., & Patri, A.K. (2011). Zeta potential measurement. *Methods in molecular biology (Clifton, N.J.)*, *697*, 63–70. https://doi.org/10.1007/978-1-60327-198-1_6

13 Mahbubul, I.M., Saidur, R., Amalina, M.A., Elcioglu, E.B., & Okutucu-Ozyurt, T. (2015). Effective ultrasonication process for better colloidal dispersion of nanofluid. *Ultrasonics sonochemistry*, *26*, 361–369. https://doi.org/10.1016/j.ultsonch.2015.01.005

14 Müller, R.H., Jacobs, C., & Kayser, O. (2001). Nanosuspensions as particulate drug formulations in therapy. Rationale for development and what we can expect for the future. *Advanced drug delivery reviews*, *47*(1), 3–19. https://doi.org/10.1016/s0169-409x(00)00118-6

15 Hwang, Y., Lee, J., Lee, J., Jeong, Y., Cheong, S., Ahn, Y.C., & Kim, S.H. (2008). Production and dispersion stability of nanoparticles in nanofluids. *Powder Technology*, *186*, 145–153. https://doi.org/10.1016/j.powtec.2007.11.020

16 Kamala Kumari, P.V. & Srinivasa Rao, Y. (2017). Nanosuspensions: A review. *International Journal of Pharmacy*. *7*(2), 77–89.

17 Taurozzi, J., Hackley, V. & Wiesner, M. (2012). Preparation of Nanoparticle Dispersions from Powdered Material Using Ultrasonic Disruption — Version 1.1. *National Institute of Standards and Technology, Gaithersburg*, MD. https://doi.org/10.6028/NIST.SP.1200-2

18 Sobenin, D.V., Solovov, R.D. & Ershov, B.G. (2026). Transformation of zerovalent iron nanoparticles in isopropanol into oxide particles: effect of water and air on mechanism and kinetics. *Journal of Molecular Liquids. 447*, 129333. https://doi.org/10.1016/j.molliq.2026.129333

19 Taurozzi, J.S., Hackley, V.A., & Wiesner, M.R. (2011). Ultrasonic dispersion of nanoparticles for environmental, health and safety assessment—issues and recommendations. *Nanotoxicology*, *5*(4), 711–729. https://doi.org/10.3109/17435390.2010.528846

20 Mane, N.P., Rane, B.R. & Jain, A.S. (2024). Advances in Nanosuspension Technology: Current Trends and Future Horizons. *Nano Biomedicine and Engineering*, *16*(4): 574–587. https://doi.org/10.26599/NBE.2024.9290092

21 Jacob, S., Nair, A. B., & Shah, J. (2020). Emerging role of nanosuspensions in drug delivery systems. *Biomaterials research*, *24*, 3. https://doi.org/10.1186/s40824-020-0184-8

22 Li, H., Zhu, M., Pang, Y., Du, H. & Liu, T. (2016). Influences of ultrasonic irradiation on the morphology and structure of nanoporous Co nanoparticles during chemical dealloying. *Progress in Natural Science: Materials International*. *26*, 562–566. https://doi.org/10.1016/j.pnsc.2016.12.002

23 Zhang, X., Jiang, X., Qu, S., Zhang, H., Yang, W., Lu, W. (2022). Effects of ultrasonication on the microstructures and mechanical properties of carbon nanotube films and their based composites. *Composites Science and Technology*. *221*, 109136. https://doi.org/10.1016/j.compscitech.2021.109136

24 Li, Y. -H., Wang, C.-C., Yi, X.-H. & Chu, H.-Y. (2023). UiO-66(Zr)-based functional materials for water purification: An updated review. *Environmental Functional Materials. 2*(2): 93–132. https://doi.org/10.1016/j.efmat.2024.02.001

25 Lin, Y., Min, K., Ma, W., Yang, X., Lu, D., Lin, Z., Liu Q. & Jiang, G. (2024). Probing the stability of metal–organic frameworks by structure-responsive mass spectrometry imaging. *Chemical Science*. *15*, 3698–3706. https://doi.org/10.1039/D4SC00021H

26 Bondarenko, L., Baimuratova, R., Dzeranov, A., Pankratov, D., Kicheeva, A., Sushko, E., Kudryasheva, N., Valeev, R., Tropskaya, N., Dzhardimalieva, G. & Kydralieva, K. (2024). Fenton reaction-driven pro-oxidant synergy of ascorbic acid and iron oxide nanoparticles in MIL-88B(Fe). *New Journal of Chemistry*. 48, 10142–10160. https://doi.org/10.1039/D4NJ00963K

27 Elmore, W.C. (1938). Ferromagnetic Colloid for Studying Magnetic Structures. *Physical Review*. *54*, 309–310. https://doi.org/10.1103/PhysRev.54.309

28 Xu, X., Ma, J., Wang, A. & Zheng, N. (2023). N-Sulfonyl amidine polypeptides: new polymeric biomaterials with conformation transition responsive to tumor acidity. *Chemical Science*. 15(5), 1769–1781. https://doi.org/10.1039/d3sc05504c

29 Sun, R., Wang, Y., Shi, W., Zhang, H., Liu, J. & He, W. (2024). Acidity-Triggered "Sticky Spotlight": CCK2R-targeted TME-sensitive NIR fluorescent probes for tumor imaging *in vivo*. *Bioconjugate Chemistry*. *35*(4), 528–539. https://doi.org/10.1021/acs.bioconjchem.4c00040

30 Liu, Y., Huang, S., Sun, H.J., Liu, Y., Liang, L., Nan, Q., Wang, T., Chen, Z., Tang, J., Hu, C. & Zhao, J.R. (2023). Amorphous Cu-Mn hopcalite as novel Fenton-like catalyst for H_2O_2-activated degradation of tetracycline at circumneutral pH. *Journal of Science: Advanced Materials and Devices. 8*(3), 100603. https://doi.org/10.1016/j.jsamd.2023.100603

31 Maniakova, G. & Rizzo, L. (2023). Pharmaceuticals degradation and pathogens inactivation in municipal wastewater: A comparison among UVC photo-Fenton with chelating agents, UVC/H_2O_2 and ozonation. *Journal of Environmental Chemical Engineering*. *11*(6), 111356. https://doi.org/10.1016/j.jece.2023.111356

32 Schwaminger, S.P., Syhr, C., & Berensmeier, S. (2020). Controlled Synthesis of Magnetic Iron Oxide Nanoparticles: Magnetite or Maghemite? *Crystals*, *10*, 214. https://doi.org/10.3390/cryst10030214

33 Gorski, C.A., & Scherer, M.M. (2010). Determination of nanoparticulate magnetite stoichiometry by Mössbauer spectroscopy, acidic dissolution, and powder X-ray diffraction: A critical review. *American Mineralogist*, *95*(7), 1017–1026. https://doi.org/10.2138/am.2010.3435

34 Bogart, L.K., Blanco-Andujar, C. & Pankhurst, Q.A. (2018). Environmental oxidative aging of iron oxide nanoparticles. *Applied Physics Letters*, *113*, 133701. https://doi.org/10.1063/1.5050217

35 Saber Braim, F., Noor Ashikin Nik Ab Razak, N., Abdul Aziz, A., Qasim Ismael, L., & Kayode Sodipo, B. (2022). Ultrasound assisted chitosan coated iron oxide nanoparticles: Influence of ultrasonic irradiation on the crystallinity, stability, toxicity and magnetization of the functionalized nanoparticles. *Ultrasonics sonochemistry*, *88*, 106072. https://doi.org/10.1016/j.ultsonch.2022.106072

36 Stolyar, S.V., Bayukov, O.A., Yaroslavtsev, R.N., Knyazev, Yu.V., Ladygina, V.P., Gerasimova, Yu.V. & Iskhakov, R.S. (2019). Ion Reduction in Iron Oxide and Oxihydroxide Nanoparticles During Ultrasonic Treatment. *Advanced Powder Technology*. *30*. 2620–2625. https://doi.org/10.1016/j.apt.2019.08.009

37 Kim, D., Lee, G., Oh, S. & Oh, M. (2019). Unbalanced MOF-on-MOF growth for the production of a lopsided core–shell of MIL-88B@MIL-88A with mismatched cell parameters. *Chemical Communications*. *55*, 43–46. https://doi.org/10.1039/C8CC08456D

38 Bondarenko, L., Baimuratova, R., Reindl, M., Zach, V., Dzeranov, A., Pankratov, D., Kydralieva, K., Dzhardimalieva, G., Kolb, D., Wagner, F.E., Schwaminger, S.P. (2024). Dramatic change in the properties of magnetite-modified MOF particles depending on the synthesis approach. *Heliyon*, *10*, 6, e27640. https://doi.org/10.1016/j.heliyon.2024.e27640

39 Pukazhselvan, D., Granadeiro, C.M., Loureiro, F.J., Shaula, A.L., Mikhalev, S.M., Goncalves, G., & Fagg, D.P. (2023). Comparative analyses of MIL-88B (Fe) and MIL-100 (Fe) metal organic frameworks as active anode materials for Li ion batteries. *Electrochimica Acta*, *465*, 142989. https://doi.org/10.1016/j.electacta.2023.142989

40 Ramos, M.D.N., Silva, G.L.S., Lessa, T.L. & Aguiar, A. (2022). Study of kinetic parameters related to dyes oxidation in ascorbic acid-mediated Fenton processes. *Process Safety and Environmental Protection*. *168*, 1131–1141. https://doi.org/10.1016/j.psep.2022.10.083

41 Gogate, P. R., & Patil, P. N. (2015). Combined treatment technology based on synergism between hydrodynamic cavitation and advanced oxidation processes. *Ultrasonics sonochemistry*, *25*, 60–69. https://doi.org/10.1016/j.ultsonch.2014.08.016

42 Pouran, S.R., Aziz, A.R., & Daud, W.M. (2015). Review on the main advances in photo-Fenton oxidation system for recalcitrant wastewaters. *Journal of Industrial and Engineering Chemistry*, *21*, 53–69. https://doi.org/10.1016/j.jiec.2014.05.005

43 Li, J., Zhao, L., Qin, L., Tian, X., Wang, A., Zhou, Y. & Chen, Y. (2016). Removal of refractory organics in nanofiltration concentrates of municipal solid waste leachate treatment plants by combined Fenton oxidative-coagulation with photo–Fenton processes. *Chemosphere*, *146*, 442–449. https://doi.org/10.1016/j.chemosphere.2015.12.069

44 Pouran, S.R., Raman, A.A., & Daud, W.M. (2014). Review on the application of modified iron oxides as heterogeneous catalysts in Fenton reactions. *Journal of Cleaner Production*, *64*, 24–35. https://doi.org/10.1016/j.jclepro.2013.09.013

45 Pouran, S.R., Aziz, A.A., Daud, W.M.A.W., & Embong, Z. (2015). Niobium substituted magnetite as a strong heterogeneous Fenton catalyst for wastewater treatment. *Applied Surface Science*, *351*, 175–187. https://doi.org/10.1016/j.apsusc.2015.05.131

46 Costa, R.C., Lelis, M.F.F., Oliveira, L.C.A., Fabris, J.D., Ardisson, J.D., Rios, R.R.V.A., Silva, C.N. & Lago, R. M. (2006). Novel active heterogeneous Fenton system based on Fe3− xMxO4 (Fe, Co, Mn, Ni): The role of M^{2+} species on the reactivity towards H_2O_2 reactions. *Journal of hazardous materials*, *129*(1-3), 171–178. https://doi.org/10.1016/j.jhazmat.2005.08.028

47 Magalhães, F., Pereira, M.C., Botrel, S.E.C., Fabris, J.D., Macedo, W.A., Mendonça, R., Lago, R.M. & Oliveira, L.C.A. (2007). Cr-containing magnetites $Fe_{3-x}Cr_xO_4$: The role of Cr^{3+} and Fe^{2+} on the stability and reactivity towards H_2O_2 reactions. *Applied Catalysis A: General*. *332*, 115–123. https://doi.org/10.1016/j.apcata.2007.08.002

48 Liang, X., Zhong, Y., He, H., Yuan, P., Zhu, J., Zhu, S., & Jiang, Z. (2012). The application of chromium substituted magnetite as heterogeneous Fenton catalyst for the degradation of aqueous cationic and anionic dyes. *Chemical Engineering Journal*, *191*, 177–184. https://doi.org/10.1016/j.cej.2012.03.001

49 Pouran, S.R., Bayrami, A., Aziz, A.A., Daud, W.M.A.W., & Shafeeyan, M.S. (2016). Ultrasound and UV assisted Fenton treatment of recalcitrant wastewaters using transition metal-substituted-magnetite nanoparticles. *Journal of Molecular Liquids*, *222*, 1076–1084. https://doi.org/10.1016/j.molliq.2016.07.120